2025 | Faculty of Engineering Technology

UHASSELT
KNOWLEDGE IN ACTION

UCLouvain

Doctoral dissertation submitted to obtain the degrees of
- Doctor of Engineering Technology | UHasselt
- Docteur en Sciences de l'ingénieur et technologie | UCLouvain

Romain Scaffidi

DOCTORAL DISSERTATION

Next-generation kesterite thin-film solar cells: development, characterization and modeling

IMO-IMOMEC
UHASSELT imec

Promoters: Prof. Dr Bart Vermang | UHasselt, Interuniversity Microelectronics Centre
Prof. Dr Denis Flandre | UCLouvain

D/2025/2451/77


imec
fwo
Energy
Ville

Do, or do not
There is no try...
MASTER YODA

Acknowledgements

Surely, this work would have not been possible without the support of many people whom I must thank dearly.

Promoters and jury First of all, I would like to especially thank my two promoters, **Professor Denis Flandre** and **Professor Bart Vermang**, as well as my daily supervisor **Professor Guy Brammertz**. Your complementarity and always interesting feedback were key during these four years, and I learned to remain pragmatic in all situations thanks to you.

Denis, I would have never discovered the beauty of academic research without you. From our first contact during your captivating course about electronic devices to our first research collaboration during the summer of 2018, you made me feel from the start that my opinion was valuable and you never expressed any form of hierarchy between us. This simplicity, combined with an extreme scientific rigor, were valuable skills that I could hopefully learned from you. You were actually part of most milestones of my academic career, from my first research internship at the end of my bachelor to giving me the opportunity to combine an Erasmus in Sweden followed by a really exciting master thesis at EnergyVille and finally proposing me a doctoral researcher position while I was selling Christmas trees on a parking lot during the COVID pandemic. Knowing that I could always have an insightful and in-depth technical discussion about any topic with you was essential along my PhD journey. Thank you very much for helping me grow over all those years.

Bart, I truly appreciate that you always trusted me with trying new things and accepting new challenges. From my very first moments as a researcher, you never told me once not to take an opportunity, whether it was about presenting my results at a Solliance meeting only a few weeks in my master thesis internship or take responsibility for managing Jonathan's master thesis in my first year of PhD. This everlasting trust you put in me provided me with a lot of self-confidence, which was key to navigate the sometimes dark waters of scientific research. You made me such a more versatile researcher, transcending my dissemination skills and always providing strategic advice when relevant. You acknowledged early on my keen for taking up challenges and my will to pursue a career in academia, for which you accompanied me as I was trying to open up to other important aspects next to purely technical research. Finally, I very much value your guidance in tempering my attempts to control and predict everything. Thanks to you, I feel now much more ready to embark on the next chapter of my career.

Guy, you taught me mostly everything I know and I can easily affirm that all of this work is an extension of your own. From you I gained not only endless knowledge but also humility and to always keep a critical mindset in science, which will be invaluable assets in the rest of my journey as a researcher. I dearly hope that closely working with you during these 4 years will have made me a more rigorous researcher as much driven by fundamental understanding as you are. I can never thank you enough for everything I learned from you on the technical point of view but also for your never ending kindness and goodwill. You always accepted to help me or anyone in the group, every time taking the time to explain, and for that I will forever be grateful. I was very lucky to have you as my mentor, and the group is very lucky to have you as one of its core members. If my master thesis internship at EnergyVille was the deciding moment for me to pursue a PhD, it was mostly the result of our interactions, as you passed on to me your scientific curiosity. For all of this, I thank you very much.

I would like to thank the other members of my jury too, **Prof. Laurent Francis** for his kind guidance, for the supervision in the LELEC2230 course and for taking the role of secretary, **Prof. Xiaojing Hao**, **Prof. Johan Lauwaert**, **Dr. Ivan Caño Prades** and **Prof. Patrizio Manganiello**, whose comments and suggestions have all contributed to improving this manuscript and myself as a researcher, and finally **Prof. Ronald Thoelen** for chairing.

In all four Belgian institutions having hosted me during these four years, UHasselt, imec, EnergyVille and UCLouvain but also in UPC where I stayed more than 5 months for a research visit, I must thank all the technical and administrative staff, my fellow students and colleagues as well as all other people whom I exchanged with or who helped me.

At UHasselt, imec and EnergyVille

- Sarallah, my partner in crime, those conferences would have been very different without your shining smile, sharp mind and sassy jokes. I learned a lot from you, both on the personal and professional levels, including the critical character of registering for an excursion at a conference. I know our paths will cross again and I wish you all the best until then.

- Daniely, you are a wonderful person and as wonderful colleague, always keeping a good mood and supportive to everyone, despite your unmatched craziness. I always enjoyed chatting with you, and I wish you and Robin anything but happiness in the future, you both deserve it.

- Gizem, in the summer 2020, you proposed to use the results I had obtained for my master thesis in your paper. It was the first time I felt like contributing to something real in research, and largely contributed to my desire to start this PhD, and for that I will forever be

grateful. Your always happy and positive mood as well as your scientific expertise was/is an essential part of the Chalcogenide PV group, and I personally always enjoyed exchanging with you. I wish you, Sven and your soon-to-be extra person a happy life.

- Busra, the EUPVSEC conference in Milan set the good mood for the years to come afterwards, and I always enjoyed meeting with you at EV to chat or in the lab to (occasionally) work. I know you would like me to take more pictures, and I will try to work on it as I am leaving Belgium. I dearly hope we meet again in the future, only the best to you.

- Jonathan, I would have never expected to be so lucky as to have such a talented researcher as my first master student, and even less to find with you the key to the EnergyVille commuting challenge. Thank you for all the interesting discussions on the way to and back from Genk, and for the amazing co-management of the EV PhD committee.

My other past and present colleagues with whom it was always possible to either have an interesting scientific discussion or simply a casual fun chat over a coffee (or beer in the best scenario): Thomas Ratz (we both started working on kesterites when everybody else around was thinking them dead, still we made it through), Robbe (special thanks for helping with the portfolio), Joao and Jacopo for the EV PhD committee, Tim, Joost, Selin, Valerie, Raju, Sownder, Sujith, Abraham, Mina, Sunil and Vishal. Also the guidance, help and kindness from senior researchers Sudhanshu, Jessica, Tom, Arantxa, Aslihan, you all contributed to making me a better researcher.

At UCLouvain

- Nicolas Roisin for always providing support and help, for the joint supervision of the amazing LELEC2330 course, for the interesting collaborations, the cool memories at the ICOOPMA conference and for that short but intense period of table tennis breaks.

- Noémie Bidoul for the long discussions in the office about our scientific struggles and trying to revolutionize the ICTEAM vision about transport to conferences.

- Thibaut Pirson for your eternal positiveness and the always enlightening discussions.

All past and present colleagues from our research group and from the A189 and A188 offices, especially Xi, Clémentine, Eléonore, Ottilie, Loic, Tom, Quentin, Qi, Anne-Sophie, Nicolas Marchal, Thomas Ratier for maintaining a happy mood and a pleasant work environment, along with senior researchers Fares, Valeriya and Léopold for their guidance and advice.

At UPC in Barcelona I must thank **Prof. Edgardo Saucedo** and his whole research group, which I hold dear in my heart. My research visit among you was a huge success and will forever remain in my memory thanks to all of you.

- Edgardo, this experience would have not happened without you kindly approaching me at the MATSUS conference and our symbolic handshake at MRS one month later. I am truly grateful to you for welcoming me in your group and lab, and giving me the opportunity to get a highly needed second wind in my PhD journey.

- Alex and Yuancai, thank you both for teaching me so much and for reigniting the flame of research within me when it was flickering. My PhD journey would not have been so pleasant and satisfying without your tremendous support. Your contribution to this work is unvaluable and I am happy to now count you as dear friends.

- Alejandro, if science was one big motivation to come work every day in the UPC lab, you were another. Our daps still resonate in the halls of the fourth floor, and you truly are a friend of mine, if not a brother.

- Maykel, my friend, hanging out with you was always a pleasure, and you were one of the first to make me feel at home in Barcelona, thank you very much for that.

Axel, we ended up sharing many late night moments, whether it was in the office or elsewhere, and it surely contributed to this beautiful experience, merci. Ivan, thank you for being part of my jury, for bringing along your unwavering passion for materials science and for your kindness during my research visit at UPC. Arnau, doing all these experiments would have been a lot less fun without your fiery playlists and I am still dreaming about your masterpiece assists delivered on Friday football. Outman, for the shared moments of hard work and good fun, and the afternoons playing football on the beach. Pol, for keeping secret the One Piece plot and the many late-night memories. Arindam, for the amazing collaboration involving countless hours spent in the characterization lab and your friendliness. Edoardo, for teaching me the true meaning of Italianship. Oriol, for designing the waffle and beer puzzle image of myself. Cibran, David, Eloi, and Joaquim, for making the EMRS Spring 2024 edition so much fun. Zac and Sergio, for the guidance and the great time together in Japan. Marcel, for your kindness and positiveness. I want to also thank the other researchers whom with I crossed path in the UPC lab, Yassine, Carla, Alice and David Payno, and in the building, Alba, Claudia, Ares, Rebecca, Helen, Kevin, Jacob; all other players I teamed up with or against on the football pitch, including my Italian friends Andrea, Vito and Mirko; and finally my friend Michiel from the pádel practice. All of you made me feel welcome in Barcelona and willing to one day return.

Friends and family Apart from the work environment, many people in my personal life in Belgium were also essential to the success of this work and must therefore be thanked too, for which the French translation is provided below.

On the one hand, I am extremely lucky to have **wonderful friends** around me, and some in particular to which I owe the biggest thank you: Guillaume, Louka, Thomas, Maxime, Martin, Pierre, Jonas, Arnaud, Léopold, Pedro, Sarah, Manon, Chloé, Yasmine, Sidonie, Lucas, Cyril et Lorenzo. Having all of you around me along this journey was vital. You were one of the keys to help me get through all the ups and downs, and I would have never been able to achieve this without each and every one of you. Thank you all, love you.

On the other hand, none of this would have been possible without the tremendous and unwavering support from all **my family**. In particular, I owe a heartfelt gratitude to my aunt Patricia and my closest-to-brother cousin Jeremy. Thank you both for being such wonderful people and for always supporting me, I am lucky to have you in my life. I would like to also dedicate this thesis to two people who are both now in a better place: my great uncle Elio, he was a wonderful, loving and kind person, and he taught me how a simple life can be easily enjoyed and bring happiness; my cousin Amandine, who was the sun of our lives and who still shines from above, I will never forget you smiling and laughing.

Finally, and most importantly, I want to thank, from the bottom of my heart, **my brothers Baptiste and Thomas, their loved ones Fanny and Céline, my nephew Alex and my parents**, whom I all love very much.

- Baptiste, you taught me persistence, to always surpass myself and open up to others. Even though there has always been competition between us, it only strengthened our bond and made me who I am today. Whether it is in sports, on the dancefloor or in life in general, you are one of my role models and for that, I thank you.
- Fanny, our late night conversations at the Carolo are long gone but I still enjoy talking to you as much as ever. Thank you for your kindness and positiveness.
- Thomas, you taught me thoroughness and to always remain critical and curious, not only in science. If not for you, I might have never found the passion for research within me. Thank you for your eternal guidance, for always listening to me when I am facing doubts and concerns and for also being a role model.
- Céline, you have been part of our family for a long time, and I have always admired your unwavering perseverance and courage, which where a personal source of inspiration.
- Alex, you do not know it yet, but I was almost there for your first moment into this world, and I have truly enjoyed watching you grow since then. I cannot wait to see you again.

- Dad, thank you for teaching me simplicity, for having passed on your sense of humor and for supporting our ambitions and projects.
- Mom, I owe you the biggest thank you of all. None of this whatsoever would have been possible without you, your bulletproof mental strength, your endless compassion and your unrelenting love. You are the most important person in my life, and there are not enough words to express how much I have learned from you. Wherever future takes me, you will always be the first one to know and the first one in my heart. Thank you for being a role model, I love you.

Amis et famille *A côté du travail, beaucoup de personnes dans ma vie personnelle en Belgique étaient également indispensables à la réussite de ce travail et doivent donc être tout autant remerciées.*

Premièrement, je suis extrêmement chanceux d'avoir autour de moi des amis formidables, dont certains en particulier que je dois remercier: Gui, Douk, Tom, Max, Mourt, Pierre, Jo, Arnaud, Léo, Pedro, Sar, Man, Chlo, Yas, Sido, Lucas, Cyril et Lolo. Vous avoir à mes côtés pendant ces 4 ans était vital. Vous étiez une des clés pour m'aider à traverser les hauts et les bas, et je n'aurais pas pu y arriver sans chacun de vous. Merci, je vous aime.

Deuxièmement, rien de tout ça n'aurait été possible sans le soutien énorme et sans faille de toute ma famille. En particuler, je dois une reconnaissance éternelle à ma tantine Patricia et mon cousin et presque 3e frère Jeremy. Merci à vous deux d'être les personnes que vous êtes et de toujours me soutenir, je suis chanceux de vous avoir dans ma vie. Je voudrais également dédier ce travail à deux personnes qui se trouvent désormais dans un endroit meilleur: mon grand oncle Elio, il était une personne formidable, aimante et bienveillante, qui m'a appris comment trouver la joie et le bonheur dans une vie simple; ma cousine Amandine, qui était le soleil de nos vies et qui brille toujours d'en haut, je n'oublierai jamais ton rire et ton sourire.

Finalement, et non des moindres, je voudrais remercier, du fond du coeur, mes frères Baptiste et Thomas ainsi que leurs moitiés respectives Fanny et Céline, mon neveu Alex et mes parents, que j'aime tous profondément.

- *Baptiste, tu m'as appris la détermination, le dépassement de soi et l'ouverture aux autres. La compétition qui existe entre nous ne fait que renforcer nos liens et a forgé la personne que je suis aujourd'hui. Que ce soit en sport, sur la piste de danse ou dans la vie en général, tu es un de mes modèles et pour ça, je te remercie.*
- *Fanny, beaucoup de temps s'est passé depuis nos premières discussions tardives à la Carolo, mais j'apprécie toujours autant parler avec toi. Merci pour ta gentillesse et ta positivité à toute épreuve.*
- *Thomas, tu m'as appris la rigueur, l'esprit critique et la curiosité, et pas seulement dans la science. Sans toi, je n'aurais probablement*

jamais trouvé la passion de la recherche en moi. Merci de toujours me guider, de prêter une oreille attentive quand j'ai des doutes et des inquiétudes et d'être aussi un modèle de réussite pour moi.

- *Céline, tu fais déjà partie de la famille depuis longtemps et j'ai toujours admiré ton courage et ton enthousiasme sans faille, qui ont été une grande source d'inspiration personnelle.*
- *Alex, tu ne le sais pas encore, mais j'étais presque là pour tes premiers instants parmi nous, et j'ai adoré te voir grandir depuis ce jour. J'ai hâte de te revoir.*
- *Papa, merci de m'avoir appris la simplicité, de m'avoir transmis ton sens de l'humour sans faille et d'avoir soutenu nos ambitions et projets.*
- *Maman, c'est à toi que je dois le plus grand des merci. Absolument rien de tout ça n'aurait été possible sans toi, ta force mentale à toute épreuve, ta compassion sans limites et ton amour infaillible. Tu es la personne la plus importante de ma vie et j'ai appris de toi tellement de choses que je ne peux toutes les citer ici. Quel que soit l'endroit où l'avenir me mène, tu seras toujours la première personne au courant et la première dans mon coeur. Merci d'être mon modèle, je t'aime.*

Summary

In order to cope with the ever-growing energy demand while cutting down greenhouse gas emissions, solar power must be deployed at the largest extent possible. This requires the widespread installation of photovoltaic technologies beyond utility-scale to comply with the greater integrability and adaptability needed in emerging markets. Thin-film solar cells based on chalcogenide compounds hold highly encouraging promises for such applications, due to their versatile architecture and tuneable properties. Among them, kesterite materials with the $Cu_2ZnSn(S,Se)_4$ crystalline structure provide an interesting alternative based on Earth-abundant elements and compatible with low-cost processes, making them a promising solution with reduced carbon footprint and cost. Yet, their performance must be increased to align their competitiveness with commercial technologies. Reaching this objective entails to resolve their still too significant deficit in open-circuit voltage, which is the main culprit for their limited efficiency around 15% for the highest-performing devices. The physical origin of these losses is manifold: control of the kesterite phase and composition in a uniform fashion, regulation of its crystalline quality to favour low disorder, monitoring of the growth environment and conditions enabling weakly defective materials and interfaces, as well as preserving all these aspects when tuning the absorber bandgap for relevant applications, among others. This thesis aims at tackling these challenges on different levels.

First of all, it is demonstrated through an extensive review of the literature that germanium (Ge) alloying constitutes a promising strategy to enhance the quality of kesterite thin films by overcoming intrinsic electronic limitations related to tin (Sn) while promoting superior structural morphology. On top of this, this approach also allows to control the absorber bandgap, which contributes to a greater versatility of the kesterite compounds. Still, most studies have focused on low to moderate proportions of Ge corresponding to a narrow bandgap range not yet matching the specifications of emerging applications. This highlights the need to pursue the exploration of the broad Ge compositional domain. The importance of the kesterite deposition process is also detailed, showing the greater potential of solution-based routes allowing finer control of composition and phases at the lab scale, thus providing conditions for high efficiency. In comparison, samples from the presented starting baseline, deposited via sequential physical processes, exhibit limited performance with symptoms of low opto-electronic kesterite quality and device non-ideality.

Following this, a molecular ink chemical route in ambient environment is developed to allow flexible Ge alloying in high-quality single-phase thin-

film kesterite absorbers. Remarkably, this updated baseline enables to tune the kesterite bandgap without compromising material quality. In particular, narrow band tails associated to mitigated open-circuit voltage radiative losses are ensured for a broad bandgap range in which the device performance potential is therefrom augmented. Resolving this prerequisite for photovoltaic absorbers is however only one of the main steps in the development of a solar cell technology. Indeed, non-radiative losses leading to low minority carrier lifetime remain an even more critical challenge to be tackled. It originates from the numerous intrinsic point defects in the kesterite lattice, the exact nature, location and dominance of which remain partly undetermined. It is therefore essential to pinpoint the underlying mechanism responsible for defect-assisted recombination and the associated performance losses. This is especially relevant for the next-generation devices based on multinary-alloyed solution-processed kesterite absorbers which are presently leading the way towards future efficiency breakthroughs.

Eventually, based on the study of temperature- and light intensity-dependent current-voltage measurements confronting analytical models and SCAPS-1D simulations, the closer-to-ideal behaviour of state-of-the-art kesterite devices is demonstrated as a consequence of weaker band tailing and bandgap and potential fluctuations. The close agreement with the single diode formalism combined with the observed dark and light reconciliation allow to gauge the various contributions to the open-circuit voltage deficit. The dominant loss mechanism is hypothesized to be a defect-rich kesterite layer at the interface with the buffer, highlighting the diode ideality factor and saturation current density as the primary causes of restrained performance. Light is also shed on carrier trapping-detrapping via shallow defect states as the mechanism behind shunt leakage currents, also contributing to lower efficiency. The applicability of this whole analysis extends across various samples, which emphasizes its potential to support further enhancements of next-generation kesterite solar cells.

Résumé

Pour faire face à la demande croissante d'énergie tout en réduisant les émissions de gaz à effet de serre, l'énergie solaire doit être déployée le plus largement possible. Pour ce faire, il est nécessaire de diversifier l'installation de technologies photovoltaïques au-delà de la simple production d'énergie à grande échelle, afin de se conformer à la plus grande intégrabilité et adaptabilité requise dans les marchés émergents. Les cellules solaires à couche mince basées sur des composés de chalcogénures sont très prometteuses pour de telles applications, en raison de leur architecture polyvalente et de leurs propriétés ajustables. Parmi eux, les matériaux kesterites avec la structure cristalline $Cu_2ZnSn(S,Se)_4$ constituent une alternative intéressante basée sur des éléments abondants sur Terre et compatibles avec des processus peu coûteux, ce qui en fait une solution prometteuse avec une empreinte carbone et un coût réduits. Cependant, leurs performances doivent être améliorées afin d'aligner leur compétitivité sur les technologies commerciales. Pour atteindre cet objectif, il faut résoudre leur déficit encore trop important en tension de circuit ouvert, qui est le principal responsable de leur efficacité limitée, de l'ordre de 15 % pour les dispositifs les plus performants. L'origine physique de ces pertes est multiple: contrôle de la phase kesterite et de sa composition de manière uniforme, régulation de sa qualité cristalline pour favoriser un faible désordre ainsi que de l'environnement et des conditions de croissance permettant d'obtenir des matériaux et des interfaces à faible densité de défauts, et finalement la préservation de tous ces aspects lors de l'ajustement de la bande interdite de l'absorbeur pour des applications pertinentes, entre autres. Cette thèse vise à relever ces défis à différents niveaux.

Tout d'abord, il est démontré à travers une revue extensive de la littérature que l'alliage de germanium (Ge) constitue une stratégie prometteuse pour améliorer la qualité des couches minces kesterites en surmontant les limitations électroniques intrinsèques liées à l'étain (Sn) tout en promouvant une morphologie structurelle supérieure. En outre, cette approche permet également de contrôler la bande interdite de l'absorbeur, ce qui contribue à une plus grande polyvalence des composés kesterite. Cependant, la plupart des études se sont concentrées sur des proportions faibles à modérées de Ge correspondant à une bande interdite étroite qui ne correspond pas encore aux spécifications des applications émergentes. Cela souligne la nécessité de poursuivre l'exploration du vaste domaine de composition en Ge. L'importance du processus de dépôt de kesterite est également détaillée, montrant à l'échelle du laboratoire le plus haut poten-

tiel des procédés réalisés en solution permettant un contrôle plus fin de la composition et de la phase crystalline, fournissant ainsi les conditions d'une plus grande efficacité. En comparaison, les échantillons provenant du procédé de départ, déposés via des processus physiques séquentiels, présentent des performances limitées avec des symptômes de faible qualité opto-électronique de la couche kesterite et de non-idéalité des dispositifs finaux.

Ensuite, un procédé chimique pour encre moléculaire en environnement ambiant est développé, permettant l'intégration flexible de Ge dans des absorbeurs couche mince kesterite de haute qualité et comportant une seule phase crystalline. Il est remarquable que cette nouvelle recette de fabrication permette d'ajuster la bande interdite de la kesterite sans compromettre la qualité du matériau. En particulier, un rétrécissement des queues de bande associé à l'atténuation des pertes radiatives de tension en circuit ouvert est assuré pour une large gamme de bandes interdites dans laquelle le potentiel de performance des dispositifs est ainsi augmenté. La résolution de cette condition préalable pour les absorbeurs photovoltaïques n'est cependant qu'une des principales étapes du développement d'une technologie de cellule solaire. En effet, les pertes non radiatives entraînant une faible durée de vie des porteurs minoritaires restent un défi encore plus important à relever. Elles proviennent des nombreux défauts ponctuels intrinsèques du réseau cristallin kesterite dont la nature exacte, l'emplacement et la dominance restent en partie indéterminés. Il est donc essentiel de mettre en évidence le mécanisme sous-jacent responsable de la recombinaison assistée par les défauts et des pertes de performance associées. Ceci est particulièrement important pour les dispositifs de prochaine génération basés sur des absorbeurs kesterite à alliage multiple produits en solution, qui ouvrent actuellement la voie à de futures percées en matière d'efficacité.

Finalement, à partir de l'étude de mesures courant-tension à différentes températures et intensités lumineuses, confrontées aux modèles analytiques et aux simulations SCAPS-1D, le comportement plus idéal des dispositifs kesterite de dernière génération est démontré comme conséquence de la réduction des queues de bande et des fluctuations de la bande interdite et du potentiel. La correspondance étroite avec le formalisme à une diode, combiné à la réconciliation observée entre le comportement dans le noir et sous lumière, permet d'évaluer les différentes contributions au déficit de tension en circuit ouvert. Le mécanisme de perte dominant est hypothétiquement une couche de kesterite riche en défauts située à l'interface avec le buffer, mettant en évidence le facteur d'idéalité de la diode et la densité de courant de saturation comme causes principales de la limitation des performances. La lumière est également faite sur le (dé-)piégeage des porteurs via des états de défaut peu profonds comme mécanisme à l'origine des courants de fuite, contribuant également à une efficacité moindre. L'applicabilité de l'ensemble de cette analyse s'étend à divers échantillons, ce qui souligne son potentiel pour mener à de nouvelles améliorations des cellules solaires kesterite de prochaine génération.

Samenvatting

Om aan de steeds groeiende vraag naar energie te kunnen voldoen en tegelijkertijd de uitstoot van broeikasgassen te verminderen, moet zonne-energie op de grootst mogelijke schaal worden ingezet. Dit vereist een brede implementatie van fotovoltaïsche technologieën die verder gaan dan enkel de utiliteitsschaal, om te voldoen aan de nood aan beter integreerbare en flexibele oplossingen in opkomende markten. Dunnefilm-zonnecellen op basis van chalcogenideverbindingen zijn veelbelovend voor dergelijke toepassingen, vanwege hun veelzijdige architectuur en afstelbare eigenschappen. Onder deze materialen bieden kesterietmaterialen met de kristalstructuur $Cu_2ZnSn(S,Se)_4$ een interessant alternatief, gebaseerd op overvloedig beschikbare elementen en compatibel met goedkope fabricageprocessen. Dit maakt ze tot een veelbelovende oplossing met een kleinere ecologische voetafdruk en lagere kosten. Desondanks dienen de prestaties ervan te worden verbeterd om competitief te worden met bestaande commerciële technologieën. Het bereiken van deze doelstelling vergt het aanpakken van het nog steeds aanzienlijke tekort aan open-klemspanning, dat de voornaamste beperking vormt voor het huidige rendement, dat rond 15% ligt voor de best presterende zonnecellen op basis van deze kesterietmaterialen. De fysische oorzaken van deze verliezen zijn veelzijdig: het uniform controleren van de kesterietfase en -samenstelling, het beheersen van de kristalliniteit om een lage mate van roosterwanorde te bevorderen, het monitoren van de groeiomgeving en -condities die de vorming van defectarme materialen en interfaces mogelijk maken, alsook het behouden van al deze aspecten bij het afstemmen van de bandgap van de absorberlaag, onder meer voor relevante toepassingen. Het bereiken van deze doelstelling vergt het oplossen van deze structurele en procesgerelateerde uitdagingen op verschillende niveaus. Deze thesis beoogt deze uitdagingen aan te pakken.

Allereerst wordt op basis van een uitgebreide literatuurstudie aangetoond dat het legeren met germanium (Ge) een veelbelovende strategie vormt om de kwaliteit van kesterietdunnefilms te verbeteren, door intrinsieke elektronische beperkingen gerelateerd aan tin (Sn) te overwinnen en tegelijkertijd een gunstiger structurele morfologie te bevorderen. Bovendien maakt deze benadering het mogelijk om de absorptiebandgap te controleren, wat bijdraagt aan de verhoogde veelzijdigheid van kesterietverbindingen.Toch richt het merendeel van de bestaande studies zich op lage tot matige Ge-gehalten, wat resulteert in een beperkt bandgapbereik dat nog niet voldoet aan de vereisten van opkomende toepassingen. Dit benadrukt de noodzaak om de verkenning van het brede Ge-

compositiedomein voort te zetten. Ook het belang van het depositieproces voor kesteriet wordt in detail toegelicht, waarbij het grotere potentieel van oplossingsgebaseerde routes wordt aangetoond. Deze maken een verfijndere controle over samenstelling en fasevorming mogelijk op labschaal, en creëren zo gunstige voorwaarden voor een hoge efficiëntie.Ter vergelijking vertonen de zonnecellen uit de hier gehanteerde initiële baseline, afgezet via sequentiële fysieke processen, een beperkte prestatie, gekenmerkt door een lage opto-elektronische kwaliteit van het kesterietmateriaal en afwijkingen ten opzichte van ideale zonnecelwerking.

Daaropvolgend wordt een chemische route met moleculaire inkt in een omgevingsomgeving ontwikkeld om flexibele Ge-legeerbaarheid in hoogwaardige enkelfasige dunnefilm-kesterietabsorbers mogelijk te maken. Opmerkelijk genoeg maakt deze geüpdatete baseline het mogelijk om de bandgap van kesteriet af te stemmen zonder dat dit ten koste gaat van de materiaalkwaliteit. In het bijzonder worden smalle bandstaarten, die verband houden met een beperking van radiatieve spanningsverliezen, over een breed bandgapbereik gerealiseerd, waarin het prestatiepotentieel van de zonnecel aanzienlijk wordt vergroot. Het oplossen van deze vereiste voor fotovoltaïsche absorbermaterialen is echter slechts één van de belangrijkste stappen in de ontwikkeling van een zonneceltechnologie. Nietradiatieve verliezen, die leiden tot een lage levensduur van minderheidsladingsdragers, blijven namelijk een nog fundamentelere uitdaging die moet worden aangepakt. Deze verliezen zijn het gevolg van de talrijke intrinsieke puntdefecten in het kesterietrooster, waarvan de exacte aard, locatie en dominantie nog slechts gedeeltelijk gekend zijn. Het is daarom essentieel om het onderliggende mechanisme te identificeren dat verantwoordelijk is voor defect-geassisteerde recombinatie en de bijbehorende prestatieverliezen. Dit is in het bijzonder relevant voor de volgende generatie zonnecellen op basis van multinary-alloyed, oplossingsverwerkte kesterietabsorbers, die momenteel de weg wijzen naar toekomstige doorbraken in efficiëntie.

Op basis van temperatuur- en lichtintensiteitsafhankelijke stroomspanningmetingen, in combinatie met analytische modellen en SCAPS-1D-simulaties, wordt aangetoond dat state-of-the-art kesterietzonnecellen een gedrag vertonen dat dichter bij het ideale benadert, als gevolg van zwakkere bandstaartvorming en beperktere bandgap- en potentiaalfluctuaties. De sterke overeenkomst met het enkeldiodeformalisme, gecombineerd met de geobserveerde consistentie tussen de metingen in het donker en licht, maakt het mogelijk om de verschillende bijdragen aan het openklemspanningsdeficit te kwantificeren. Het dominante verliesmechanisme wordt verondersteld een defectrijke kesterietlaag te zijn op het grensvlak met de buffer, wat de diodidealiteitsfactor en de saturatiestroomdichtheid benadrukt als de belangrijkste oorzaken van de beperkte prestaties. Daarnaast werpt de analyse ook licht op carrier trapping-detrapping via ondiepe defecttoestanden als het mechanisme achter shuntlekstromen, wat ook bijdraagt aan een lagere efficiëntie. De toepasbaarheid van deze hele analyse strekt zich uit over verschillende stalen, wat het potentieel ervan onder-

streept om de verdere efficiëntieverbeteringen in kesterietzonnecellen van de volgende generatie te ondersteunen.

Contents

CHAPTER 1
Introduction

This first chapter introduces the current socio-economical context in which solar energy, or photovoltaics (PV), must evolve in parallel with the present climate crisis. To elaborate on the remaining challenges faced by such technologies, the related theory is developed via the conceptualization of an ideal PV device, then refined towards a more realistic structure very relevant to the central topic herein: kesterite thin-film solar cells. The corresponding state-of-the-art is eventually covered in order to emphasize key research questions and objectives tackled throughout this thesis.

1.1 Global context

Human society heavily depends on energy to properly function. Biologically speaking, humans only require 2000 kcal or 8.4 MJ on an average day to sustain the needs of their bodies. Still, the global energy demand in 2023 was 445 EJ[1]. Considering a world population of 8 billion people, this means that 1.5 GJ of energy is daily consumed on average per each citizen of this world, representing close to 200 times our biological requirement. This excess of required energy, mostly related to the increase of our comfort, is even greater in high-income countries which globally demand more than 2.5 times as much energy per capita as developing states[1]. Within this enormous amount of energy consumed by human society, 20 % accounted for electricity in 2023[1]. To supply those needs while taking into account losses in conversion and transport, around 30 000 TWh of electrical energy was generated worldwide that year. By 2050, this required electricity supply is projected to double whereas its proportion in the global energy mix will further increase to reach around a third of the whole energy demand[1]. One reason for this is the remarkable versatility of electrical energy, which can be substituted to nearly any other energy source to achieve the same function.

However, nowadays electricity is still mainly produced via strongly carbonized means. Indeed, in 2023, 70 % of the total electricity supply relied

on a single well-known process: the combustion of fossil fuels (coal, gas and oil)[1], which is responsible for more than 90 % of all emissions of carbon dioxide (CO_2) around the world. Considering that roughly half of all the 37 Gt of CO_2 emitted in 2023[1] entered the atmosphere[2], it means that human activity alone contributes to 0.5% of the global atmospheric concentration. This is far from negligible if one considers that humans represent a 50 times lower proportion of all living beings on Earth, i.e. 0.01% of the global biomass[3]. This enormous quantity of emitted CO_2 has been continuously increasing over the past years and is not likely to significantly decrease in the coming decades. This is due, among others, to the growing world population, the feeding of which requires intensive agriculture and immense cattle sizes causing the emission of other gases such as methane (CH_4) and nitrous oxide (N_2O). Initially, those 3 gases contribute to Earth's ability to regulate its own temperature by retaining heat within its atmosphere through the greenhouse effect, hence called greenhouse gases (GHG). However, the rampant development of human activity has brought their concentration to levels never reached before (Figure 1.1).

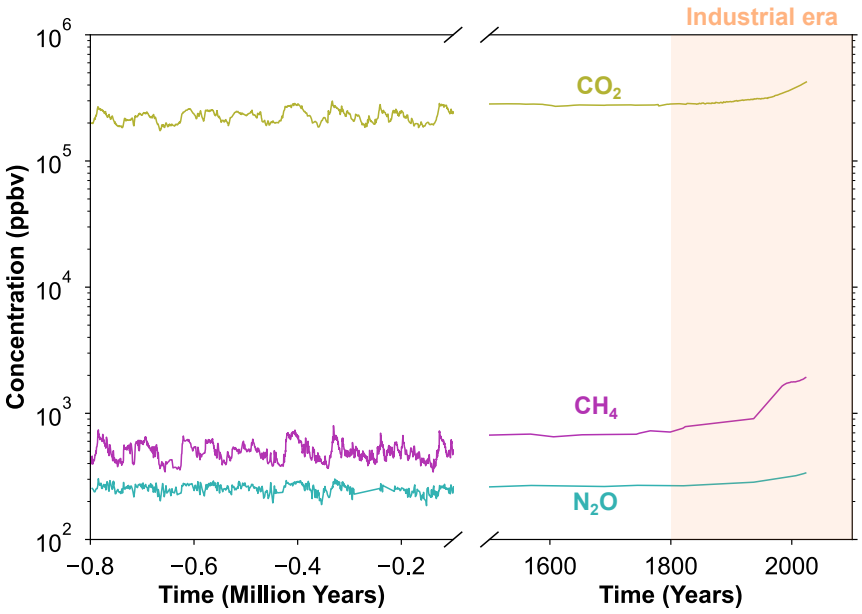

Figure 1.1: Timely evolution of the atmospheric concentration of 3 GHG (CO_2 in green, CH_4 in purple and N_2O in cyan) in parts per billion volume from the most ancient estimations to the present values[4]. The horizontal axis is cut to emphasize the recent increases within the industrial era.

A serious consequence is the fast and steady increase of the global average temperature, which recently breached the associated planetary

boundary[5,6]. This induces a pressure so strong on the Earth environmental equilibrium that it cannot compensate for it on its own, bringing us worryingly close to dangerous tipping points. Tangible consequences are already felt around the globe, with an increased frequency of extreme climate events (wildfires due to heatwaves, floodings due to heavy rains, droughts, ...) to which low-income countries are more vulnerable despite having a comparatively much smaller responsibility[4]. The global average temperature, higher by +1.54 °C in 2024 as compared to the pre-industrial era, has officially broken the first safety threshold of +1.5 °C defined by the Paris Agreement, legally binding the 196 signing countries to pursue effort against climate change. Theoretically, to remain within this target, GHG emissions must peak by 2025 at the latest[4], meaning that the years ahead are going to be key with regards to environmental policies and energy defossilization. Indeed, if the current GHG emission rate of roughly 40 Gt per year is maintained, less than 3 decades will be sufficient to reach the second safety threshold of +2 °C defined by the Paris Agreement[4]. This stresses the extreme urgency with which global GHG emissions must be cut down and the monumental efforts that must be devoted to operate a fair transition towards a carbon-neutral society that no longer degrades the equilibrium of the planet on which it depends to thrive.

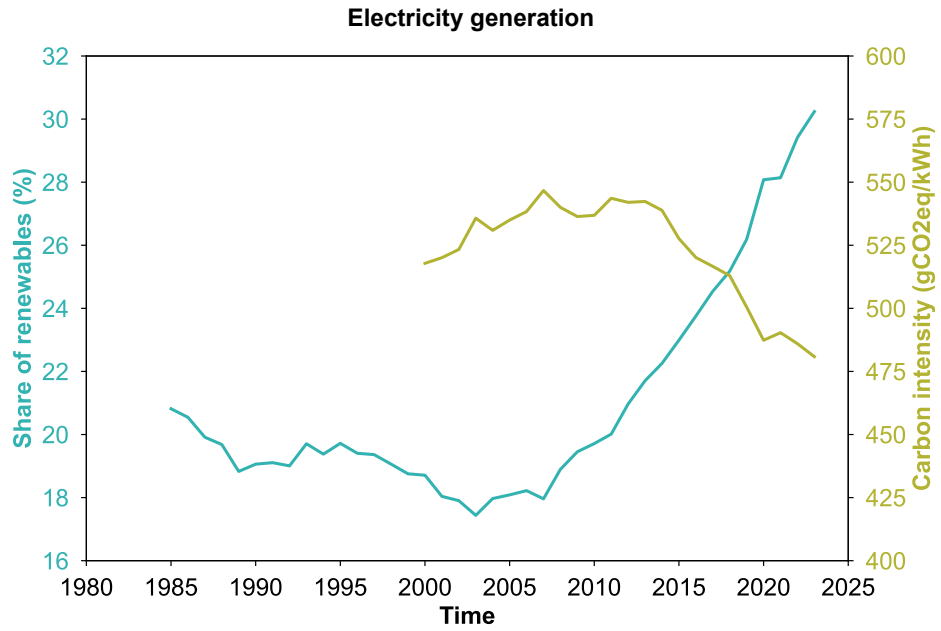

Figure 1.2: Timely evolution of the share of renewables (cyan) and the carbon intensity (green) in the global electricity generation.[7]

Fighting climate change may be one of the greatest challenges that

humanity has ever faced. In order to tackle it, we could simply reduce the total amount of energy consumed worldwide so as to mitigate GHG emissions. Since 80% of those are related to industry and transport[1], decreasing the energy demand would require society to operate radical socio-economical changes and the populations to strongly rethink their life habits and consumption behaviour, among others. This reduction in energy consumption would likely translate into decreasing gross domestic products while not necessarily compromising human and economic development as developed in the newly established theory of degrowth[8]. However, in the past decades, global energy demand has been steadily increasing, growing on average by 2 % per year with no strong evidence of slowing down in a near future[7]. Therefore, it does not appear feasible to counteract global warming solely through energetic sobriety. In parallel, one must also improve energetic efficiency not only in terms of yield but also in terms of carbon footprint. Indeed, approximately 30 % of the global primary energy supply is lost during conversion and transport while the CO_2 intensity of electricity generation should be scaled down by at least a factor 10 over the next decade to reach the Net-Zero 2050 target[1]. Fortunately, renewable energies (solar-, wind-, geothermal- and hydro-power as well as bioenergy) have recently proven their great potential to cope with human energy needs while cutting down carbon emissions[7], as illustrated in Figure 1.2. Over the past two decades, the share of renewables in the global electricity supply soared significantly to reach 30% in 2023, contributing to a parallel reduction of the associated carbon intensity. This trend was enabled, among others, by large technological developments of renewable energy sources making them more competitive, as discussed in the next section.

1.2 Solar energy

Within the energy market, competitiveness is quantified by the price to pay for generating 1 kWh of energy, i.e. the levelized cost of energy (LCOE). For solar power, the general topic of this thesis, this metric has been remarkably plummeting in the last decade, in parallel with a skyrocketing installed capacity (Figure 1.3). In 2023, 1 kWh produced by PV costed less than 0.5 c$ while more than 1 TW of PV power was cumulatively installed worldwide. Although wind power held a similar record that year, its progression up to that point happened to be much slower.

1.2.1 Technological development

This trend can be understood through the learning rate, which determines the pace at which a technology becomes cheaper as its deployment in-

creases. Indeed, since their early days in the 1970's, the price of solar modules has on average become lower by 20% for every doubling of the cumulative installed capacity[9]. From 2010 to 2019, the technological learning rate of PV reached 36 %[7,9], which strongly contrasts with nuclear and fossil energies while largely outperforming other renewable technologies. Solar power is thus in a positive feedback learning loop, which is only possible via a strong research effort in parallel of the industrial development, both mutually feeding in each other. The remarkable self-learning ability of the PV industry is an indication of its pivotal role in the transition towards a sustainable energy production system in the future. While its total installed capacity is currently growing exponentially, saturation is still far from reach as solar resources are nearly unlimited: in a single hour without clouds, the Sun is irradiating approximately as much energy towards Earth as human society consumes over a whole year. Besides this, compared to other energy sources, solar power has the advantage of minimal visual impact and safety hazards, low maintenance requirements and long lifetime over 30 years. Nevertheless, major research and development challenges still need to be tackled so as to maintain the spreading of PV on a large scale, e.g. reducing the consumption of silver and improving module recycling strategies[10], or implementing adapted energy storage solutions[11]. The emergence of important new market segments such as tandem devices and sector-integrated PV also raises the need for more versatile, modular and seamless solar cell architectures as well as alternative materials that are complementary with the mainstream utility-scale technologies based on crystalline Si (c-Si)[11].

Thin-film solar cells based on chalcogenide materials provide an adapted solution to many of those new constraints. Indeed, this family of semiconductor alloy compounds includes a broad variety of crystalline structures, all composed of metallic cations (Cu, Ag, Zn, Cd, Sn, Ge, Sb, ...) chemically bound to chalcogen elements (S, Se, Te, ...) and characterized by strong light absorption in a range of the solar spectrum that can be tuned via their stoichiometry[12]. The resulting solar panels could theoretically reach the same performance as c-Si for a largely reduced thickness combined with controllable opacity and colour. These features make them very relevant for different applications such as building-, infrastructure- and vehicle-integrated PV (BIPV, IIPV and VIPV) due to their lower weight, seamless aesthetics and potentially bendable designs. Their versatile optical properties are also relevant to filter the incoming radiation over agricultural lands to enhance crop yield (agrivoltaics) or to harness indoor light for powering small-scale portable electronics (indoor PV). Advances in such sectors constitutes a step forward towards greater public acceptance, beyond the traditional solar power plants and domestic rooftop PV panels.

Among the chalcogenide materials adapted to PV applications, one in

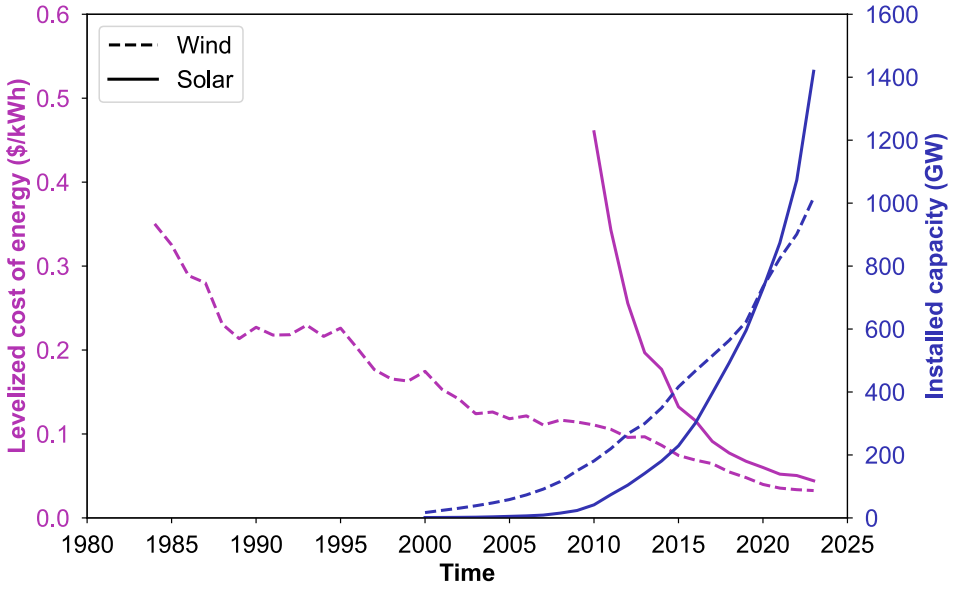

Figure 1.3: Timely evolution of the levelized cost of energy (purple) and total installed capacity (blue) for solar (solid) and wind (dashed) power.[7]

particular has attracted significant research activity in the past decades, i.e. chalcopyrite Cu(In,Ga)Se_2 (CIGS), enabling solar cells with very high performance at the lab scale[13], expected to provide an interesting platform for low-carbon footprint all-thin-film tandem solar cells[14] and relying on largely Earth-abundant Cu. However, the latter aspect is negatively compensated by the parallel usage of rare metals such as In and Ga[15], which significantly restrains the large-scale deployment potential of that technology. Fortunately, there exists one akin family of compounds called kesterites which share equivalent versatility as CIGS while relying on more abundant elements. Still, PV devices based on these materials currently remain at a lower stage of development than CIGS and showcase lower performance in the lab, thus demanding large research efforts to make them more relevant and mature on a technological standpoint. To reach this objective, this thesis proposes strategies to increase their efficiency through a deeper understanding of the main performance barriers while enhancing their versatility to extend the range of potential applications. Doing so inevitably requires to build a prior fundamental understanding of the physics of solar cells and their inner workings, which is done in the following section.

1.2.2 Theoretical background

This section, greatly inspired from P. Wurfel's book[2], develops the fundamental theory of solar cells with a phenomenological description of the intrinsic thermodynamics while providing the essential criteria for an effective conversion of light to electrical energy. The development then narrows down towards the relevant case of PN junctions, the opto-electrical behaviour and final performance of which are eventually detailed.

1.2.2.1 Ideal 3-layer device

A generic 3-layer solar cell device is considered with the idealistic band diagram in Figure 1.4. At the center is located the absorber, a semiconductor material with bandgap E_g which is the main photoactive layer of the structure. The absorber is sandwiched in between two membranes that are selective for either type of charge carriers, i.e. holes or electrons, as elaborated further. Each membrane is connected to the external circuit via a metallic contact or terminal. For this theoretical case, it is considered that the selective membranes and the metallic contacts do not interact with the incident light, which is thus completely let through to the absorber. The solar cell working principle is herein developed in the framework of an engine that converts energy from one form to another in different steps. Its function is to produce an output electrical current from the incoming solar energy.

Indeed, the Sun is continuously irradiating large amounts of light, composed of photons with various energies hv, in all directions including Earth. This is the consequence of its surface temperature of 5800 K, due to fusion reactions in its core, predicted to cover a broad part of the electromagnetic spectrum according to Kirchhoff's law of thermal radiation. The emitted solar irradiation reaches Earth with a certain spectrum, i.e. the exact quantity of photons at each energy or wavelength composing it, determined among others by the Sun-to-Earth distance and the various atmospheric absorptions along the way due for instance to water vapour, ozone, CO_2, etc, ... Widely used in the PV field, the standard AM1.5G solar spectrum, which considers an incidence angle of roughly 48° and includes diffuse as well as direct light, is the input energy of the generic solar cell in Figure 1.4. In order to convert it into an output electrical power, three conversion steps are operated.

As a first step, the absorber transforms a certain part of the incident light into thermal energy. Indeed, within the whole solar spectrum, only photons with an energy $hv > E_g$ interact with the absorber. This comes from the fact that, upon light absorption, the energy of a photon is actually transmitted to an electron in the valence band of the absorber, meaning that only energies greater than the bandgap allow it to jump towards

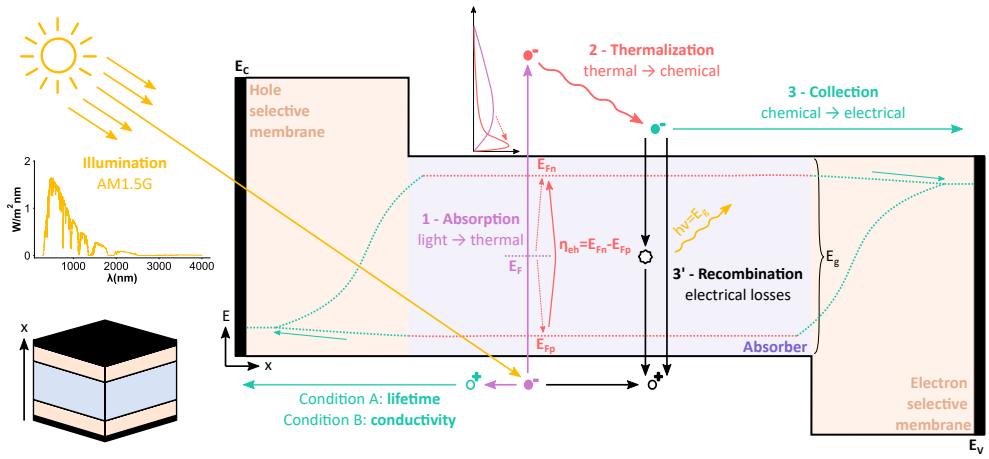

Figure 1.4: Schematic representation of the band structure of an ideal 3-layer solar cell and the different steps associated to the energy conversion mechanism. The corresponding energy (E) and position (x) axes are shown as black perpendicular arrows, with E_C the conduction band minimum and E_V the valence band maximum. The solar illumination and AM1.5G spectrum are illustrated on the left. The black rectangles on both sides of the device are metallic contacts which do not impede light from reaching the absorber. The gradients in E_{Fn} and E_{Fp} towards these terminals, normally not discernible, are exaggerated for the sake of clarity. A geometrical representation of the solar cell stack is provided in the bottom left.

higher-energy permitted states in the conduction band. Following Beer-Lambert's law, a greater proportion of incident photons is absorbed as the absorber is thicker. Immediately after the photon absorption, the photoexcited electron gains an energy hv and leaves behind a vacancy or hole in the valence band, both sharing the exact same broad energy distribution as the incident photon and forming together a so-called electron-hole (e-h) pair. Applying this to the whole valence band electron population of the absorber and taking into account the intense solar irradiation, the concentrations of photogenerated electrons in the conduction band and associated holes in the valence band become much greater than in the situation without illumination. During this process, the charge carriers produced upon solar irradiation remain in thermo-chemical equilibrium with the Sun, which has two implications. First, there exists only one constant electrochemical potential in the structure, herein also denoted Fermi level E_F, meaning that the total current is zero. Second, e-h pairs share the same high temperature of 5800 K as the Sun, thus carrying a tremendous quantity of thermal energy which shall be converted into a chemical potential during the following conversion step.

Indeed, in a timescale of the order of $1ps$ after the photon absorption, photogenerated electrons and holes are losing a significant part of their thermal excitation in the form of vibrations or phonons transferred to the

absorber crystalline lattice, generating entropy. Consequently, the e-h pairs quickly cool down to the same temperature as the lattice while their concentration remains unchanged. This important process, called thermalization, is inherent to the conversion of thermal to chemical energy using a semiconductor absorbing the broad solar spectrum. Once thermal equilibrium with the lattice is reached, photogenerated charge carriers must obey Pauli's principle and minimize their free energy. This implies that the energy distribution of electrons in the conduction band (resp. holes in the valence band) is transitioning towards a Fermi-Dirac statistics with an associated quasi-Fermi level E_{Fn} (resp. E_{Fp}). Following the photo-induced increase in the concentration of both electrons and holes, E_{Fn} must move closer to E_C and E_{Fp} must move closer to E_V. This phenomenon by which E_{Fn} and E_{Fp} move away from each other by simultaneously approaching their respective band edge is named quasi-Fermi level splitting. This entails the establishment of an electrochemical potential $\eta_{eh} = E_{Fn} - E_{Fp}$ carried by each e-h pair in the absorber, an important requirement for the appearance of a voltage difference between the device terminals as detailed in the next section. In order to eventually generate an output electrical current towards an external circuit, photogenerated carriers must be extracted out of the solar cell.

In the context of this thesis, this last step is the most critical in comparison with the two former. Indeed, in the present state-of-the-art kesterite solar cells, sufficient light absorption is typically ensured by adapted absorber thickness and optical management of surrounding layers while thermalization losses are an unavoidable yet essential part of the physical functioning of solar devices. In contrast, for most technologies still at the research level, completing the chemical to electrical conversion in an efficient way remains a significant challenge, which unfolds in two conditions herein named A and B. On the one hand, within the absorber, the photogenerated carriers must persist during a sufficiently long time in their respective bands to be collected at the device terminals. Indeed, after a certain period called the lifetime, excited e-h pairs naturally fall back into their resting state and are lost in the conversion process. This phenomenon, called recombination, happens when an electron in the conduction band jumps down towards a lower energy state in the valence band, thereby eliminating a hole and losing energy either as heat or light as discussed further below. It should be mitigated as much as possible in order to guarantee that the lifetime of carriers is sufficiently long for them to be collected at the device terminals, which constitutes condition A. On the other hand, within this carrier lifetime, electrons and holes must be driven out of the solar cell to generate an output power. Since e-h pairs are electrically neutral, only a migration of electrons and holes in opposite directions leads to a nonzero net current. An important prerequisite is that electron and hole currents can be controlled separately, which must be first verified. To as-

sess this, one should determine the possible mechanisms responsible for carrier transport. In the present case, the two main driving forces are an electric field, i.e. drift, or a gradient in carrier concentration, i.e. diffusion. Even though the usual mathematical development considers the total current of one carrier type as the sum of drift and diffusion currents having opposite directions, a more legitimate physical representation considers it as resulting from a gradient in the associated quasi-Fermi energy, itself the sum of drift and diffusion forces. Therefore, the electron and hole currents are driven by the gradient in E_{Fn} and E_{Fp}, respectively. Since in the present case both energy levels are split due to the incident illumination, the electron and hole currents can indeed be individually controlled. Still, there remains the challenge, in our generic structure in Figure 1.4, to effectively separate e-h pairs towards the desired terminals, i.e. electrons at the right contact and holes at the left contact. As such, the E_{Fn} gradient is much less significant towards the right than it is towards the left, potentially driving electrons towards the hole selective membrane. However, the position of E_{Fp} close to the valence band in that part of the device implies that electron conductivity is low and thus that the undesired leftward electron current is small. The complementary reasoning applies to the undesired rightward hole current through the electron selective membrane. Therefore, the actual driving force for carrier collection at the desired terminals is a selective conductivity on either side of the absorber. This is in no way contradicting the previous statement that quasi-Fermi energy gradients are driving carrier currents. The selective conductivity of the electron and hole membranes actually lead to gradients in E_{Fn} and E_{Fp}, respectively, as emphasized by the solid red arrows in Figure 1.4. These gradients, usually too weak to be graphically discernible are yet strong enough to drive carriers in the desired directions, justifying the exaggeration of their magnitude for the sake of clarity. Overall, the splitting of the quasi-Fermi levels is not only a consequence of the carrier thermalization towards chemical energy storage per e-h pairs but also provides the fundamental condition to individually drive electrons and holes within the solar cell, which can be achieved by placing membranes with selective conductivities on both sides of the absorber. This constitutes condition B for an effective conversion of chemical energy towards a significant output electrical current.

In practice, fulfilling this requirement for the electron selective membrane in Figure 1.4 is done through n-type doping so as to largely increase the electron conductivity and reduce the hole conductivity. The band properties of this membrane are also chosen so that it has not only the same electron affinity as the absorber to allow significant electron current towards the right-hand terminal but also a wider bandgap to ensure that its low p-type conductivity is not counteracted by hole injection from the absorber. The reciprocal reasoning can be applied to the p-doped hole

selective membrane. For a minimum doping level of both membranes, detailed in the next section, the ideal 3-layer device thus eventually respects conditions A and B, meaning that the conversion of chemical to electrical energy is effective. This completes the whole energy conversion process and realizes the targeted function of the solar cell: using incoming sunlight to produce a decent electrical power output. However, finding experimentally relevant materials that perfectly mimic the function and band structure of the theoretical solar cell in Figure 1.4 is challenging. To overcome this barrier, large research efforts have been devoted to developing alternative device architectures which deliver a similar function while being practically realizable and potentially scalable. One of them, the PN junction, is particularly important for the present topic, as detailed in the next section.

1.2.2.2 PN junctions

The PN junction architecture, in its simplest form, is a stack composed of two layers, one p-type doped and the other n-type doped. Its most common example in the field of PV is the n-Si/p-Si homojunction getting its name from using the same material, i.e. Si, for both layers. Although this structure does not totally fulfill the requirements provided by the ideal structure in Figure 1.4, tremendous research efforts have been devoted to its enhancement over the past decades. The resulting solar cell technology, supported by the great abundance of Si on Earth, is highly competitive and largely market-dominant. Yet, kesterite solar cells studied herein are based on another variation of this architecture, i.e. the PN heterojunction (HJ). Its generic structure shown in Figure 1.5 is composed of two different materials. On the left, a thicker semiconductor layer with a bandgap E_g matching the solar spectrum plays the role of absorber. It is also p-doped with acceptor concentration N_A to simultaneously act as hole selective membrane. On the right, a thinner semiconductor layer is n-doped with donor concentration N_D to serve as electron selective membrane, and called buffer in the rest of the text. This material is chosen with a wider bandgap to let most of the light through to the absorber as desired in the HJ architecture while avoiding hole photogeneration to maintain its selective conductivity for electrons. This last feature is further guaranteed by its large hole barrier in the valence band preventing hole injection from the absorber. The choice of different materials for the absorber and buffer make the HJ structure closer to the ideal 3-layer device than the standard Si-based homojunction. It also leads to a conduction band discontinuity and associated potential barrier at the HJ interface due to the difference in electron affinity. Figure 1.5 depicts the case of spike-like alignment in which the electron affinity of the absorber is higher than for the buffer, as typically seen in kesterite devices studied in this thesis.

The constant illumination induces a splitting of the quasi-Fermi levels $\eta_{eh} = E_{Fn,abs} - E_{Fp,abs}$ in the absorber, with E_{Fp} maintained close to the valence band towards the left-hand contact due to the absorber p-type doping and E_{Fn} maintained close to the conduction band towards the right-hand contact due to the buffer n-type doping. Both quasi-Fermi levels must rejoin at the electrodes due to their metallic character. The band bending around the junction induced by the doping asymmetry pushes free electrons and holes away from that so-called space-charge region (SCR) where only fixed ionized doping atoms remain, with opposite signs on either side. Thus, there exists an intrinsic electric field in the HJ structure. Yet, its presence is an inevitable consequence of realizing the selective conductivity requirement through doping of materials, but not a necessary condition for the solar cell to properly function. The gradients in quasi-Fermi energy towards the metallic contacts, i.e. E_{Fn} to the right and E_{Fp} to the left not discernible in Figure 1.5, act as the driving force for e-h pair separation and current generation in the HJ structure.

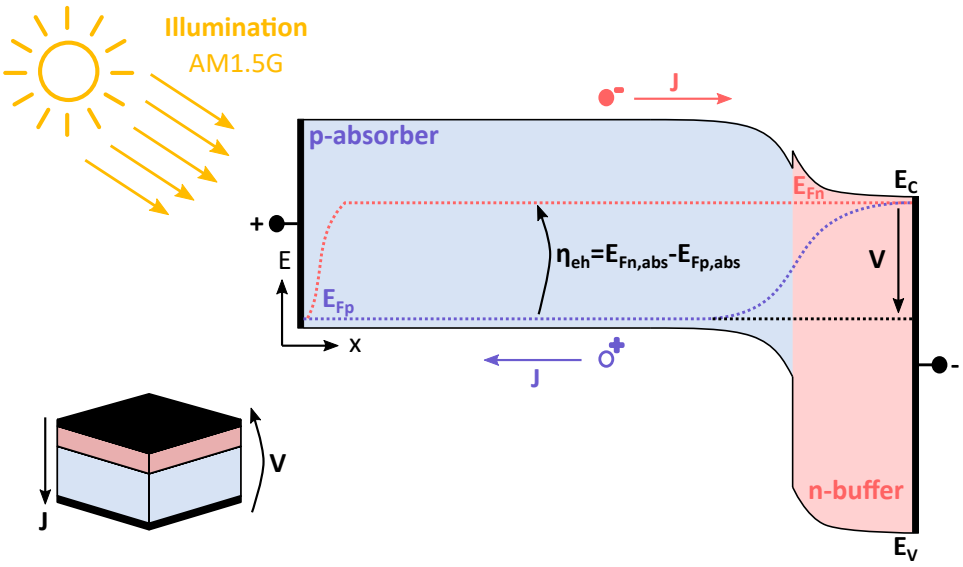

Figure 1.5: Schematic representation of the HJ band structure under constant AM1.5G illumination, with the perpendicular axes for energy (E) and position (x) shown as black arrows. The black rectangles on both sides of the device are metallic contacts which do not impede light from reaching the absorber, with the positive electrode on the left and the negative electrode on the right leading to a positive voltage difference V as indicated by the black arrow. The positive direction of the current density J is given by the black arrow next to the hole in the valence band, i.e. towards the left of the device. A geometrical representation of the HJ stack is provided in the bottom left.

At this point, the HJ structure is demonstrated to fulfill the theoretical

solar cell requirements provided by the development in Section 1.2.2.1 but its energy conversion yield is not yet quantified. In particular, one must assess the ratio between the input solar power P_{in} fixed to $1000W/m^2$ for the AM1.5G solar spectrum and the output electrical power P_{out} delivered to the external circuit via the metallic contacts. This is also called the power conversion efficiency (PCE) expressed as $\eta = \frac{P_{out}}{P_{in}}$, which is herein determined through P_{out} since P_{in} typically is a problem parameter. The overarching goal in PV research thus consists in maximizing P_{out} for a given P_{in} so as to obtain the best PCE. As highlighted previously for the energy conversion mechanism in Figure 1.4, the separation and collection of photogenerated e-h pairs is the most critical process for the PV technology of interest. This is therefore the focus point when determining P_{out} in the rest of this section. To do so, a theoretical approach relevant to PN junctions in general is realized based on the notations and HJ device stack in Figure 1.5, considered under constant AM1.5G illumination and thus in steady-state conditions. As for any electronic device, the output power P_{out} can be expressed as the product of the voltage difference V between its terminals and the current density J flowing through it. When $P_{out} = J * V > 0$, the device is generating power, e.g. when J and V follow the positive directions illustrated in Figure 1.5. Determining P_{out} eventually translates into relating V and J to specific properties of the HJ stack.

As mentioned above, the light-induced quasi-Fermi level splitting in the absorber $\eta_{eh} = E_{Fn,abs} - E_{Fp,abs}$ provides an important condition for the establishment of a potential difference V here defined as the difference between E_{Fp} at the left-hand contact and E_{Fn} at the right-hand contact. The quantity η_{eh} actually represents the total amount of light-harvested chemical energy carried by e-h pairs, the greatest part of which must be preserved along their way to the metallic contacts to maximize P_{out}. In other terms, η_{eh} defines the theoretical upper bound for V. The ideal situation $|V| = |\eta_{eh}|$ in Figure 1.5 requires two conditions. On the one hand, appropriate contact materials with work functions matching the relevant quasi-Fermi level position must be used. On the other hand, the doping levels in the buffer and absorber must be sufficient to induce, in the dark, a distance between E_{Fp} at the left-hand contact and E_{Fn} at the right-hand contact that matches η_{eh}. Respecting both criteria as in Figure 1.5 ensures that the reservoir of chemical energy harnessed from the incoming sunlight is not wasted due to the solar cell design, but not yet resolves the issue of collecting photogenerated carriers at the device electrodes.

Indeed, the current of charge carriers J reaching the device terminals in a given time is mainly limited by their natural inclination to be lost through recombination, as transport properties are first assumed ideal for the sake of simplicity in this development. Their impact is discussed in the next section. Quantifying J in our structure still requires to determine the rate of recombination, considered only radiative at this point, i.e. photoexcited

electrons directly recombine with valence band holes by emitting light of an energy equal to the absorber bandgap E_g. In steady state, the charge continuity provides that the recombination rate, limiting the current J, must be equal to the generation rate, determining the voltage difference $V = -\eta_{eh}$ through light absorption. A mathematical link between the recombination-limited current J and the photogeneration-induced voltage V is obtained via the Boltzmann relation

$$J(V) = J_{ph} - J_0\big(\exp(\frac{qV}{k_BT}) - 1\big) \tag{1.1}$$

in which k_B is the Boltzmann constant, q the electronic charge and T the temperature. J_{ph} is the photogenerated current due to the desired migration of e-h pairs towards their relevant contacts. Since the impact of transport properties is here neglected, J_{ph} is mainly dependent on the illumination level. In the dark, $J_{ph} = 0$ and the total current is equal to $J_0\big(\exp(\frac{qV}{k_BT})-1\big)$, hence usually referred to as the dark diode current, which is opposing J_{ph} and related to the loss of light-generated carriers through radiative recombination. Its expression that includes the characteristic exponential dependence on the ratio between the voltage V and the thermal energy k_BT/q of the system is typical of all PN diodes and encompasses the saturation current density J_0, the value of which depends on the amount and dominant type of recombination.

Equation 1.1 is generally called the current-voltage (JV) characteristics of solar cells. It defines the voltage V as single coordinate for the device electrical behaviour and operating point, while implying that the total current under light can be found by adding J_{ph} to the dark current, known as the superposition principle. Two points on this curve are especially important to the definition of the solar cell performance. First, when $V = 0$, i.e. when the solar cell is short-circuited, it produces a maximum positive current called the short-circuit current density J_{sc} defined by $J(0) = J_{ph} = J_{sc}$. Second, when $J = 0$, i.e. when the solar cell is an open circuit, it develops a maximum positive voltage between its terminals called the open-circuit voltage V_{oc} defined by $J(V_{oc}) = 0$. This particular state of the system occurs when the current contributions from e-h pair photogeneration and recombination are equal to one another so that $J_{sc} = J_0(\exp(\frac{qV_{oc}}{k_BT}) - 1)$. This leads to the general expression of V_{oc}:

$$V_{oc} = \frac{k_BT}{q} \ln(\frac{J_{sc}}{J_0}) \tag{1.2}$$

in which the "+1" term normally in the logarithm is neglected. Equation 1.2 defines the important role played by the dark recombination current through J_0 in the determination of V_{oc}.

The theoretical values $J_0 = 10^{-12} A/cm^2$ and $J_{sc} = 40 mA/cm^2$, close-to-ideal for typical chalcogenide thin-film solar cells, are first assumed to

pursue the development of the device PCE. Injecting those in Equation 1.1 provides the example JV curves in Figure 1.6 for both dark and lights conditions, along with the corresponding power-voltage (PV) characteristics using $P_{out}(V) = J(V) * V$, at a temperature of 300 K. The solar cell is producing power, i.e. $P_{out} > 0$, when placed under illumination, i.e. $J_{ph} > 0$, and for voltages in the first quadrant between 0 and V_{oc}. Bias points outside of this range as well as the dark curve shown in Figure 1.6 still contain useful information about the device behaviour, as discussed in Chapter 4. Figure 1.6 also highlights the existence of a certain voltage V_{max} at which P_{out} is maximum for a current J_{max} so that $P_{max} = V_{max} * J_{max}$. This metric is universally used to quantify the best-case performance of the solar cell, and can be graphically related to J_{sc} and V_{oc} by the unitless fill factor (FF) following $FF = \frac{V_{max} * J_{max}}{V_{oc} * J_{sc}}$. This provides $P_{max} = V_{oc} * J_{sc} * FF$ and the well-established definition of the PCE $\eta = \frac{V_{oc} * J_{sc} * FF}{P_{in}}$, which is the highest when J_{sc}, V_{oc} and FF are all maximized for a fixed P_{in}.

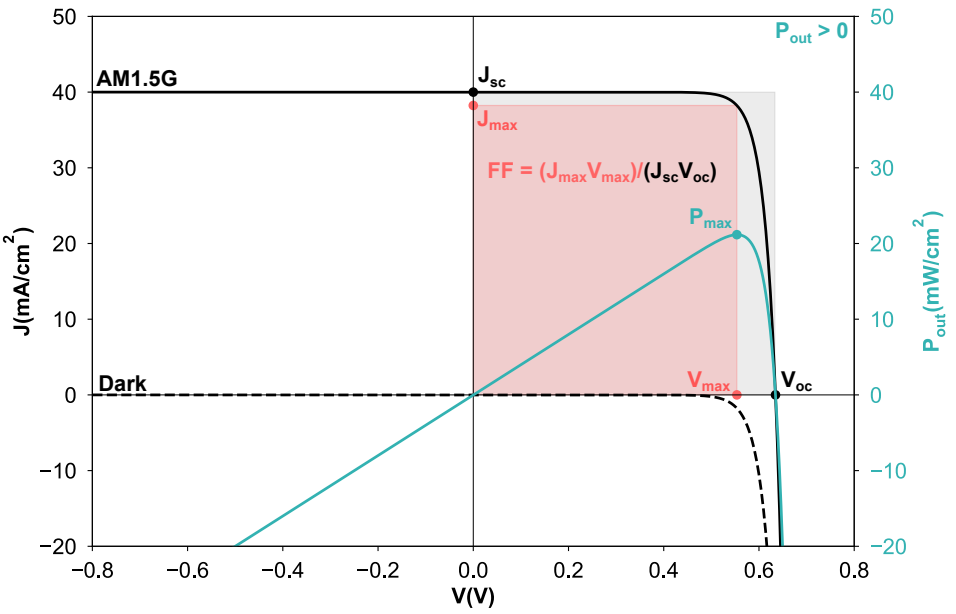

Figure 1.6: Current-voltage (JV) and power-voltage (PV) characteristics of an ideal solar cell under AM1.5G illumination (black and cyan solid line) at the room temperature of 300 K. The corresponding JV curve in the dark is shown as a black dashed line. The first quadrant corresponding to power generation (P_{out}>0) and delimited by the open-circuit voltage V_{oc} and short-circuit current density J_{sc} is highlighted in pink. The definition of the maximum power point and the graphical representation of the fill factor are illustrated.

Considering the only source of non-ideality to be the inevitable radiative recombination, the maximum values for J_{sc}, V_{oc}, FF and thus η under AM1.5G illumination are given by the Shockley-Queisser (SQ) limit[16], as functions of the absorber bandgap E_g only (Figure 1.7). In theory, this represents the most advanced level of technological development for a single-junction solar cell. Yet, in practice, radiative recombination is rarely the only source of losses in actual solar cells.

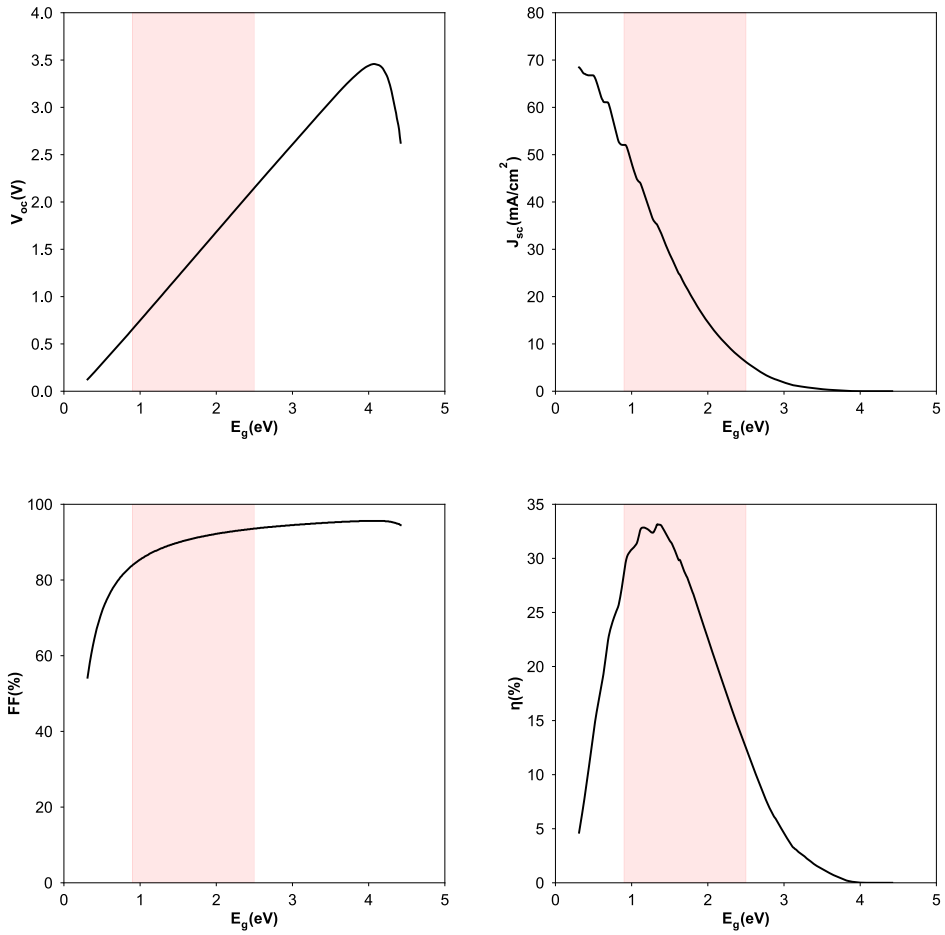

Figure 1.7: Shockley-Queisser limits for V_{oc}, J_{sc}, FF and η in function of the absorber bandgap E_g from a previous study[17], with the accessible range of bandgap values for kesterite materials highlighted in pink.

Indeed, the non-radiative counterpart of recombination (NRR) is much more likely to happen and hence usually the dominant loss mechanism. It occurs when the photoexcited electron natural return to the valence band

is facilitated by an intermediate energy level within the absorber bandgap corresponding to a defect in its crystalline lattice. The associated energy transitions are narrower than the bandgap and are usually dissipated thermally rather than in the form of light, hence its name. Following the JV formalism developed hereabove, NRR is also characterized by J_0 and therefore essential in the establishment of V_{oc} and η. Its existence also implies the addition of the ideality factor n in Equation 1.2, providing

$$V_{oc} = \frac{nk_BT}{q} \ln\left(\frac{J_{sc}}{J_0}\right) \tag{1.3}$$

Both J_0 and n depend on the defect properties and thus constitute two key metrics to quantify NRR. They are studied in-depth in Chapter 4 using a more complete version of Equation 1.1. NRR is especially critical in highly defective materials such as kesterites and the main reason for the associated thin-film solar cells to currently remain far from the corresponding SQ limits, as discussed in the next section.

1.2.3 Kesterite thin-film solar cells

Kesterite materials are quaternary chalcogenide semiconductor alloys with I_2-II-IV-VI_4 as general formula in which each roman number designates the chemical group or valency, with I, II and IV being metallic cations while VI is a chalcogen. They owe their name to their crystalline structure, which corresponds to a particular cation ordering pattern of the stannite system[18]. The most popular example is $Cu_2ZnSn(S,Se)_4$ (CZTSSe), initially investigated as an Earth-abundant alternative to CIGS relying on Sn and Zn and also exhibiting strong light absorption with a direct bandgap. Despite its central role in the development of kesterite PV absorbers, CZTSSe is only one of many possible variations of the kesterite structure, since each one of the three cation positions may be occupied by a mixture of several atoms of the relevant group, e.g. I= Cu, Ag, Li, II= Zn, Cd, Fe, Co, Ba, and IV=Sn, Ge, Si, while VI usually always remains S, Se or a combination of both. This provides numerous degrees of freedom to tune important PV properties, with as main example the bandgap possibly ranging from 0.9 to 2.5 eV and covering an optimal part of the SQ limits domain in Figure 1.7. The resulting versatility makes them promising candidates in different types of thin-film PV applications.

In order to develop real solar cells as in Figure 1.8, the kesterite materials must be deposited as thin-film layers with an adapted thickness usually between 0.5 to 2.5 μm (x direction), and over a sufficient area (y and z directions) of the order of 0.1-1 cm^2 at the lab-scale and well beyond 10 cm^2 at the industrial-scale. They also should have the expected polycrystalline morphology and the desired single-phase structure. To deposit the kesterite thin films, various processing techniques can be employed,

usually implying tradeoffs between cost, scalability and yield, and globally divided between physical- and chemical-based deposition routes. This thesis provides a basis for comparison between both approaches in Chapter 2 and 3. Once a process is established for processing kesterite absorbers of sufficient quality, an adapted buffer material must be found to complete the HJ and achieve the final solar cell function. Historically inspired from CIGS, the most popular buffer material in kesterite solar cells is n-type CdS, deposited by chemical bath deposition as a thin layer not exceeding 100 nm. It has an electron affinity similar to CZTSSe, with a larger bandgap around 2.4 eV, in agreement with the electron selective membrane requirements provided in the previous section. The CdS buffer is an essential part of the device electrical behaviour since it enables the extraction of photogenerated electrons. The completed HJ must be able to transfer the photogenerated current to an external circuit via appropriate contacts. On the one hand, the collection of photogenerated holes is typically done through a micron-thick Molybdenum fully-contacted electrode. In most fabrication processes, the kesterite absorber growth takes place atop this Mo layer, hence called the back contact and itself resting on a soda-lime glass substrate, as depicted in Figure 1.8. On the other hand, the collection of light-generated electrons over the much greater y and z dimensions is ensured by the deposition of transparent conducting oxide materials with high n-type lateral conductivity, called window layers, also used to protect the underlying layers from potential damage of subsequent processing steps. A patterned metallic electrode is then deposited at the very top of the device in order to complete its connection to the external circuit. This whole development amounts to the typical stack of kesterite thin-film solar cells depicted in Figure 1.8.

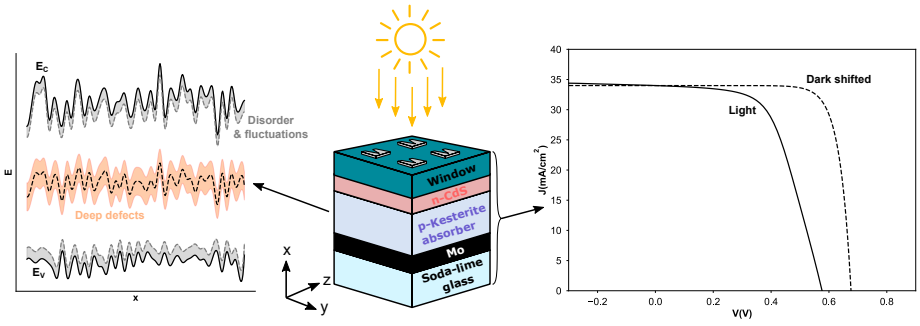

Figure 1.8: Schematic representation of the general kesterite solar cell stack under AM1.5G illumination, with the geometrical axes shown as black perpendicular arrows. The non-ideal absorber band structure is illustrated on the left, showing the effects of crystalline disorder, bandgap and potential fluctuations as well as intrinsic defects. The effect of voltage-dependent collection efficiency leading to dark-light discrepancy in JV characteristics is depicted on the right.

The latest kesterite state-of-the-art solar cells showcase an efficiency approaching 16 %[19], which constitutes a breakthrough in their development which had been previously stagnating for over a decade. They are still facing two major hurdles to become an interesting solution in the relevant PV markets.

On the one hand, their efficiency remains much lower than commercial technologies. The main reason for that is their much higher V_{oc} deficit[20–29], the origin of which is manifold. First, the intricacy of the kesterite structure induces an even more complex growth mechanism which, depending on the conditions, may happen in numerous paths involving intermediate reactions and secondary phases. This narrow phase stability range leads to the usual co-existence of multiple phases within the same kesterite layer, some of which are detrimental[25,27–30]. The complex kesterite quaternary structure is prone to the formation of intrinsic electronic defects in high densities, which raises the need to control the kesterite composition in the well-established Cu-poor and Zn-rich optimal ranges[20–23,26,27,31,32]. Certain of these defects are shallow acceptors responsible for the necessary p-type doping of the kesterite material[33]. Others are non-radiative recombination centers and the cause of important V_{oc} losses such as the Sn_{Zn} antisite originating from the Sn multivalency and believed to be particularly critical regarding performance[33–40]. The high rate of defect-assisted recombination in kesterites leads to low carrier lifetime[20,22,23,25,27–30,41] which, combined with their low mobility[42], induces short diffusion lengths and eventually voltage-dependent collection of photogenerated carriers[43,44]. This phenomenon plays a role in the determination of J_{ph}, which is not anymore simply equal to J_{sc} but also bias-dependent. To account for this effect in the JV formalism, the collection efficiency $\eta_C(V)$ is defined such that $J_{ph}(V_{oc}) = \eta_C(V_{oc}) * J_{sc}$ replaces J_{sc} in Equation 1.3. Consequently, dark-light discrepancy is typically observed in JV measurements of thin-film devices including kesterites, as illustrated in Figure 1.8. On top of this, using atoms with similar sizes, e.g. Cu and Zn, within the same crystalline lattice may lead to structural disorder due to permutation of their effective sites, eventually inducing fluctuations of both the absorber bandgap and the potential to which carriers are subjected[20–23,27,29,45]. Defects and disorder are two key components of the V_{oc} deficit of kesterites, and must be counteracted to obtain the purest material possible on the opto-electronic standpoint. Their effect on the absorber band structure is represented in Figure 1.8. Other sources of losses also exist at the absorber interfaces with adjacent layers, namely interface defects, potential barriers and secondary phases that mainly degrade carrier collection[20,25,27–29].

On the other hand, their potential to respond to emerging markets where thin-film architectures are relevant has not been yet fully exploited and/or demonstrated. In particular, such applications require to precisely control the kesterite bandgap while preserving device performance. The

traditional solution relies on tuning the S-Se ratio as inspired from CIGS technologies, but it is usually complex and realized at the expense of opto-electronic quality[20,46–49].

Various strategies are currently investigated to tackle these inherent challenges faced within the development of kesterites for PV applications. Indeed, substantial performance enhancements were attained through improvements of the kesterite/CdS interface quality[50] combined with a finer control of reaction mechanisms and kinetics as well as phase formation[26,36,38,51–56]. These were among other the results of the transition towards molecular ink processing routes which, in parallel, facilitate the multinary alloying of alternative metallic cations to overcome the defective and disordered character of the standard kesterites[23,31,36,57], e.g. replacing Cu by Li and Ag[51,52,54,58], Zn by Cd[36,59,60], and Sn by Ge[36,38,61–70], among others. The particular case of substituting Ge to Sn is highly interesting since it partially resolves the aforementioned Sn multivalency issue while also enabling bandgap engineering.

1.3 Objectives and research questions

In line with these improvement strategies, this thesis attempts to contribute to the development of next-generation kesterite solar cells, regarding both the processing of high-quality and versatile kesterite absorbers and the current understanding of their opto-electrical response and performance limitations. This is done in a three-fold structure, with each chapter articulated around a central objective and an associated research question along with the publications from which they are greatly inspired, provided both as bibliographic references throughout this thesis and in the List of Disseminations.

Chapter 2 addresses the research question ”How mature are the current kesterite solar cell technologies and what are the promising strategies to push them further ?” by assessing the current state-of-the-art of the kesterite solar cell technology within the scope of the promising Ge alloying approach, through a thorough review of nearly all the existing literature[71].

Chapter 3 treats the research question ”How can the quality and versatility of kesterite materials be improved ?”. First, the starting baseline for physically-deposited bandgap-graded Ge-alloyed kesterite solar cells is presented[72], exhibiting limited efficiency and largely improvable material quality. Then, inspired from the molecular ink chemical routes having provided recent record devices, the development of a simple and flexible process for Ge alloying in a broad composition range allows to enhance both material quality and device performance in a wide range of bandgaps[73].

Chapter 4 attempts to provide an answer to the research question ”Have there been changes in the behaviour of recently developed kesterite de-

vices and are there still unexplored facets of their opto-electrical response ?". Through a comprehensive analysis procedure of current-voltage measurements under various temperature and illumination conditions, this last part tries to establish a link between the enhanced material properties of next-generation kesterite absorbers and the device performance potential[74].

Chapter 5 concludes the thesis with a global summary of the main achievements, followed by an insight about the possible future prospects for kesterite solar cells and the associated follow-up research work.

A list of all scientific disseminations is provided in page 137. Further details about the experimental characterization techniques used in this thesis are given in Table A.1 in Appendix, along with the supplementary information of the publications from which the different chapters are inspired.

Bibliography

[1] IEA. *World Energy Outlook 2024*. Oct. 2024. URL: https://www.iea.org/reports/world-energy-outlook-2024.

[2] P. Würfel and U. Würfel. 3. Auflage. 2016.

[3] H. Ritchie. *Our World in Data* (2019).

[4] H. Ritchie, P. Rosado, and M. Roser. *Our World in Data* (2023).

[5] J. Rockström et al. *Nature* 461.7263 (2009), pp. 472–475. DOI: 10.1038/461472a.

[6] L. Caesar et al. *Potsdam Institute for Climate Impact Research, Potsdam, Germany* (2024).

[7] H. Ritchie, P. Rosado, and M. Roser. *Our World in Data* (2023).

[8] J. Hickel et al. *Nature* 612.7940 (2022), pp. 400–403. DOI: 10.1038/d41586-022-04412-x.

[9] M. Roser. *Our World in Data* (2023).

[10] P. J. Verlinden. *Journal of Renewable and Sustainable Energy* 12.5 (2020), p. 053505. DOI: 10.1063/5.0020380.

[11] G. M. Wilson et al. *J. Phys. D: Appl. Phys.* 53.49 (2020), p. 493001. DOI: 10.1088/1361-6463/ab9c6a.

[12] S. Hadke et al. *Chemical Reviews* 122.11 (2022), pp. 10170–10265. DOI: 10.1021/acs.chemrev.1c00301.

[13] M. A. Green et al. *Progress in Photovoltaics* 30.1 (2022), pp. 3–12. DOI: 10.1002/pip.3506.

[14] A. Martulli et al. *Solar Energy Materials and Solar Cells* 279 (2025), p. 113212. DOI: 10.1016/j.solmat.2024.113212.

[15] EU. *Critical raw materials*. https://single-market-economy.ec.europa.eu/sectors/raw-materials/areas-specific-interest/critical-raw-materials_en.

[16] W. Shockley and H. J. Queisser. *Journal of Applied Physics* 32.3 (1961), pp. 510–519. DOI: 10.1063/1.1736034.

[17] S. Rühle. *Solar Energy* 130 (2016), pp. 139–147. DOI: 10.1016/j.solener.2016.02.015.

[18] Y. Zhang et al. *Journal of Applied Physics* 111.6 (2012), p. 063709. DOI: 10.1063/1.3696964.

[19] M. A. Green et al. *Progress in Photovoltaics: Research and Applications* 33.7 (2025), pp. 795–810. DOI: 10.1002/pip.3919.

[20] M. He et al. *Adv. Sci.* 8.9 (2021), p. 2004313. DOI: 10.1002/advs.202004313.

[21] T. Gershon et al. *Current Opinion in Green and Sustainable Chemistry* 4 (2017), pp. 29–36. DOI: 10.1016/j.cogsc.2017.01.003.

[22] K. J. Tiwari et al. 2022, pp. 41–66. DOI: 10.1007/978-981-19-3724-8_3.

[23] S. Giraldo et al. *Adv. Mater.* 31.16 (2019), p. 1806692. DOI: 10.1002/adma.201806692.

[24] A. Wang et al. *Advanced Energy Materials* 13.2 (2023), p. 2203046. DOI: 10.1002/aenm.202203046.

[25] M. Baid et al. *Opt Quant Electron* 53.11 (2021), p. 656. DOI: 10.1007/s11082-021-03272-5.

[26] J. Li et al. *Nat Energy* 7.8 (2022), pp. 754–764. DOI: 10.1038/s41560-022-01078-7.

[27] K. Sun, F. Liu, and X. Hao. 2022. DOI: 10.5772/intechopen.101744.

[28] K. Pal et al. *Solar Energy Materials and Solar Cells* 196 (2019), pp. 138–156. DOI: 10.1016/j.solmat.2019.03.001.

[29] M. Sahu et al. *Solar Energy* 230 (2021), pp. 13–58. DOI: 10.1016/j.solener.2021.10.005.

[30] M. Kumar et al. *Energy Environ. Sci.* 8.11 (2015), pp. 3134–3159. DOI: 10.1039/C5EE02153G.

[31] Y. E. Romanyuk et al. *J. Phys. Energy* 1.4 (2019), p. 044004. DOI: 10.1088/2515-7655/ab23bc.

[32] S. Schorr et al. *J. Phys. Energy* 2.1 (2019), p. 012002. DOI: 10.1088/2515-7655/ab4a25.

[33] S. Kim et al. *Energy Environ. Sci.* 13.5 (2020), pp. 1481–1491. DOI: 10.1039/D0EE00291G.

[34] K. Biswas, S. Lany, and A. Zunger. *Appl. Phys. Lett.* 96.20 (2010), p. 201902. DOI: 10.1063/1.3427433.

[35] Y. Deng et al. *Journal of Energy Chemistry* 61 (2021), pp. 1–7. DOI: 10.1016/j.jechem.2021.02.011.

[36] J. Shi et al. *Nat Energy* (2024). DOI: 10.1038/s41560-024-01551-5.

[37] Z. Zhang et al. *Sol. RRL* 4.5 (2020), p. 2000059. DOI: 10.1002/solr.202000059.

[38] J. Wang et al. *Advanced Materials* 34.27 (2022), p. 2202858. DOI: 10.1002/adma.202202858.

[39] H. Nishihara et al. *Jpn. J. Appl. Phys.* 56.4S (2017), 04CS08. DOI: 10.7567/JJAP.56.04CS08.

[40] T. Ratz et al. *J. Mater. Chem. A* 10.8 (2022), pp. 4355–4365. DOI: 10.1039/D1TA09620F.

[41] C. J. Hages et al. *Advanced Energy Materials* 7.18 (2017), p. 1700167. DOI: 10.1002/aenm.201700167.

[42] M. Grossberg et al. *J. Phys. Energy* 1.4 (2019), p. 044002. DOI: 10.1088/2515-7655/ab29a0.

[43] C. J. Hages et al. *Journal of Applied Physics* 115.23 (2014), p. 234504. DOI: 10.1063/1.4882119.

[44] S. Hegedus, D. Desai, and C. Thompson. *Progress in Photovoltaics* 15.7 (2007), pp. 587–602. DOI: 10.1002/pip.767.

[45] T. Gokmen et al. *Applied Physics Letters* 103.10 (2013), p. 103506. DOI: 10.1063/1.4820250.

[46] D. W. Miller et al. *Applied Physics Letters* 101.14 (2012), p. 142106. DOI: 10.1063/1.4754834.

[47] T. Schnabel, M. Seboui, and E. Ahlswede. *Energies* 10.11 (2017), p. 1813. DOI: 10.3390/en10111813.

[48] J. Andrade-Arvizu et al. *ACS Appl. Mater. Interfaces* 11.36 (2019), pp. 32945–32956. DOI: 10.1021/acsami.9b09813.

[49] F. Liu et al. *ACS Appl. Mater. Interfaces* 7.26 (2015), pp. 14376–14383. DOI: 10.1021/acsami.5b01151.

[50] Y. Gong et al. *Nat Energy* 7.10 (2022), pp. 966–977. DOI: 10.1038/s41560-022-01132-4.

[51] Y. Gong et al. *Adv Funct Materials* 31.24 (2021), p. 2101927. DOI: 10.1002/adfm.202101927.

[52] Y. Gong et al. *Adv Funct Materials* (2024), p. 2404669. DOI: 10.1002/adfm.202404669.

[53] Y. Cui et al. *Advanced Science* 9.20 (2022), p. 2201241. DOI: 10.1002/advs.202201241.

[54] J. Zhou et al. *Nat Energy* (2023). DOI: 10.1038/s41560-023-01251-6.

[55] J. A. Clark et al. *J. Am. Chem. Soc.* 141.1 (2019), pp. 298–308. DOI: 10.1021/jacs.8b09966.

[56] Y. Gong et al. *Energy Environ. Sci.* 14.4 (2021), pp. 2369–2380. DOI: 10.1039/D0EE03702H.

[57] Q. Tian and S. Liu. *J. Mater. Chem. A* 8 (47 2020), pp. 24920–24942. DOI: 10.1039/D0TA08202C.

[58] S. Moser et al. *ACS Appl. Energy Mater.* 6.24 (2023), pp. 12515–12525. DOI: 10.1021/acsaem.3c02483.

[59] C. Yan et al. *ACS Energy Lett.* 2.4 (2017), pp. 930–936. DOI: 10.1021/acsenergylett.7b00129.

[60] Z. Su et al. *Advanced Energy Materials* 5.19 (2015), p. 1500682. DOI: 10.1002/aenm.201500682.

[61] J. Fu et al. *J. Mater. Chem. A* 8.42 (2020), pp. 22292–22301. DOI: 10.1039/D0TA06318E.

[62] J. Liu et al. *ACS Appl. Mater. Interfaces* 13.47 (2021), pp. 56302–56308. DOI: 10.1021/acsami.1c16861.

[63] Y. Atasoy et al. *Solar Energy* 267 (2024), p. 112247. DOI: 10.1016/j.solener.2023.112247.

[64] M. C. Baek et al. *Chemical Engineering Journal* 479 (2024), p. 147842. DOI: 10.1016/j.cej.2023.147842.

[65] X. Tan et al. *Journal of Alloys and Compounds* 981 (2024), p. 173645. DOI: 10.1016/j.jallcom.2024.173645.

[66] C. Xu et al. *Materials Today Energy* 40 (2024), p. 101518. DOI: 10.1016/j.mtener.2024.101518.

[67] A. D. Collord and H. W. Hillhouse. *Chem. Mater.* 28.7 (2016), pp. 2067–2073. DOI: 10.1021/acs.chemmater.5b04806.

[68] L. Choubrac et al. *ACS Appl. Energy Mater.* 3.6 (2020), pp. 5830–5839. DOI: 10.1021/acsaem.0c00763.

[69] D. Nowak et al. *Applied Sciences* 12.3 (2022), p. 1376. DOI: 10.3390/app12031376.

[70] C. J. Hages et al. *Prog. Photovolt: Res. Appl.* 23.3 (2015), pp. 376–384. DOI: 10.1002/pip.2442.

[71] R. Scaffidi et al. *J. Mater. Chem. A* 11.25 (2023), pp. 13174–13194. DOI: 10.1039/D3TA01218B.

[72] R. Scaffidi et al. *Energy Adv.* 2.10 (2023), pp. 1626–1633. DOI: 10.1039/D3YA00359K.

[73] R. Scaffidi et al. *Materials Today Energy* 46 (2024), p. 101715. DOI: 10.1016/j.mtener.2024.101715.

[74] R. Scaffidi et al. *Newton, accepted* (2025).

CHAPTER 2
Reviewing the potential of Ge alloying

This chapter is based on the following article:

- R. Scaffidi, G. Birant, G. Brammertz, J. De Wild, D. Flandre, and B. Vermang. "Ge-alloyed kesterite thin-film solar cells: previous investigations and current status – a comprehensive review". *J. Mater. Chem. A* 11.25 (2023), pp. 13174–13194. DOI: 10.1039/D3TA01218B

2.1 Motivation

The interest of cationic alloying for enhancing kesterite solar cells is discussed at the end of Chapter 1. This chapter treats the specific case of substituting Ge to Sn by thoroughly reviewing the related literature, covering most previously reported studies.

In particular, the focus is put on the alloying of Ge to partially or completely replace Sn in the CZTSSe kesterite materials, leading to the $Cu_2ZnSn_{1-x}Ge_x(S_y,Se_{1-y})_4$ (CZTGSSe) compounds in which the $x = Ge/(Ge+Sn)$ and $y = S/(S+Se)$ ratios are of particular importance. Theoretically, Ge inclusion is expected to mainly counteract two loss mechanisms greatly affecting kesterite absorbers, namely defect-assisted recombination and band tailing, partly through the replacement of detrimental Sn^{2+} species[2–5]. Simultaneously, this strategy should improve PV-related characteristics and allow bandgap tuning[6,7], particularly interesting for both band alignment optimization and for enhanced versatility in alternative applications such as tandems or indoor PV among others. On top of this, experimental studies discussed herein demonstrate that integrating Ge into kesterites also enhances crystalline morphology by mitigating secondary phases formation. These promising advantages of Ge alloying apply to both the bulk and interfaces of the kesterite absorber, as illustrated on Figure 2.1(a). At the solar cell level, intensive research effort has provided a steep increase in the PCE of Ge-alloyed kesterites from 6.8 % in 2011, the first ever report of a CZTGSSe-based solar cell[8], to 14.2 % in 2024[9], closing the gap with the all-time kesterite record performance of 15.8 % in 2025[10]. This is depicted in Figure 2.1(b).

From the available literature reports, Chapter 2 attempts to highlight the most promising Ge inclusion strategy, regarding composition and processing, both in terms of thin-film quality and solar cell performance. Given the undeniable role played by the kesterite absorber and both its surfaces in the solar cell performance, the processing technique and conditions used to deposit CZTGSSe thin films with a sufficient quality and suitable PV features are essential, as treated thoroughly in Section 2.2. Based on this, their integration in complete solar cells is discussed in Section 2.3, along with a classification of reported performances with regards to composition. A general summary serves as conclusion in Section 2.4, opening up the discussion about future studies needed to push CZTGSSe solar cells performance to higher levels.

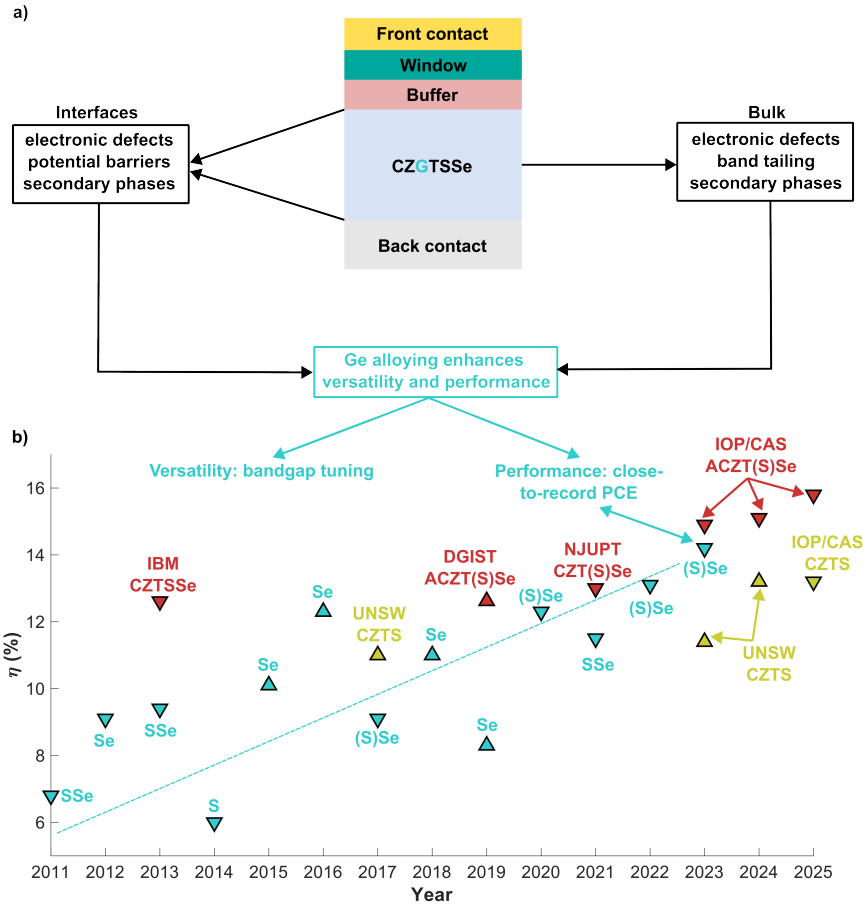

Figure 2.1: Graphical representation of a generic kesterite solar cell highlighting the main culprits of V_{oc} deficit and the theoretically expected solutions provided by Ge alloying (a). Evolution of the best reported CZTGSSe solar cell efficiency per year in cyan symbols[8,9,11–21], the trendline of which is depicted by the dashed cyan line (b). S and Se respectively stand for sulfur and selenium, put between brackets when present in minute amounts, e.g. (S)Se means Se-rich composition while A refers to Ag alloying. Certified efficiency records of Ge-free kesterites are also provided for comparison, with red symbols for lower bandgap devices[10,22–30], and green symbols for higher bandgap devices[10,26,28,31–33]. The downward pyramids correspond to solution-processed kesterite absorbers while the upward pyramids correspond to physically-deposited absorbers.

2.2 Thin Films

This section aims at gathering most of the findings related to CZTGSSe thin films, both in terms of processing and material properties. On the one hand, the respective challenges associated with each processing strategy and the differences between them are highlighted, not only concerning material quality and working principle but also more practical aspects. On the other hand, the critical requirements for these materials to make suitable absorbers for thin-film solar cells are put in evidence, their dependence on the processing method and conditions and most importantly the incorporation of Ge. The scope of this section is limited to references that (1) rely only on solar cell-compatible deposition techniques and (2) at least include characterization of the CZTGSSe absorber material itself. The results concerning solar cell performance, as well as the references only treating complete CZTGSSe solar cells, are addressed subsequently in Section 2.3.

The first distinction made herein is between vacuum-based and non-vacuum-based thin-film deposition methods. For vacuum-based deposition, another distinction is made to differentiate 1-step from 2-step processes. Then, for each processing approach, the different references are classified according to their x =Ge/(Ge+Sn) and y =S/(S+Se) composition ratios as defined in the $Cu_2ZnSn_{1-x}Ge_x(S_y,Se_{1-y})_4$ formula. Chapter 2 covers Ge-Sn and S-Se ratios going from 0 to 100 % ($0 < x \leq 1$ and $0 \leq y \leq 1$), while pure Sn variations (x=0) are used as Ge-free reference case. Apart from x and y, two other stoichiometric ratios are also discussed, namely I/(II+IV)=Cu/(Zn+Sn+Ge) and II/IV=Zn/(Sn+Ge). These determine important kesterite PV properties and their respective optimal values are widely believed to be Cu-poor (I/(II+IV) $\simeq$ 0.8) and Zn-rich (II/IV $\simeq$ 1.2) for standard CZTSSe[34–39], though still to be discussed in the following.

2.2.1 Vacuum-based deposition

Similarly to their chalcogenide counterpart, kesterite thin films are largely produced under vacuum with physical deposition techniques. This is typically achieved in two different approaches: one-step processes, such as co-evaporation, during which all the elements are simultaneously deposited in various high temperature stages leading to the formation of the desired material; two-step or sequential processes consisting in firstly depositing a stack of metallic precursors usually via sputtering or evaporation, then annealed at high temperature in a S- and/or Se-containing environment, called the Selenization and Sulfurization (SAS) step, to obtain the final thin film.

2.2.1.1 One-step processes

CZGSe CZGSe was firstly deposited on glass via co-evaporation of Cu, ZnSe, Ge and Se at temperatures from 250 °C to 450 °C to study the impact on the crystalline lattice, surface and bulk morphology, composition and phase as well as optical bandgap[40]. The authors observed that their films contained considerable amounts of Cu while a significant proportion of Ge escaped from the layer especially at higher substrate temperatures. They adapted their processing recipe accordingly and obtained the best results with a 300 °C annealing and 10 % less Cu, leading to a single-phase material with p-type conductivity and a bandgap of 1.63 eV.

CZTGSe Later on, another research group processed CZTGSe thin films by co-evaporation of all pure elements on glass/Mo substrates at temperatures below 250 °C[41–43], greatly inspired from deposition recipes of non-Ge-alloyed kesterites. At the film level, the importance of including $GeSe_2$ within the annealing environment to prevent elemental losses and preserve optimal composition was stressed[41]. With an x ratio varying from 0 to 1, the evolution of crystalline phases was presented[41], along with the quasi linear increase (resp. decrease) of optical bandgap (resp. electron affinity)[41–43], in agreement with theoretical predictions[44]. It was showed through advanced characterization on similar structures that relatively shallow defects are formed close to the CZTGSe top surface[42]. The density of these defects is sufficient to induce a hole-deficiency and compensate the parallel evolution of bulk states but not high enough to cause Fermi level pinning[42,43]. Using similar targets to the first report[40], one group performed co-evaporation of CZTGSe at 150 °C substrate temperature to minimize Sn and Ge loss followed by 330 °C/480 °C two-stage annealing in excess Se to promote grain growth[45]. Relying on processing temperatures below 500°C makes the deposition procedure potentially compatible with flexible polyimide substrates. As an upgrade, they also evaporated a thick Se capping layer before high-temperature annealing to guarantee homogeneity and prevent oxidation[46]. With these samples, they revealed the importance of moderate Zn quantity and appropriate substrate/back contact stack to limit detrimental ZnSe formation while sufficient Na content enhances both carrier concentration and Ge inclusion (Figure 2.2). Overall, enhanced grain size was also observed.

CZGSSe The same team conducted alike experiments on wide-bandgap CZGSSe thin films with and without Se capping layer[47,48]. They highlighted the intricate interplay between NaF precursor layer, Se capping layer and S inclusion within the absorber. In general, higher Na quantities promote the integration of more S within the bulk which reduces its surface segregation,

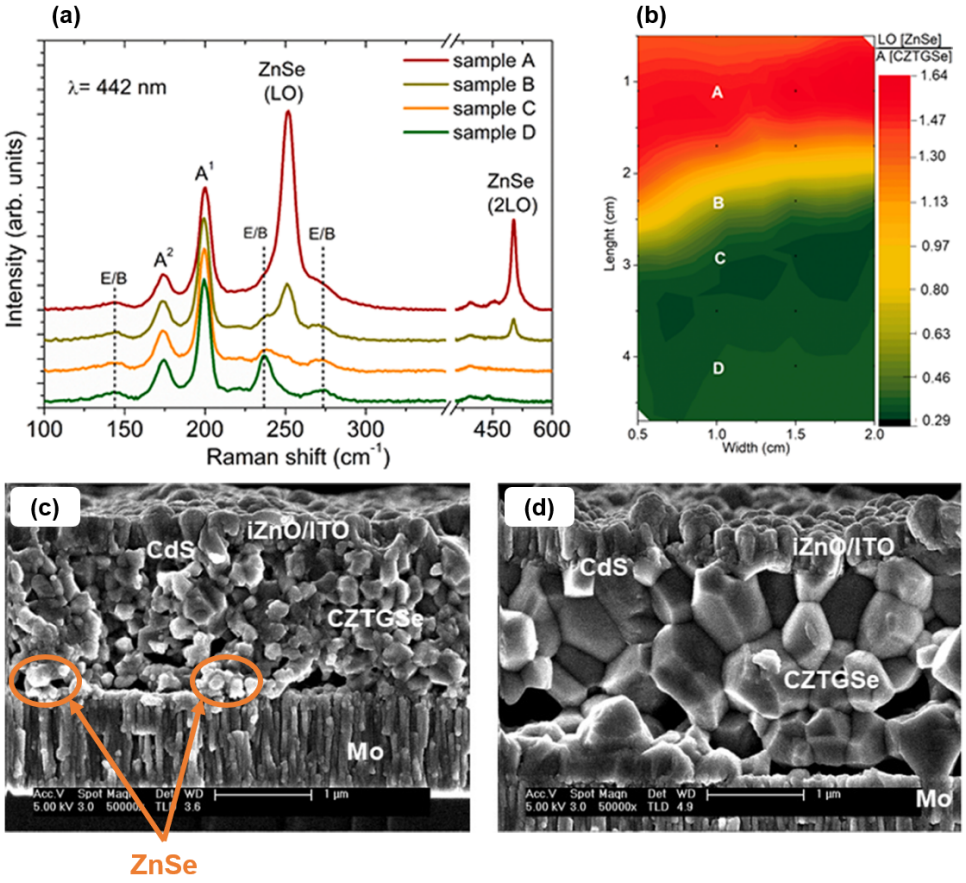

Figure 2.2: Raman peaks of compositional sample with varying Zn content (a). Ratio between ZnSe and CZTGSSe Raman peaks height mapped over the compositional sample surface (b). Scanning electron microscopy (SEM) cross sections of complete solar cells including absorbers with sample A (c) and D (d) of the compositional sample, with ZnSe traces highlighted by orange arrows and circles. Adapted with permission.[45] Copyright 2020, Elsevier.

thus smoothens the S-gradient along the absorber thickness and narrows total bandgap grading.

CZTGS In parallel, CZTGS films were grown via single-stage flash evaporation of a Zn-rich compound with x=0.5 produced through a modified Bridgman method[49], normally used to produce single crystals. Sn loss was reduced as Ge successfully integrated the film at a substrate temperature of 350 °C, which then exhibited good crystallinity and composition even before subsequent higher-T° annealing. Significant dependencies between growth conditions and elemental composition were highlighted, in

particular the evolution of Ge, Sn, S and Na during the sulfurization step.

2.2.1.2 Two-step/sequential processes

CZGSe The pioneer investigations about CZGSe thin films relied on simple Cu/Zn/Ge metallic stacks evaporated in vacuum on both glass and glass/Mo substrates, then annealed in Se environment between 400 °C and 500 °C[50]. These lead to p-type absorber layers with micrometer grain size and bandgap around 1.6 eV.

Subsequent works from another research group enabled to optimize CZGSe thin films processed similarly: first, optimizing the Zn precursor thickness, stack ordering, and annealing temperature to prevent the formation of ZnSe binary phase and enhance grain size[51], supported by a deep understanding of the crystallization dynamics[52]; second, pushing further the elimination of secondary compounds (ZnSe, Ge, Ge_xSe_y, ...) on the absorber top surface by applying chemical treatments based on hot HCl and aqueous $(NH_4)_2S$[53]. They also revealed the mitigation of deep defect states and band tailing in CZGSe as compared to standard CZTSe[54]. Most of these experiments jointly confirmed acceptable grain size, single CZGSe phase formation in the 400-500 °C range and suitable p-type doping, conductivity and bandgap for PV applications.

In the continuation of these studies, equivalent experiments were carried out on the same precursor stack, though sputtered and not evaporated, in collaboration with multiple teams of researchers[55–57]. In order to improve the absorber crystallinity and mitigate secondary phases formation, the implementation of an optimized selenization recipe with an appropriate surface treatment was investigated[55]. The best recipe consisting in a 330 °C/480 °C two-step annealing in Se-$GeSe_2$ lead to both high crystalline quality and low Urbach energy[55,56], with only slight traces of ZnSe secondary phases in one study[55]. In these two references, KCN etching seems efficient to remove detrimental phases from the top surface with possible non-toxic alternatives based on $(NH_4)_2S$ combined with $KMnO_4$, but not from the bottom surface where a thin layer with smaller grains in observed. The third investigation consisted in an innovative combinatorial analysis on a sample with graded composition[57]. They demonstrated that (1) Cu/(Zn+Ge) = 0.65-0.7 and (2) Zn/Ge =1.05-1.15 should guarantee CZGSe to be mostly free of secondary phases including those related to Ge, as reported elsewhere[51–56]. This seems to be an argument in favour of Ge alloying since for similar Cu-poor and Zn-rich stoichiometry in standard CZTSe, traces of volatile Sn-Se secondary phases can be observed, leading to Sn-loss and defect formation[36,37].

Investigations from independent groups attempted to adjust the precursor stack in this two-step process, namely with solid-phase Se integration within the precursor stack[58], or directly evaporating the CZGSe material

with the targeted composition[59]. Both managed to obtain, for a processing temperature above 450 °C, thin films nearly free of secondary phases and with a similar bandgap as the previous groups, but with an overall poorer morphology.

CZGS Wide bandgap CZGS films exhibited improved morphology and grain size for higher Cu content, as well as a single CZGS phase, whether they are deposited from RF-sputtered Cu, Zn and Ge precursors then tube furnace sulfurized[60], or from thermally evaporated binary sulfide precursor then annealed in a S-containing oven[61]. The second group also highlighted the relationship between low Ge content and enhanced crystalline quality, mobility, photoconductivity, as well as reduced defect densities at grain boundaries[61]. CZGS thin films were also processed from sputtered CuS/Ge/ZnS precursors on glass/Mo/TiN then sulfurized, which lead to the formation of detrimental secondary phases, ZnS in particular but also Ge- and Sn-related oxides[62]. These oxide phases were successfully etched by KCN surface treatment.

All three groups reported the expected wider bandgap (1.8-2.2 eV) and evolution with regards to composition[60–62]. However, as compared to the studies about two-step-processed CZGSe discussed above, these investigations about CZGS showed more evidence of detrimental secondary phases, mainly ZnS, and an overall reduced grain size, potentially explained by the higher volatility of S making grain growth more challenging. Particular attention should be drawn on these aspects to reach high-quality CZGS material, e.g. for tandem device applications.

CZGSSe One work reported attempts to process a mixed sulfo-selenide CZGSSe thin film by sequential annealing of a Ge-Zn-Cu precursor stack, first in H_2Se at 460 °C then in H_2S at 510 °C[63]. Sulfur inclusion from 30 to 100 % with increased bandgap seemed successfully achieved, at the expense of non-uniform composition and degraded morphology. Both the presence of Zn(S,Se) secondary phase and the lower structural quality observed for high S content seem in agreement with the differences highlighted just above between CZGSe and CZGS.

CZTGSe Many references report investigations about CZTGSe absorbers deposited by two-step processes under vacuum, most of them attributed to one research group from IREC and close collaborations[14,17,64–72], and a few other investigations carried out by other teams[73–76].

The IREC group implemented and extensively used one approach to process Ge-doped CZTSe, or CZTSe:Ge, thin films on glass/Mo, i.e. sputtering/evaporation of a Cu/Sn/Cu/Zn precursor stack with addition of a thin thermally evaporated Ge nanolayer at a certain position within the stack,

followed by reactive annealing in Se (and Sn) atmosphere. This recipe is designed to incorporate rather low amounts of Ge, with x ratios typically below 0.1 apart from a few exceptions. The first works of the series tried to put in evidence an optimum thickness for the superficial Ge layer deposited on top of the metallic stack[14,64,65]. Below 15nm, they suggested that Ge is barely incorporated within the absorber, apart from GeO_x traces visible on Figure 2.3(a), explaining the globally unchanged bandgap value as compared to Ge-free references[65]. This is a consequence of the significant Ge loss by evaporation of volatile $GeSe_2$ during reactive annealing. Still, for that very range of Ge thicknesses, the parallel formation of a Se-rich Ge_xSe_y liquid phase at 385 °C significantly favours crystallization dynamics[14], as well as Na diffusion[64,65]. The consequence is an enhanced grain morphology (Figure 2.3(b)-(c)) accompanied by higher doping, less dense grain boundaries and thus lower defect densities, which are promising for PV applications. However, for thicker Ge precursors, the excess Ge_xSe_y liquid phase allows discriminated Na atoms to flow towards the surface of the absorber where they oxidize in the form of Na-O needles[64,65]. Even though these Na-O particles can be etched by surface treatments, they contribute to lower bulk doping density. For higher Ge content, delamination near the back contact (Figure 2.3(d)) as well as ZnSe and Cu-related secondary phases at the top surface were also observed[14,65].

In the continuation of these investigations, they pushed further their understanding of Ge incorporation[17]. The main conclusion is that Ge doping allows to fundamentally change the kesterite formation mechanism, going from a triple reaction of binary selenides in the Ge-free case to a bi-molecular reaction providing a quaternary phase at an earlier stage in the Ge-doped case. This is due to the Ge inclusion preventing strong elemental segregation, i.e. Cu at the front and Zn/Sn at the back, either by an increased Sn solubility, by a flux-driven crystallization through liquid Ge_xSe_y, or a combination of both. The consequence is a less abrupt bi-layer morphology (Figure 2.3(b)-(c)) with mitigated presence of highly volatile $SnSe_2$ phase, thus impeding important Sn loss-related void formation and ensuring higher integrity near the back contact compared to pure Sn kesterites. In the same study, they changed the Ge precursor position keeping the total Ge thickness constant between 10 to 15 nm, and demonstrated that the beneficial effect of Ge-doping is not limited to the absorber surface and mainly depends on the total thickness of Ge precursors rather than their position in the stack. Another investigation about CZTSe:Ge layers processed with this recipe provided supplementary insight into the distribution of Ge by using characterization methods with lower detection threshold[69]. Actually, Ge is incorporated over the whole absorber thickness in a heterogeneous fashion, creating Ge-rich and Ge-deficient zones within grains and at their boundaries, under the form of previously observed GeO_2 inclusions and possible secondary phases. As

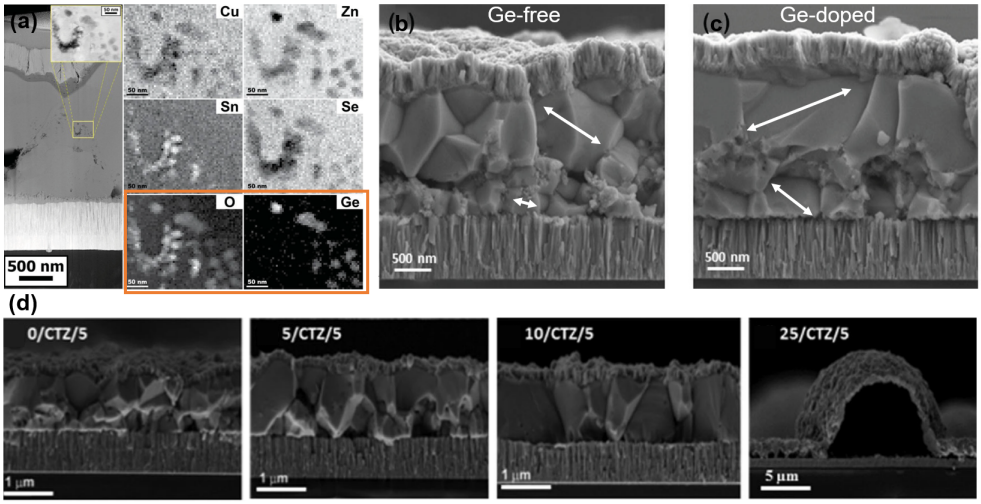

Figure 2.3: Transmission Electron Microscopy (TEM)/ Electron Energy Loss Spectroscopy (EELS) analysis revealing traces of GeO_x nanoinclusions highlighted by the orange rectangle (a). SEM cross sections showing grain growth improvement (white arrows) due to Ge doping of CZTSe absorber (b)-(c). Adapted with permission.[14] Copyright 2015, Wiley-VCH. SEM cross sections of CZTSe:Ge absorbers with increasing Ge content, showing delamination issues for 25 nm Ge bottom layer (d). Adapted from[17] with permission from the Royal Society of Chemistry.

complementary studies, this research group investigated alternatives to sputtering for depositing the precursor stack, such as thermal evaporation[71], or molecular beam epitaxy[66]. The former lead to mostly identical results compared to sputtered precursors apart from the remarkable absence of Sn-Se secondary phases, whereas the latter still requires further optimization in the control of elemental diffusion, composition and processing parameters.

Alike experiments performed in parallel within the same team focused on pre-selenized nanocrystalline CZTSe precursors[67,68], then doped with Ge and annealed using the usual IREC approach. These studies demonstrate that x values below 2 to 4 % (1) induce low Ge incorporation evidenced by nearly constant bandgap values (2) restrict formation of both bulk defects (Figure 2.4(a)-(c)) and chemically etchable surface secondary phases (3) enhance carrier density through Na interaction (Figure 2.4(d)-(e)), while inverse trends are observed for higher Ge content[67,68]. All these conclusions coincide with the standard IREC processing results[14,64,65]. However, in this case, Ge doping does not allow further grain size improvements than those already induced by the pre-selenization[67,68], and apparently has no influence on band tailing[68].

Another important aspect of Ge-alloying is the possibility to perform

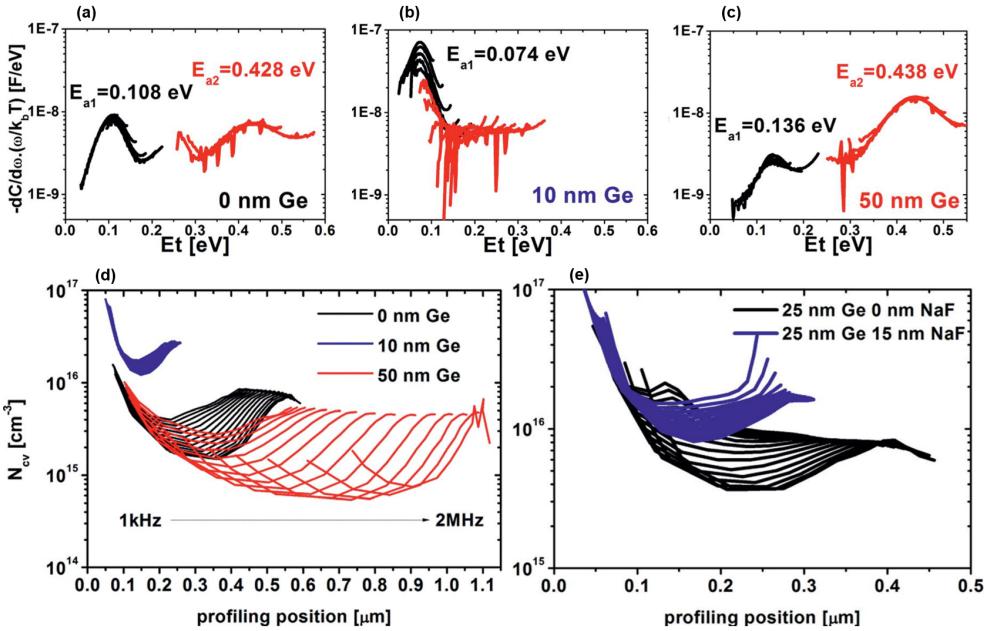

Figure 2.4: Bulk defect energy profile with Ge nanolayer of 0nm (a), 10 nm (b) and 50nm (c). Capacitance-voltage-derived doping profile for various Ge nanolayer thickness without NaF layer (d) and fixed 25 nm Ge with and without NaF layer (e). Adapted from [68] with permission from the Royal Society of Chemistry.

bandgap grading without relying on the S/(S+Se) ratio, equivalently to the Ga/(Ga+In) ratio in CIGS-based devices[77]. Since the references discussed above reported little influence of Ge doping on the bandgap value, Sn-Ge bandgap grading was studied for higher Ge content in two different studies[70,72]. They described a natural Sn-Ge segregation appearing in CZTGSe thin films as resulting from the reaction of GeSe with CZTSe near the back contact, subsequently leading to the formation of CZTGSe and $SnSe_2$ in the same region. These findings are well in agreement with the CZTSe/CZTGSe bi-layer morphology reported before[14,17,67], and happens concomitantly to the diffusion of Na, Cu and Ge precipitates towards the bottom surface where $MoSe_2$ is also detected[72]. The observed irregular compositions along the absorber thickness could support the formation of secondary phases. As a direct consequence of the graded Sn-Ge ratio, natural bandgap grading was demonstrated in these absorbers[70,72], sometimes with a steep profile fashion going from x =0.8 at the back to x =0.1 at the front and mainly controlled by the annealing conditions[72]. As the global Ge content increases above x =0.2, a trade-off appears between the mitigated void formation due to $SnSe_2$ evaporation and the reduced grain size.

Another work presented Sn-Ge gradient for CZTGSe absorbers grown from different variations of the same metallic precursor stack, leading to shallow bandgap grading towards the back[73]. Besides that, one study reproduced similar improvements related to Ge doping as those brought by the IREC Ge nanolayer approach[76], namely increased doping concentration and enhanced morphology. This improved structural quality was jointly observed by two different teams investigating an alternative strategy that consists in integrating Ge only during the selenization step of a sputtered stack, either in a $GeSe_2$-Se[74], or a pure Se-Sn-Ge environment[75] as in Figure 2.5(a). The former focused on Ge doping (x <0.02) and highlighted the widely seen bi-layered absorber with a Ge gradient towards the back promoting alkali diffusion, no secondary phases and reduced band tails[74]. The latter discovered two dependencies on the value of x ranging from 0 to 1[75]: first, an enlarging spread of Sn-Se binary phase in both the bulk and at the surface, the evaporation of which may likely explain the voids observed in between the Ge-enlarged grains (Figure 2.5(b)). Second, a linearly increasing bandgap value (Figure 2.5(c)) in parallel with a more pronounced band tailing. Besides that, they also concluded that Ge integrates the film at temperatures above 400°C, thus not interfering with the kesterite phase formation but only its transition from Cu-rich to Cu-poor stoichiometry.

CZTGS Four different methods are investigated and optimized to deposit high-quality CZTGS films on glass/Mo through tube furnace sulfurization of a precursor stack. First, a sputtered Zn/Cu/Ge/Sn stack is sulfurized in sulfur vapour, covering x ratios from 0 to 1 by changing the thicknesses of the Ge and Sn layers[78]. When the x ratio increases from 0 to around 0.7, grains become bigger whereas the absorber surface gets rougher. For even higher Ge content, the inverse trend is observed, along with void formation near the back contact which is attributed to Ge sulfides escape, as similarly highlighted for CZTGSe[70]. Second,[79] more recently investigated the co-sputtering of a pioneering CZGS/CZTS bi-layer precursor sulfurized at high temperature. This enabled to obtain bandgap-engineered CZTGS films with a Sn-Ge gradient along the absorber thickness possibly creating a beneficial back surface field, similarly to the Ga gradient in CIGS devices[77]. The counterpart of this graded morphology is a bi-layered structure constituted of (1) large and compact Sn-rich grains in the upper half of the absorber (2) small Ge-rich grains accumulated at the back with GeO_x phases, cracks and voids observed at their boundaries. This bottom layer with higher Ge content and poorer morphology suffers from the same delamination issues reported in other studies to be related to Ge-(S,Se) escape[17,65,70,72,78]. Later on, the same group successfully tackled these adhesion issues related to the Ge-rich bottom layer by us-

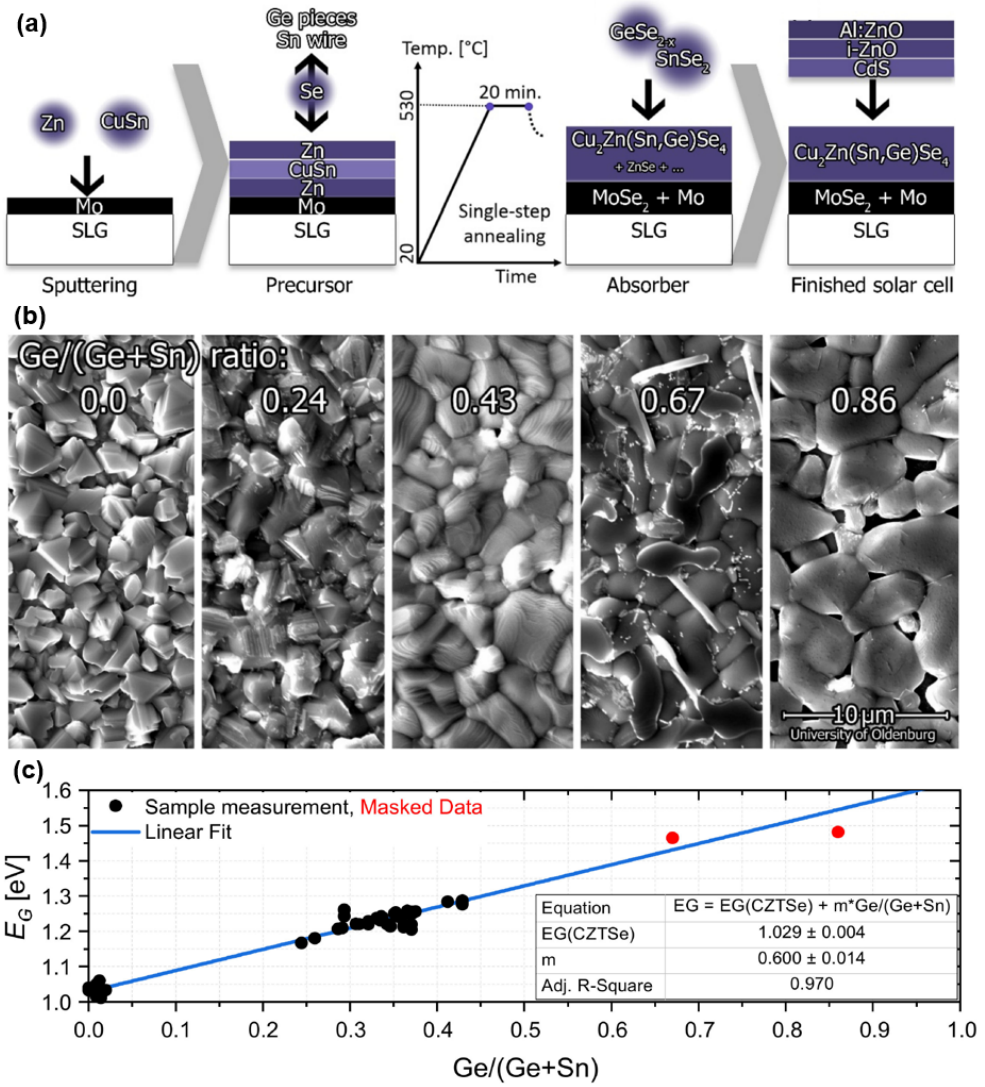

Figure 2.5: Graphical workflow of the CZTGSe absorber and solar cell processing based on vapor-phase incorporation of Ge (a). SEM pictures showing evolution of the surface morphology in function of the Ge content (b). Evolution of the bandgap extracted from external quantum efficiency (EQE) measurements (c), in function of the x=Ge/(Ge+Sn) ratio, following the linear relationship: $E_g(x) = 1.03 + 0.6x$. Adapted with permission.[75] Copyright 2022, MDPI.

ing a TiN interlayer between the Mo electrode and the CZTGS absorber[80]. Third, the evaporation of 20nm Ge followed by the sputtering of a stacked Cu/SnS/Zn precursor with varying Zn thickness before sulfurization was performed[81]. As also demonstrated for one-step-processed CZTGSe[45,46],

lower Zn content tend to restrain the spreading of ZnS phases which tend to concentrate near the back contact. If one further reduces the amount of Zn to reach Zn-poor compositions, high density of deep Sn_{Zn} defects would be expected, but the substitution of Sn by Ge probably helps preventing their detrimental activity as compared to standard CZTS[81]. One conclusion of this study is that slightly Zn-deficient stoichiometry may reveal more ideal for CZTGS than the widely accepted Zn-rich optimal composition for CZTS. Fourth, the last research group studied the addition of a Ge nanolayer of different thicknesses and at different positions in a sputtered Cu/Sn/Cu/Zn stack[82]. 5nm Ge on top of the precursor stack seemed to provide the most efficient Ge incorporation into the Ge-doped CZTS (or CZTS:Ge) absorber. They revealed that such small amounts of Ge have no significant impact on morphology but are sufficient to mitigate, though not totally eliminate, SnS_2 secondary phases which are commonly observed in pure Sn kesterites.

Several observations were common to the CZTGS references discussed hereabove. First, ZnS was detected in nearly all studies[78–81], agglomerating at grain boundaries or both the top and bottom surfaces of the absorber, where it limits grain size. Second, they all reported the appearance of a layer with poorer morphology near the back contact[78–82], exhibiting voids creation and back surface delamination through the escape of Ge sulfides[78], the formation of Ge oxides[79,80], and the segregation of ZnS phase[81], or a combination of these effects. Third, joint evidence of enhanced grain size for moderate Ge incorporation is reported[78–81]. Fourth, bandgap values between 1.4 and 1.5 eV for low amounts of Ge[79,81,82], reaching up to 2.23 eV for x=1[79]. Overall, the advantages of Ge inclusion in CZTS tend to be less obvious than for the Se-based equivalent, potentially explained by the absence of liquid phase-assisted crystallization in the S-based compounds[17,60,64,65,82].

CZTGSSe Two studies investigated the addition of a thin sputtered Ge layer either below and/or above the Mo back contact of CZTSSe absorbers on flexible Ti[83,84]. In these structures, the CZTSSe absorber is co-sputtered in a Zn+CZTS/Cu+CZTS/Zn+CZTS 3-layer approach and then selenized. On the whole, inserting Ge below the Mo back contact tends to significantly improve adhesion and limit residual stress which are important aspects for flexible devices. Similarly to Ge-doped CZTSe and CZTS discussed above, a thin Ge nanolayer below the CZTSSe absorber induces greater crystallinity and bigger grains with nearly unchanged bandgap and no undesired phases, but the cost is a rougher surface. All these observations tend to be correlated with the substitution of Sn by Ge that promotes Sn^{+4} over Sn^{2+} species, a well-known defect-prone issue in kesterites[2] which needs to be mitigated for enhanced efficiency[85].

Reviewing the potential of Ge alloying

Sputtering CZTG precursor stacks followed by rapid thermal annealing in Se-rich (S,Se) atmosphere was used to deposit CZTGSSe films over glass/Mo substrates in two different studies[86,87]. For Ge-doping with x <0.2, evidence was found of single-phase CZTGSSe kesterite without bulk secondary phases, increased grain size and reduced IV-loss leading to mitigated void formation, compared to pure Sn CZTSSe. Fine control of the Ge nanolayer thickness and position allows to preserve proper stoichiometry and enhance both morphology and crystallinity. Similar findings were obtained with a single-target sputtering of CZTS before $GeSe_2$-Se anneal[88]. The main differences are, as compared to the two previous works[86,87], a homogeneous morphology over the whole thickness potentially supported by the use of $GeSe_2$ annealing and the presence of ZnSe phase likely due to the high Zn content. Finally, another processing strategy was used[89], relying on CZTGS single-target pulsed laser deposition (PLD) with varying selenization conditions. It appears to be the only report of Ge-alloyed kesterite absorber processed via PLD, considered to be easily controllable with regards to film composition[89]. As most references up to this point, they found that Ge incorporation tends to improve structural quality of the layer. On top of this, optimizing the selenization process in terms of Se content, duration and temperature revealed that all three parameters simultaneously influence the crystallinity, phase formation, grain size, composition and bandgap, with an optimal recipe of 45mg Se for 10 mins at 550°C.

Nanopowders Several experiments were also carried out on Ge-containing kesterite polycrystalline powders[90–92]. Even though not concerning actual thin films, these respectively reveal: the dominance of defect-assisted recombination for $x < 0.2$ and of valence band tail-assisted recombination for $x > 0.2$ in CZTGSe[90]; alternative Cu-related point defects in Cu-rich CZGSe[91]; the challenge to process single-phase CZGSSe[92].

Comparison Overall, both one-step and two-step vacuum-based processes allow to reach proper film morphology and grain structure, while facing the same critical challenge of single-phase CZTGSSe material growth, with various detrimental secondary phases detected and their formation mechanism deeply studied. One striking difference between the two approaches is the significantly larger amount of references for sequential deposition, thus making thorough comparisons more difficult to realize. Still, from the few reports available[40,41,45], one can notice that one-step co-evaporation processes do not seem to suffer from the same secondary phases issues widely observed for two-step deposition, leading for instance to poor adhesion and strong delamination related to IV-$(S,Se)_2$ evaporation[17,51,52,61,63,65,70,72,75,78,79]. This may likely be explained by the fact that

evaporating the necessary elements near the phase transition temperature without leaving vacuum restricts the formation of potentially unstable binary phases. On the contrary, sequential processes involve complex intra-precursor diffusion mechanisms influenced by stack design, physical state of elements, annealing conditions, and air exposure or time delays before the selenization and sulfurization. Yet, two-step processes remain the preferential approach among research groups to deposit CZTGSSe in vacuum, possibly because they provide acceptable structural quality and equally promising PV properties while being more versatile and easier to monitor, implement and optimize. These aspects may come as an important decision criterion, as demonstrated by the great interest in even more straightforward non-vacuum-based methods discussed below.

2.2.2 Non-vacuum-based deposition

Contrarily to their CIGS cousin, it is not yet clear for kesterite PV absorbers, including Ge-alloyed ones, whether physical vacuum-based or chemical non-vacuum-based depositions provide higher material quality and device performance. Indeed, there nearly are as many investigations reported on these admittedly more simple and low-cost solution-based methods than on those relying on in-vacuum steps. Non-vacuum processes have a similar sequence to the two-step vacuum-based techniques discussed above. The main difference is the precursor deposition step, typically realized in ambient solution with a much wider panel of deposition methods and resulting in a non-layered thin-film precursor yet to be annealed. Consequently, the relevant deposition parameters and possible recipe modifications greatly differ from those of two-step vacuum processing, with for instance the importance of choosing the appropriate solvent or adding adapted catalysts. The reported investigations are discussed below, at the absorber material level.

CZGSe and CZGS In parallel with their co-evaporated counterpart, pure-Ge kesterite CZGSe and CZGS were firstly deposited on glass/Mo substrates by chemical spray pyrolysis of aqueous precursor solutions with different Cu content[93]. The sulfide and selenide variations were obtained by different annealings of the same film, 35mins at 500°C in S vapour for the former and 30mins at 520°C in Se vapour for the latter. Evidence was shown that this subsequent annealing step is essential to ensure proper composition, crystalline morphology, absorption coefficient, bandgap and absence of secondary phases.

An alternative precursor processing based on binary sulfides paste doctor blade deposition was investigated for CZGS[94], targeting a Cu-poor stoichiometry. They concluded that suitable post-sulfurization temper-

ature and duration would be 500°C for around 30mins to guarantee much-improved crystallinity and no secondary phases compared to the as-deposited film, similarly to a former study[93]. In both references, films with similar I/II+IV and II/IV ratios exhibit alike micron-wide grain size and bandgap values. This is quite well adapted to PV applications along with the processing solutions used that are theoretically compatible with large-area production.

CZGSSe One group investigated the preparation of CZGSSe absorbers from blade coating different metal salt solutions on glass/Mo, and their impact on optical and structural properties[95,96]. First, for a targeted Cu-poor and Zn-rich composition, they found mostly no secondary phases whichever the solution, but a significant influence on film morphology and crystallinity as well as S/(S+Se) ratio. Second, this S and Se content was varied at the annealing step to successfully tune the bandgap value, while revealing the expected kesterite phase evolution.

CZTGSe Four different approaches were reported to deposit CZTGSe absorbers. First, pure metals and binary metal chalcogenides were diluted in highly toxic hydrazine solvent, before spin-coating and high-temperature N_2 annealing to evaporate S and only keep Se within the film[11]. These absorbers exhibited micrometer grain size and voids near the back contact whatever the Ge content, while higher x ratios around 40% promoted phase segregation and ZnSe formation. Second, Cu-Ge/Cu/Sn/Zn stacks deposited on glass/Mo via solution-target electrodeposition were annealed in Se-Sn atmosphere to produce Ge-doped CZTSe films[97,98]. Optimized electrodeposition of the Cu-Ge bottom precursor allows to simultaneously modify the dendritic morphology of the above Cu layer and mitigate elemental segregation after the N_2 pre-heating step. These in turn lead to a more uniform and enhanced morphology with limited binary phases, defects formation and band tailing possibly through the mitigation of Sn^{2+} species via Ge substitution (Figure 2.6). The third group focused on using non-toxic solvents, either water-based spray pyrolysis[99] or butylamine-based doctor blading[100], to deposit the precursors before sulfurization. The last research team carried out an alternative CZTGS deposition method based on oxide ink doctor blade coating followed by S vapor annealing[101]. Both groups studied absorbers with x =0 to x =1, and reported bigger grains and enhanced morphology due to effective Ge incorporation, without evidence of secondary phases. The evolution of the bandgap value with x is demonstrated to follow the band bowing model: $E_g(x) = x * E_{g,CZGSe} + (1-x) * E_{g,CZTSe} - b * x * (1-x)$ with b the bowing parameter. This constant is experimentally estimated to be either 0.1 eV[99,100] or 0.29 eV[101]. However, the theoretical predictions support the former result, meaning high

miscibility of CZTGSe alloys[6].

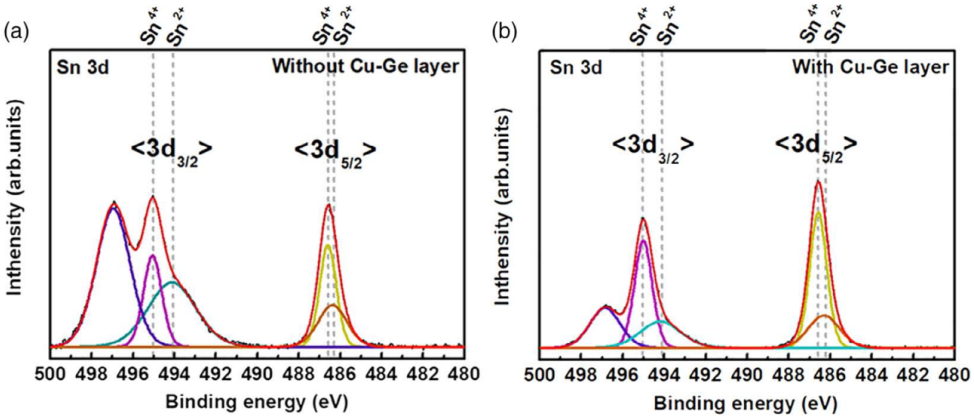

Figure 2.6: X-ray photoelectron spectroscopy (XPS) results showing the reduction of Sn^{2+} species when going from no Cu-Ge layer (a) to a Cu-Ge bottom nanolayer (b), in the kesterite absorber processing via electrodeposition. Adapted with permission.[97] Copyright 2020, Wiley-VCH.

CZTGS The same two last teams also explored bandgap engineering in solution-processed CZTGS[99–101]. In parallel, a third group presented an innovative way to realize Sn-Ge bandgap-graded absorbers by dispersing oleylamine ligand-capped CZGS nanocrystals in a Sn-containing formamide solution, before spin coating and film sulfurization[13]. Their modified process led to a large grain monolayer morphology with high structural integrity[13], while[99,100] obtained slightly poorer morphology. For the last group, Ge inclusion also boosted grain growth but finished CZTGS thin films appeared significantly more porous and less dense than in the two former studies. All three approaches allowed the following: Ge-incorporated crystalline CZTGS kesterite absorbers; absence of detrimental binary phases and extrinsic residues (C, O, ...); accurately tunable and/or graded composition by monitoring either Sn incorporation via the ligand concentration[13] or Ge precursor solution molarity[99–101]. This last aspect enables bandgap values roughly spanning from 1.5 to 2 eV for $x = 0$ to $x = 1$ with a bowing parameter b $\simeq$ 0.1-0.2 eV.

Similar trends were reported for two alternative methods to process the precursors before annealing. On the one hand, a Ge nanolayer is vacuum-sputtered below the solution coated CZTS film[102], leading to more compact and large-grain CZTS:Ge layers after sulfurization. On the other hand, a chloride-based CZTG precursor solution of varying x ratio is spin-coated and annealed in H_2S:Ar at various flow rates[103].

As observed for vacuum-processing, the improvements related to Ge

inclusion are more striking for CZTGSe than CZTGS also in solution-based methods, especially the enhanced grain growth and film morphology. Since these two aspects are closely related to the annealing process, it sounds plausible to explain the higher effectiveness of Ge inclusion for improving CZTGSe absorbers by the liquid-phase assisted crystallization[17,60,64,65,82], as done for two-step vacuum processes above.

CZTGSSe A plethora of different research groups investigated non-vacuum processing of Sn-Ge alloyed and S-Se mixed CZTGSSe thin films for PV applications.

The pioneer work of Ge-alloyed kesterite solar cells relied on CZTGS nanocrystals processed through hot injection (batch reaction) in oley-lamine, then doctor blade coated on glass/Mo and selenized at 500-550°C to form the final CZTGSSe thin film[8,104,105]. Three observations were jointly reported: (1) bi-layer morphology with Ge-integrated large crystalline grains along the upper half and small Se- and carbon-rich grains towards the back contact (2) tunable bandgap above 1.09 eV for increasing Ge content (3) group IV elemental loss due to the evaporation of Sn or Ge sulfides and selenides during annealing. The last phenomenon should be avoided, which was tackled successfully within the bulk but not at the surface using different Ge precursors[105]. Similar trends regarding bandgap and Sn-Ge loss were highlighted in two other studies also relying on nanocrystal-based deposition route[106,107], with a few supplementary findings. First, within the same group, chloride salt-based molecular ink spray-coating of precursors before selenization allowed to evidence the Ge loss to be greater than for Sn in CZTGSSe thin films[107]. Second, in another research team, an air-stable GeO_2-based processing recipe mixing CZGS and CZTS inks lead to crystalline films with increased grain size for low to moderate Ge incorporation[106].

Besides that, various solvents and Ge sources were employed in the solution spin-coating-based precursor deposition before SAS: polymer-assisted aqueous solution including GeO_2[108], non-toxic butylamine-based including $GeSe_2$[109], Ge-free dimethyl-sulfoxide solution[16,110], organic solvent-stabilized precursor solution including either GeO_2[19] or an evaporated Ge bottom nanolayer[20], water- and metallic oxides-based solution[111], GeO_2 precursor layer below a CZTSSe precursor[21] (Figure 2.7(a)), Ge-containing chlorine-based solution drop casted during annealing[112]. In all these references, effective Ge inclusion is reported (Figure 2.7(b)), by substitution onto Sn sites and/or under the form of oxides. This arguably led to globally increased grain size for higher Ge content, in turn improving the large-grain/fine-grain ratio of the typical bi-layer morphology usually observed[19–21,108,109,111]. Except for one group that integrated Ge only at the annealing step and for which liquid-phase assisted crystallization may

have allowed a uniform structure[16,110]. Closely related is the importance of fine composition tuning, once again stressed to prevent the appearance of (1) detrimental secondary phases such as Zn(S,Se) and Cu_xSe[16,110,111] or (2) voids and cracks through excess Ge sulfides and selenides sublimation[21,106,109]. Apart from the usually demonstrated tunable bandgap[108,111], other opto-electronic properties such as doping concentration[21,108,111], mobility[108,111], resistivity[108,111] can be controlled by the amount of Ge incorporated, and globally enhanced for $x < 0.4$. Eventually, Ge alloying exhibited strong abilities to mitigate both defect-assisted recombination and band tailing[16,19–21,110] (Figure 2.7(c)-(d)), likely by the neutralization of well-known Sn_{Zn} and Cu_{Zn} "killer" defects due to the lowering of undesired Sn^{2+} species concentration[20,21].

Nanostructures Besides this, CZTGSSe nanoparticles[113–115], along with nanocrystals[116] and nanopowders[117,118] were processed in solution and then characterized, though not at the thin film level.

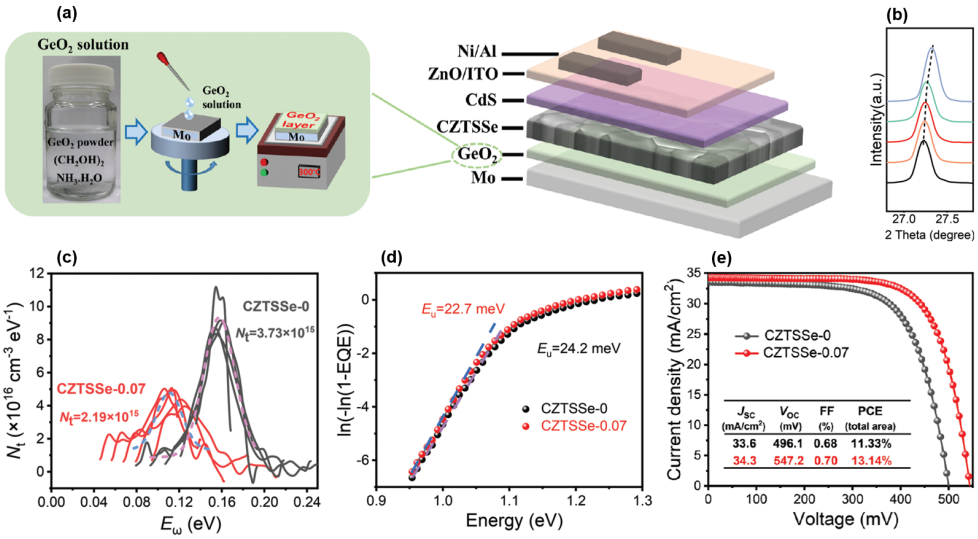

Figure 2.7: Graphical representation of the processing setup (a). X-ray diffraction spectroscopy (XRD) results proving the proper inclusion of Ge within the kesterite crystalline lattice, for varying x ratio (b). Opto-electrical characterization showing reduced bulk defect density (c) and Urbach energy E_u (d). Current-voltage (I-V) curves under AM1.5G illumination exhibiting 13.14% PCE for Ge-doped kesterite (e). Adapted with permission.[21] Copyright 2022, Wiley-VCH.

2.2.3 Discussion

Ge inclusion The alloying of Ge into kesterite thin-film absorbers is mainly motivated by the expected decrease of the V_{oc} deficit for the corresponding solar cell devices. Still, the physical implications of partially or completely substituting Sn by Ge in CZTGSSe compounds are quite intricate and go beyond the sole improvement of V_{oc}. The numerous challenges and (dis-)advantages related to Ge inclusion into kesterite thin films are summarized in the following:

- Overall, Ge can be properly incorporated into the kesterite crystalline lattice onto Sn sites. Still, it may also be detected under the form of GeO_x nanoinclusions at grain boundaries, possibly acting as passivation elements (electron back reflectors), in excess at surfaces or within secondary phases. All these Ge phases are not always uniformly distributed, with a global concentration near the back contact following the natural Ge down-diffusion, but also segregated between grain interiors and boundaries.

- Compared to Ge-free kesterites, the most obvious improvement related to Ge alloying is morphological. First, enlarged grain size close to or beyond the micron scale is nearly always reported, depending on the amount of Ge, sometimes at the expense of a rougher surface. Second, the typical bi-layer kesterite morphology is partly resolved with a more prominent large-grain top layer than the fine-grain bottom layer. Third, void formation due to the evaporation of group IV-$(S,Se)_2$ compounds near the back contact is mitigated given their lower volatility in the case of Ge, thus diminishing chances of delamination and shunting. These observations are especially verified in the case of Se-rich kesterites, for which the explanation seems to reside in a modified reaction mechanism[14,17,64,65,67–70]. Indeed, Ge tends to integrate the kesterite phase at a lower temperature than Sn which lessens elemental segregation between back and front, namely through a Ge_xSe_y liquid-phase assisted flux-crystallization. This in turn supports grain growth and facilitates the diffusion of metal and alkali elements, leading to a higher structural integrity and thin-film quality.

- This Ge-boosted morphology along with kesterite phase purity is attainable as long as the appropriate composition and Ge concentration are ensured. For standard kesterites, Zn-rich (II/IV $\simeq$ 1.2) and Cu-poor (I/(II+IV) $\simeq$ 0.8) ranges are widely recognized as optimums with respect to solar cell performance. Equivalent values are also found in the particular case of Ge alloying, with slight refinements claimed in certain studies. Respecting such compositions allows to mitigate the

spreading of undesired binary phases that are detrimental to solar cell performance, e.g. Cu_x(S,Se), IV-(S,Se), IV-$(S,Se)_2$, elemental Ge or Zn(S,Se). This last compound is mostly eliminated in Zn-rich stoichiometry but still largely observed and particularly disadvantageous through increased leakage and/or reduced grain size. Since Ge tends to greatly modify the reaction mechanism during kesterite formation, the final composition is quite dependent on the Ge proportion itself. In that regard, most reports highlight the importance of non-excessive Ge content (roughly $x <$0.4) to guarantee large-grain, dense and non-porous absorber layers without voids, surface impurities and detrimental secondary phases. Even the slightest composition change may have a great impact on the final thin film. Thus, accurate control of the stoichiometry is key to minimize large variations between the different processing stages, for instance by compensating elemental loss during the annealing step, and guarantee absorber homogeneity.

- The elemental composition also has a great influence on the opto-electronic properties of the kesterite materials. First and foremost, it is possible to finely tune the bandgap of $Cu_2ZnSn_{1-x}Ge_x(S_y,Se_{1-y})_4$ absorbers through x instead of y, which is advantageous as mentioned in Section 2.1. Moreover, the bandgap itself tends to be naturally graded towards the back following the Sn-Ge segregation occurring during the annealing step. This should allow to counteract interface recombination through bandgap engineering at solar cell level. Second, Ge alloying also enables a reduction of both bulk recombination and band tailing through the mitigation of, respectively, highly detrimental deep defects such as Cu_{Sn} or Sn_{Zn} donor states complexed with Cu_{Zn} into [2Cu_{Zn} +- Sn_{Zn}], and Cu-Zn disorder [Cu_{Zn} + Zn_{Cu}]. This is likely related to the effective substitution of bivalent Sn^{2+} and Sn^{4+} by monovalent Ge^{4+} species. Finally, incorporating proper amounts of Ge into CZTGSSe absorbers also globally enhances essential parameters such as the carrier lifetime, mobility and carrier concentration among others. Physically, the two former seem rather related to the improved morphology whereas the latter is partly explained by the creation of Cu_{Ge} and V_{Ge} acceptors as well as the demonstrated interaction between Ge and Na through the liquid Ge-Se phase.

Processing approach Determining the best Ge inclusion strategy must also include the aspect of adapted processing technique and practical challenges to actually deposit CZTGSSe absorbers of sufficient quality and adapted elemental composition and opto-electronic properties. As discussed hereabove, there exist many different techniques to deposit these

materials, whether it is based on physical deposition in vacuum or solution processing in ambient atmosphere. Overall, most of these methods manage to eventually provide a single-phase layer with acceptable morphology, associated with promising PV-related features. Still, they each present respective advantages and drawbacks, which may help in deciding which processing route to follow as further discussed below.

The first noticeable difference between processing strategies is the higher quality and integrity of CZTGSSe thin films processed in vacuum in one-step[40,41,45], as compared to two-step recipes[17,51,52,61,63,65,70,72,75,78,79]. For the former, secondary phases mitigation appears relatively straightforward while the latter globally demonstrates poorer adhesion and morphology, respectively explained to a certain extent by the escape of Ge or Sn sulfides and selenides[63,70,78,79] and grain growth-limiting Zn(S,Se) phases[52,58,60,61,63,78]. The second and even more remarkable difference is the nearly complete absence of secondary phases for solution-based deposition techniques, which thus globally provide kesterite films with higher crystallinity than vacuum-based physical processing. One could have expected the inverse as in the case of CIGS, given that vacuum should typically reduce the risks of external contamination or elemental losses, among others. Different hypotheses could explain this peculiar observation. First, an accurate and reproducible control of the stoichiometry seems equally feasible, if not more, by monitoring the diluted quantities in a solution than by physically depositing stacked layers of expected thicknesses as done in sequential vacuum-based recipes. Second, the importance of elemental dynamics and physical state in the growth of kesterite compounds has been largely put in evidence for sequential vacuum processes, namely leading to back surface delamination and voids formation[17,51,52,58,61,63,65,69,70,72,75,78,79]. On the contrary, this is much less observed for Ge-alloyed kesterites processed in ambient solution[11,109,112], with adapted solutions to be implemented already at the precursor level[108]. Third, mixing sulfur and selenium is particularly challenging to be realized in the gas phase[41], given the much higher volatility of the former, which may be resolved more easily when already integrated at the precursor level in the liquid or solid phase as for solution-based processing.

From the above discussion, one could conclude that non-vacuum-based methods are the optimal approach for processing CZTGSSe thin-film absorbers. Indeed, it globally enables equivalent absorber quality as vacuum-based deposition with a more accurate composition tuning and less secondary phases, while relying on less complex and more affordable experimental setups. However, they presently have a lower up-scaling potential than industrially established vacuum-based techniques such as (co-)evaporation or sputtering for instance, which remains an essential aspect in the wide spreading of PV technologies. Moreover, the performance of the resulting solar cells remains a major decision criterion and should then

be discussed before taking any conclusion, as done below.

2.3 Solar cells

In this section, the performance of CZTGSSe solar cells is detailed with nearly all reported efficiencies up to the time of writing. The primary figures-of-merit used to gauge solar cell performance typically are the efficiency (η) in %, the open-circuit voltage (V_{oc}) in mV, the short-circuit current density (J_{sc}) in mA cm^{-2}, and the fill factor (FF) in %. To take into account the variations of V_{oc}, J_{sc} and FF that are not only bandgap-related as well as putting them in parallel with the theoretical limits famously established by Shockley-Queisser (SQ)[119], it is here considered that the SQ deficits are instead defined as $V_{oc,def}^{SQ}$=$V_{oc}^{SQ} - V_{oc}$, $J_{sc,def}^{SQ} = J_{sc}^{SQ} - J_{sc}$ and $FF_{def}^{SQ} = FF^{SQ} - FF$ using the same units. These are fixed for a certain bandgap, either taken from the reference itself or deducted from the composition following $E_g(x) = x*E_{g,CZGSSe} + (1-x)*E_{g,CZTSSe} - b*x*(1-x)$ with b=0.1 eV[6,13,99–101] when not applicable. To do so, the tabulated values of V_{oc}^{SQ}, J_{sc}^{SQ} and FF^{SQ} for the AM1.5G solar spectrum[120] are used, to which is subtracted the reported value of V_{oc}, J_{sc} and FF. These deficit metrics are displayed in function of both the x =Ge/(Ge+Sn) ratio and the y =S/(S+Se) ratio in "compositional maps" (Figure 2.8) and as a list in Table A.2. These data values are separated in four different composition groups corresponding to the subsections in the reasoning below: Group 1 (Ge-doping and Se-rich) in light blue diamonds, Group 2 (Ge-doping and S-rich) in purple circles, Group 3 (Ge-moderate and Se-rich) in black stars and Group 4 (Pure-Ge) in orange triangles. Other aspects that are specific to complete solar cells are also addressed in this section, e.g. buffer material, diode parameters (ideality factor n and saturation current J_0), electrical parasitics (shunt resistance R_{sh} and series resistance R_s), or interfaces optimization.

2.3.1 Ge-doping and Se-rich (Group 1)

The first remarkable feature on the efficiency map appears in the bottom left corner, i.e. the low-Ge and Se-rich region for x <0.1 and y <0.1, designated as Group 1 and shown as light blue diamonds in Figure 2.8(a). Not only concentrating a large amount of references relying on either sequential physical or solution-based processing, this composition area includes a significant part of the highest reported efficiencies from 8 % up to 13 %, with low SQ deficits around 300 mV, 10 mA cm^{-2} and 15 % for V_{oc}, J_{sc} and FF, respectively. Within the numerous studies related to these CZTSe:Ge absorbers, hypotheses explaining this "sweet spot" for efficiency can be found, and more particularly through the low SQ deficits accounted for V_{oc}

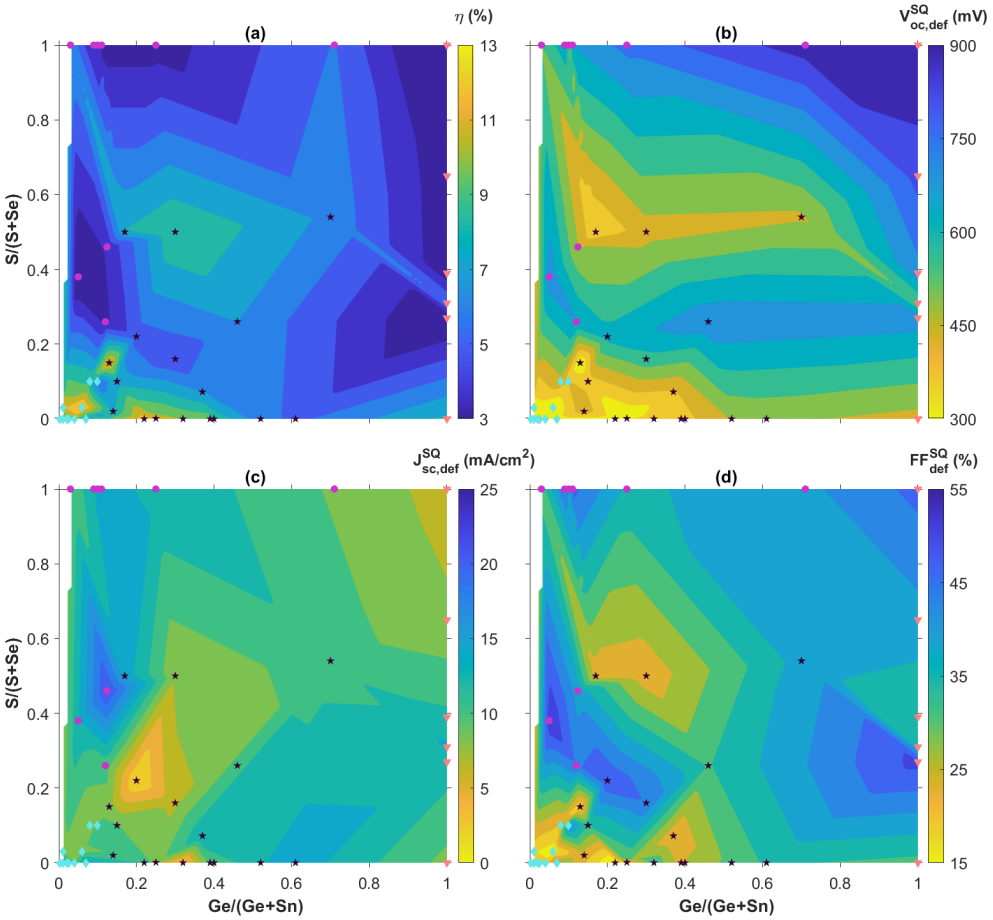

Figure 2.8: Reported champion solar cell efficiency η (a), and extracted SQ deficits $V_{oc,def}^{SQ}$, $J_{sc,def}^{SQ}$, FF_{def}^{SQ} (b) to (d), expressed in function of the composition ratios x =Ge/(Ge+Sn) and y =S/(S+Se) as reported in the references reviewed. The highest efficiencies and lowest deficits are highlighted in yellow. The color levels are equally spaced between the minimum and maximum values for each map and chosen in a sufficient number to ensure clarity. Data points are separated in 4 different groups corresponding to the subsections herein: Group 1 (Ge-doping and Se-rich) in light blue diamonds, Group 2 (Ge-doping and S-rich) in purple circles, Group 3 (Ge-moderate and Se-rich) in black stars and Group 4 (Pure-Ge) in orange triangles. The narrow white area along the left edge of the maps corresponds to lacking reports. Solar cell figures-of-merit beyond the SQ limits are left out of the compositional maps but their (x, y) composition pair is still displayed for statistical relevance. The corresponding data are provided in Table A.2.

and FF (Figure 2.8). Using their pioneer Ge nanolayer approach, IREC highlighted that Ge doping onto Sn sites does not either significantly affect the bandgap value or solve the widely recognized V_{oc}-detrimental band tailing effect[68]. Still, they revealed that Ge doping seems promising to coun-

teract two other important culprits for V_{oc} deficit[14,17,64,65,67–69], i.e. large defect concentration and low net doping, recently put in evidence as the main limiting factors towards high performance[121]. On the one hand, high-density deep bulk defects are partially neutralized, likely as a consequence of Sn^{2+} species mitigation, thus reducing recombination as suggested by the lower n and J_0 values reported. On the other hand, carrier density is increased following the interaction between Ge and Na that is boosted by the IREC-discovered "liquid phase-assisted flux crystallization" mechanism in CZTSe:Ge. Another essential outcome of this novel reaction pathway is a greatly improved morphology, i.e. more uniform, void-free and grain-enhanced, that likely justifies the enhanced FF values, usually via higher shunt resistances. All these observations typically stand as long as the x ratio is kept low[14,17,64,65,67–69], revealing the importance of fine composition tuning. Following this wholesome study about the absorber quality, IREC pushed the optimization further with back and front contacts characterization[18,122]. They proposed that limited Ge quantities help reducing the detrimental Mo/$MoSe_2$ back contact barrier height and the associated series resistance through a reduced defect concentration, possibly also contributing to the low V_{oc} and FF deficits as observed elsewhere[21].

Other groups reported similar observations[16,20,21,74,86,97,98], sometimes with even higher solar cell performance possibly explained to some extent by the alternative Ge doping or absorber deposition approaches used, i.e. either solution-based[20,21,97,98] and/or relying on Ge-atmosphere annealing[16,74] which respectively mitigate secondary phases formation and Ge-loss[105], as discussed in Section 2.2. It is quite remarkable to notice that the natural Sn-Ge segregation appearing in these materials may be either an asset or a disadvantage. In one case, it is used as a way to create shallow back bandgap grading[73,74], acting together with grain boundaries potential barriers to improve carrier separation via limited rear interface recombination[74]. In another case, it is resolved via a Cu-Ge bottom layer and arguably linked to deep defects neutralization and band structure enhancement[97]. The fact that these two antinomial approaches both lead to large V_{oc} and FF gains stresses the difficulty to design efficient kesterite solar cells and the need for further investigations. Besides that, slightly relieved band tails were also observed after Ge doping[16,21,74]. Tackling most of the loss mechanisms discussed herein led to one of the best ever efficiencies for Ge-alloyed kesterite solar cells[21], i.e. 13.1 %, based on a CZTSSe absorber deposited on a GeO_2 bottom nanolayer, both solution-processed (Figure 2.7(e)).

2.3.2 Ge-doping and S-rich (Group 2)

For similarly small amounts of Ge, S-rich compounds have been less investigated and the reports available exhibit much lower performance than

Se-rich kesterites, gathered in Group 2 and shown as purple circles in Figure 2.8. With a vast majority of physical sequential processing[80–84], only one group followed the solution-based route to obtain similar performance with higher V_{oc} but poorer J_{sc} and FF[102]. The explanation for the poor efficiencies observed in Group 2 in Figure 2.8(a) seems two-fold: first, S-rich stoichiometry for kesterite solar cells generally induces higher V_{oc} deficit than the Se-rich alternative[15,123,124], whether it is for record standard Ge-free cells[26] or Ge-alloyed kesterites reviewed herein (Figure 2.8(b)); second and more importantly, the morphology improvements induced by Ge doping tend to be less significant for S-containing kesterite materials, likely due to the absence of GeSe fluxing agent during thin-film growth (Section 2.2) that could explain the striking differences in FF_{def}^{SQ} between Group 1 and 2 in Figure 2.8(d).

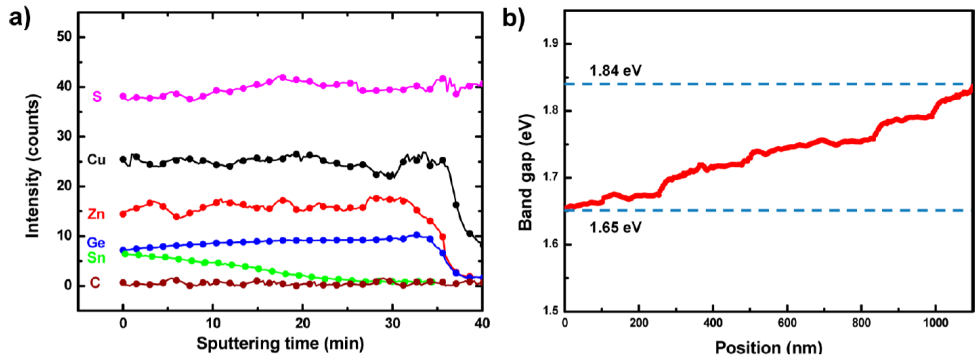

Figure 2.9: Secondary ion mass spectrometry (SIMS) data showing the Sn-Ge graded composition along the absorber thickness (a), with corresponding bandgap values (b). Reprinted (adapted) with permission from [13]. Copyright 2014 American Chemical Society.

Moving away from this low-Ge and high-S composition range was investigated in four different studies (purple circles far from the top left corner in Figure 2.8), but did not lead to a clear reduction of the SQ deficits. On the side of the chalcogen ratio, reducing the S content for Ge-doped kesterites towards a S-Se mixed stoichiometry was attempted on flexible substrates[83,84] or by pulsed laser deposition[89], both with efficiencies not exceeding 4 %. On the side of the group IV ratio, trespassing the 40 % Ge limit previously established in Section 2.2 to realize bandgap grading in CZTGS (Figure 2.9) reached not more than 6% PCE[13].

2.3.3 Ge-moderate and Se-rich (Group 3)

A second efficiency sweet spot seems to be located quite close to the first one on the compositional maps (Group 3 depicted as black

stars in Figure 2.8(a)), with PCE values ranging from 7.1 % to 12.3 %[11,15,19,41,72,75,87,88,107,110], for an x ratio staying between 10 % and 40 % while the chalcogen content is below 20 % S. This is likely resulting from the same Ge-related morphological and opto-electrical improvements seen above for Group 1 which apparently extend until x =0.4, as discussed in Section 2.2 and observed in a few references[41,75,107]. Besides, certain research teams relied on a Ge-containing atmosphere at the annealing step[15,41,75,88,109,110], which should help preventing elemental losses and maintaining the desired composition as also mentioned in Section 2.2. Apart from the usual mitigation of bulk defects and band tailing that boosts V_{oc} and FF[11,15,107,110], various studies highlighted the importance of interface recombination[11,15,19,72]. Solving this very aspect is particularly made possible with x ratios beyond 0.1 that allow a Sn-Ge back bandgap grading leading to improved carrier collection and J_{sc}[19,72]. In one case, this strategy is combined with a Cu-Ag gradient in an innovative double Ag,Ge bandgap gradient design that tackles recombination losses also at the front interface for enhanced V_{oc} and a final efficiency of 12.3%[19] (Figure 2.10). This demonstrates not only the possibility to overcome the present V_{oc} deficit challenges faced by kesterites with novel architecture but also the great potential of extrinsic alloying for solving them. Besides the efficiency itself, its evolution over time is a critical parameter with regards to up-scaling. It is then likely a supplementary advantage and remarkable feature of Ge alloying to seemingly induce performance increase after aging[75,107], for which the physical explanation still needs to be found.

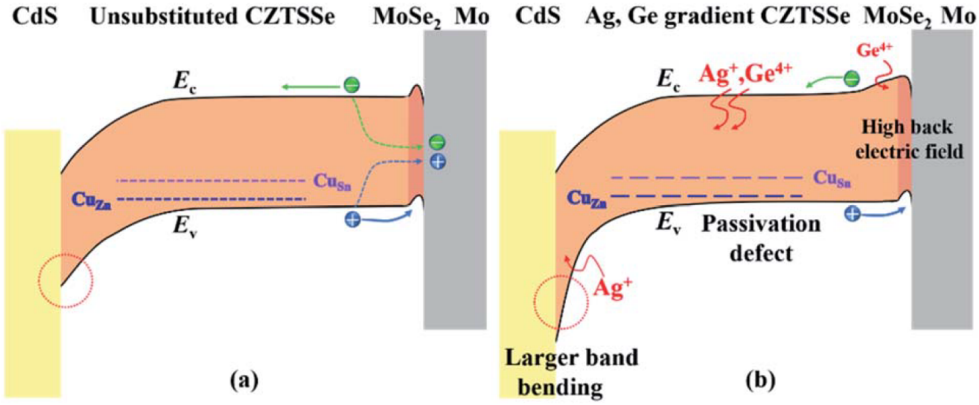

Figure 2.10: Graphical representation of the band diagram of a CZTSSe solar cell in (a) the standard situation (b) the Ag,Ge double bandgap gradient situation. Reproduced from [19] with permission from the Royal Society of Chemistry.

As for Group 2, a few research teams investigated neighbouring composition ranges[8,45,46,104,105,111,112], i.e. mainly towards Ge-rich (x =0.7)

and S-Se mixed (y =0.5) areas (scattered black stars in Figure 2.8). Overall, the obtained performance was lower but promising Shockley-Queisser deficits for V_{oc} and FF were reported for the solution-processed CZTGSSe pioneer studies[8,104,105] around the y =0.5 line in Figure 2.8(b) and (d), for a record PCE of 9.4 %[105]. These devices still underperform as compared to cells from Group 1 and the Se-rich part of Group 3, due to slightly higher V_{oc} and FF deficits. One possible explanation is their higher S content, as discussed for Group 2 devices. Further research is needed to confirm this hypothesis.

This result was obtained mainly through process and composition optimization, more precisely with a control of elemental losses and improved carrier dynamics. It is worth mentioning that other studies managed to process these kesterite compounds either in a low-cost and harmless manner[111,112] or on flexible and semi-transparent substrates at low temperature[45,46]. Even though reported performance was diminished, this may still pave the way for relevant applications with specific techno-economical requirements. Eventually, given the encouraging SQ deficits and the low number of references in such a large composition region, deeper investigations seem likely to push the performance of corresponding kesterite solar cells to higher levels.

2.3.4 Pure-Ge (Group 4)

The fourth and last group gathers all the solar cell performance reported for pure-Ge kesterites (x =1), with particularly poor champion efficiencies below 1 % for S-pure CZGS compounds[80,101], likely for the same reasons as Group 2. On the contrary, Se-pure compounds once again allowed to reach higher PCE, overall close to or beyond 6 %,[53–57,125,126]. On the one hand, Ge substitution enables again to tackle the critical SQ deficit of V_{oc} at the bulk level through a reduction of bulk defects activity and band tailing[54]. On the other hand, it reveals ineffective to completely resolve the significant V_{oc} losses appearing at the top and back interfaces, for which surface treatments provide a more adapted solution[53,55,56]. The detrimental back contact barrier is also identified through simulations as a main culprit for the poor fill factor globally observed in this case[127]. Consequently, combined optimization of buffer material and interface quality is an essential pathway towards higher performance for these wide-bandgap pure-Ge absorbers. This enabled the 8.5 % current champion efficiency for CZGSe[53], as well as the efficiency of S-Se mixed CZGSSe with y =0.3 to increase from 2 % to 6 %[95,96,128] (Figure 2.11). Besides that, fine tuning of the global stoichiometry remains a key factor with regards to defects and secondary phases formation[57,125], which was investigated in one case with an innovative machine learning-based approach, leading to refined composition ranges for high-yield CZGSe[57]. Even though their current ef-

ficiency remains strongly limited in comparison with Group 1 and 3, these wide bandgap CZGSSe compounds could well fit in the increasingly popular tandem solar cells, as long as a sufficient research effort is provided to solve the aforementioned issues.

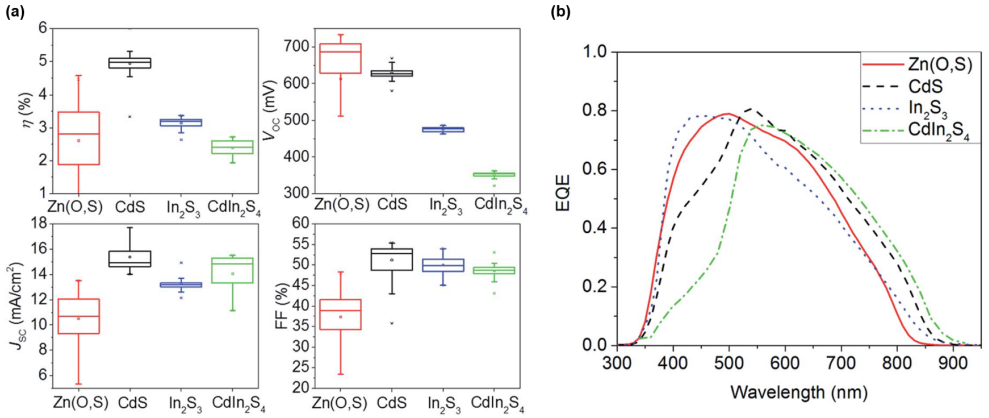

Figure 2.11: Evolution of CZGSSe solar cell performance for different buffer materials in terms of (a) I-V parameters (b) EQE response. Adapted from[128] with permission from the Royal Society of Chemistry.

2.4 Conclusion

The first conclusion that can be drawn from this analysis is that alloying Ge into kesterite absorbers appears as a promising strategy towards higher solar cell efficiencies, with best efficiencies beyond 13 % for solution-processed CZTGSSe[9,21] while similar performance was recently attained for Ag-incorporated kesterites[24,27,30]. This emphasizes the great potential of extrinsic alloying for standard CZTSSe kesterites, even enabling combined approaches such as the successful double Ag,Ge gradient design discussed herein[19]. Given similarly well-controlled stoichiometry, Ge alloying provides advantages at both the thin film and solar cell level compared to Ge-free kesterites. First, it modifies the kesterite formation mechanism to favour crystallization dynamics towards greatly improved structural morphology, which raises the fill factor among other things. Second, it strongly mitigates electronic defects as well as crystalline disorder to systematically decrease the V_{oc} deficit of CZTSSe materials, which remains the most critical barrier towards higher performance. Third, it allows Sn-Ge bandgap grading to strengthen carrier collection and increase J_{sc}, which is arguably less dependent on composition than V_{oc} and FF in Figure 2.8. This further highlights their crucial roles as performance limiting factors in kesterite

PV devices, which may be partially overcome through Ge incorporation as studied in-depth within the present chapter.

The second conclusion concerns the optimal Ge/(Ge+Sn) content with regards to performance, which requires a preliminary comment about statistical relevance. Indeed, a large majority of research groups concentrated their efforts only on certain parts of the whole x and y composition domain, likely motivated by the previous theoretical and/or experimental studies. The most actively investigated areas of the composition maps are groups 1 and 3 in Figure 2.8, i.e. Se-rich kesterites with Ge contents not exceeding 40 %, which also tend to be the most successful with regards to performance. Whether this is the consequence of more optimal stoichiometry only or of longer optimization effort too, still needs to be clarified as investigated in Chapter 3. The herein presented review of the current state-of-the-art suggests that Ge contents beyond 40 % may lead to new challenges and efficiency limitations. Actually, even minute amounts of Ge below 1 % already bring significant upgrades to kesterite performance. This is particularly well aligned with the critical raw materials requirements related to Ge[129], and maintains kesterites as a more sustainable substitute to replace CIGS. As observed also in Ge-free kesterite devices (Figure 2.1b)), Se-rich composition remains favorable with regards to PCE as compared to S-rich for Ge-alloyed kesterite solar cells. All of this then puts in evidence the Ge-low and Se-rich efficiency sweet spot for all CZTGSSe devices up to the time of writing, obtained for x =Ge/(Ge+Sn) and y =S/(S+Se) respectively below 40 and 20 %.

Whether a high-efficiency potential also resides for Ge contents beyond 40 %, where the wider absorber bandgap is more adapted for novel PV applications, is investigated in Chapter 3. In practice, the exploration of other composition regions has already been initiated to some extent with promising results, especially for V_{oc} and FF deficits of group 3 in Figure 2.8. Pushing this further may not only help to either challenge or confirm previous assumptions about Ge alloying, but also to better understand the physical reasons explaining the benefits of Ge incorporation. Such studies would then inevitably bring a clearer and more global understanding of the main loss mechanisms affecting kesterites and the best ways to counteract them. Combining this in parallel with the transfer of valuable knowledge between composition regions, e.g. buffer and interface optimization from low-efficiency CZGSSe to high-efficiency CZTSe:Ge, may be one pathway to reach the next PCE milestone. Combining this exploration of Ge-rich alloying with S-rich wide-bandgap compounds would contribute to position kesterites as interesting alternatives in tandem solar cells[80,130,131], for which the current literature is limited and mostly theoretical[132–134], as well as indoor PV[135,136].

While the potential of Ge alloying for enhancing the quality and versatility of kesterites is made clear in this chapter, the challenge to integrate

high Ge contents into the current processing baselines while maintaining material quality and device performance is also put in evidence, along with the tradeoff between physical and chemical deposition approaches. These aspects are experimentally investigated in the next chapter.

Bibliography

[1] R. Scaffidi et al. *J. Mater. Chem. A* 11.25 (2023), pp. 13174–13194. DOI: 10.1039/D3TA01218B.

[2] K. Biswas, S. Lany, and A. Zunger. *Appl. Phys. Lett.* 96.20 (2010), p. 201902. DOI: 10.1063/1.3427433.

[3] H. Nishihara et al. *Jpn. J. Appl. Phys.* 56.4S (2017), 04CS08. DOI: 10.7567/JJAP.56.04CS08.

[4] R. B. Wexler, G. S. Gautam, and E. A. Carter. *J. Mater. Chem. A* 9.15 (2021), pp. 9882–9897. DOI: 10.1039/D0TA11603C.

[5] T. Ratz et al. *J. Mater. Chem. A* 10.8 (2022), pp. 4355–4365. DOI: 10.1039/D1TA09620F.

[6] Q. Shu et al. *Phys. Rev. B* 87.11 (2013), p. 115208. DOI: 10.1103/PhysRevB.87.115208.

[7] T. Ratz et al. *J. Phys. Energy* 3.3 (2021), p. 035005. DOI: 10.1088/2515-7655/abefbe.

[8] G. M. Ford et al. *Chem. Mater.* 23.10 (2011), pp. 2626–2629. DOI: 10.1021/cm2002836.

[9] J. Shi et al. *Nat Energy* (2024). DOI: 10.1038/s41560-024-01551-5.

[10] M. A. Green et al. *Progress in Photovoltaics: Research and Applications* 33.7 (2025), pp. 795–810. DOI: 10.1002/pip.3919.

[11] S. Bag et al. *Chem. Mater.* 24.23 (2012), pp. 4588–4593. DOI: 10.1021/cm302881g.

[12] C. J. Hages et al. (2013).

[13] I. Kim et al. *Chem. Mater.* 26.13 (2014), pp. 3957–3965. DOI: 10.1021/cm501568d.

[14] S. Giraldo et al. *Adv. Energy Mater.* 5.21 (2015), p. 1501070. DOI: 10.1002/aenm.201501070.

[15] S. Kim et al. *Appl. Phys. Express* 9.10 (2016), p. 102301. DOI: 10.7567/APEX.9.102301.

[16] Y. Sun et al. *Materials Letters* 195 (2017), pp. 76–78. DOI: 10.1016/j.matlet.2017.02.090.

[17] S. Giraldo et al. *Energy Environ. Sci.* 11.3 (2018), pp. 582–593. DOI: 10.1039/C7EE02318A.

[18] S. Lee et al. *Solar Energy* 194 (2019), pp. 114–120. DOI: 10.1016/j.solener.2019.10.042.

[19] J. Fu et al. *J. Mater. Chem. A* 8.42 (2020), pp. 22292–22301. DOI: 10.1039/D0TA06318E.

[20] Y. Deng et al. *Journal of Energy Chemistry* 61 (2021), pp. 1–7. DOI: 10.1016/j.jechem.2021.02.011.

[21] J. Wang et al. *Advanced Materials* 34.27 (2022), p. 2202858. DOI: 10.1002/adma.202202858.

[22] M. A. Green et al. *Prog Photovolt Res Appl* 29.7 (2021), pp. 657–667. DOI: 10.1002/pip.3444.

[23] W. Wang et al. *Advanced Energy Materials* 4.7 (2014), p. 1301465. DOI: https://doi.org/10.1002/aenm.201301465.

[24] M. A. Green et al. *Progress in Photovoltaics* 30.1 (2022), pp. 3–12. DOI: 10.1002/pip.3506.

[25] D.-H. Son et al. *J. Mater. Chem. A* 7.44 (2019), pp. 25279–25289. DOI: 10.1039/C9TA08310C.

[26] M. A. Green et al. *Progress in Photovoltaics* 30.7 (2022), pp. 687–701. DOI: 10.1002/pip.3595.

[27] Y. Gong et al. *Nat Energy* 7.10 (2022), pp. 966–977. DOI: 10.1038/s41560-022-01132-4.

[28] M. A. Green et al. *Progress in Photovoltaics* 32.1 (2024), pp. 3–13. DOI: 10.1002/pip.3750.

[29] M. A. Green et al. *Progress in Photovoltaics: Research and Applications* 32.7 (2024), pp. 425–441. DOI: 10.1002/pip.3831.

[30] J. Zhou et al. *Nat Energy* (2023). DOI: 10.1038/s41560-023-01251-6.

[31] C. Yan et al. *Nat Energy* 3.9 (2018), pp. 764–772. DOI: 10.1038/s41560-018-0206-0.

[32] X. Cui et al. *Energy & Environmental Science* 12.9 (2019), pp. 2751–2764. DOI: 10.1039/C9EE01726G.

[33] K. Yin et al. *Nature Energy* 10.2 (2025), pp. 205–214. DOI: 10.1038/s41560-024-01681-w.

[34] T. Gershon et al. *Current Opinion in Green and Sustainable Chemistry* 4 (2017), pp. 29–36. DOI: 10.1016/j.cogsc.2017.01.003.

[35] Y. E. Romanyuk et al. *J. Phys. Energy* 1.4 (2019), p. 044004. DOI: 10.1088/2515-7655/ab23bc.

[36] S. Giraldo et al. *Adv. Mater.* 31.16 (2019), p. 1806692. DOI: 10.1002/adma.201806692.

[37] M. He et al. *Adv. Sci.* 8.9 (2021), p. 2004313. DOI: 10.1002/advs.202004313.

[38] K. J. Tiwari et al. 2022, pp. 41–66. DOI: 10.1007/978-981-19-3724-8_3.

[39] K. Sun, F. Liu, and X. Hao. 2022. DOI: 10.5772/intechopen.101744.

[40] P. Uday Bhaskar et al. *Thin Solid Films* 534 (2013), pp. 249–254. DOI: 10.1016/j.tsf.2013.03.001.

[41] S. Kim et al. *Solar Energy Materials and Solar Cells* 144 (2016), pp. 488–492. DOI: 10.1016/j.solmat.2015.09.039.

[42] T. Nagai et al. *ACS Appl. Mater. Interfaces* 11.4 (2019), pp. 4637–4648. DOI: 10.1021/acsami.8b19200.

[43] T. Nagai et al. *Phys. Status Solidi RRL* 14.4 (2020), p. 1900708. DOI: 10.1002/pssr.201900708.

[44] D. Chen and N. Ravindra. *Journal of Alloys and Compounds* 579 (2013), pp. 468–472. DOI: 10.1016/j.jallcom.2013.06.048.

[45] A. Ruiz-Perona et al. *Solar Energy* 199 (2020), pp. 864–871. DOI: 10.1016/j.solener.2020.02.082.

[46] A. Ruiz-Perona et al. *Solar Energy* 206 (2020), pp. 555–563. DOI: 10.1016/j.solener.2020.06.044.

[47] A. Ruiz-Perona et al. *Journal of Alloys and Compounds* 868 (2021), p. 159253. DOI: 10.1016/j.jallcom.2021.159253.

[48] A. Ruiz-Perona et al. *Solar Energy* 226 (2021), pp. 251–259. DOI: 10.1016/j.solener.2021.08.032.

[49] R. Caballero et al. *Solar Energy Materials and Solar Cells* 139 (2015), pp. 1–9. DOI: 10.1016/j.solmat.2015.03.004.

[50] H. Matsushita, T. Ochiai, and A. Katsui. *Journal of Crystal Growth* 275.1-2 (2005), e995–e999. DOI: 10.1016/j.jcrysgro.2004.11.154.

[51] M. Buffière et al. *Thin Solid Films* 582 (2015), pp. 171–175. DOI: 10.1016/j.tsf.2014.09.024.

[52] G. Brammertz et al. *Thin Solid Films* 670 (2019), pp. 76–79. DOI: 10.1016/j.tsf.2018.12.015.

[53] L. Choubrac et al. *ACS Appl. Energy Mater.* 3.6 (2020), pp. 5830–5839. DOI: 10.1021/acsaem.0c00763.

[54] S. Sahayaraj et al. *Solar Energy Materials and Solar Cells* 171 (2017), pp. 136–141. DOI: 10.1016/j.solmat.2017.06.050.

[55] N. Benhaddou et al. *Solar Energy Materials and Solar Cells* 216 (2020), p. 110701. DOI: 10.1016/j.solmat.2020.110701.

[56] I. Anefnaf et al. *Solar Energy Materials and Solar Cells* 227 (2021), p. 111106. DOI: 10.1016/j.solmat.2021.111106.

[57] E. Grau-Luque et al. *J. Mater. Chem. A* 9.16 (2021), pp. 10466–10476. DOI: 10.1039/D1TA01299A.

[58] G. Swapna Mary et al. *Vacuum* 131 (2016), pp. 264–270. DOI: 10.1016/j.vacuum.2016.06.020.

[59] C. Sripan et al. *Surfaces and Interfaces* 7 (2017), pp. 134–138. DOI: 10.1016/j.surfin.2017.03.009.

[60] L. Huang et al. *Materials Letters* 159 (2015), pp. 1–4. DOI: 10.1016/j.matlet.2015.05.170.

[61] M. Courel et al. *J. Phys. D: Appl. Phys.* 51.9 (2018), p. 095107. DOI: 10.1088/1361-6463/aaa7db.

[62] N. Saini et al. *Solar RRL* 6.2 (2022), p. 2100837. DOI: 10.1002/solr.202100837.

[63] T. Kohl et al. *Thin Solid Films* 660 (2018), pp. 247–252. DOI: 10.1016/j.tsf.2018.06.038.

[64] S. Giraldo et al. *IEEE J. Photovoltaics* 6.3 (2016), pp. 754–759. DOI: 10.1109/JPHOTOV.2016.2535236.

[65] S. Giraldo et al. *Prog. Photovolt: Res. Appl.* 24.10 (2016), pp. 1359–1367. DOI: 10.1002/pip.2797.

[66] S. Giraldo et al. *Prog Photovolt Res Appl* 27.9 (2019), pp. 779–788. DOI: 10.1002/pip.3147.

[67] M. Neuschitzer et al. *J. Phys. Chem. C* 120.18 (2016), pp. 9661–9670. DOI: 10.1021/acs.jpcc.6b02315.

[68] M. Neuschitzer et al. *J. Mater. Chem. A* 6.25 (2018), pp. 11759–11772. DOI: 10.1039/C8TA02551G.

[69] M. Ritzer et al. *ACS Appl. Energy Mater.* 3.1 (2020), pp. 558–564. DOI: 10.1021/acsaem.9b01784.

[70] J. Márquez et al. *Chem. Mater.* 29.21 (2017), pp. 9399–9406. DOI: 10.1021/acs.chemmater.7b03416.

[71] J. González-Castillo et al. *Materials Science in Semiconductor Processing* 83 (2018), pp. 96–101. DOI: 10.1016/j.mssp.2018.04.024.

[72] J. Andrade-Arvizu et al. *ACS Appl. Energy Mater.* 3.11 (2020), pp. 10362–10375. DOI: 10.1021/acsaem.0c01146.

[73] C. Andres et al. *Thin Solid Films* 665 (2018), pp. 168–172. DOI: 10.1016/j.tsf.2018.09.022.

[74] J. Liu et al. *ACS Appl. Mater. Interfaces* 13.47 (2021), pp. 56302–56308. DOI: 10.1021/acsami.1c16861.

[75] D. Nowak et al. *Applied Sciences* 12.3 (2022), p. 1376. DOI: 10.3390/app12031376.

[76] S. Padhy et al. *Materials Science in Semiconductor Processing* 138 (2022), p. 106276. DOI: 10.1016/j.mssp.2021.106276.

[77] M. Powalla et al. *Applied Physics Reviews* 5.4 (2018), p. 041602. DOI: 10.1063/1.5061809.

[78] J. Chen et al. *Journal of Alloys and Compounds* 621 (2015), pp. 154–161. DOI: 10.1016/j.jallcom.2014.09.097.

[79] N. Saini et al. *Phys. Status Solidi A* 216.22 (2019), p. 1900492. DOI: 10.1002/pssa.201900492.

[80] N. Saini et al. *Journal of Alloys and Compounds* 880 (2021), p. 160478. DOI: 10.1016/j.jallcom.2021.160478.

[81] K.-S. Lim et al. *Materials Science in Semiconductor Processing* 89 (2019), pp. 194–200. DOI: 10.1016/j.mssp.2018.09.020.

[82] T. Sanchez et al. *Solar Energy Materials and Solar Cells* 198 (2019), pp. 44–52. DOI: 10.1016/j.solmat.2019.04.011.

[83] J. Li et al. *Materials Letters* 190 (2017), pp. 188–190. DOI: 10.1016/j.matlet.2016.12.106.

[84] L. Sun et al. *Vacuum* 165 (2019), pp. 186–192. DOI: 10.1016/j.vacuum.2019.04.026.

[85] Y. Gong et al. *Energy Environ. Sci.* 14.4 (2021), pp. 2369–2380. DOI: 10.1039/D0EE03702H.

[86] D. B. Khadka, S. Kim, and J. Kim. *J. Phys. Chem. C* 120.8 (2016), pp. 4251–4258. DOI: 10.1021/acs.jpcc.5b11594.

[87] B. H. Lee et al. *Materials Letters* 284 (2021), p. 128981. DOI: 10.1016/j.matlet.2020.128981.

[88] L. Du et al. *Journal of Alloys and Compounds* 737 (2018), pp. 184–188. DOI: 10.1016/j.jallcom.2017.12.040.

[89] A. Lokhande et al. *Solar Energy Materials and Solar Cells* 161 (2017), pp. 355–367. DOI: 10.1016/j.solmat.2016.12.016.

[90] M. Grossberg et al. *Thin Solid Films* 582 (2015), pp. 176–179. DOI: 10.1016/j.tsf.2014.10.055.

[91] G. Gurieva et al. *Journal of Physics and Chemistry of Solids* 99 (2016), pp. 100–104. DOI: 10.1016/j.jpcs.2016.08.017.

[92] S. Niedenzu, G. Gurieva, and S. Schorr. *Thin Solid Films* 669 (2019), pp. 625–628. DOI: 10.1016/j.tsf.2018.11.039.

[93] D. B. Khadka and J. Kim. *CrystEngComm* 15.48 (2013), p. 10500. DOI: 10.1039/c3ce41387j.

[94] A. M. Ayala et al. *Thin Solid Films* 676 (2019), pp. 68–74. DOI: 10.1016/j.tsf.2019.02.049.

[95] T. Schnabel, M. Seboui, and E. Ahlswede. *RSC Adv.* 7.1 (2017), pp. 26–30. DOI: 10.1039/C6RA23068G.

[96] T. Schnabel, M. Seboui, and E. Ahlswede. *Energies* 10.11 (2017), p. 1813. DOI: 10.3390/en10111813.

[97] Z. Zhang et al. *Sol. RRL* 4.5 (2020), p. 2000059. DOI: 10.1002/solr.202000059.

[98] Y. Han et al. *ACS Appl. Energy Mater.* 4.10 (2021), pp. 11793–11801. DOI: 10.1021/acsaem.1c02519.

[99] D. B. Khadka and J. Kim. *J. Phys. Chem. C* 119.4 (2015), pp. 1706–1713. DOI: 10.1021/jp510877g.

[100] M. Singh, T. R. Rana, and J. Kim. *Journal of Alloys and Compounds* 675 (2016), pp. 370–376. DOI: 10.1016/j.jallcom.2016.03.138.

[101] G. Chen et al. *Journal of Alloys and Compounds* 718 (2017), pp. 236–245. DOI: 10.1016/j.jallcom.2017.05.150.

[102] S. Sun et al. *International Conference on Optoelectronic and Microelectronic Technology and Application*. 2020, p. 165. DOI: 10.1117/12.2585461.

[103] C. Aytug Ava et al. *Optical Materials* 121 (2021), p. 111565. DOI: 10.1016/j.optmat.2021.111565.

[104] Q. Guo et al. *Solar Energy Materials and Solar Cells* 105 (2012), pp. 132–136. DOI: 10.1016/j.solmat.2012.05.039.

[105] C. J. Hages et al. *Prog. Photovolt: Res. Appl.* 23.3 (2015), pp. 376–384. DOI: 10.1002/pip.2442.

[106] A. S. R. Chesman et al. *Chem. Mater.* 26.19 (2014), pp. 5482–5491. DOI: 10.1021/cm501393h.

[107] A. D. Collord and H. W. Hillhouse. *Chem. Mater.* 28.7 (2016), pp. 2067–2073. DOI: 10.1021/acs.chemmater.5b04806.

[108] Q. Yi et al. *ACS Appl. Mater. Interfaces* 9.2 (2017), pp. 1602–1608. DOI: 10.1021/acsami.6b13683.

[109] W. Zhao, D. Pan, and S. Liu. *Nanoscale* 8.19 (2016), pp. 10160–10165. DOI: 10.1039/C6NR00959J.

[110] C. Gao, Y. Sun, and W. Yu. *Coatings* 8.9 (2018), p. 304. DOI: 10.3390/coatings8090304.

[111] X. Lv et al. *Ceramics International* 46.16 (2020), pp. 25638–25645. DOI: 10.1016/j.ceramint.2020.07.039.

[112] P. Punathil et al. *Solar Energy* 236 (2022), pp. 599–607. DOI: 10.1016/j.solener.2022.03.027.

[113] X. Peng, S. Zhang, and Y. Xiang. *Journal of Alloys and Compounds* 640 (2015), pp. 75–81. DOI: 10.1016/j.jallcom.2015.03.248.

[114] F. Li, Z. Xia, and Q. Liu. *J. Phys. Chem. C* 120.30 (2016), pp. 16969–16976. DOI: 10.1021/acs.jpcc.6b05894.

[115] F. E. Cancino-Gordillo, J. V. Cab, and U. Pal. *Applied Surface Science* 571 (2022), p. 151261. DOI: 10.1016/j.apsusc.2021.151261.

[116] D. Mora-Herrera, M. Pal, and F. Paraguay-Delgado. *Materials Chemistry and Physics* 257 (2021), p. 123764. DOI: 10.1016/j.matchemphys.2020.123764.

[117] Y. Li et al. *RSC Adv.* 4.98 (2014), pp. 55016–55022. DOI: 10.1039/C4RA10780B.

[118] J. Li et al. *Materials Letters* 163 (2016), pp. 111–114. DOI: 10.1016/j.matlet.2015.10.065.

[119] W. Shockley and H. J. Queisser. *Journal of Applied Physics* 32.3 (1961), pp. 510–519. DOI: 10.1063/1.1736034.

[120] S. Rühle. *Solar Energy* 130 (2016), pp. 139–147. DOI: 10.1016/j.solener.2016.02.015.

[121] J. Li et al. *Nat Energy* 7.8 (2022), pp. 754–764. DOI: 10.1038/s41560-022-01078-7.

[122] S. Lee, K. J. Price, and E. Saucedo. *J. Phys. D: Appl. Phys.* 54.33 (2021), p. 335501. DOI: 10.1088/1361-6463/ac03e9.

[123] H.-S. Duan et al. *Advanced Functional Materials* 23.11 (2013), pp. 1466–1471. DOI: 10.1002/adfm.201201732.

[124] K. Pal et al. *Solar Energy Materials and Solar Cells* 196 (2019), pp. 138–156. DOI: 10.1016/j.solmat.2019.03.001.

[125] R. Gunder et al. *CrystEngComm* 20.11 (2018), pp. 1491–1498. DOI: 10.1039/C7CE02090B.

[126] L. Choubrac et al. *Phys. Status Solidi A* 215.13 (2018), p. 1800043. DOI: 10.1002/pssa.201800043.

[127] S. Yang et al. *J. Phys. D: Appl. Phys.* 53.38 (2020), p. 385102. DOI: 10.1088/1361-6463/ab936b.

[128] T. Schnabel et al. *RSC Adv.* 7.64 (2017), pp. 40105–40110. DOI: 10.1039/C7RA06438A.

[129] EU. *Critical raw materials*. https://single-market-economy.ec.europa.eu/sectors/raw-materials/areas-specific-interest/critical-raw-materials_en.

[130] B. Vermang et al. *Sustainable Energy Fuels* 3.9 (2019), pp. 2246–2259. DOI: 10.1039/C9SE00266A.

[131] S. Khelifi et al. *Solar Energy Materials and Solar Cells* 219 (2021), p. 110824. DOI: 10.1016/j.solmat.2020.110824.

[132] A. D. Adewoyin et al. *Optik* 176 (2019), pp. 132–142. DOI: 10.1016/j.ijleo.2018.09.033.

[133] M. Umehara et al. *Journal of Alloys and Compounds* 689 (2016), pp. 713–717. DOI: 10.1016/j.jallcom.2016.08.039.

[134] M. Jamil et al. *Journal of Alloys and Compounds* 821 (2020), p. 153221. DOI: 10.1016/j.jallcom.2019.153221.

[135] M. Placidi et al. *Solar RRL* 9.11 (2025), p. 2500030. DOI: 10.1002/solr.202500030.

[136] Y. Gong et al. *Solar RRL* 9.4 (2025), p. 2400756. DOI: 10.1002/solr.202400756.

CHAPTER 3
Enhancing kesterite quality and versatility via Ge alloying

This chapter is based on the following articles:

- R. Scaffidi, G. Brammertz, Y. Wang, A. U. Zaman, K. Sasikumar, J. De Wild, D. Flandre, and B. Vermang. "A study of bandgap-graded CZTGSe kesterite thin films for solar cell applications". *Energy Adv.* 2.10 (2023), pp. 1626–1633. DOI: 10.1039/D3YA00359K
- R. Scaffidi, Y. Gong, A. Jimenez-Arguijo, A. G. Medaille, S. Suresh, G. Brammertz, S. Giraldo, J. Puigdollers, D. Flandre, B. Vermang, and E. Saucedo. "Tuning the bandgap without compromising efficiency: Ambient solution processing of Ge-alloyed (Ag,Cu)2Zn(Sn,Ge)(S,Se)4 kesterite thin-film solar cells". *Materials Today Energy* 46 (2024), p. 101715. DOI: 10.1016/j.mtener.2024.101715

3.1 Motivation

The challenge of varying the kesterite bandgap while preserving its quality as a PV absorber remains largely unsolved. As developed in the previous chapter, a promising solution resides in the isovalent alloying of Ge to replace Sn, so as to widen the kesterite absorber bandgap for tandem or indoor PV applications[3–8], or to realize bandgap gradient designs known to typically boost the device efficiency[1,9–16]. Still, most studies up to this day have focused on Ge contents below 40%[5], which corresponds to absorber bandgaps not high enough to comply with the specifications of such applications. This is a direct consequence of the difficulty to reach higher Ge incorporation while preserving material quality and device performance, which is the overarching goal of this chapter, structured as follows. First, this section serves as motivation for the whole chapter by firstly introducing the starting baseline for Ge-alloyed kesterites and its main limitations. Second, the updated baseline relying on a molecular ink recipe is presented in details along with multiple characterization experiments realized at both the material and device levels. Finally, both baselines are compared on diverse key aspects to highlight the resulting improvements.

The starting baseline consists in a sequential physical deposition process developed to fabricate $Cu_2Zn(Sn,Ge)Se_4$ (CZTGSe) absorbers[1]. Inspired from previous literature studies, those thin films are grown in the expected kesterite structure via the annealing of an evaporated Ge/Zn/Sn/Cu/Sn/Zn/Ge metallic stack in H_2Se. They fulfill the basic requirements of an intermediate-quality starting baseline for PV absorbers, i.e. decent polycrystalline morphology with micron-size grains in the kesterite structure, Cu-poor stoichiometry for the desired p-type intrinsic doping and sufficient photoluminescence yield with carrier lifetime of the order of the nanosecond[1]. Nevertheless, these thin-film CZTGSe layers have one particular feature going beyond the expected standards. Indeed, ToF-SIMS experiments calibrated by EDX measurements demonstrate a gradient in the Ge/(Ge+Sn) ratio from around 20% at the front absorber surface to slightly above 60 % at the rear side in Figure 3.1a), likely due to their opposite migration during the reactive annealing step[1]. Since Ge/(Ge+Sn) determines the conduction band level, the Sn-Ge profile in Figure 3.1a) induces the bandgap of the absorber to widen toward its back surface. Although such a design is typically considered beneficial, these CZTGSe absorbers suffer from other limitations. Indeed, the significant discrepancy between the bandgap estimates from the EQE derivative maximum $E_{g,EQE} = 1.23eV$ and the PL spectrum peak position $E_{g,PL} = 1.04eV$ is usually considered an evidence of high crystalline disorder in kesterite materials[17,18], and herein correlates rather well with the large Urbach tail within which $E_{g,PL}$ is located in Figure 3.1b). The corresponding Urbach

energy E_u of 42 meV is well beyond the sub-20 meV range considered ideal for chalcogenide PV absorbers[18–20]. These are indicators of a global non-ideal opto-electronic character of the CZTGSe absorbers due to band tails and potential fluctuations, i.e. a common source of radiative V_{oc} losses. The non-ideality also extends at the device level as attested by the significantly lower V_{oc} activation energy $E_{a,Voc}$ compared to $E_{g,EQE}$ and $E_{g,PL}$ in Figure 3.1c). This suggests the parallel presence of strong non-radiative recombination limiting the HJ quality, as also evidenced by their poor diode parameters $n > 2$ and $J_0 \simeq 10^{-6} A/cm^2$. These are important contributors to the limited performance of this starting baseline, as illustrated in Figure 3.1d) with a champion PCE of only 6% and large V_{oc} SQ deficit of 475 mV. The starting baseline also showcases low resilience to changes in the absorber composition, whether they are intentional, e.g. to tune the overall stoichiometry, or unpredictable, e.g. variations in the precursor stack exact thickness. These observations emphasize the need for an enhanced Ge-alloyed kesterite baseline resulting in closer-to-ideal opto-electronic device behaviour and providing a flexible Ge alloying strategy over large stoichiometric ranges, presented as the updated baseline in the following.

More precisely, a molecular ink solution process in ambient air that incorporates beyond 40% of Ge to control the bandgap of high-quality Ag-alloyed $(Ag,Cu)_2Zn(Sn,Ge)(S,Se)_4$ (ACZTGSSe) kesterite thin films in a wide range is developed. By a simple substitution to Sn directly in the precursor solution, Ge is properly integrated into single-phase polycrystalline kesterite absorbers with flexible bandgap tuning from 1.15 to 1.5 eV for 0 to 100% Ge. The incorporation of Ge and associated bandgap widening do not compromise opto-electronic quality since benign Urbach tail coupled to low V_{oc} deficit is observed regardless of the bandgap. In particular, the champion device containing 40% Ge reaches a remarkable 12.1% efficiency without anti-reflective coating (ARC) and 62% of the detailed balance limit for V_{oc}, which sets a new record for Ge-alloyed kesterites with a bandgap of 1.2 eV. The outstanding resilience of Urbach energy to larger bandgaps, demonstrated in this chapter, is an important milestone in the development of high-quality kesterite absorbers processed via cheap solution-based routes and adapted to tandem and indoor PV applications, among others. This shall require the optimization of HJ band alignment and mitigation of detrimental electronic defects for the highest Ge contents.

3.2 Materials and Methods

The device fabrication process is schematically illustrated in Figure 3.2 and inspired from a previous work[21]. The precursor solutions are prepared following the same molecular ink chemical route in ambient air.

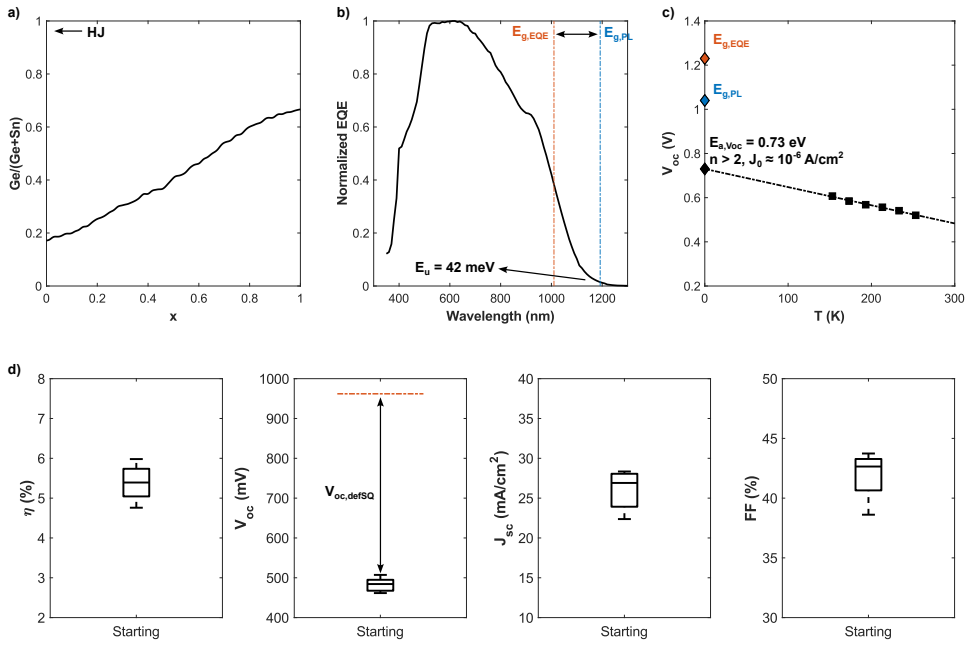

Figure 3.1: Main characteristics of the Ge-alloyed kesterite starting baseline based on physical process. a) Ge/(Ge+Sn) ratio in function of the position x along the absorber thickness, extrapolated from the EDX-calibrated ToF-SIMS data. The black arrow indicates the kesterite/CdS HJ interface. b) EQE response of the champion CZTGSe cell at 0 V, with $E_{g,PL}$ and $E_{g,EQE}$ represented by respectively blue and orange dashed lines. The Urbach energy $E_u = 42meV$ extracted from the EQE tail beyond 1100nm is also indicated. c) Temperature evolution of V_{oc}, linearly extrapolated to a value $E_{a,Voc} = 0.77eV$ at 0K with $E_{g,PL}$ and $E_{g,EQE}$ represented by diamonds of the same colour as in b). d) Statistical dispersion of η, V_{oc}, J_{sc} and FF for the CZTGSe solar cells. For each box, the central line represents the median, while its top and bottom edges, respectively, indicate the 25th and 75th percentiles. The whiskers, i.e. the dashed lines extending from both edges of each box, indicate the most extreme data points. The dashed orange line depicts the V_{oc} Shockley-Queisser limit for $E_{g,EQE}$.

First, the CuCl, AgCl, $SnCl_4$, $GeCl_4$ and $Zn(CH_3CO_2)_2$ precursors are mixed with Thiourea (TU) in Dimethyl Formamide (DMF) solvent with a molarity of TU/(Ag+Cu+Zn+Sn+Ge) = 1.8 M. The ratios of $SnCl_4$ and $GeCl_4$ are adapted to cover the following target compositions: Ge/(Ge+Sn) = 0, 40, 60, 80 and 100% with the corresponding device batches designated 0Ge, 40Ge, 60Ge, 80Ge and 100Ge in the text. The other compositional ratios are kept fixed at Ag/(Ag+Cu) = 0.15, (Ag+Cu)/(Zn+Sn+Ge)=0.80 and Zn/(Sn+Ge)=1.10. Before proceeding to the next steps, between 50 μL to 100 μL of 37% concentrated HCl was added to the precursor solutions of 60Ge, 80Ge and 100Ge to achieve full dissolution. The final filtered pre-

cursor solution, clear and stable for weeks, is subsequently spin-coated on cleaned SLG/Mo substrates for 60 s at 3000 rpm, then placed on a hotplate for 3 minutes at a temperature of 340 °C also in ambient environment. This sequence is repeated 8 times with the objective to obtain 1 μm-thick precursor films. The precursor films are placed inside semi-closed graphite boxes, i.e. with holes through their top cover lids as illustrated in Figure 3.2b), with 400 mg Se pellets in a tube furnace filled with Ar at a pressure around 500 mbar. The selenization then starts by ramping up at 20 °C/min to reach 560 °C, remains at high temperature for 15 min before naturally cooling down. The 50 nm CdS buffer layer is deposited by chemical bath, followed by RF sputtering of 40 nm i-ZnO and 150 nm indium tin oxide (ITO) window layers and finally thermal evaporation of 500 nm-thick Ag grid to complete the 0.23 cm^2 solar cells. No ARC is deposited on the studied samples.

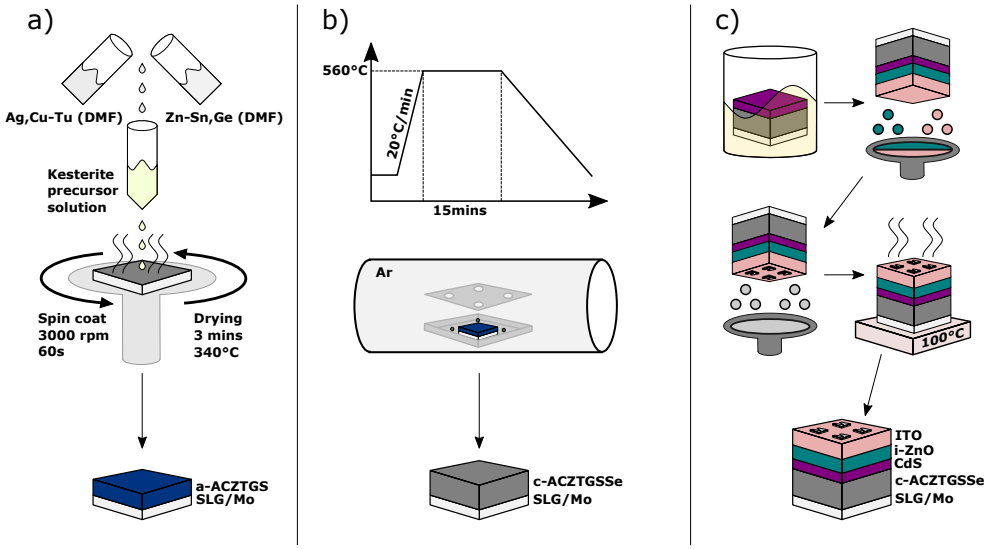

Figure 3.2: Fabrication process of the ACZTGSSe thin-film solar cells. (a) Preparation of the molecular ink precursor solution and spin-coating of the amorphous a-ACZTGS precursor film with around 1 to 1.5 μm thickness. (b) Selenization of the precursor film to grow polycrystalline c-ACZTGSSe thin-film absorbers. (c) Deposition of the CdS buffer, i-ZnO/ITO window layers and Ag grid over the finished absorber, followed by a soft annealing of the finished device.

X-Ray Diffraction (XRD) experiments are realized in Bruker D8 Advance with CuKα = 1.54187 Å in the Bragg-Brentano geometry. Raman measurements were performed using Renishaw's inVia Qontor microRaman microscope, with an excitation wavelength of 532 nm, nominal incident power of 1 mW and spot size of 0.25 μm. X-Ray Fluorescence (XRF) measure-

ments were carried out on Fischerscope XDV to monitor the composition ratios of the different elements, namely (Ag+Cu)/(Zn+Sn+Ge), Zn/(Sn+Ge) and Ge/(Ge+Sn). Scanning Electron Microscopy (SEM) cross-section pictures are taken using a TESCAN microscope with an acceleration voltage of 5 kV at a working distance around 7 mm. Time-of-flight secondary ion mass spectrometry (ToF-SIMS) measurements were performed by sputtering the samples with 2 keV O_2 ion beam for metal cations (Cu, Ag, Zn, Sn, Ge) and 2 keV Cs ion beam for chalcogen anions (Se), using 350x350 mm^2 sputter area and 100x100 mm^2 analysis area. The raw ToF-SIMS data all normalized to a constant reference, i.e. the Mo back contact, and background corrected, hence can provide a semi-quantitative description of the samples considering they have a similar chemical environment. Steady-state photoluminescence (PL) spectra are measured in a wavelength range from 900 nm to 1300 nm using a Picoquant FluoTime 300 system, with an excitation wavelength of 532 nm (25 ps, 3 MHz). It should be noted that the PL data shown are the ones corrected by the detector quantum efficiency, and that it has been checked whether the final peak position lies within a range of wavelength where this detector quantum efficiency remains sufficient. The External Quantum Efficiency (EQE) spectra were obtained on the Enlitech QE-R system calibrated with Si and Ge photodiodes, between 300 and 1300 nm. Current-voltage (IV) experiments under 1 sun illumination were realized with a Keithley 6430 source meter in a four-point configuration from -0.3 V to 0.9 V, using a LED-based G2V calibrated AAA solar simulator and a light intensity of 87.8 mW/cm^2.This setup was combined with a temperature-controlled Heating and Cooling Stage from Microptik (MHCS600-P) to conduct close to 1 sun IV measurements at various temperatures, in vacuum and using liquid N_2 as a cooling agent. Dark IV measurements are performed also using a 4-point probe setup with a Keithley 2401 SourceMeter from -1 to 1 V. Capacitance-voltage-frequency (CVf) measurements were performed in the dark on the Agilent E4980A Precision LCR meter in a four-point configuration, at frequencies between 1 kHz and 1 MHz and at voltages between -1 and 1 V, with a 50 mV AC peak-to-peak amplitude.

3.3 Results

First of all, the growth of kesterite polycrystalline thin films can be confirmed via XRD and Raman experiments on the completed absorbers, presented in Figure 3.3 for the different targeted Ge contents. The presence of the characteristic Se-rich kesterite response is observed for both type of measurements, i.e. the two A Raman modes around 200 and 180 cm^{-1} in Figure 3.3a and the (112) XRD reflection around 27° in Figure 3.3b). The exact XRD peak positions are given in Table 3.1 along with the lattice

parameters a and c. The Se-rich kesterite response is by far dominant in both the Raman spectra and the XRD diffractograms, indicating well-grown ACZTGSSe thin film absorbers are obtained following the selenization of the amorphous precursor films. It is also highlighted in Figure A.1 by the transition from the main peak at 340 cm^{-1} and 28.5° for S-pure precursor film towards the much narrower peak of Se-rich absorbers at lower Raman shift and diffraction angle. The intensity of the (112) peak is roughly 5 times and 20 times higher compared to the (220) and (312) respectively at 46° and 54° in Figure A.2a). The intensity ratios of the same XRD reflections for the $CuZnSnSe_4$ (CZTSe#26-0575) and $CuZnGeSe_4$ (CZGSe#29-0914) powder diffraction reference cards are much lower, i.e. respectively 2.5 and 5. This highlights the preferential growth of the kesterite layers studied here along the (112) direction on glass/Mo substrates.

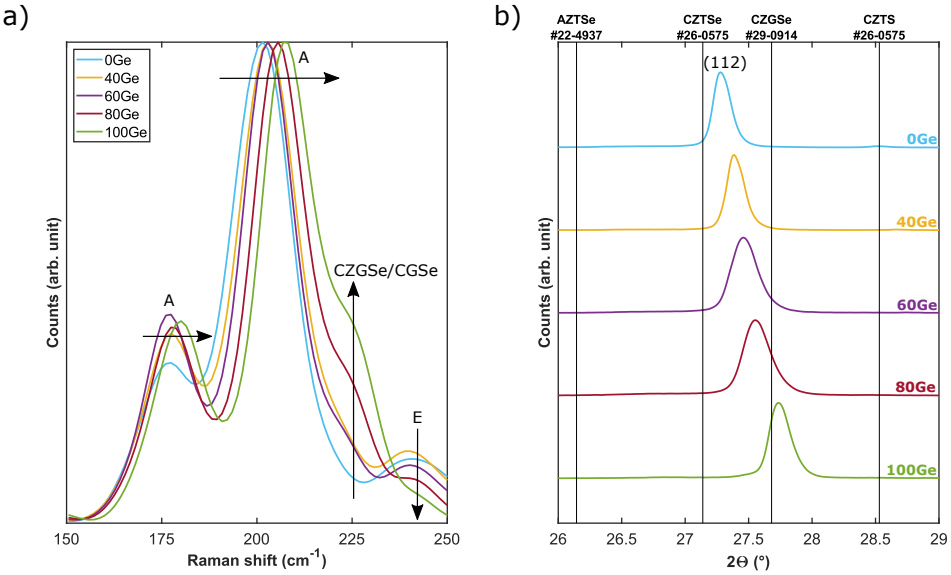

Figure 3.3: Evolution of the crystalline structure of the ACZTGSSe thin-film solar cells with various Ge concentrations. (a) Normalized Raman spectra highlighting the main kesterite A modes around 180 and 200 cm^{-1}, both shifting towards higher wavenumber following the addition of Ge as shown by black arrows. The emergence of a CZGSe/Cu_2GeSe_3 contribution at 225 cm^{-1} in parallel with the E mode disappearance at 240 cm^{-1} is also emphasized. (b) XRD diffractograms showing the main kesterite (112) peak displaced towards higher angle when the Ge content is increased. The XRD Powder Diffraction reference cards of pure phase kesterites are represented to gauge the composition ranges.

Second, the effective integration of Ge within the kesterite lattice is demonstrated by the displacement of the A Raman mode from 201.5 to 206.9 cm^{-1} and of the (112) XRD peak from 27.28° to 27.74° from 0Ge to 100Ge, as reported in numerous other studies[22–26]. A similar shift is

XRD metric	0Ge	40Ge	60Ge	80Ge	100Ge
(112) peak position (°)	27.277	27.387	27.458	27.548	27.739
a (Å)	5.655	5.628	5.612	5.585	5.543
c (Å)	11.359	11.334	11.310	11.314	11.252
V = a^2c (Å^3)	362.215	358.932	356.239	352.840	345.768

Table 3.1: Position of the (112) peak and lattice parameters extracted from the XRD diffractograms for each Ge concentration.

observed on the second A Raman mode at 180 cm^{-1} in Figure 3.3a), as well as on the secondary kesterite XRD peaks in Figure A.2a) and b), further emphasizing the proper incorporation of Ge inside the kesterite crystalline system. The observed shift of the XRD reflections towards higher angle proportionally to the Ge concentration is explained by the reduced atomic radius of Ge as compared to Sn and the associated diminution of the unit cell volume[22,24], shown in Table 3.1. For Raman measurements, the change in bonding strength between the chalcogen species (S-Se) and the group IV elements (Sn-Ge) when alloying lighter and smaller Ge atoms is responsible for the displacement of the main vibrational modes[23]. Besides that, the transition of the E-type mode at 240 cm^{-1} for 0Ge towards the B-type mode at 270 cm^{-1} for 100Ge in Figure A.2c) is also reported in the literature[23,24]. The shoulder of the main A peak appearing at 225 cm^{-1} is observed more clearly than in those other studies and is likely related to one of the characteristic modes of either CZGSe or Cu_2GeSe_3 (CGSe)[23,27]. Another observation is the lower intensity of the second A Raman mode at 180 cm^{-1} for the 0Ge reference as compared to other samples including Ge. According to another study[28], this could be interpreted as the consequence of higher Cu-Zn disorder related to Cu-Zn and Cu-Sn,Ge vibrations for 0Ge. This would indicate a higher opto-electronic quality of the Ge-containing absorbers as compared to the pure-Sn reference, also discussed below based on optical measurements.

Evaluating the shift of Raman modes and XRD peaks for 40Ge, 60Ge and 80Ge in between the pure-Sn and pure-Ge samples should provide estimates for Ge/(Ge+Sn). These can be compared with the XRF data in Table 3.2, already showing close agreement with the targeted Ge content. Yet, the positions of XRD peaks and Raman bands are also affected by the group 1 elements ratio Ag/(Ag+Cu) and chalcogen proportion S/(S+Se), which must then be determined first. Using the same molarity in AgCl and CuCl for all precursor solutions logically leads to similar Ag content around

the desired 15% in all samples. Besides that, the other composition ratios (Ag+Cu)/(Zn+Sn+Ge) and Zn/(Sn+Ge) are also confirming the intended Cu-poor and slightly Zn-rich stoichiometry. Since the Raman A mode is not shifted when alloying Ag[29], it can be used to estimate the S-Se ratio by comparison with the pure phases CZTSe and CZTS respectively located at 196 and 338 cm^{-1}[24]. The A mode position around 200 cm^{-1} indicates very low S content below 5% as shown in Table 3.2. This S-poor stoichiometry could be expected from absorbers processed at high temperature in a highly saturated Se atmosphere. The Se-rich composition is further supported by the much higher intensity of the main A-Se peak at 200 cm^{-1} with regards to the secondary A-S peak around 340 cm^{-1} in Figure A.2c)[30]. Having demonstrated Se-rich stoichiometry and a nearly equal Ag content in all samples, the XRD peak shift can provide a second estimation of the Ge concentration in Table 3.2. The XRD shift confirms a progressive increase of the Ge content with some deviation compared to the XRF ratios, likely caused by the mismatch between multi-alloyed kesterites thin-films and pure powder diffraction references. Obtaining numerical estimations from the Raman spectra is here not relevant given the very small wavenumber difference of 10 cm^{-1} between CZTSe and CZGSe[24] compared to the measurement resolution of 1.3 cm^{-1}.

Technique	Ratio	0Ge	40Ge	60Ge	80Ge	100Ge
XRF	Ge/(Sn+Ge)	0	0.4	0.6	0.79	1
	Ag/(Ag+Cu)	0.15	0.13	0.15	0.14	0.15
	(Ag+Cu)/ (Zn+Sn+Ge)	0.79	0.79	0.86	0.88	0.89
	Zn/(Sn+Ge)	0.99	1.06	1.04	0.99	0.98
Raman	S/(S+Se)	0.04	0.02	0.01	0.01	0.01
XRD	Ge/(Sn+Ge)	0	0.27	0.40	0.60	1

Table 3.2: Composition ratios of ACZTGSSe kesterite absorbers estimated from XRF, Raman and XRD.

Combining Raman and XRD data usually also helps gauging the presence of mixed compounds or binary phases within the kesterite absorbers, using the full range Raman spectra and XRD diffractograms provided in Figure A.2. Firstly, the main kesterite peaks have a much higher relative intensity than other maxima within both measurements. Secondly, the developed kesterite molecular ink processing route relies on Sn^{4+}, which is believed to ensure a growth mechanism avoiding the formation of killer

binary phases[29,31]. Thirdly, expect for the potential CGSe phase, no peak is emerging or disappearing when going from pure-Sn to pure-Ge stoichiometry. Therefore, it is unlikely for detrimental secondary phases such as (Sn,Ge)-S,Se, Zn-S,Se or Cu_x-S,Se to be largely present in the studied absorbers. Further experiments involving cross-sectional Transmission Electron Microscopy (TEM) combined with EDX measurements would help corroborate the absence of secondary phases and provide another point of comparison for the ToF-SIMS profiles discussed below. Besides that, Mo(S_x,Se_{2-x}) is quite distinctively detected by XRD in all samples at fixed diffraction angles around 32 and 56° in Figure A.2b), following its usual natural formation during the high-temperature annealing in Se excess.

Such a Mo(S_x,Se_{2-x}) interlayer can be recognized in between the ACZT(G)SSe absorber and the Mo back contact on the SEM cross section images in Figure 3.4 for all Ge contents, with 1 to 2 times lower thickness than the absorber layer as illustrated in Figure A.3. According to Figure 3.4, conformal and continuous thin-film absorbers are effectively grown with micron-size well-defined crystalline grains. There is no evidence for significant secondary phases, which aligns with the large dominance of the kesterite characteristic peaks in both Raman and XRD data for all samples. From 0Ge to 60Ge, the kesterite crystals cover most of the absorber thickness which correlates well with the nearly flat profiles of all metallic elements along the ToF-SIMS profiles in Figure 3.5. However, 80Ge exhibits a much denser and thicker fine-grain sub-layer along the bottom half of the absorber thickness whereas 100Ge presents an overall smeared-out morphology, as also reported in other studies also relying on the molecular ink route[22,32,33]. These observations are in agreement with the greater variations in ToF-SIMS composition levels of 80Ge and 100Ge along their thickness than for samples with lower Ge, as emphasized by the black arrows in Figure 3.5. Especially, 100Ge displays a relatively important change in the Ag and Cu profiles along its bottom half, which might be at the origin of its less defined crystalline structure. The degradation of absorber morphology for 80Ge and 100Ge could also relate to the 10 times lower solubility of $GeCl_4$ in DMF compared to $SnCl_4$[34] and the subsequent addition of HCl to circumvent this very issue, which would require further experiments to be verified. Another hypothesis for this poorer structural quality would be an excess of the liquid phase associated to Ge-rich kesterite phases with lower melting point than those including Sn[13,35]. Contrarily to kesterite layers deposited via different routes either in vacuum[1,13–16] or in solution[11,12], there are here no evidence for a gradient of the Sn-Ge ratio along the absorber thickness in Figure 3.5. Indeed, the Sn and Ge profiles appear to always evolve in the same direction, and their ratio is mostly constant from the back to the front of the Sn-Ge mixed ACZTGSSe films (40Ge, 60Ge and 80Ge), as highlighted in Figure A.3. This can be probably explained by the solution-based processing route used here. Indeed, the

formation of an amorphous kesterite precursor film with the constitutive elements already bonded to each other occurs more homogeneously than in the case of stacked precursor layers. Given the absence of Sn-Ge gradient and the negligible influence of the extremely low amount of sulfur in the absorbers, the bandgap of the studied absorbers can arguably be considered constant along their thickness.

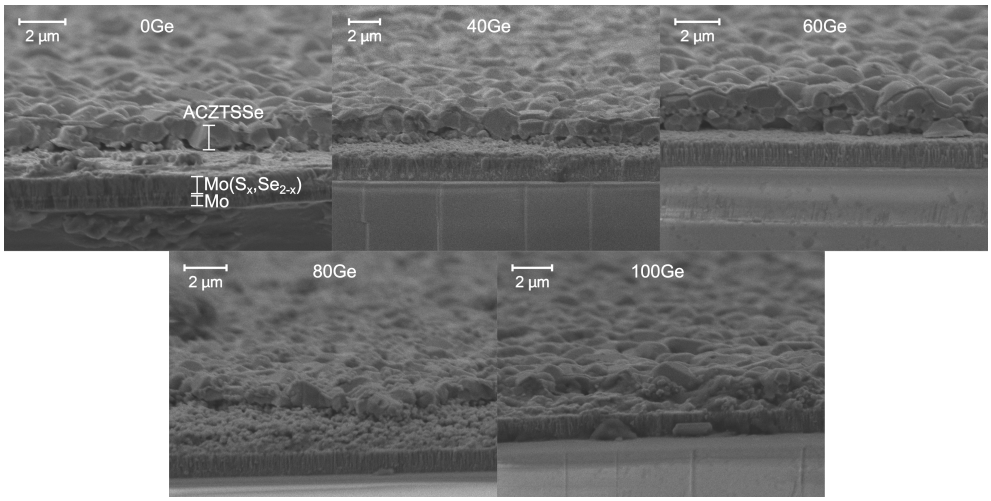

Figure 3.4: Evolution of the SEM cross section of the ACZTGSSe thin-film solar cells with various Ge concentrations. The growth of polycrystalline absorbers with mostly conformal morphology is demonstrated, with a more pronounced bi-layer structure for 80Ge and 100Ge. The kesterite absorber, Mo(S_x,Se_{2-x}) interlayer and Mo back contact are shown for the Ge-free reference sample.

Photoluminescence spectra of the finished devices in Figure 3.6a) reveal a main peak in the expected wavelength range of the kesterites absorbers, progressively shifted to the blue for higher Ge content. The central wavelength of those peaks are considered as first estimates of the absorber bandgap, i.e. $E_{g,PL}$ shown in Table 3.3. The PL peak width is reduced when adding Ge, highlighting the compatibility of combined Ag- and Ge-alloying to obtain kesterite compounds with high opto-electronic quality. The clear blueshift of the EQE spectra in Figure 3.6b) leads to second bandgap estimates $E_{g,EQE}$ in excellent agreement with $E_{g,PL}$ in Table 3.3. The negligible discrepancy between those two values suggests that band tailing caused by crystalline disorder as well as bandgap and potential fluctuations are not significant inside the kesterite absorbers processed herein[17,18]. This aligns with the rather low Urbach energy (E_u) values between 20 and 23 meV obtained in Figure 3.6c) and Table 3.3, which is rather expected for kesterites including Ag or low to moderate amounts of Ge[16,21,29,36–38]. This is turn could relate to a reduced density of the [2I_{II}+IV_{II}] defect complex, due to an increased formation energy when alloying Ag and the monovalency

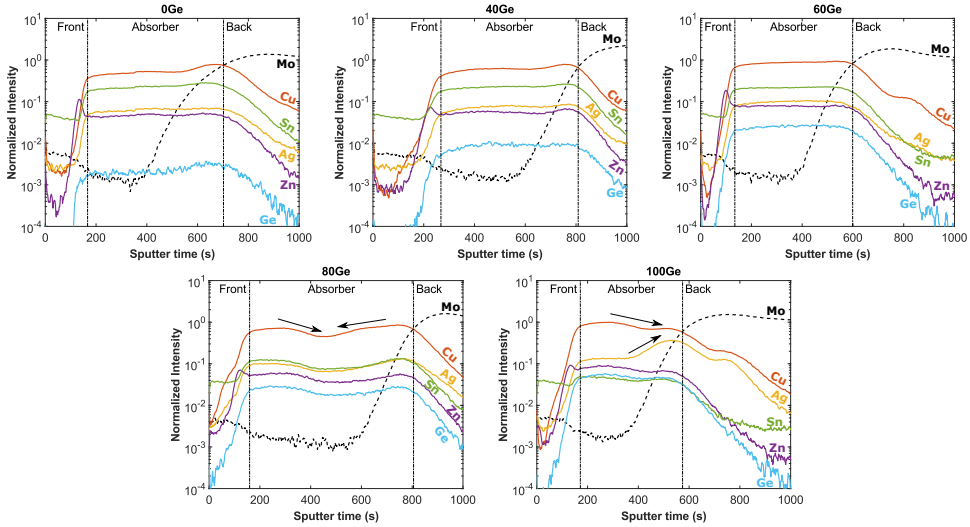

Figure 3.5: Evolution of the ToF-SIMS profiles for the metallic elements of the ACZTGSSe thin-film solar cells with various Ge concentrations. The front interface with the CdS buffer and the back interface with the Mo rear electrode are shown by vertical black dotted lines, while the Mo signal is shown with a black dashed line. The black arrows highlight the variations in signal intensity and composition gradients for 80Ge and 100Ge, possibly related to their more layered morphology in Figure 3.4. A specific focus on the relative thicknesses of the ACZTGSSe absorbers and the Mo(S_x,Se_{2-x}) layers along with a qualitative evolution of the Sn-Ge gradient are provided in Figure A.3.

of Ge in the 4+ oxidation state[20]. However, for the Ge-rich kesterite samples studied here with bandgaps larger than 1.2 eV, i.e. 60Ge, 80Ge and 100Ge, E_u is not increased at all. This demonstrates the ability of the proposed recipe to preserve the opto-electronic quality of Ge-alloyed kesterite absorbers with wider bandgaps, contrarily to previous works[37,39–41]. Exploring further the sub-bandgap region of the EQE spectra in Figure 3.6c), emerging contributions are observed for 80Ge and 100Ge as highlighted by the black arrows. Seeing such responses for photon energies below the absorber bandgap relates to intermediate defect states, as reported in other studies for different types of PV materials[42,43]. The appearance of those peaks for the high-Ge samples correlates relatively well with literature studies also reporting changes in sub-bandgap optical transitions and dominant defects with the Ge content[44–46]. Eventually, the enhancement of non-radiative recombination via those bandgap states might explain the degraded EQE of the 80Ge and 100Ge devices in the absorber wavelength range, i.e. following the black arrow in Figure 3.6b).

The PV parameters, i.e. V_{oc}, short-circuit current density (J_{sc}), fill factor (FF) and efficiency (η) of the champion device per Ge concentration are re-

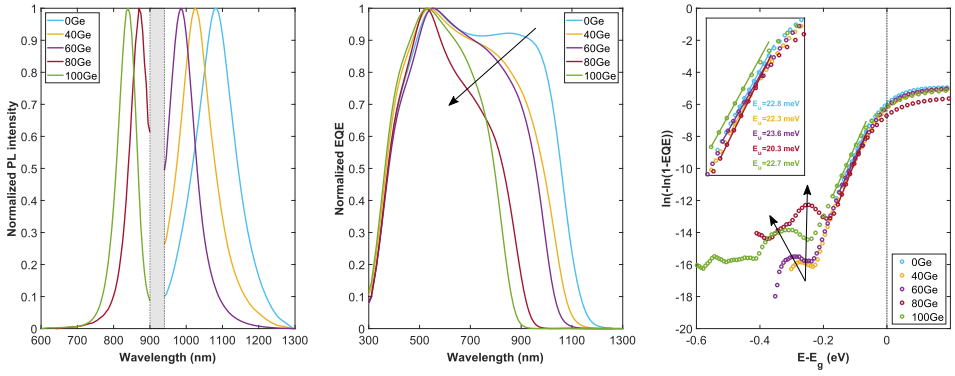

Figure 3.6: (a) Normalized photoluminescence and (b) EQE spectra of the ACZTGSSe thin-film solar cells with various Ge concentrations. The PL peak position and the EQE absorber's edge are shifted towards higher energy following the bandgap increase due to higher Ge content. Despite the decrease in quantum efficiency of the low- and high-wavelength detectors in (a), shown by the gray area from 900 to 930 nm, the absorber bandgaps of the 60 and 80Ge devices can be extracted accurately from the PL peak position. (c) Extraction of the Urbach energy (E_u) for energies below the absorber bandgap. The black arrows highlight the poorer collection efficiency and the emergence of sub-bandgap contributions for 80 and 100Ge. The inset magnifies the linear extrapolation to obtain E_u and the corresponding estimates.

ported in Table 3.3 and Figure A.5, as obtained from the 1 sun IV curves in Figure 3.7a). Given the varying absorber bandgap, computing the deficits in J_{sc}, V_{oc} and FF with respect to the Shockley-Queisser (SQ) limit ensures more straightforward comparisons. More precisely, $X_{SQdef} = X_{SQ} - X$ where X is either J_{sc}, V_{oc} or FF and X_{SQ} are extracted from a literature report[47]. Those SQ deficits are provided in Table A.3 for the champion cells and depicted along with other representative devices in Figure 3.7b) for V_{oc} and in Figure A.4 for J_{sc} and FF. The gradual increase of V_{oc} from 527 to 647 mV and decrease of J_{sc} from 32.89 to 20.35 mA/cm^2 following the arrows in Figure 3.7a) logically relate to the wider absorber bandgap as more Ge is incorporated. The optimal composition appears to be 40Ge with a champion efficiency of 12.1%. The devices with Ge-richer stoichiometries exhibit lower PCEs. Indeed, 60Ge approaches the 10% efficiency barrier while 80Ge and 100Ge suffer from rather large performance diminution down to 6.5 and 5.5% respectively. The rather low J_{sc} deficit around 10 mA/cm^2 observed for all samples, i.e. between 70 to 80 % of the SQ limit in Figure A.5, demonstrates that the proposed recipe enables to deposit well-grown kesterite absorbers with excellent absorption for any bandgap between 1.15 and 1.5 eV. This tends to exclude J_{sc} as main culprit for poorer performance and rather points out towards V_{oc} and FF as the primary performance limiting factors, as typically observed for

kesterite solar cells. Indeed, Figure 3.7b) shows promisingly low values of V_{oc} deficit around 350 mV from 0Ge to 60Ge, whereas it then skyrockets up to 500 mV and above 600 mV for 80Ge and 100Ge, respectively. These are possibly related to changes regarding the main electronic defects as hypothesized above from the sub-bandgap EQE spectra but also potentially from the conduction band mismatch with the CdS buffer layer for absorber bandgaps above 1.4 eV, as discussed below. A progressive increase of the FF deficit from pure-Sn to pure-Ge stoichiometry can be observed in Figure A.4, especially important again for 80Ge and 100Ge. This is likely connected to the poorer EQE response of those two devices.

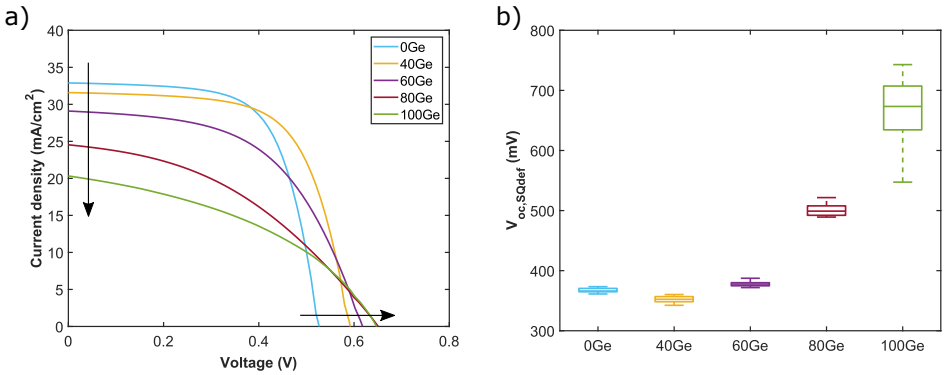

Figure 3.7: (a) IV curves obtained under 1 sun illumination for the champion devices per Ge concentration. The black arrows highlight the increase and decrease of V_{oc} and J_{sc} following the bandgap increments due to higher Ge content. (b) Statistical dispersion of the V_{oc} deficit with respect to the Shockley-Queisser limit for representative devices of each Ge content, exhibiting a minimum around 340 mV for 40Ge.

To better understand the evolution of the PV figures-of-merit in function of the Ge content, the dark IV characteristics of representative devices in Figure 3.8a) is examined. Indeed, analyzing such data provides an image of the junction properties and the importance of carrier recombination via the dark ideality factor n and saturation current density J_0, along with the prominence of parasitic current paths through the shunt resistance R_{sh}. These three figures-of-merit are presented in Figure 3.8b) and attain more than decent values, i.e. $n \lesssim 2$, $J_0 \lesssim 10^{-7} A/cm^2$ and $R_{sh} \gtrsim 10k\Omega.cm^2$, for the 0Ge, 40Ge and 60Ge devices in line with their PCE close to or beyond 10%. Their favourable n and J_0 correlate well with their low V_{oc} deficit while their high R_{sh} validate their conformal large-grain absorber morphology conjectured from Figure 3.4. The optimal combination of parameters is showcased by the champion 40Ge device, i.e. good junction quality with $n = 1.85$ and $J_0 = 7.6 * 10^{-9} A/cm^2$ as well as mostly leakage-free structure with $R_{sh} = 4.76 * 10^4 \Omega.cm^2$. Despite retaining promising values of

Metric	0Ge	40Ge	60Ge	80Ge	100Ge
$E_{g,PL}$ **(eV)**	1.15	1.21	1.26	1.43	1.48
$E_{g,EQE}$ **(eV)**	1.14	1.19	1.24	1.40	1.49
E_u **(meV)**	22.8	22.3	23.6	20.3	22.7
J_{sc} **(mA/cm^2)**	32.89	31.59	27.48	22.12	20.35
V_{oc} **(mV)**	527	592	618	650	647
FF **(%)**	65.93	64.89	55.78	45.06	41.21
η **(%)**	11.42	12.13	9.47	6.48	5.43

Table 3.3: Device parameters extracted from PL, EQE and 1 sun IV data for the champion device of each Ge concentration batch.

$J_0 \simeq 10^{-7} A/cm^2$ and $R_{sh} \simeq 10^4 \Omega.cm^2$ that suggest preserved absorber structural quality, the performance of 80Ge is dropping significantly. This is likely the consequence of n surpassing 2 which indicates an increase in carrier recombination and consequently losses in V_{oc}. This poorer charge extraction and collection also correlates with the degraded EQE response of 80Ge and the hypothesized emergence of sub-bandgap states, which would explain the lower FF. Alloying even more Ge induces a critical decrease of R_{sh} down to the order of 100 $\Omega.cm^2$ for 100Ge, thus clearly dominating its IV characteristic as compared to other devices. This leads to less ideal diode parameters n and J_0 which can largely justify the lower performance associated to greater V_{oc} and FF deficits.

To further investigate the physical origin of those efficiency barriers for 80Ge and 100Ge, capacitance-voltage-frequency (CVf) experiments are realized in the dark to provide complementary information about the device internal behaviour and limitations. Those measurements are performed with similar resolution in both frequency and voltage so as to obtain admittance spectroscopy "loss maps" shown in Figure A.6 and described in previous studies[48,49]. This representation of capacitance variations with both frequency and voltage is useful to possibly detect, identify and locate loss mechanisms affecting solar cell devices, appearing as red areas over the blue map background. Based on the underlying theory combined with simulations[48], it is possible to give another meaning to the frequency and voltage domains that is more relevant to the understanding of a solar cell band structure. On the one hand, moving along the vertical axis allows to scan different types of loss mechanisms and associated ranges of activation energies given their different characteristic response frequencies. On the other hand, scrolling through the horizontal axis by varying

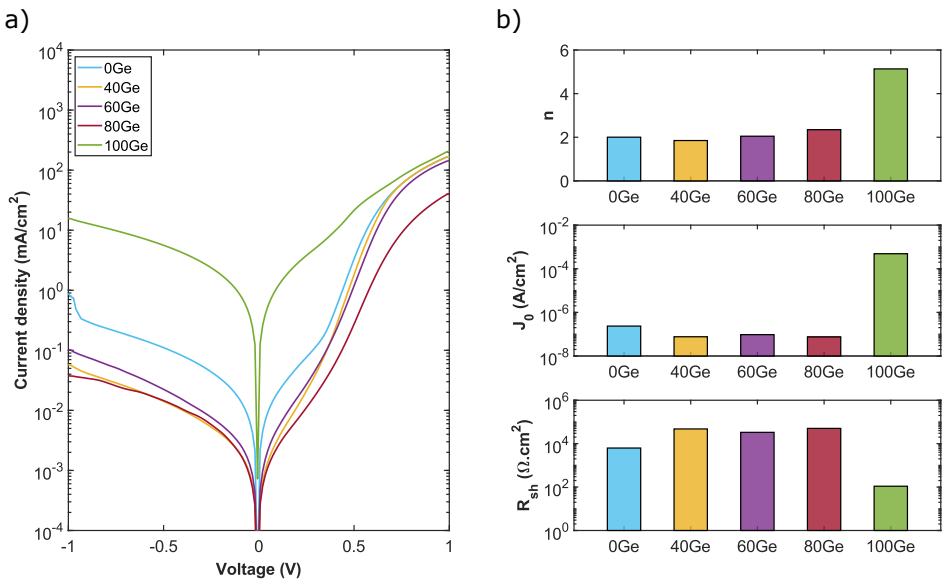

Figure 3.8: (a) Dark IV curves for the ACZTGSSe devices with various Ge concentrations. (b) Corresponding parameters: ideality factor n, saturation current density J_0 and shunt resistance R_{sh}. All three figures-of-merit preserve encouraging values for 40Ge and 60Ge, R_{sh} and J_0 remain favourable whereas n is slightly degraded for 80Ge while a global degradation is observed for 100Ge.

the DC bias point corresponds to shifting the geometrical position of the depletion width edge and simultaneously of the point at which a charge transfer possibly happens in the device, e.g. where the Fermi level crosses a defect level. Thus, the voltage-frequency domain could be qualitatively substituted to a position-energy representation. Building on the experience provided by numerous CVf measurements realized on both CIGS and kesterite devices, the loss map formalism enables to define a few qualitative cases of typical loss mechanisms response in a solar cell. For instance, series resistance values between 1-10 $\Omega.cm^2$, which are typical of lab-scale thin-film solar cells, would typically affect higher frequencies around 1MHz over most of the voltage range. In contrast, DC currents related to shunt leakage would appear at lower frequencies up to 1 kHz and in reverse bias only. Furthermore, the enormous DC currents delivered at high forward bias induce an overcompensation of the measurement tool, materialized as a red ”island” in the bottom right corner of the loss maps. Eventually, shallower defects typically showcase loss map responses at higher frequencies as compared to deeper states, and similarly for smaller and greater potential barriers, while their breadth in voltage is an image of their geometrical location and width, i.e. concentrated near the interface or present in the whole bulk.

The objective at this point is to inspect the evolution in free carrier concentration N_{dop} in the absorber in function of the Ge content so as to potentially explain the degradation of dark parameters and performance for 80Ge and 100Ge. To do so, one must ensure that the apparent doping profile used to determine N_{dop} does not overlap with the possible charge-related loss mechanism signatures coloured in red in Figure A.6 so that its value is as close as possible to the actual free carrier concentration. On the loss maps in Figure A.6, the voltage range from -0.75 V to 0.25 V at the fixed frequency of 10 kHz offers no overlap with the red areas, hence it was used for the apparent doping profiles displayed in Figure 3.9a). This is especially important for the low-efficiency devices 80Ge and 100Ge which exhibit such signatures over large voltage-frequency domains respectively in the top right and bottom right corner of their respective loss maps. Considering this, the free carrier density N_{dop} is extracted as the minimum point of the charge profile, represented in Figure 3.9b). Starting from a value of approximately $2 * 10^{15} cm^{-3}$ for 0Ge, N_{dop} is nearly doubled for 40Ge and 60Ge and then increases by one order of magnitude up to $2 * 10^{16} cm^{-3}$ for 80Ge. This increase of apparent doping from 0Ge to 80Ge content could be caused by the addition of Ge-related shallow states Cu_{Ge} and V_{Ge}, as reported elsewhere[11]. However, the enhanced N_{dop} of 80Ge does not lead to an improved device performance, for two reasons. First, its depletion width W_D is greatly reduced due to the higher doping visible in Figure 3.9b), which deteriorates carrier extraction and likely explains the largely degraded EQE. Second, all the additional bandgap states induced by substituting Ge to Sn are not necessarily shallow doping levels. On the contrary, certain of those intrinsic defects may possess deep energy levels within the absorber bandgap and act as recombination centers which induce the increase of n compared to lower-Ge samples. Such traps could possibly be responsible for the large signature on the 80Ge loss map in Figure A.6[48]. This defect-like signature appears located near the kesterite/CdS HJ interface following the white arrow direction. It matches also quite well with the steep increase of the apparent doping of 80Ge towards low depths in Figure 3.9a) and correlates with the appearance of surface defects for Ge-rich kesterites studied in other works[44,45]. Eventually, for 100Ge, N_{dop} falls back to a similar level as 0Ge, which translates into a recovered W_D and probably accounts for the improved EQE as compared to 80Ge. In parallel with this evolution of the defect landscape following the Ge concentration, the band structure is changing as well since not only the absorber bandgap is becoming wider but the electronic affinity is also lowered[45,46,50]. In particular, the heterojunction conduction band alignment, which is key to determine the final device performance, transitions from a favourable spike-like barrier to an undesired cliff-like alignment at the ACZTGSSe/CdS interface when reaching Ge-rich compositions. This in turn would be the main cause for the high DC current signature on the

100Ge loss map in Figure A.6, and also for the V_{oc} saturation under light for that sample[44,46].

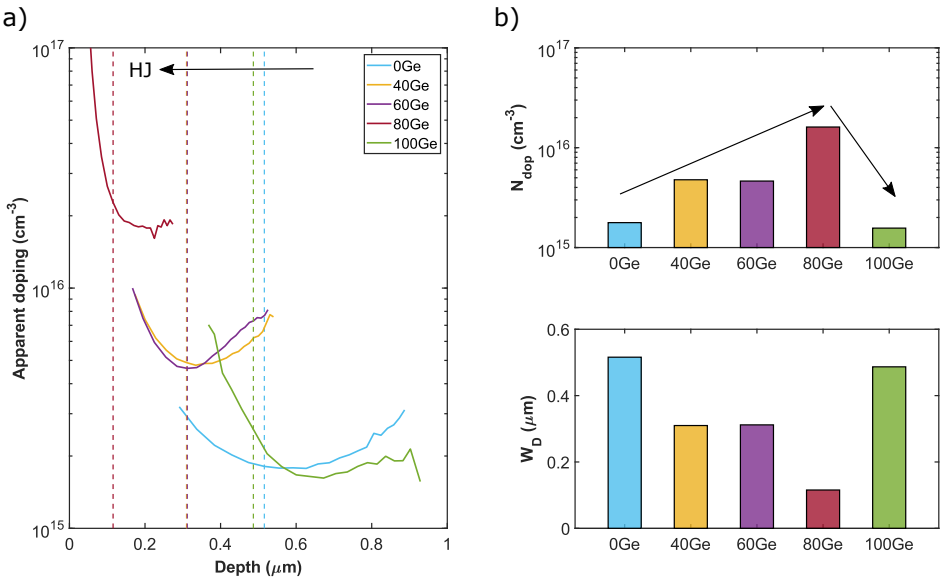

Figure 3.9: (a) Apparent doping profiles for the ACZTGSSe devices with various Ge concentrations, for voltages between -0.75 V and 0.25 V and at a frequency of 10 kHz. The black arrow points towards the HJ while the vertical dashed lines indicate the data point corresponding to 0V applied bias (superimposed for 40Ge and 60Ge). (b) Evolution of the corresponding free carrier concentration N_{dop} and depletion width W_D. As highlighted by the black arrows, N_{dop} increases from 0Ge to 80Ge followed by a collapse until 100Ge. W_D follows the inverse trend compared to N_{dop} since they are inversely proportional to each other.

The main outcome herein is that adding moderate amounts of Ge to the ACTZSSe baseline recipe maintains highly promising PCEs of 12.1% and 9.7% for 40Ge and 60Ge respectively, with still much room for improvement regarding FF and J_{sc}. Those constitute record efficiencies for Ge-alloyed kesterite solar cells with bandgaps of 1.2 and 1.25 eV as illustrated in Figure 3.10a). In particular, the optimal performance is obtained by the 40Ge champion cell showcasing a remarkably low V_{oc} deficit around 340 mV, corresponding to around 62% of the detailed balance limit for its bandgap (Figure A.5). This surpasses most other Ge-alloyed kesterite studies, except four reporting equivalent or higher PCE than 40Ge[11,36,37,51] illustrated by red squares in Figure 3.10a. With respect to the device fabrication, two main differences with 40Ge are worth mentioning. On the one hand, all these higher-performing devices were coated with ARC contrarily to 40Ge, arguably contributing to their better performance. On the other hand, both their bandgap and Ge alloying proportion are lower,

respectively not exceeding 1.1 eV and 20 %. Regarding PV figures-of-merit, 40Ge appears to be mainly lagging in FF, which seems to be the consequence of its higher ideality factor and series resistance. Therefore, increasing FF beyond 70 % appears especially important to position 40Ge higher in the PCE landscape since it currently belongs to the same quartile in terms of V_{oc} and J_{sc} deficit in comparison with those higher-performing reports (Figure A.5). Besides, for the 40Ge champion device, the quasi absence of low-temperature roll-over for V_{oc} in Figure A.7 indicates negligible second order effects and thus reliable linear extrapolation until 0K[50]. The resulting V_{oc} at 0 K only has a 50 mV discrepancy with the 1.2 eV bandgap which constitutes evidence for a high-performance potential. These record V_{oc} deficits can surely be attributed to some extent to the low E_u values around 20 meV obtained for all samples[19]. As illustrated in Figure 3.10b), the study presented in this chapter is one of the very few showing such a preservation of small Urbach tails while increasing the bandgap of a kesterite absorber of any type. This sets an excellent baseline in terms of material opto-electronic quality before proceeding to further device performance optimization for the high-Ge samples. Indeed, the record V_{oc} deficits observed for the 80Ge and 100Ge devices do not translate into record efficiencies. This could originate from the various mechanisms mentioned above, namely variations of the defect states coupled to conduction band misalignment and less efficient carrier extraction, all inducing V_{oc} and FF losses. Potential solutions could for instance include a more adapted buffer material for absorber bandgaps above 1.4 eV[52], an alternative to HCl for reaching complete dissolution of the Ge precursors or heterojunction interface passivation[40]. Those should be combined with a deeper understanding of the interaction between defect landscape and band structure, and its evolution for higher Ge concentration, which are some of the numerous possible follow-up studies to this chapter. It is also worth noting that the 100Ge champion device presents the appropriate bandgap and $J_{sc} \simeq 20mA/cm^2$ requirements for a typical top cell in a tandem configuration with c-Si or low-bandgap CIGS bottom cell as bottom cell. Provided that the V_{oc} and FF deficits are counteracted following the above discussion, this might extend the range of viable combinations in for instance all thin-film tandems[53].

3.4 Conclusion

To conclude, in this chapter, a molecular ink chemical route for processing high-quality Ag,Ge-alloyed kesterite absorbers with great device performance potential in a wide range of bandgaps is implemented. During the simple preparation of the precursor solution and film in ambient air, the ratio of Sn and Ge salts is varied to cover the whole Ge composition spectrum

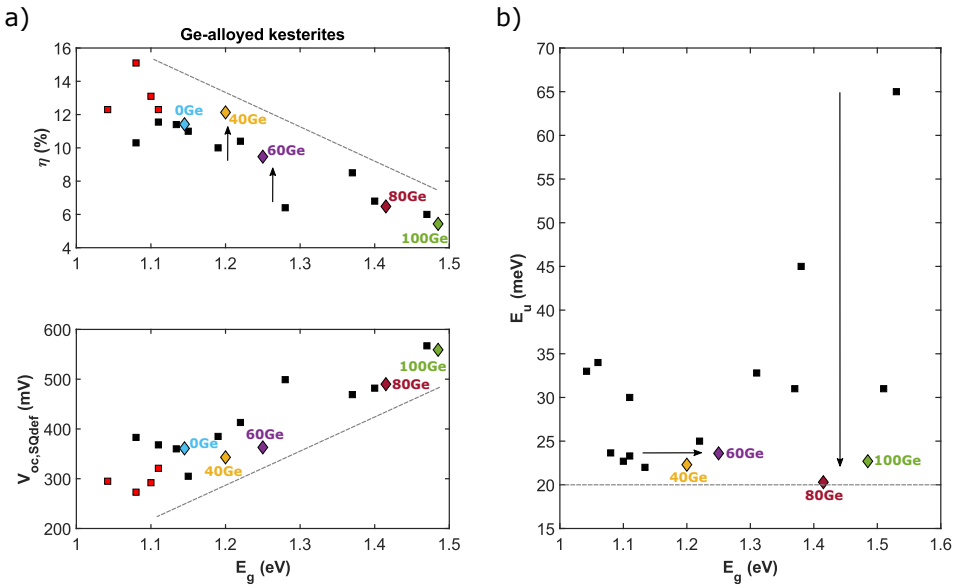

Figure 3.10: (a) Representation of the obtained champion efficiencies and corresponding V_{oc} SQ deficits with respect to the absorber bandgap (coloured diamonds), compared to other values reported in literature for Ge-alloyed kesterites (black squares for lower PCE than 40Ge, red squares for higher PCE than 40Ge)[11,16,34,36–40,51,52,54–56]. The black arrows emphasize the higher efficiency and lower V_{oc} deficit for devices with bandgaps between 1.2 and 1.25 eV. (c) Urbach energy E_u of the champion devices (coloured diamonds), in comparison with other studies about all types of kesterites (black squares)[11,16,36–40,54,57–60]. The black arrows highlight the maintained low E_u values around 20 meV for all bandgaps between 1.15 and 1.5 eV. The gray dashed lines are guides to the eye.

from 0 to 100%. Ge contents beyond 40% are especially investigated, demonstrating the potential of the presented recipe to complement the existing literature mostly limited to lower Ge concentrations. The ACZTGSSe thin films obtained after selenization exhibit excellent polycrystalline morphology, no secondary phases nor structural flaws. These absorbers properly integrate Ge into their lattice, which allows flexible tuning of their bandgap from 1.15 to 1.5 eV when ranging from pure-Sn to pure-Ge stoichiometry. The champion efficiency of 12.1% obtained for 40% Ge without ARC sets a new record for Ge-alloyed kesterites solar cells with a bandgap of 1.2 eV. This is mainly the consequence of an outstanding 62% of the V_{oc} Shockley-Queisser limit reached for this device, with still room for improvement regarding FF in particular. The developed process interestingly maintains such encouraging PCE and V_{oc} deficit when reaching a bandgap of 1.25 eV and 60% Ge. The reason for this promising performance 40Ge and 60Ge is two-fold. On the one hand, excellent heterojunction properties are characterized by low recombination and efficient carrier collection.

On the other hand, high opto-electronic quality of the kesterite material confirmed by the low Urbach energy slightly above 20 meV. This is the very sign of mitigated crystalline disorder and benign band tailing, known to be one of the main challenges faced by kesterites. The small Urbach front is remarkably extended up to the highest bandgap of 1.5 eV for the pure-Ge sample, probably enabled by the combined alloying of Ag and Ge in solution. Therefore, the proposed deposition strategy provides an interesting solution to overcome the intrinsic limitations of kesterites in a wide range of bandgaps while proving the interest to transition from physical processes to chemical routes. This chapter establishes a basis for high-quality kesterite materials with tuneable bandgap, still requiring optimization regarding the evolution of defect landscape and band structure for Ge contents higher than 60%. More precisely, the deficit in FF should be further mitigated for those devices. Tackling this issue may bring kesterite solar cells to a stronger position in the thin-film PV field, especially regarding tandem and indoor applications.

Eventually, using a representative device of the champion 40Ge batch, Figure 3.11 compares both the starting and updated baselines. The main asset of the former is the realization of bandgap-graded CZTGSe absorbers for a fixed stoichiometry, while it is outperformed over most indicators by the latter and in a wide bandgap range. Indeed, the bandgap-tuneable solution-processed ACZTGSSe absorbers from the updated baseline showcase much weaker band tailing associated to a significantly smaller discrepancy between bandgap estimates from EQE and PL. The resulting reduction in radiative V_{oc} losses is in line with the current state-of-the-art kesterites solar cells[61] and constitutes a breakthrough in their development[18,20]. The 40Ge champion batch of the updated baseline also ensures closer agreement between $E_{a,Voc}$ and $E_{g,EQE} \simeq E_{g,PL}$, indicating potentially better applicability of classical solar cell theory. In parallel, higher diode quality characterized by $n < 2$ and $J_0 \simeq 10^{-8} A/cm^2$ is attained, suggesting mitigated non-radiative recombination which contributes to the largely reduced V_{oc} deficit brought down to 340 mV. Combined with the parallel improvement of FF and J_{sc}, these updated characteristics naturally translate into increased device performance. However, as compared to record CIGS devices[62], the diode parameters J_0 and n remain too high. Their link with intrinsic electronic defects in chalcogenide solar cells is hardly questionable, and Sn_{Zn} antisites have been highlighted as particularly critical[51] in the case of kesterites. Besides, this chapter demonstrates via admittance spectroscopy that the region surrounding the HJ is key to the device behaviour and performance. Indeed, the performance impairment in devices with Ge contents exceeding 60 % seemingly coincides with the appearance of loss mechanisms with a bias position likely indicating close-to-interface location. Therefore, further investigations are required to decorrelate the dominant non-radiative recombination path in terms of both the location

along the device structure and the main associated defect. These shall contribute to future reductions of the kesterites V_{oc} deficit to eventually reach new efficiency milestones. This is investigated in the next chapter, along with verifying whether the updated material quality implies changes in the characterization and modeling state-of-the-art.

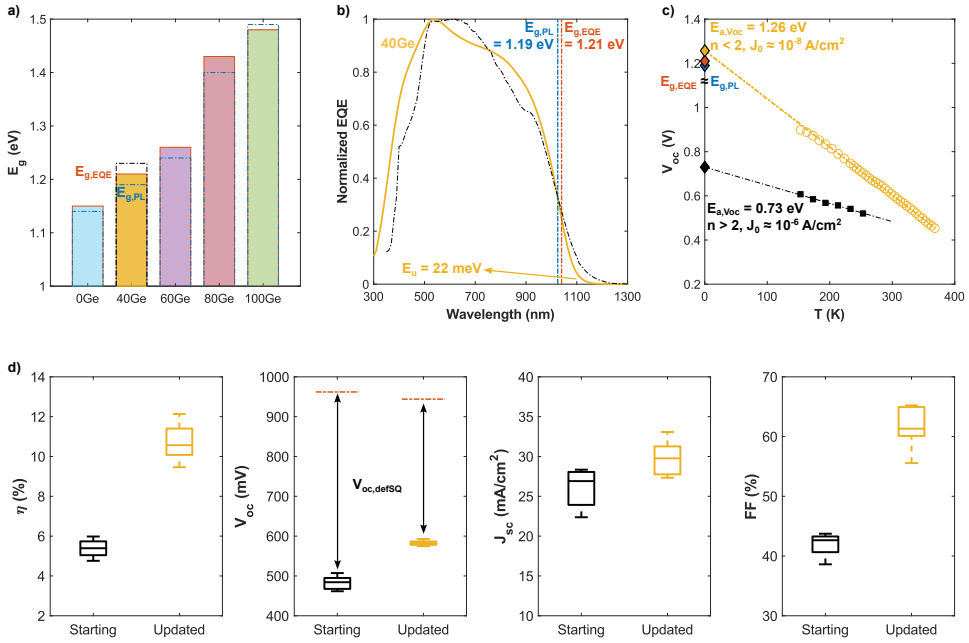

Figure 3.11: Main characteristics of the Ge-alloyed kesterites updated baseline based on molecular ink solution process, presenting a comparison between the 40Ge champion batch in yellow and the starting baseline in black. a) Bandgap values corresponding to the maxima of EQE characteristics derivative ($E_{g,EQE}$, orange outline) demonstrating the flexible bandgap tuning following the change in Ge alloying ratio, with the 40Ge recipe put in evidence. The PL peak position $E_{g,PL}$ for each Ge concentration is shown as a blue dashed line. The EQE estimate of the starting baseline bandgap of 1.23 eV is shown as black dashed line in comparison with the 40Ge batch. b) Example EQE response of the champion 40Ge recipe at 0 V, with much closer agreement between $E_{g,PL}$ (dashed blue line) and $E_{g,EQE}$ (orange dashed line) and lower Urbach energy $E_u = 22meV$ than the starting baseline. c) Temperature evolution of V_{oc}, linearly extrapolated to a value $E_{a,Voc} = 1.26eV$ at 0K which is close to the bandgap estimates $E_{g,PL}$ and $E_{g,EQE}$. d) Statistical dispersion of η, V_{oc}, J_{sc} and FF for the 40Ge solar cell batch, exhibiting better overall performance than the starting baseline. For each box, the central line represents the median, while its top and bottom edges, respectively, indicate the 25th and 75th percentiles. The whiskers, i.e. the dashed lines extending from both edges of each box, indicate the most extreme data points. The dashed orange line depicts the V_{oc} Shockley-Queisser limit for $E_{g,EQE}$.

Bibliography

[1] R. Scaffidi et al. *Energy Adv.* 2.10 (2023), pp. 1626–1633. DOI: 10.1039/D3YA00359K.

[2] R. Scaffidi et al. *Materials Today Energy* 46 (2024), p. 101715. DOI: 10.1016/j.mtener.2024.101715.

[3] B. Vermang et al. *Sustainable Energy Fuels* 3.9 (2019), pp. 2246–2259. DOI: 10.1039/C9SE00266A.

[4] S. Giraldo et al. *Adv. Mater.* 31.16 (2019), p. 1806692. DOI: 10.1002/adma.201806692.

[5] R. Scaffidi et al. *J. Mater. Chem. A* 11.25 (2023), pp. 13174–13194. DOI: 10.1039/D3TA01218B.

[6] S. Khelifi et al. *Solar Energy Materials and Solar Cells* 219 (2021), p. 110824. DOI: 10.1016/j.solmat.2020.110824.

[7] Y. Gong et al. *Solar RRL* 9.4 (2025), p. 2400756. DOI: 10.1002/solr.202400756.

[8] M. Placidi et al. *Solar RRL* 9.11 (2025), p. 2500030. DOI: 10.1002/solr.202500030.

[9] M. He et al. *Adv. Sci.* 8.9 (2021), p. 2004313. DOI: 10.1002/advs.202004313.

[10] J. Andrade-Arvizu et al. *ACS Appl. Mater. Interfaces* 11.36 (2019), pp. 32945–32956. DOI: 10.1021/acsami.9b09813.

[11] J. Fu et al. *J. Mater. Chem. A* 8.42 (2020), pp. 22292–22301. DOI: 10.1039/D0TA06318E.

[12] I. Kim et al. *Chem. Mater.* 26.13 (2014), pp. 3957–3965. DOI: 10.1021/cm501568d.

[13] J. Márquez et al. *Chem. Mater.* 29.21 (2017), pp. 9399–9406. DOI: 10.1021/acs.chemmater.7b03416.

[14] C. Andres et al. *Thin Solid Films* 665 (2018), pp. 168–172. DOI: 10.1016/j.tsf.2018.09.022.

[15] J. Andrade-Arvizu et al. *ACS Appl. Energy Mater.* 3.11 (2020), pp. 10362–10375. DOI: 10.1021/acsaem.0c01146.

[16] J. Liu et al. *ACS Appl. Mater. Interfaces* 13.47 (2021), pp. 56302–56308. DOI: 10.1021/acsami.1c16861.

[17] S. Siebentritt et al. *Solar Energy Materials and Solar Cells* 158 (2016), pp. 126–129. DOI: 10.1016/j.solmat.2015.10.017.

[18] T. Gokmen et al. *Applied Physics Letters* 103.10 (2013), p. 103506. DOI: 10.1063/1.4820250.

[19] J. Chantana et al. *Solar Energy Materials and Solar Cells* 210 (2020), p. 110502. DOI: 10.1016/j.solmat.2020.110502.

[20] A. Crovetto et al. *Energy Environ. Sci.* 13.10 (2020), pp. 3489–3503. DOI: 10.1039/D0EE02177F.

[21] Y. Gong et al. *Adv Funct Materials* (2024), p. 2404669. DOI: 10.1002/adfm.202404669.

[22] D. B. Khadka and J. Kim. *CrystEngComm* 15.48 (2013), p. 10500. DOI: 10.1039/c3ce41387j.

[23] D. B. Khadka and J. Kim. *J. Phys. Chem. C* 119.4 (2015), pp. 1706–1713. DOI: 10.1021/jp510877g.

[24] E. Garcia-Llamas et al. *Journal of Alloys and Compounds* 692 (2017), pp. 249–256. DOI: 10.1016/j.jallcom.2016.09.035.

[25] M. Guc et al. *Journal of Applied Physics* 114.19 (2013), p. 193514. DOI: 10.1063/1.4830028.

[26] R. Caballero et al. *Solar Energy Materials and Solar Cells* 139 (2015), pp. 1–9. DOI: 10.1016/j.solmat.2015.03.004.

[27] G. Marcano et al. *Solid State Communications* 146.1-2 (2008), pp. 65–68. DOI: 10.1016/j.ssc.2008.01.018.

[28] M. Dimitrievska et al. *Applied Physics Letters* 106.7 (2015), p. 073903. DOI: 10.1063/1.4913262.

[29] Y. Gong et al. *Adv Funct Materials* 31.24 (2021), p. 2101927. DOI: 10.1002/adfm.202101927.

[30] F. Liu et al. *ACS Appl. Mater. Interfaces* 7.26 (2015), pp. 14376–14383. DOI: 10.1021/acsami.5b01151.

[31] J. Zhou et al. *Nat Energy* (2023). DOI: 10.1038/s41560-023-01251-6.

[32] T. Schnabel, M. Seboui, and E. Ahlswede. *Energies* 10.11 (2017), p. 1813. DOI: 10.3390/en10111813.

[33] T. Schnabel, M. Seboui, and E. Ahlswede. *RSC Adv.* 7.1 (2017), pp. 26–30. DOI: 10.1039/C6RA23068G.

[34] J. A. Clark et al. *J. Am. Chem. Soc.* 141.1 (2019), pp. 298–308. DOI: 10.1021/jacs.8b09966.

[35] S. Giraldo et al. *Energy Environ. Sci.* 11.3 (2018), pp. 582–593. DOI: 10.1039/C7EE02318A.

[36] J. Wang et al. *Advanced Materials* 34.27 (2022), p. 2202858. DOI: 10.1002/adma.202202858.

[37] S. Kim et al. *Appl. Phys. Express* 9.10 (2016), p. 102301. DOI: 10.7567/APEX.9.102301.

[38] X. Tan et al. *Journal of Alloys and Compounds* 981 (2024), p. 173645. DOI: 10.1016/j.jallcom.2024.173645.

[39] D. Nowak et al. *Applied Sciences* 12.3 (2022), p. 1376. DOI: 10.3390/app12031376.

[40] L. Choubrac et al. *ACS Appl. Energy Mater.* 3.6 (2020), pp. 5830–5839. DOI: 10.1021/acsaem.0c00763.

[41] K. Nagaya et al. *Applied Physics Letters* 113.9 (2018), p. 093901. DOI: 10.1063/1.5031799.

[42] C. M. Sutter-Fella et al. *ACS Energy Lett.* 2.3 (2017), pp. 709–715. DOI: 10.1021/acsenergylett.6b00727.

[43] D. Wang et al. *Adv Funct Materials* 32.2 (2022), p. 2107359. DOI: 10.1002/adfm.202107359.

[44] A. D. Collord and H. W. Hillhouse. *Chem. Mater.* 28.7 (2016), pp. 2067–2073. DOI: 10.1021/acs.chemmater.5b04806.

[45] T. Nagai et al. *ACS Appl. Mater. Interfaces* 11.4 (2019), pp. 4637–4648. DOI: 10.1021/acsami.8b19200.

[46] T. Nagai et al. *Phys. Status Solidi RRL* 14.4 (2020), p. 1900708. DOI: 10.1002/pssr.201900708.

[47] S. Rühle. *Solar Energy* 130 (2016), pp. 139–147. DOI: 10.1016/j.solener.2016.02.015.

[48] G. Brammertz et al. *IEEE J. Photovoltaics* 10.4 (2020), pp. 1102–1111. DOI: 10.1109/JPHOTOV.2020.2992350.

[49] T. Kohl et al. *Solar Energy Materials and Solar Cells* 231 (2021), p. 111289. DOI: 10.1016/j.solmat.2021.111289.

[50] C. J. Hages et al. *Journal of Applied Physics* 115.23 (2014), p. 234504. DOI: 10.1063/1.4882119.

[51] J. Shi et al. *Nat Energy* (2024). DOI: 10.1038/s41560-024-01551-5.

[52] T. Schnabel et al. *RSC Adv.* 7.64 (2017), pp. 40105–40110. DOI: 10.1039/C7RA06438A.

[53] A. Martulli et al. *Solar Energy Materials and Solar Cells* 279 (2025), p. 113212. DOI: 10.1016/j.solmat.2024.113212.

[54] M. C. Baek et al. *Chemical Engineering Journal* 479 (2024), p. 147842. DOI: 10.1016/j.cej.2023.147842.

[55] A. Ruiz-Perona et al. *Solar Energy* 206 (2020), pp. 555–563. DOI: 10.1016/j.solener.2020.06.044.

[56] G. M. Ford et al. *Chem. Mater.* 23.10 (2011), pp. 2626–2629. DOI: 10.1021/cm2002836.

[57] C. J. Hages, N. J. Carter, and R. Agrawal. *Journal of Applied Physics* 119.1 (2016), p. 014505. DOI: 10.1063/1.4939487.

[58] D. W. Miller et al. *Applied Physics Letters* 101.14 (2012), p. 142106. DOI: 10.1063/1.4754834.

[59] E. Ojeda-Durán et al. *Solar Energy* 198 (2020), pp. 696–703. DOI: 10.1016/j.solener.2020.02.009.

[60] C. Yan et al. *ACS Energy Lett.* 2.4 (2017), pp. 930–936. DOI: 10.1021/acsenergylett.7b00129.

[61] L. Wong et al. (2024). DOI: 10.21203/rs.3.rs-5136540/v1.

[62] J. Keller et al. *Nat Energy* 9.4 (2024), pp. 467–478. DOI: 10.1038/s41560-024-01472-3.

CHAPTER 4
Advancing next-generation kesterite solar cell modeling

This chapter is based on the following article:

- R. Scaffidi, A. Jimenez-Arguijo, Y. Gong, G. Brammertz, A. Basak, Z. Jehl Li-Kao, E. Saucedo, D. Flandre, and B. Vermang. "Modelling of current-voltage characteristics of high-efficiency kesterite solar cells". *Newton, accepted* (2025)

4.1 Motivation

To reach further enhancements in the efficiency of next-generation kesterite solar cells fabricated via solution-processing as presented in the previous chapter, a deeper understanding of their opto-electrical behaviour and the dominant recombination path is required. The analysis of the current-voltage response of a solar cell within the single diode model formalism proves particularly useful in that regard, as it establishes a direct relationship between V_{oc} and the intrinsic electronic properties of the pn diode. Therefore, understanding which underlying mechanisms are governing the model parameters is key to determine strategies for counteracting the V_{oc} deficit.

The need for a refined device state-of-the-art modeling is even greater given the recent developments within the kesterite baselines. On the one hand, large reductions in radiative V_{oc} losses were obtained through mitigated band tailing and potential fluctuations[2–6], which were a main culprit for divergences with the standard single diode model in previous nanoparticle-based samples as previously reported[7]. On the other hand, most of the current best-performing devices are based on kesterite absorbers deposited via molecular ink chemical routes[3,4,8], which at the current laboratory scale development provide good control and reproducibility[9]. The kesterite solar cells resulting from such solution-based processes exhibit reduced shunt leakage making them well-suited for indoor environment applications[10]. This emphasizes the interest to investigate the underlying mechanisms by exploring the device response in the reverse bias regime.

To do so, a unified and comprehensive analysis of temperature-dependent current-voltage measurements realized in both dark and light and in both forward and reverse bias on high-quality solution-processed Ag-alloyed kesterite devices is developed in this chapter. The presented methodology leads to important conclusions about material quality, device behaviour and performance improvement pathways, solely based on the measurement of a single physical quantity, i.e. the current density (J), in function of the voltage (V), temperature (T) and light intensity (I), denoted as JVTI in the following. The first part of this chapter concerns the analysis of dark JVT experiments, highlighting the existence of a broad range temperature in which close agreement with the unaltered single diode model is reached. Based on this robust modeling, the two cases of bulk- and interface-limited recombination are discussed, relying on SCAPS-1D[11] simulations to complement previously established theoretical models. This leads to the hypothesis of a thin defective kesterite layer close the absorber/buffer interface dominating recombination in the studied devices at room temperature, while the importance of determining the buffer car-

rier concentration is stressed. At lower temperatures, the enhancement of recombination by tunneling enables to explain the divergence from the single diode model. The second part focuses on JVTI measurements and demonstrates a remarkably weak dark-light discrepancy in the samples response, indicating not only a closer-to-ideal opto-electrical behaviour but also a common dominant recombination channel in either dark or light conditions. This allows to quantify the potential V_{oc} gains and confirm the pivotal role of the ideality factor n and saturation current prefactor J_{00} regarding non-radiative losses in kesterite solar cells. Finally, the last part describes a preliminary exploration of the dark JVT data in reverse bias, shedding light on carrier trapping-detrapping via shallow defects as potential physical origin of shunt currents.

4.2 Materials and Methods

4.2.1 Sample processing and characteristics

The kesterite absorber in the studied devices is prepared following a molecular ink baseline recipe targeting around 15% Ag and less than 10% S, corresponding to $E_g = 1.15eV$ and $E_u = 22meV$ with high reproducibility and good device performance[4]. On top of the absorber are successively deposited a 50 nm CdS buffer by chemical bath, 40 nm i-ZnO and 150 nm ITO window layers by RF sputtering and 500 nm Ag grid by thermal evaporation, for a total device area of $0.23cm^2$ determined by hand scribing over the Ag grid mask, without antireflection coating. Samples A1, A2 and A3 are repetitions of this whole process, hence highly comparable as attested by their similar PV figures-of-merit in Table A.6. These values are all extracted at 25°C under AM1.5G spectrum with $950W/m^2$ (0.95 sun) illumination intensity, explained by the 5% glass window loss subtracted from the $1000W/m^2$ solar simulator output as described in the JVTI measurement conditions below. Samples B differs from other devices by its kesterite absorber being 10% Li-alloyed, which induces marginally higher bandgap[4] while exhibiting slightly reduced performance as shown in Table A.6. Sample B is thus useful to highlight the validity of the presented methodology to devices with different absorbers. All samples have power conversion efficiencies ranging roughly between 10 and 12%, which makes their comparison relevant and aligned with state-of-the-art solution-processed Ag-alloyed kesterite solar cell baselines[3–5,8,12].

4.2.2 Measurement procedure

The JVTI setup relies on a Keithley 6430 source meter used in a four-point configuration to realize current-voltage measurements. It is connected

via coaxial cables to a temperature-controlled Heating and Cooling Stage from Microptik (MHCS600-P), enclosed in a vacuum-sealed box equipped with a N_2 circuit for cooling down. The box is placed directly below a LED-based G2V AAA solar simulator, with the incident light reaching the whole device area of $0.23cm^2$ through a glass window cast within the box top cover. The incident irradiance on the outside of the measurement box is AM1.5G $1000W/m^2$, the magnitude of which is uniformly scaled up or down to tune the illumination intensity. The measurement procedure is as follows.

1. A verification measurement is performed with the box sealed in both dark and light to ensure the quality of contacts and the proper working of the device. The loss of incident power through the box glass window at the sample position is evaluated to be 5% at any light intensity. Taking this into account provides the close-to-1 sun irradiance reference of $950W/m^2$ (0.95 sun) used throughout this chapter and especially in the JVTI analysis.

2. The actual measurement starts by cooling down the sample to the lowest temperature. Once reached and for each subsequent temperature point, a waiting time of at least 3 minutes is applied before any action. Dark and light intensity-dependent measurements are done separately to exclude the possible influence of light soaking on the dark measurements.

    - For dark JVT experiments, the temperature is increased in steps of 10 K from 143.15 K (-130 °C) until 233.15 K (-40 °C) and in steps of 5 K from 233.15 K (-40 °C) until the highest temperature of 368.15 K (95 °C), corresponding to 37 different temperatures.
    - For JVTI experiments, where measurement time is more critical, the temperature is increased in steps of 10 K from 173.15 K (-90 °C) until the highest temperature of 363.15 K (90 °C), corresponding to 20 different temperatures.

3. At each temperature point stabilized after the waiting time, JV curves are measured from -0.3 to 0.9 V in 5 s with a 0.05 s dwell time, either in the dark or at 10 different light intensities from $129W/m^2$ (0.13 sun) to $950W/m^2$ (0.95 sun).

4.3 Results

4.3.1 Single diode model theory

The goal of this chapter is to gauge if the single diode model can predict the behaviour of new-generation thin-film solar cells with kesterite absorbers,

despite the usual non-ideal character of such devices. To achieve so, an analysis methodology is herein built based on one central sample called A1, to which the main text and figures are all referring. The data and figures concerning the other samples A2, A3 and B used to demonstrate the extended model applicability are provided in Appendix and clearly mentioned in the text. Details about all samples are provided in Section 4.2. The dark single diode model can be represented with an equivalent circuit containing only a few elements[13], as shown in Figure A.8: the main diode with current J_d, corresponding to the pn heterojunction (HJ) between the (Ag,Cu)$_2$ZnSn(S,Se)$_4$ (ACZTSSe) absorber and CdS buffer characterized by a saturation current density J_0 and ideality factor n; a parallel shunt resistance R_{sh} with current J_{sh}; a series resistance R_s with voltage drop V_s. Upon illumination, the photogenerated current source J_{ph} appears in the circuit and is usually considered bias-dependent for thin-film devices[14], such as those studied here. Therefore, at a certain temperature T of the system, the total measured current density J in mA/cm^2 can be expressed in function of the applied voltage V in V as:

$$J(V,T) = J_{ph}(V,T) - J_0(T)\Big[\exp\big[\frac{q(V+R_s(T)J)}{n(T)k_BT}\big] - 1\Big] - \frac{V+R_s(T)J}{R_{sh}(T)} \quad (4.1)$$

with R_s and R_{sh} in $\Omega.cm^2$, q the elementary charge in C and k_BT the thermal energy in eV. The dependence on light intensity I is not written explicitly because it is not developed herein but rather used as another way to extract the diode parameters in Section 4.3.3. The saturation current density J_0 is considered to be thermally activated with diode activation energy E_a and exponential pre-factor J_{00}, both usually considered mostly independent of temperature, following:

$$J_0(T) = J_{00}\exp\Big(\frac{-E_a}{n(T)k_BT}\Big) \quad (4.2)$$

This expression means that Arrhenius plots representing $\ln(J_0)$ vs $1/k_BT$ should yield E_a and $\ln(J_{00})$ as respectively the slope and intercept of the straight line passing through the linear region of the data, provided that n is temperature-independent as theoretically expected[15]. In other terms, measuring JV curves at varying temperatures gives access to J_0, n, E_a and J_{00} which all detain essential information about the device performance limiting factors and recombination mechanisms. Therefore, a robust extraction procedure of these parameters at all measured temperatures is required, based on the JVT(I) dataset obtained via the methodology detailed in Section 4.2.

At a given measurement temperature in dark conditions, the analysis procedure from a previous study is applied[13] in order to extract the aforementioned parameters. The extraction of R_s, R_{sh}, J_0 and n relies on the determination of 3 voltage ranges V_{rs}, V_{rsh} and V_{rd} in which the JV curve

is dominated by either R_s, R_{sh} or the diode (J_0 and n), respectively. Qualitatively, one must find:

1. V_{rsh} so that the $\frac{dV}{dJ}$ vs V curve is the flattest possible, typically for negative voltages. In the V_{rsh} range, R_{sh} equals the quantity $\frac{dV}{dJ}$.

2. V_{rs} so that the $\frac{dV}{dJ}$ vs $\frac{1}{J}$ curve is linear at high currents (low inverse currents), typically for high positive voltages. In the V_{rs} range, R_s equals the intercept of the linear fit to $\frac{dV}{dJ}$ vs $\frac{1}{J}$ with the vertical axis.

3. V_{rd} so that $\frac{d\ln(J)}{dV}$ reaches a peak, or equivalently that $\ln(J)$ vs V is linear, typically for voltages slightly below V_{oc} and in between V_{rsh} and V_{rs}. In the V_{rd} range, a straight line is fitted to the $\ln(J)$ vs V curve to find J_0 as the intercept with the vertical axis and n as the inverse slope $n = \frac{q}{k_B T \frac{dln(J)}{dV}|_{V_{rd}}}$.

This is all illustrated in Figure A.8 using 3 example measurements at 3 different temperatures from the dataset of this chapter. It can be observed that V_{rs} must decrease with temperature, V_{rd} must increase with temperature while V_{rsh} can mostly remain constant with temperature for the studied sample. These adaptations are used to first estimate and gauge the impact of R_s and R_{sh} on the measured JV curves before extracting J_0 and n at all temperatures. Following this, the evolution of J_0 and n with temperature is used to determine the diode temperature parameters E_a and J_{00} following Equation 4.2. The implications of these parameters regarding material properties and dominant recombination paths are then discussed. Eventually, a comparison with JVTI experiments is performed, followed by an exploration of shunt mechanisms via the reverse bias regime of the dark JVT data.

4.3.2 Dark JVT in forward bias to study recombination mechanisms

The dark JVT curves are shown in Figure 4.1, corresponding to $J_{ph}(V,T) = 0$ in Equation 4.1 in which all parameters are extracted following the procedure detailed above. At 300 K, $J_0 = 6.66{*}10^{-8} A/cm^2$, $n = 1.56$, $R_s = 0.89\Omega.cm^2$ and $R_{sh} = 3340\Omega.cm^2$ as reported previously for an equivalent baseline with excellent performance[4]. Before performing the analysis of diode parameters, it is important to gauge the impact of the series and shunt resistances R_s and R_{sh} on the applied voltage and measured current, respectively. The parasitic voltage drop V_s and leakage current J_{sh} represent only a small fraction of the total voltage across the diode (0.5%) and the current flowing through it (5%) within the relevant voltage range, i.e. V_d. The impact of parasitic resistances thus appears minute. Besides this, correcting a JV curve for their effect while preserving its essence is usually complex,

especially for thin-film devices where the physical origin of for instance shunt mechanisms may differ from standard ohmic conduction, as discussed herein. For these reasons, the uncorrected JVT data is used after having verified that the trends discussed herein are not influenced by R_s and R_{sh}. The high confidence interval of the single diode model fitting demonstrated below also confirms that the intrinsic HJ diode response can be distinguished from the influence of external parasitic elements.

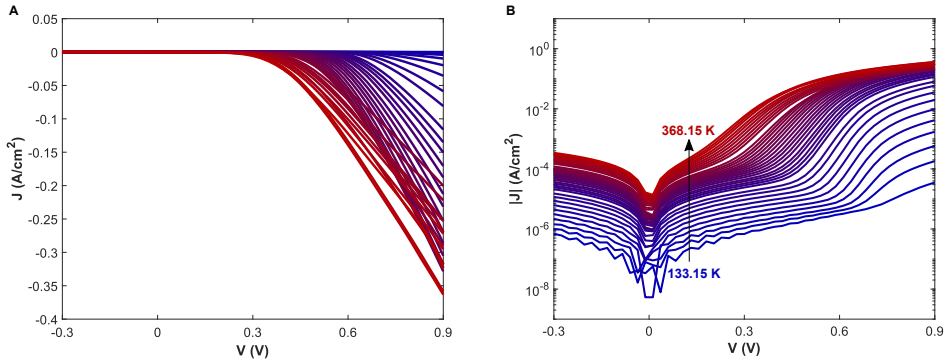

Figure 4.1: Dark current-voltage curves of the A1 sample at different temperatures in either (A) linear scale or (B) logarithmic scale in absolute value for the current. The colour gradient ranges from blue at the lowest temperature of 133.15 K until red at the highest temperature of 368.15 K, also emphasized by the black arrow.

4.3.2.1 Applicability of the single diode model

Equation 4.2 provides that the single diode model applies if an Arrhenius plot of $\ln(J_0)$ vs $1/k_BT$ is linear on a temperature range in which $n(T)$ is constant (Figure 4.2A and 4.2B), meaning that E_a can be extracted as the linear slope for an arbitrary J_{00}. However, in real devices, the condition for n to be unchanged with temperature is rarely met[7,16–19], as shown in Figure 4.2B for the sample studied here. To overcome this issue, a modified Arrhenius plot of $n(T) * \ln(J_0)$ vs $1/k_BT$ is drawn in Figure 4.2C to account for the variations of n with temperature when extracting E_a and J_{00} as in the following:

$$n(T) * \ln(J_0(T)) = n(T) * \ln(J_{00}) + \frac{-E_a}{k_BT} \tag{4.3}$$

which is equivalent to Equation 4.2. From this representation, estimates of $E_a = 1.15eV$ and $J_{00} = 1.85 * 10^5 A/cm^2$ are obtained by linear regression. In this chapter, the temperature-dependent ideality factor, noted either n or $n(T)$ and shown in Figure 4.2B, is distinguished from the so-called true

ideality factor n'. This terminology is taken from a former study[15], while the value of n' is herein defined as the average of n above 223.15 K where it is constant. In the present case, $n' = 1.56$, which allows to compute J_0 predictions $J_{0,pred} = J_{00} * exp(\frac{-E_a}{n'k_BT})$. As shown in Figure A.9, those predictions have a relative error below 1% in the whole temperature range from 368.15 K down to 223.15 K, hence called the Model Applicability (MA) region and represented as red symbols or lines in all relevant figures. This temperature range encompasses room temperature, so that the model outcomes concern the behaviour of the studied sample in real operation conditions, i.e. at 300 K.

The observed linearity of the modified Arrhenius plot in the whole MA region does not necessarily mean that all possible temperature dependencies have been taken into account in Equation 4.3. Indeed, a previous study proposes an empirical model in which E_a is linearly dependent on temperature too[7], meaning that such a feature would not be detected simply by gauging linearity in Arrhenius plots. Instead, this previous work suggests to assess if the linear slopes of $n(T) * \ln(\frac{J_0(T)}{J_{00}}) = \frac{-E_a}{k_BT}$ and $\ln(\frac{J_0(T)}{J_{00}}) = \frac{-E_a}{n(T)k_BT}$ are equal. Besides this, one should estimate the intercept of $n(T) * \ln(\frac{J_0(T)}{J_{00}})$ with the vertical axis, denoted as α and quantifying the temperature-dependent empirical character of E_a such that $E_a(T) = E_{a0} - \alpha T$. α is composed of two terms: on the one hand, the bandgap linear dependence on temperature coefficient β; on the other hand, local bandgap and electrostatic potential fluctuations characterized by a standard deviation σ_{EA}. This formalism leads to $E_a(T) = \bar{E}_{a0} - \beta T - \frac{\sigma_{EA}^2}{2n(T)k_BT}$. In the present case, both $n(T) * \ln(\frac{J_0(T)}{J_{00}})$ and $\ln(\frac{J_0(T)}{J_{00}})$ yield similar E_a in Figure A.9C, which was not observed for previous kesterite samples[7]. $\alpha = 0.075meV/K$ is also 10 times lower than previously reported[7]. Both observations indicate that the influence of both mechanisms is significantly weaker for the studied sample, i.e. that β and σ_{EA} are both smaller. The reduced potential fluctuations for the studied baseline align with the associated lower Urbach energy (E_u) around 20 meV[4,5] compared to previous kesterite standards[7,20,21] for which band tailing are likely causing more important local bandgap non-uniformity[22,23]. $\alpha = 0.075meV/K$ actually corresponds to only a slight 10 meV variation of E_a over the whole MA range, which largely falls within the resolution of the Arrhenius plot extraction. For these reasons, bandgap variation with temperature and potential fluctuations are considered negligible, for the device under study in the MA range, inducing that $E_a(T) = E_a$ is temperature-independent. This implies that all temperature variations in Equation 4.3 are accounted for by the modified Arrhenius plot which is therefore sufficient to estimate $E_a = 1.15eV$ and $J_{00} = 1.85 * 10^5 A/cm^2$ accurately in the MA region. The dark JVT response of sample A1 in Figure 4.2 is also observed in additional samples A2, A3 and B with similar model agreement, as shown in Figure A.10 and A.11, which

extends the validity of the methodology developed herein. The resulting estimates of n', J_0 at 300 K, E_a and J_{00} for A2, A3 and B are comparable to those obtained for A1, as summarized in Table A.4. This hints towards a common behaviour of kesterite solar cells processed with that baseline (samples A1, A2, A3) and its variations (sample B). The analysis is pursued below for the specific case of sample A1.

Below 233.15 K, ln (J_0) is no longer linear with $1/k_BT$ while $n(T)$ increases significantly (Figure 4.2A and 4.2B), meaning that the single diode model, even using the modified Arrhenius plot, is no longer applicable. This is obvious from the divergence of the J_0 predictions in that temperature range in Figure A.9. For this reason, it is denoted herein as Out-of-Model (OoM) region, represented as blue symbols or lines in all relevant figures. The divergence with the single diode model in OoM means other mechanisms come into play and additions should be made to take them into account. This is discussed at the end of this section, after the thorough analysis of the MA range to unveil the implications of E_a, $n(T)$ and J_{00} regarding material properties and device limitations.

4.3.2.2 Activation energy E_a

First, the value of E_a is essential as it theoretically encloses information about the main V_{oc}-limiting factor, which is key to enhance performance, especially in the case of kesterites. The typical analysis consists in comparing the value of E_a to the absorber bandgap E_g, and the usual conclusion if $E_a < E_g$ is observed is that interface recombination is dominating the diode response. In practice, grain boundary recombination or a cliff-like HJ band alignment can also lead to $E_a < E_g$[7,15]. In this case, $E_a \simeq E_g = 1.15eV$, which relates to a positive conduction band offset at the HJ[15], or the so-called spike-like band alignment, usually considered a condition for efficient chalcogenide/CdS solar cells. Another consequence is that the presence of Fermi level pinning can be ruled out since E_a is much greater than the HJ hole barrier at 0V $\phi_b^{p,0}$. Indeed, $E_a = 1.15eV >> \phi_b^{p,0} = qV_{bi}(1-\theta) + (E_F - E_V) \simeq qV_{bi} + \frac{E_g}{2} - k_BTln(\frac{N_A}{n_i}) = 0.6eV$ in which the HJ built-in voltage $V_{bi} = 0.4V$ and the absorber carrier concentration $N_A = 10^{15}cm^{-3}$ are estimated from capacitance-voltage (CV) measurements[4], in agreement with the theoretical value of $(E_F - E_V) = 0.2eV$ from another study[24]. The theta parameter $\theta = \frac{\epsilon_{abs}N_A}{\epsilon_{abs}N_A + \epsilon_{buff}N_D}$ quantifies the asymmetric/abrupt character of the HJ, with the dielectric permittivity of the absorber $\epsilon_{abs} = 9\epsilon_0$[24] (resp. the buffer $\epsilon_{buff} = 10\epsilon_0$[25]) and doping density N_D of the buffer. In the present case, θ is considered equal to 0, meaning $N_D >> N_A$, since it leads to the highest possible value for $\phi_b^{p,0}$. Still, even in this case $\phi_b^{p,0}$ remains largely smaller than E_a, hence confirming the absence of Fermi level pinning for the studied device and suggesting another culprit for its improvable V_{oc} of 497 mV in Table A.6,

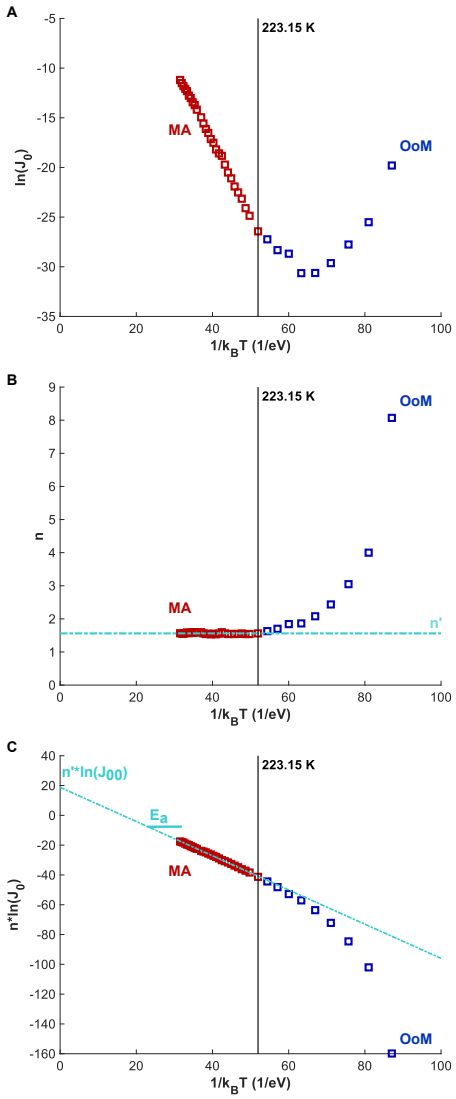

Figure 4.2: Evolution of (A) the saturation current density J_0, (B) the ideality factor n and (C) their product $n * \ln(J_0)$ in function of the inverse thermal energy $1/k_BT$ for the A1 sample. Data points are shown as red and blue squares for respectively the Model Applicability (MA) and Out-of-Model (OoM) ranges described in the text. The temperature of 223.15 K delimiting these ranges is represented by a solid black vertical line. The value of the true ideality factor $n' = 1.56$ as well as the linear fit to $n * \ln(J_0)$ leading to $E_a = 1.15eV$ and $J_{00} = 1.85 * 10^5 A/cm^2$ are shown as cyan dashed lines.

as discussed in the following. However, since the carrier concentration of CdS layers grown on kesterite layers is difficult to accurately determine and not reported in the literature, the quantity N_D is left as undetermined at this point and θ is considered as a parameter.

4.3.2.3 Ideality factor n

Observing $n(T) = n' = 1.56 > 1$ in MA provides another insight into the dominant recombination type as well as certain material properties. Indeed, theory provides that $n > 1$ could be caused by either tail-like energy-distributed defects in the bulk of the absorber[18,19], or by interface-limited recombination[15]. In the former case, the model states that n should depend on temperature, which is not observed herein, and does not cover the possibility of gaussian-distributed defects usually probed by admittance spectroscopy[26,27]. In the latter case, n is correctly predicted as temperature-invariant but its constant value in MA is such that $n' = \frac{1}{1-\theta} = 1.56$, leading to $\theta = 0.36$ and $N_{D,th} = 1.6 * 10^{15} cm^{-3}$ which appears relatively lower than usual expectations in the case of a CdS buffer, hinting that a more realistic model might be required.

SCAPS-1D[11] simulations are realized to cope with the limitations of both theoretical models and provide a more refined prediction of the ideality factor value in function of defect properties and buffer doping, using material constants inspired from a previous study[28]. The main objective of these SCAPS-1D simulations is to point out towards qualitative cases of defect (deep or shallow, high or low density, bulk or interface, narrow or broad distribution) and HJ inversion types (high or low CdS doping) that could provide $n' = 1.56$ at 300 K. The goal is not to reach a perfect match with the experiments since SCAPS-1D only covers 1D structure with basic models for temperature-dependence. The parameters used in the model are provided in Table A.5. SCAPS-1D is used to produce full JV curves, to which the same n extraction procedure as for the experiments is applied to allow more relevant comparison. The change in n is simulated in function of the important parameters in two different cases which are used throughout this section:

1. a defect in the absorber bulk with varying gaussian energy distribution width E_{char}, volume defect density N_t and central energy level above the absorber valence band E_t (case 1)

2. a single defect at the HJ interface with varying surface defect density N_{ts}, central energy level above the interface valence band E_{ts} and buffer doping N_D (case 2)

In each case, the absorber carrier concentration is fixed at $N_A = 10^{15} cm^{-3}$ and E_t is kept sufficiently far away from the neighbouring bands to remain

an active recombination center, i.e. to be located in between the quasi Fermi levels[29]. This means that the simulated defects type, acceptor or donor, has only little influence on the final results. The buffer carrier concentration N_D is also kept as a parameter.

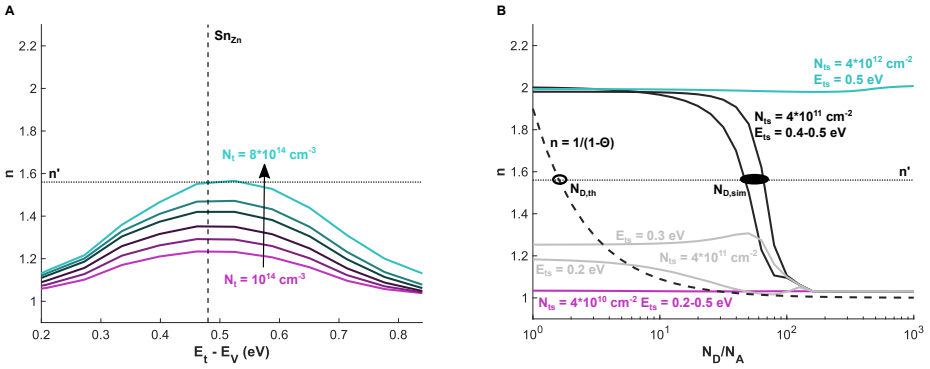

Figure 4.3: Evolution of the ideality factor n in function of defect properties from the SCAPS-1D model in Table A.5. (A) Simulation results for a bulk defect in the absorber with gaussian energy distribution width of 100 meV and for varying central energy level E_t and density N_t (case 1 in the text). The different curves corresponds to varying values of N_t from $10^{14}cm^{-3}$ (pink solid line) to $8*10^{14}cm^{-3}$ (cyan solid line) and the vertical dashed line represents the calculated energy level of the Sn_{Zn} antisite defect[24]. The horizontal dashed line represents $n' = 1.56$. (B) Simulation results for a single defect at the heterojunction interface for varying depth E_{ts} and density N_{ts} (case 2 in the text). The black solid lines illustrate deep defects at a fixed median density of $N_{ts} = 4*10^{11}cm^{-2}$, the gray solid lines represent shallow defects at a fixed median density of $N_{ts} = 4*10^{11}cm^{-2}$, while the cyan and pink solid lines respectively depict higher and lower N_{ts}. The full black ellipse highlight the range $N_{D,sim} = 4.7 - 6.6*10^{16}cm^{-3}$ of N_D values predicted by SCAPS-1D simulations to match $n' = 1.56$. The black dashed curve depicts the theoretical interface model $n = \frac{1}{1-\theta}$ detailed in the text, which intercepts the experimental n value at a buffer doping of $N_{D,th} = 1.6*10^{15}cm^{-3}$ as shown by the hollow black circle. The horizontal dashed line represents $n' = 1.56$.

In case 1, N_t, E_t and E_{char} are kept as parameters in order to help predicting their relationships with n, usually not provided by theoretical models. On the one hand, N_t is varied in between $10^{14}cm^{-3}$ and $8*10^{14}cm^{-3}$ to represent the evolution between an ideal solar cell with low defect density and a less ideal device with high defect density. N_t is kept sufficiently lower than N_A to guarantee the expected behaviour of a device with decent performance corresponding to the studied sample. On the other hand, both E_t and E_{char} are varied over large ranges to cover the whole bandgap since previous experimental studies on kesterite devices report a broad range of possible values[26,27,30–33]. Still, as mentioned above, the scope is here limited to active recombination centers with sufficiently deep energy levels, which means, following past studies[24,34], that the V_{Cu} and Cu_{Zn} shallow ac-

ceptors responsible for p-type doping are not considered herein since the objective is to study recombination. The capture cross section for electrons is set to $\sigma_n = 10^{-13} cm^2$ in accordance with both experimental[27] and numerical estimations[24]. In the case of high buffer doping ($N_D = 10^{17} cm^{-3}$), as shown in Figure 4.3A, n is logically closer to 1 as the defect is shallower while it is maximum for E_t close to the midgap. The $E_t - n$ curves are scaled up as N_t progressively approaches N_A. At this point, the simulations provide qualitative information about the properties of a defect that would explain n' close to 1.5. Indeed, Figure 4.3A demonstrates that such a true ideality factor value could be explained by a gaussian defect in the bulk of the absorber with a density comparable to the absorber doping, an energy level close to the midgap and $\sigma_n = 10^{-13} cm^2$. Such characteristics are precisely close to those of the Sn_{Zn} antisite donor defect identified to be highly detrimental to performance from density functional theory (DFT) calculations[24], with its (2+/+) state located at $E_t = 480meV$ above the valence band edge (shown in Figure 4.3A) and an electron capture cross section close to the one used here. Sn_{Zn} could thus be a relevant candidate as dominant recombination center inducing $n' = 1.56$, further supported by its critical role in kesterites devices similar to the studied sample[3] and the reports of equivalent defect depths around 500 meV from deep-level transient spectroscopy[26,27]. N_D and E_{char} have a much weaker influence on n as shown in Figure A.12A and Figure A.12B..

In case 2, i.e. when recombination is taking place via interface defects, the ratio between the doping on the p-side N_A and the n-side N_D is important since both layers can now exchange carriers. In other terms, $N_D/N_A \propto \frac{\theta-1}{\theta}$ determines the inversion strength at the HJ surface. Considering $N_A = 10^{15} cm^{-3}$, the evolution of n in function of N_D/N_A in Figure 4.3B is obtained for various combinations of N_{ts} and E_{ts}. Two extreme cases which do not match $n' = 1.56$ are visible: if the surface density is low $N_{ts} = 4 * 10^{10} cm^{-2}$, the ideality factor remains close to 1 regardless of the defect depth and the buffer doping; if the surface density is high $N_{ts} = 4 * 10^{12} cm^{-2}$ and the defect is 500 meV away from the valence band, i.e. close to midgap, n is beyond 2 at all values of N_D. Another case that can be ruled out is when $N_{ts} = 4 * 10^{12} cm^{-2}$ and $E_{ts} < 500meV$ (Figure A.12C), n remains close to 1 as predicted by the theory of Fermi level pinning at high surface defect densities[15]. In the other cases (gray and black lines in Figure 4.3B), an intermediate surface density $N_{ts} = 4 * 10^{11} cm^{-2}$ is used, with varying defect depths. All curves share the same characteristic transition: at $N_D << 10^{17} cm^{-3}$, a higher n value proportional to the defect depth is observed while for $N_D >> 10^{17} cm^{-3}$, n is mostly equal to 1, explained by the strengthening of the n-type inversion at the HJ surface for higher buffer carrier concentration. In order to approach the experimentally determined value of $n' = 1.56$ at 300 K with $N_{ts} = 4 * 10^{11} cm^{-2}$, a certain range of defect depths between 350 and 500 meV are possible,

defining a range $N_{D,sim} = [47; 66]N_A = [4.7 * 10^{16}; 6.6 * 10^{16}]cm^{-3}$ of matching N_D values. Thus, according to simulations, relatively deep traps at the HJ interface may be responsible for $n' = 1.56$, provided that the CdS doping is higher than theoretically predicted $N_{D,th} = 1.6 * 10^{15}cm^{-3}$ from $n = \frac{1}{1-\theta}$[15] as shown in Figure 4.3B. Experimentally determining the energy depth and density of defects located at the HJ interface is tedious, hence the values predicted by simulations herein cannot be directly compared to literature reports.

To cope with this issue, a third simulation structure is developed to simulate the impact of a defect located close to the HJ surface thus depending on the n-type inversion while having the properties of a bulk defect in the kesterite absorber that can be compared to either experimental or computational results. To do so, a thin defective layer (DL) is added at the ACZTSSe/CdS interface, constituting an hybrid situation between case 1 and 2. The volume defect density in the DL is obtained by dividing the initial interface defect density of $N_{ts} = 4 * 10^{11}cm^{-2}$ by the DL thickness t_{DL}, leading to $N_{DL} = N_{ts}/t_{DL}$. The defect depth is $E_{ts} = 500meV$ so that it is close to the Sn_{Zn} antisite level[24], while the DL thickness is $t_{DL} = 10nm$ providing $N_{DL} = 4 * 10^{17}cm^{-3}$. Even though N_{DL} is higher than the absorber doping, its concentration along a much thinner layer does not impede proper functioning of the simulation model as in the bulk situation (case 1). From the comparison shown in Figure A.12D, it appears that n behaves similarly in function of the HJ doping ratio in both cases, with the only difference being that that the CdS doping required to transition from the high-n high-recombination case to the low-n low-recombination case is roughly 4 times higher for the DL. For the present case, this demonstrates that if there exists a thin layer in the kesterite absorber close to the HJ surface with high defect densities, n may be greater than 1 even at very high CdS doping above $10^{17}cm^{-3}$.

Based on the analysis of n with theoretical models and SCAPS-1D simulations in agreement with literature reports from both defects experimental characterization and first-principle calculations, both the bulk and interface defect hypotheses possibly justify the observed $n' = 1.56$. The study of E_a provides that the HJ interface is spike-like and free of Fermi level pinning but cannot individually determine whether recombination in the studied sample is dominated by defects in the absorber bulk or at the interface with the buffer. Therefore, the dark analysis is pushed further with the study of J_{00} in MA to gather new insights about recombination and possibly reach a more definite conclusion.

4.3.2.4 Saturation current exponential prefactor J_{00}

Indeed, J_{00} can be studied independently from n and E_a to possibly confirm or infirm the hypotheses drawn hereabove. In general, J_{00} depends on

the localization of the dominant recombination path along the absorber thickness: quasi-neutral zone, space-charge region (SCR) or HJ interface. The first and second both happen in the absorber bulk. Still, it is well established that the maximum recombination point in thin-film devices is located in the SCR where the electron and hole densities are equal, hence it contributes much more to the whole recombination than carriers diffusing through the quasi-neutral zone, especially within low-mobility low-lifetime materials such as kesterites[35,36].

Therefore, in the bulk (case 1), only SCR recombination is considered herein, for which J_{00} at 300 K can be expressed as[7,16]:

$$J_{00,SCR}(300K) = \pi k_B 300 \sqrt{\frac{\epsilon_{abs} N_{C,abs} N_{V,abs}}{2qV_{bi}N_A}} \frac{1}{\tau_n} \tag{4.4}$$

Evaluating $J_{00,SCR}(T)$ would require the tedious inspection of all individual temperature dependencies which, when all combined, usually remain globally weak[7,15]. Therefore, the focus is rather put on the single value of J_{00} at 300 K. Thus, the value of the effective density of states respectively in the conduction and valence band of the absorber are taken at room temperature, i.e. $N_{C,abs} = 7.48 * 10^{16} cm^{-3}$ and $N_{V,abs} = 6.02 * 10^{19} cm^{-3}$[24]. $N_A = 10^{15} cm^{-3}$ and $V_{bi} = 0.4V$ are experimentally determined via CV measurements as already mentioned. The only undetermined quantity is the electron lifetime $\tau_n = \frac{1}{v_{th}\sigma_n N_t}$ associated to a recombination center having a volume density N_t and an electron capture cross section σ_n, with the electron thermal velocity $v_{th} = 10^7 cm/s$. Setting Equation 4.4 equal to the experimental $J_{00} = 1.85 * 10^5 A/cm^2$ provides $\tau_n = 0.12ns$. Even though standard time-resolved photoluminescence (TRPL) decays in kesterites are rather of the order of 1 to 10 ns[4,20,36], careful analysis of such experiments reveal that such a sub-nanosecond estimate may better correspond to the actual minority lifetime in the ACZTSSe absorber[35]. In the aforementioned case of Sn_{Zn} with $\sigma_n = 9.3 * 10^{-14} cm^2$[24], $\tau_n = 0.12ns$ would require a bulk defect density of $9 * 10^{15} cm^{-3}$. From the SCAPS-1D simulations, a purely bulk defect extending across the whole absorber thickness with $N_t = 9 * 10^{15} cm^{-3} > N_A$ would not be compatible with decent efficiency or $n' = 1.56$, while surpassing the experimentally estimated densities from defect spectroscopy techniques[26]. Still, such N_t values could be reconciled with the observed ideality factor if the corresponding defects rather extend along a thin DL close to the HJ, according to the developed SCAPS-1D model. To verify this assumption, the theoretical model for interface-limited J_{00} can be used to check for consistency, since the SCAPS-1D structures for defects either in a DL or at the HJ interface prove to behave similarly.

For interface (IF) recombination (case 2) at the HJ with spike-like alignment and no Fermi level pinning, J_{00} is theoretically predicted independent

of temperature and determined by the hole surface recombination velocity S_p in cm/s at that surface[15]:

$$J_{00,IF} = qS_pN_A\Big(\frac{N_{C,buff}N_{V,abs}}{N_DN_A}\Big)^{1-\theta} \tag{4.5}$$

In the present case, the following values are considered: $N_A = 10^{15}cm^{-3}$, $N_{C,buff} = 2.24 * 10^{18}cm^{-3}$, and N_D varying from 10^{15} to $10^{18}cm^{-3}$. Injecting these values into Equation 4.5 leads to the 3 theoretical curves in Figure 4.4, each corresponding to the one value of S_p that provides a match with both $J_{00,exp}(300K) = 1.85 * 10^5 A/cm^2$ and the plausible N_D values identified in the n analysis. Using the CdS doping estimated from the theoretical n model $N_{D,th} = 1.6 * 10^{15}cm^{-3}$, $S_{p,th} = 9 * 10^3 cm/s$ is obtained. A simpler expression $J_{00,IF} = qS_pN_{V,abs}$ is often used in the literature but it corresponds to specific situations such as Fermi level pinning or assumptions about the CdS doping, not considered herein. In contrast, the CdS carrier concentration estimated from the SCAPS-1D simulations $N_{D,sim} = 4.7 - 6.6 * 10^{16}cm^{-3}$ provides $S_{p,sim} = 5.0 - 6.4 * 10^2 cm/s$, which is lower than $S_{p,th}$ by one order of magnitude. This emphasizes the importance to determine the doping of the CdS buffer grown on kesterite absorbers for further studies. Assuming $\sigma_p = 10^{-15}cm^2$[34], the estimated $S_{p,sim}$ values correspond to N_{ts} of the order of $10^{11}cm^{-2}$. This aligns rather well with the defect density ranges used in the SCAPS-1D analysis of n above in either the interface or the DL case, thus supporting their possible role as the dominant recombination channel in the studied device. As a final step of this dark JVT analysis, the OoM range is investigated to possibly unveil further insight about the device behaviour.

4.3.2.5 Tunneling-enhanced recombination at low temperature

As mentioned above, for temperatures below 223.15 K, the single diode model is no longer applicable. This is attested by the non-linearity of $\ln(J_0)$ in the Arrhenius plot as well as the increase of n in the OoM region in Figure 4.2A and 4.2B. In that temperature range, the parameters E_a and J_0 extracted from the MA can no longer predict the evolution of J_0 with $1/k_BT$, as observed in Figure A.9. Still, some preliminary conclusions of the MA range analysis can help to build an analysis framework for the OoM region. Indeed, it is demonstrated above that high-density defects located at the HJ interface and possibly extended as a thin DL could explain the E_a, n and J_{00} values in MA, hence that the interface-limited recombination formalism should be applied to understand the device under study. This theory provides that, in the demonstrated absence of Fermi level pinning, such an increase in ideality factor at low temperatures can have three different physical explanations[7,15]: (1) temperature-dependent bandgap and potential fluctuations, (2) tunneling-enhanced recombination (TER),

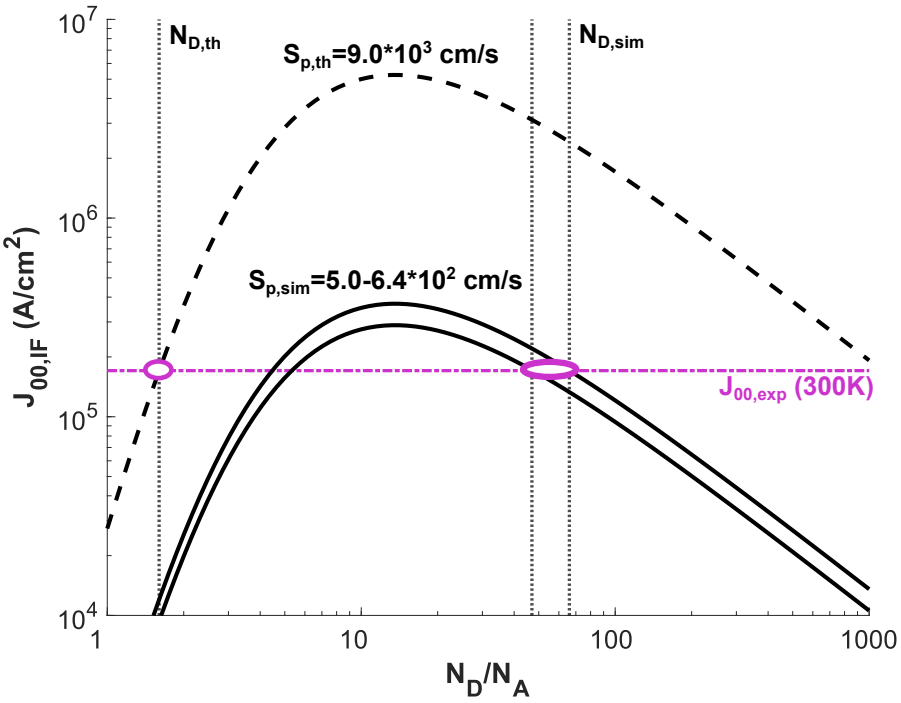

Figure 4.4: Theoretical analysis of $J_{00,IF}$ in the case of interface-dominated recombination (case 2 in the text) in function of the HJ doping ratio N_D/N_A for different values of the interface recombination velocity S_p in cm/s. The horizontal pink dashed line represents the experimentally extracted value of J_{00} at 300 K, i.e. $J_{00,exp}(300K)$. The 3 vertical dashed lines highlight the previously estimated values of $N_{D,sim}$ and $N_{D,th}$ as provided by the n analysis, which cross $J_{00,exp}(300K)$ at the pink circles. Those intercepts define 3 $J_{00,IF}$ curves in black lines, solid for $N_{D,sim}$ and dashed for $N_{D,th}$, obtained by tuning S_p to reach these N_D values.

(3) recombination through an exponential tail-like defect distribution towards the valence band at the HJ interface (IF-tail), or a combination of these mechanisms. Since it is shown above using SCAPS-1D simulations that theory may underestimate the buffer doping, especially in the case of a DL, both $N_{D,th}$ and $N_{D,sim}$ values are again considered in this section. Model fitting is realized on the inverse ideality factor $1/n$, as represented in Figure 4.5A.

The negligible impact of (1) in MA is already demonstrated in Section 4.3.2.1 by the intercepts of modified Arrhenius diagrams being close to 0 with $\alpha = 0.075meV/K$. It is further confirmed by the tentative fitting of the associated ideality factor model in Figure A.13A, attesting of the small variations with temperature of the absorber bandgap and the weak potential fluctuations in the studied sample. This corresponds to an absorber with not only more homogeneous local composition, phase, lattice strain, and/or donor/acceptor compensation degree across its surface but also narrower band tails and lower-density point defects[7,22,23], all considered favorable regarding device performance.

In the case of TER (2), one important quantity called the characteristic tunneling energy E_{00} defines a certain temperature such that for $E_{00} > k_BT$, carriers can tunnel through the concerned band for a part of the energy transition associated to the defect-assisted recombination, explaining the temperature dependence of n. E_{00} depends on the defect concentration N_{TER} via which recombination is taking place and on the concerned material dielectric permittivity and effective mass: $E_{00} = \frac{q\bar{h}}{2}\sqrt{\frac{N_{TER}}{m^*\epsilon}}$. The model differs if the defects through which TER is occurring are located at the interface (IF-TER) or in the bulk (Bulk-TER). IF-TER depends solely on E_{00} and exhibits poor agreement with the experimental data as detailed in Figure A.13A. In contrast, Bulk-TER may actually be in competition with the last possible source of $n(T)$, i.e. (3) IF-tail with k_BT^* the damping factor of its exponential energy distribution away from the valence band edge. Therefore, based on the corresponding unified model for $1/n$ in a previous study[7], a more general expression is developed by considering the individual impact of θ on the Bulk-TER and IF-tail mechanisms separately as detailed in another work[15], providing:

$$\frac{1}{n_(T)} = (1-\theta)\Big(1 + \frac{\theta}{1-\theta}\frac{T}{T^*} - \frac{1}{3}(\frac{E_{00}}{k_BT})^2\Big) \tag{4.6}$$

A fitting of the unified model in Equation 4.6 is realized to estimate E_{00} and the corresponding N_{TER}, for either $N_D = N_{D,sim}$ or $N_D = N_{D,th}$. The results for the two cases are shown in Figure 4.5A. Bulk-TER is the dominant mechanism with N_{TER} neighbouring $1 * 10^{18}cm^{-3}$ while IF-tail only plays a secondary role in the case of low N_D with $k_BT^* = 28meV$, as detailed in Figure A.13. The temperature of 223.15 K at which the OoM range starts precisely corresponds to the point where k_BT and E_{00} become comparable

(Figure 4.5B), i.e. when Bulk-TER contributions become significant, which is the very definition of the characteristic tunneling energy E_{00}. Physically speaking, this means that as k_BT approaches E_{00}, the capture of carriers by bulk traps with N_{TER} of the order of $10^{18}cm^{-3}$ is enhanced by tunneling through the neighbouring band[37], marking the beginning of OoM and the decrease of $1/n(T)$. One necessary condition for such a mechanism to occur is the presence of a strong electric field, which is precisely the case in the SCR close to the HJ, further confirming the critical importance of this region with regards to recombination mechanisms for the studied sample.

4.3.2.6 Defective layer as best working hypothesis

The close agreement of the measured device behaviour with the single diode model is demonstrated in a broad temperature range including 300 K, at which $J_0 = 6.66 * 10^{-8}A/cm^2$ and $n' = 1.56$. The extracted diode temperature dependency parameters $E_a = 1.15eV$ and $J_{00} = 1.85 * 10^5 A/cm^2$ combined with the true ideality factor $n' = 1.56$ lead to highly accurate predictions of $J_0(T)$ with relative error below 1%, indicating that their analysis should allow to draw meaningful hypotheses about the dominant recombination channel in the device under study. Observing $E_a = E_g$ confirms the desired spike-like conduction band alignment at the HJ while ruling out the possibility of Fermi level pinning, but does not allow to discriminate between bulk- or interface-limited recombination. Still, based on the combined analysis of n and J_{00}, this chapter proposes an hybrid model in which a thin defect-rich kesterite layer at the interface with the CdS buffer is the main recombination path. This hypothesis allows to reconcile (1) the high bulk defect densities of the order of $10^{17} - 10^{18}cm^{-3}$ implied by both the $J_{00,SCR}$ model and the predicted increase of n at low temperatures under the bulk-TER formalism, (2) the interface-related behaviour highlighted by both the SCAPS-1D-driven qualitative analysis justifying $n > 1$ even at high CdS doping and the quantitative matching with $J_{00,IF}$, (3) the semi-quantitative agreement with the Sn_{Zn} defect, as described from first-principle simulations[24], which is experimentally designated as most detrimental in state-of-the-art kesterite devices[3]. These observations and hypotheses arguably also apply to comparative samples A2, A3 and B since their dark JVT response is highly similar to the A1 device on which the above development is built. The corresponding reasoning as well as the underlying models are summarized in Figure 4.6. The location of this DL very close to the HJ interface stresses the importance of the buffer carrier concentration in determining the diode quality, and aligns with the ideality factor improvement under illumination discussed in the next section. This kesterite layer concentrating high defect densities arguably dominates non-radiative recombination in the studied samples, but its chemical origin is still unresolved at this point. Previous studies have

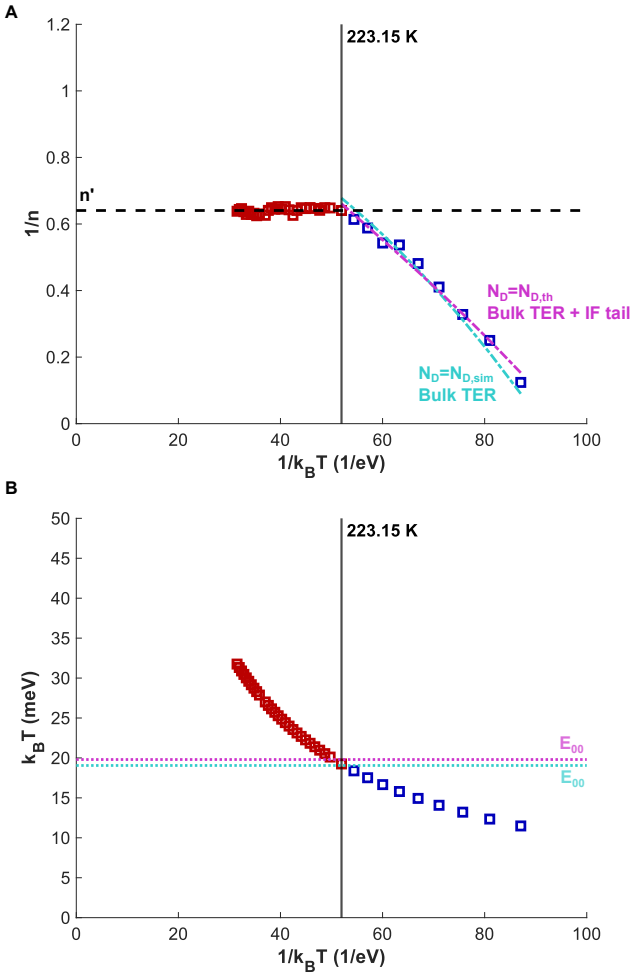

Figure 4.5: (A) Evolution of the inverse ideality factor $1/n$ in function of the inverse thermal energy $1/k_BT$ for the A1 sample, with data shown as red and blue squares for respectively the Model Applicability (MA) and Out-of-Model (OoM) ranges as described in the text. The temperature of 223.15 K delimiting these ranges is represented by a solid black vertical line. The horizontal dashed line illustrates the value of the true ideality factor $n' = 1.56$, from which $\theta = 0.36$ can be obtained using $n' = \frac{1}{1-\theta}$ [15]. The cyan (resp. pink) dotted lines illustrate the temperatures variations of n due to tunneling-enhanced recombination (TER) in the bulk of the absorber using the $N_{D,sim}$ value identified from the SCAPS-1D simulations (resp. the $N_{D,th}$ value identified from the theoretical expression). (B) Comparison between the thermal energy k_BT and the characteristic tunneling energies E_{00} corresponding to the fitting in (A), shown in the same colours.

suggested the existence in CIGS absorbers of a superficial layer rich in Cu vacancies (V_{Cu}), called ordered vacancy compound (OVC), typically thick of a few tens of nm and playing an important role regarding the device functioning[38,39]. The same hypothesis could potentially apply to kesterite materials, historically inspired from CIGS and also including V_{Cu} defects potentially clustered with Sn_{Zn} among others[24,34].

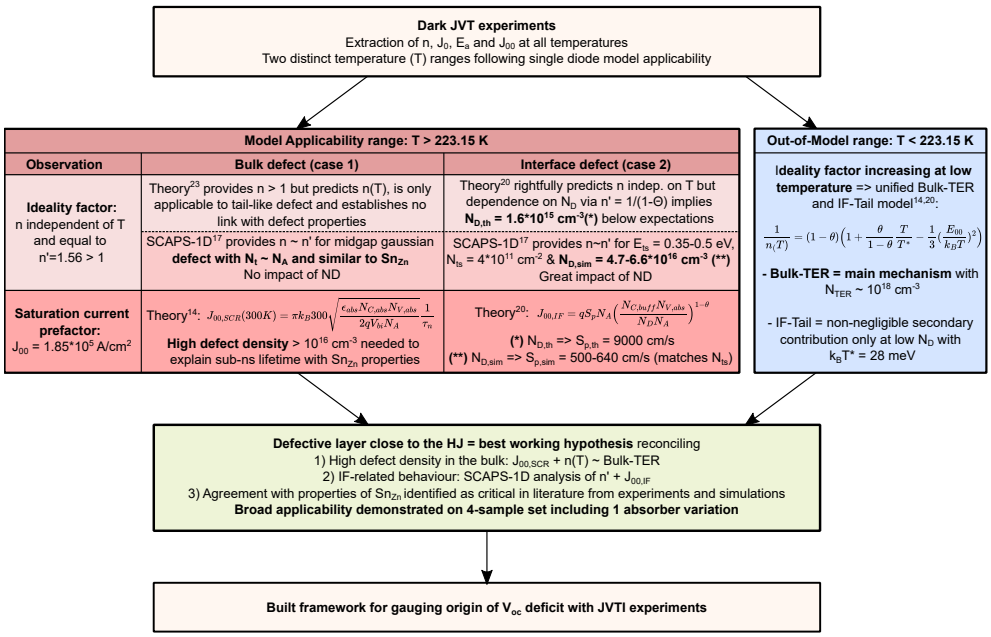

Figure 4.6: Schematic overview of the main models used in the reasoning to develop the dark JVT analysis and the most important resulting conclusions. Reference numbers provided in superscript are referring to the main text bibliography.

4.3.3 Light intensity-dependent JVT to gauge performance limitations

With the dark analysis completed and an hypothesis drawn about the main recombination path, it is interesting to verify if the A1 device behaviour under light can similarly be predicted to assess the relationship with performance limitations. To do so, the JVTI dataset obtained under various light intensities and the corresponding V_{oc} and short-circuit current density (J_{sc}) values are used (Figure 4.7A). The corresponding measurement procedure is detailed in Section 4.2.

4.3.3.1 J_{sc}-V_{oc} methodology

In this section, the J_{sc}-V_{oc} methodology[40] is applied to the JVTI measurements in order to extract the same parameters as for the dark JVT analysis. In particular, at each temperature, a $\ln(J_{sc}) - V_{oc}$ characteristics is obtained by varying the illumination intensity from $129 W/m^2$ (0.13 sun) to $950 W/m^2$ (0.95 sun), the linear fitting of which provides J_{0L} and n_L as respectively the intercept and inverse slope (Figure 4.7B). The "L" subscript is used to distinguish the JVTI estimates from the dark JVT estimates. At 300 K, $J_{0L} = 6.15 * 10^{-9} A/cm^2$ and $n_L = 1.2$, which are both lower than in the dark, attesting an improvement of the diode opto-electronic quality under illumination. Then, both their temperature dependence is analyzed to estimate the parameters E_{aL} and J_{00L}. The impact of R_s on V_{oc} is null since there is no voltage drop across it for zero current at open-circuit while R_{sh} does not modify the value of J_{sc} for zero voltage at short-circuit. Both would only respectively influence J_{sc} and V_{oc} for extreme values, which is ruled out in the previous section.

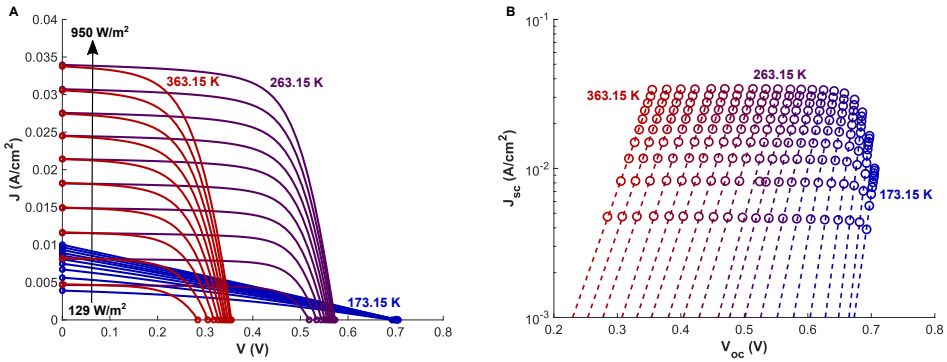

Figure 4.7: (A) Current-voltage curves in linear scale from $129 W/m^2$ to $950 W/m^2$ illumination intensity (black arrow) for the A1 sample at 3 example temperatures (363.15 K in red, 263.15 K in purple, 173.15 K in blue) with J_{sc} and V_{oc} values indicated by circles along the axes. (B) $\ln(J_{sc}) - V_{oc}$ characteristics at all measurement temperatures for the A1 sample depicted as circles in a colour gradient from blue at the lowest temperature of 173.15 K until red at the highest temperature of 363.15 K, with their respective linear fitting shown as a dashed line of the same colour.

4.3.3.2 Diode parameters under light

Similarly to the dark JVT experiments, there is a temperature range above 263.15 K in which $\ln(J_{0L})$ vs $1/k_B T$ is linear and $n_L = n'_L = 1.20$ is constant, as shown in Figure 4.8A and 4.8B. In this range also called MA, the J_{0L} predictions have a relative error below 1% as illustrated in Figure A.14A

and A.14B, indicating an as good agreement with the single diode model as in the dark. The modified Arrhenius plot is herein used again (Figure 4.8C) to extract $E_{aL} = 1.17eV$ and $J_{00L} = 7.77 * 10^7 A/cm^2$. Observing $E_{aL} = 1.17eV \simeq E_a = 1.15eV = E_g$ confirms the weak dark-light discrepancy and suggests that the illuminated HJ diode has the same characteristics as in the dark, i.e. a spike-like conduction band alignment without Fermi level pinning. As also similarly concluded in the dark JVT analysis, Figure A.14C demonstrates that all temperature variations are accounted for by $n_L(T)$ so that α_L is nearly equal to 0 and E_{aL} and J_{00L} can be considered mostly temperature-independent. The similarity in the device behaviour in MA in both dark and light conditions is further emphasized when directly comparing the evolution of the respective diode parameters in Figure 4.8. This feature is usually not observed among inorganic thin-film solar cells still in development such as kesterites[7,14]. This very point attests the closer-to-ideal behaviour of the device under study as well as the more mature state of recent molecular ink kesterite baselines[2]. Still, $n'_L < n'$ is observed in Figure 4.8, suggesting changes in the junction properties upon illumination. A possible culprit is the CdS buffer doping N_D, which has been reported to change under light in chalcogenide devices under the "CdS photodoping effect"[41–48]. In the interface or defective layer formalism developed above using both theoretical and SCAPS-1D models, an increase in the carrier concentration of the buffer layer would indeed provide a decrease of the true ideality factor n'_L. This is illustrated in Figure A.15 for either the theoretical interface model[15], or for the IF and DL SCAPS-1D models implemented in this chapter, all predicting that even minute N_D changes may be responsible for large n improvements. In other terms, the DL layer hypothesis drawn from the dark analysis would also justify the reduction of n under light, through the photodoping-induced increase in the CdS carrier concentration.

In contrast, below 263.15 K, the illuminated device enters the OoM region and the error on the J_{0L} predictions starts to increase in Figure A.14. In that temperature range, J_{0L} starts decreasing much faster at lower temperatures before saturating and increasing again similarly as in the dark. The decrease of n_L reaching non-physical values below 1 in OoM is not provided by the theoretical models used herein. Furthermore, the objective of this section is to evaluate the efficiency impairments caused by the main recombination channel to the device under real operation, i.e. in MA. Therefore, the analysis of the light diode parameters in the OoM range is out of the scope of the present study and shall require further experiments.

After developing the hypothesis of the thin defect-rich kesterite layer at the HJ surface, it is important to gauge its impact on the device performance in real operation conditions, i.e. at room temperature and close to 1 sun irradiance. The main indicator of the significance of such a non-

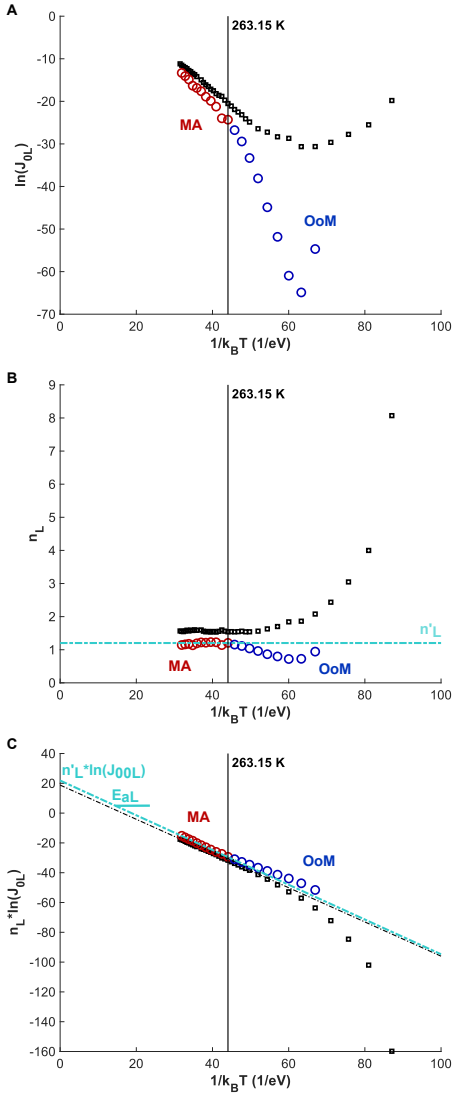

Figure 4.8: Evolution of (A) the saturation current density J_{0L}, (B) the ideality factor n_L and (C) their product $n_L * \ln(J_{0L})$ in function of the inverse thermal energy $1/k_BT$ for the A1 sample, all obtained via the J_{sc}-V_{oc} methodology. Data points are shown as red and blue circles for respectively the Model Applicability (MA) and Out-of-Model (OoM) ranges described in the text. The temperature of 263.15 K delimiting these ranges is represented by a solid black vertical line. The value of the true ideality factor $n'_L = 1.2$ as well as the linear fit to $n_L * \ln(J_{0L})$ leading to $E_{aL} = 1.17eV$ and $J_{00L} = 7.77 * 10^7 A/cm^2$ are shown as cyan dashed lines. The dark results already shown in Figure 4.2 are shown again as black squares and black dashed lines to facilitate comparison.

radiative recombination-related feature is logically V_{oc}, widely recognized as the primary culprit for kesterite solar cells limited efficiency. The linear extrapolation of V_{oc} at all light intensities in MA until 0 K provide activation energies $qV_{oc,0K}$ comprised between 1.14 and 1.16 eV in Figure 4.9A, thus corresponding very well with the absorber bandgap E_g. Observing $qV_{oc,0K} \simeq E_g$ and weak V_{oc} roll-over are important updates of the recent kesterite solar cells behaviour[4,5] in comparison with previous studies[7,40,49]. The nearly perfect match between $qV_{oc,0K}$, E_{aL} and E_a as well as the roll-over starting at the temperature of 263.15 K delimiting the MA and OoM ranges imply that V_{oc} is governed by the same mechanism as the light diode parameters, proposed to be a defective layer in this chapter. Thus, in order to estimate the corresponding losses in V_{oc} and the respective contributions of each parameter, V_{oc} is expressed in function of temperature and at a given light intensity as

$$V_{oc,pred}(T) = E_{aL} - \frac{n'_L k_B T}{q} \ln\left(\frac{J_{00L}}{J_{ph}(V_{oc},T)}\right) \tag{4.7}$$

This expression originates in imposing open-circuit conditions and neglecting parasitic resistances in Equation 4.1, implying zero total current at a voltage equal to V_{oc}, while developing J_{0L} through Equation 4.2 using the diode parameters extracted under light. The only quantity still not determined is $J_{ph}(V_{oc},T)$, which can be expressed through the voltage-dependent collection efficiency at V_{oc} so that $J_{ph}(V_{oc},T) = \eta_C(V_{oc},T)J_{sc}(T)$[7,14], in which $J_{sc}(T)$ is mostly constant over the MA range. In the following, $\eta_C(V_{oc},T)$ refers to the estimation at 0.95 sun obtained through the difference between JV curves at that irradiance and in the dark: $\eta_C(V_{oc},T) = \frac{J_{0.95sun}(T)-J_{dark}(T)}{J_{sc}(T)}$[7]. This leads to $\eta_C(V_{oc}) = 46$% at 300 K in Figure A.16A. This value largely surpasses previous reports[7] and tends to confirm the interest of updating the characterization state-of-the-art for kesterites, while correlating rather well with recent studies about similar baselines[3]. With all parameters ($E_{aL} = 1.17eV$, $n'_L = 1.2$, $J_{00L} = 7.77 * 10^7 A/cm^2$ and $\eta_C(V_{oc},T)$) determined in Equation 4.7, the V_{oc} predictions at 0.95 sun in Figure A.16B and A.16C exhibit a relative error within 5 to 10% as compared to the experimental values, mostly due to the typical uncertainty in the estimation of J_{00L} and $\eta_C(V_{oc})$. Despite this, the high qualitative agreement between theoretical predictions and experimental values of $V_{oc}(T)$ indicate that the former can be used to gauge the respective contribution of the different loss sources at 300 K and 0.95 sun. To do so, an ideal case is defined from Equation 4.7 in which $E_{aL} = E_g$, $n'_L = 1$ and $J_{00L} = J_{00,ideal}$ such that $V_{oc,ideal} = E_g - \frac{k_B T}{q} \ln(\frac{J_{00,ideal}}{J_{sc}})$, considering that J_{sc} is only affected by the illumination intensity and thus unchanged in both cases. The performance improvement potential ΔV_{oc} is thus quantified as the difference with that

ideal situation $\Delta V_{oc} = V_{oc,ideal} - V_{oc,pred}$ or equivalently

$$\Delta V_{oc} = (E_g - E_{aL}) + \frac{n'_L k_B T}{q} \ln\left(\frac{1}{\eta_C(V_{oc})}\right) + \frac{k_B T}{q} \ln\left(\frac{J_{00L}^{n'_L} J_{sc}}{J_{00,ideal} J_{sc}^{n'_L}}\right) \quad (4.8)$$

in which T = 300 K and the different terms have been grouped to isolate the contribution of E_{aL}, $\eta_C(V_{oc})$ and n'_L together with J_{00L}. First, since the theoretical limit $E_{aL} = E_g$ is already reached in the studied device, there is no associated V_{oc} gain possible and $\Delta V_{oc-E_{aL}} = (E_g - E_{aL}) = 0$. Second, $\eta_C(V_{oc}) = 46\%$ represents a potential V_{oc} enhancement of $\Delta V_{oc-\eta_C(V_{oc})} = \frac{n'_L k_B T}{q} \ln\left(\frac{1}{\eta_C(V_{oc})}\right) = 24mV$ if the related mechanisms, e.g. series resistance and low mobility-lifetime product[7,14], are mitigated. Finally, the most important contribution is $\Delta V_{oc-n'_L,J_{00L}} = \frac{k_B T}{q} \ln\left(\frac{J_{00L}^{n'_L} J_{sc}}{J_{00,ideal} J_{sc}^{n'_L}}\right) = 363mV$ if $J_{00,ideal} = 5{*}10^3 A/cm^2$ is taken from the latest state-of-the art CIGS device[50]. This $J_{00,ideal}$ value corresponds to $J_{0,ideal} = 12 * 10^{-12} A/cm^2$ which is much lower than in the present case where $J_{0L} = 6.15{*}10^{-9} A/cm^2$ at 300 K, further highlighting J_0 as the main culprit for the significant V_{oc} deficit in recent kesterites baselines for which radiative losses have been largely mitigated[2]. These potential V_{oc} gains are compared to the actual V_{oc} at 0.95 sun and the corresponding Shockley-Queisser (SQ) limit in Figure 4.9B, highlighting future prospects in terms of performance enhancements. Similarly to the dark JVT analysis, the JVTI formalism developed herein also applies to sample A2 and leads to highly similar parameter estimates, as shown in Figure A.17 and Table A.4. Therefore, in the studied devices, V_{oc} losses are largely dominated by non-radiative recombination, hypothesized to mainly take place in a thin defective layer at the HJ interface and quantified by the ideality factor n and saturation current density prefactor J_{00}, while the imperfect collection efficiency only plays a secondary role. Given the applicability of the presented analysis in both dark and light across multiple devices with different absorbers, the resulting conclusions may potentially affect a broad range of kesterite devices. The adoption of specific defect passivation strategies in the ACZTSSe/CdS HJ vicinity should thus be investigated in the future so as to mitigate the associated V_{oc} deficit.

4.3.4 Dark JVT in reverse bias to explore origin of shunt

Besides the V_{oc} losses, the fill factor (FF) deficit of kesterite solar cells is the second most important performance limitation. It is not only impacted by the diode parameters studied above but also by the device JV response in low forward bias. Therefore, the reverse currents and their physical origin are also analyzed. Typically, reverse currents are considered dominated by ohmic shunt conduction in parallel of the absorber/buffer HJ, namely via absorber pinholes or low-resistance grain boundaries[51]. This implies that

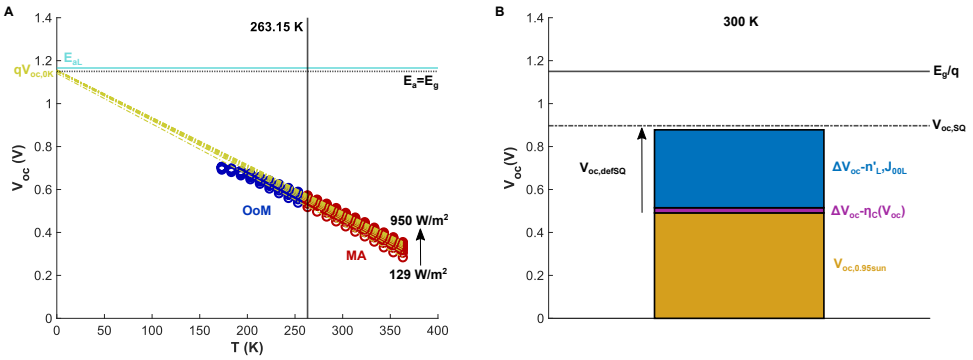

Figure 4.9: (A) Evolution of V_{oc} in function of the temperature T for the A1 sample at different light intensities indicated by the black arrow, with data shown as red and blue circles for respectively the Model Applicability (MA) and Out-of-Model (OoM) ranges as described in the text. The horizontal solid cyan (resp. dashed black) line represents the light diode activation energy $E_{aL} = 1.17eV$ (resp. dark diode activation energy equal to the absorber bandgap $E_a = E_g = 1.15eV$) at 300 K. The dashed green lines depict the linear fits to the V_{oc} data in MA, leading to an extrapolated value at 0 K $qV_{oc,0K}$ between 1.14 and 1.16 eV. The temperature of 263.15 K delimiting the MA and OoM ranges is represented by a solid black vertical line. (B) Graphical representation of the experimental V_{oc} at 0.95 sun (orange bar) compared to the potential gains due to voltage-dependent collection efficiency $\Delta V_{oc-\eta_C(V_{oc})}$ (purple bar) and improvement of the light ideality factor and saturation current density prefactor $\Delta V_{oc-n'_L,J_{00L}}$ (blue bar), for the A1 sample. The black dashed and solid lines respectively represent the SQ limit $V_{oc,SQ}$ and the corresponding bandgap E_g/q. The black arrow highlights the V_{oc} deficit according to the SQ limit $V_{oc,defSQ}$.

reverse currents depend linearly on voltage and weakly on temperature, following the usual model for the temperature-dependent resistance of a semiconductor $R(T) = R_0 + \frac{dR}{dT}T$. While the linear dependence on voltage is here verified in Figure A.8B, ruling out the existence of higher-order polynomial space-charge limited current[51], the exponential increase of R_{sh} at low temperatures in Figure 4.10A rather points out towards a thermally activated transport mechanism. This phenomenon should be identified in order to apply the correct temperature-dependent model and extract relevant activation energy values.

Thermionic emission over or tunneling through a potential barrier, thermal generation-recombination currents as well as trap-assisted tunneling also exhibit thermal activation but all incur non-linear bias dependence, correspond to other regimes of absorber doping or temperature and lead to ideality factor values differing from the one observed. The most likely candidate for the reverse current mechanism in the studied sample is thus trapping-detrapping (TD)[52], as it provides the observed linear dependence with voltage and exponential dependence with temperature while being already reported for kesterite materials[35]. It consists in a variation of the material conductivity related to trapping of free carriers within shallow bandgap states. In the case of kesterite solar cells, it is reported to happen via shallow traps close to the conduction band and may be one of the keys to reconcile the widely observed discrepancy between measured TRPL decay and actual minority carrier lifetime[35]. The theory of this effect provides the effective thermal emission rate $e_n^*(T) = v_{th}(T)\sigma_d N_{C,abs}(T)\,\mathrm{exp}(\frac{-E_{TD}}{k_B T})$ in $1/s$ with temperature-independent σ_d related to Shockley-Read-Hall recombination[35,53,54]. E_{TD} is the energy difference between the conduction band minimum and the trap level. The total TD volume rate $U_{TD}(T)$ in $1/cm^3 s$ logically depends on their total volume density N_{TD} so that $U_{TD}(T) = e_n^*(T) * N_{TD}$. At an applied bias V, this provides a resistance $R_{TD}(T) \propto \frac{V}{U_{TD}(T)} = \frac{V}{e_n^*(T) * N_{TD}}$. Considering $N_{C,abs}(T) = N_{C0} * T^{3/2}$ as well as $v_{th}(T) = v_{th0} * T^{1/2}$, this leads to

$$R_{TD}(T) \propto \frac{V}{v_{th0}\sigma_d N_{C0} N_{TD}} \frac{\mathrm{exp}(\frac{E_{TD}}{k_B T})}{T^2} \tag{4.9}$$

which is in perfect agreement with the temperature dependence of trap emission decay time $\frac{1}{e_n^*(T)} = \tau_e^*(T) \propto T^{-2}\,\mathrm{exp}(\frac{E_D}{k_B T})$ given in a previous study[35]. Therefore, considering that R_{sh} in the dark is dominated by TD, an Arrhenius plot of $R_{sh}T^2$ vs $1/k_B T$ should yield E_{TD} as its linear slope. Applying this formalism to the JVTI dataset would require strong assumptions which are out of the scope of this chapter, hence this analysis is limited to the dark JVT experiments. As illustrated in Figure 4.10B, the existence of 3 distinct slopes at high, medium and low temperatures is observed, with corresponding E_{TD} values of respectively $E_{aTD1} = 130meV$,

$E_{aTD2} = 103meV$ and $E_{aTD3} = 60meV$ in agreement with previously reported estimates[35]. The transition between the different activation energies as temperature varies indicates a change in the defect through which TD is taking place. In particular, the fact that E_{TD} successively decreases with temperature could relate to the simultaneous downward movement of the Fermi level as well as the decrease of the thermal energy k_BT required by electrons in the conduction band to be captured and emitted by the shallow neighbouring states. Under the current formalism, the shallow trap seemingly dominating dark shunt currents via TD at room temperature is $103meV$ away from the conduction band. Such a close-to-band edge trap depth could correspond to DFT-computed Zn_{Cu} donors with low formation energy[34], the shallower (+/0) state of Sn_{Zn}[24], band tailing-related $Sn_{Zn} + 2Cu_{Zn}$ complexes and out-of-plane $(Cu_{Zn} + Zn_{Cu})_{\perp}$ clusters[55], or experimentally characterized shallow defect levels[30–32]. The TD process appears responsible for the exponential temperature dependence of the linearly voltage-dependent reverse currents and dominates the value of R_{sh} in the dark, not only for the A1 sample but also for all other studied devices around room temperature as shown in Figure A.18. Even though the study of this mechanism upon illumination would require further experiments, the contributions of TD to reverse currents are likely also affecting the response of such devices under light and thus eventually impacting the FF. Therefore, a careful inspection of the related processes is needed in the future to pursue further performance improvements and device physics understanding.

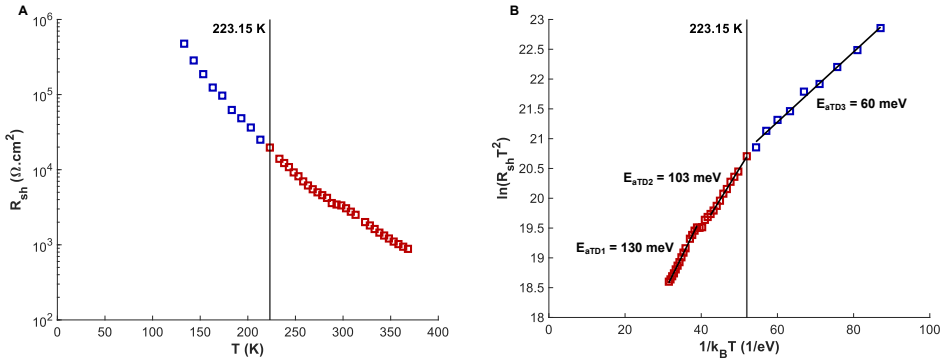

Figure 4.10: Evolution of (A) R_{sh} in function of the temperature T and of (B) $\ln(R_{sh}T^2)$ in function of the inverse thermal energy $1/k_BT$ following the dark extraction for the A1 sample, with data shown as red and blue squares for respectively the Model Applicability (MA) and Out-of-Model (OoM) ranges. The black solid lines represent the linear fittings in the 3 ranges described in the text, providing the 3 activation energies related to trapping-detrapping (TD). The temperature of 223.15 K delimiting the MA and OoM ranges is represented by a solid black vertical line.

4.4 Conclusion

A thorough analysis of dark and light-intensity dependent current-voltage measurements at different temperatures emphasizes the need for an update of the device modeling for recent kesterite baselines based on molecular ink chemical routes. Their higher opto-electronic quality characterized by benign band tailing and potential fluctuations allows excellent agreement with the standard single diode model, facilitating the understanding and prediction of their closer-to-ideal behaviour in both dark and light conditions. Through a combination of well-established semi-analytical models and simulations, the values and temperature dependencies of all parameters are studied, pointing towards a thin defective layer at the absorber/buffer interface as main recombination channel at room temperature. Qualitative and semi-quantitative agreement is obtained with the Sn_{Zn} donor properties recently highlighted as one of the most detrimental intrinsic point defects in the kesterite lattice. The key role played by the CdS carrier concentration with regards to recombination at the HJ interface is defined more precisely by SCAPS-1D simulations. Divergences with the single diode model at low temperatures can be explained by tunneling-enhanced recombination. The remarkable weakness of dark-light discrepancy for the studied thin-film solar cell allows to gauge the various contributions to the still too significant V_{oc} deficit. The critical importance of the hypothesized defective layer is emphasized as it largely determines the value of the ideality factor n and the saturation current density prefactor J_{00}, both responsible for the resulting large V_{oc} improvements still to be accomplished. To do so, passivation schemes at the heterojunction interface and strategies to increase the carrier concentration in the buffer seem promising. Besides, the impact of the heterojunction annealing and of alternative buffer materials with different doping levels regarding the model applicability and the formation of the defective layer should be further assessed. Specific studies aiming at verifying the existence of such a defective layer and determining its chemical nature need to be pursued in the future through depth-dependent analysis of composition and opto-electrical response. It appears especially important as the validity of the whole analysis and the resulting conclusions extend across multiple devices including different kesterite absorber compositions. This is also true for the reverse bias analysis, for which this chapter eventually suggests that carrier trapping-detrapping via shallow states may dominate reverse currents in the investigated samples. This phenomenon likely contributes to shunt leakages which are particularly essential with regards to performance of indoor PV systems.

Bibliography

[1] R. Scaffidi et al. *Newton, accepted* (2025).

[2] L. Wong et al. (2024). DOI: 10.21203/rs.3.rs-5136540/v1.

[3] J. Shi et al. *Nat Energy* (2024). DOI: 10.1038/s41560-024-01551-5.

[4] Y. Gong et al. *Adv Funct Materials* (2024), p. 2404669. DOI: 10.1002/adfm.202404669.

[5] R. Scaffidi et al. *Materials Today Energy* 46 (2024), p. 101715. DOI: 10.1016/j.mtener.2024.101715.

[6] J. Li et al. *Nat Energy* 7.8 (2022), pp. 754–764. DOI: 10.1038/s41560-022-01078-7.

[7] C. J. Hages et al. *Journal of Applied Physics* 115.23 (2014), p. 234504. DOI: 10.1063/1.4882119.

[8] J. Zhou et al. *Nat Energy* (2023). DOI: 10.1038/s41560-023-01251-6.

[9] R. Scaffidi et al. *J. Mater. Chem. A* 11.25 (2023), pp. 13174–13194. DOI: 10.1039/D3TA01218B.

[10] Y. Gong et al. *Solar RRL* 9.4 (2025), p. 2400756. DOI: 10.1002/solr.202400756.

[11] M. Burgelman, P. Nollet, and S. Degrave. *Thin Solid Films* 361-362 (2000), pp. 527–532. DOI: 10.1016/S0040-6090(99)00825-1.

[12] Y. Gong et al. *Nat Energy* 7.10 (2022), pp. 966–977. DOI: 10.1038/s41560-022-01132-4.

[13] S. S. Hegedus and W. N. Shafarman. *Progress in Photovoltaics* 12.2-3 (2004), pp. 155–176. DOI: 10.1002/pip.518.

[14] S. Hegedus, D. Desai, and C. Thompson. *Progress in Photovoltaics* 15.7 (2007), pp. 587–602. DOI: 10.1002/pip.767.

[15] R. Scheer. *Journal of Applied Physics* 105.10 (2009), p. 104505. DOI: 10.1063/1.3126523.

[16] U. Rau and H. Schock. *Applied Physics A: Materials Science & Processing* 69.2 (1999), pp. 131–147. DOI: 10.1007/s003390050984.

[17] U. Rau et al. *Thin Solid Films* 361-362 (2000), pp. 298–302. DOI: 10.1016/S0040-6090(99)00762-2.

[18] T. Walter, R. Herberholz, and H.-W. Schock. *SSP* 51-52 (1996), pp. 309–316. DOI: 10.4028/www.scientific.net/SSP.51-52.309.

[19] T. Walter et al. *Proc. 12th EC Photovoltaic Solar Energy Conference*. 1994, p. 1755.

[20] T. Gokmen et al. *Applied Physics Letters* 103.10 (2013), p. 103506. DOI: 10.1063/1.4820250.

[21] C. J. Hages, N. J. Carter, and R. Agrawal. *Journal of Applied Physics* 119.1 (2016), p. 014505. DOI: 10.1063/1.4939487.

[22] U. Rau and J. H. Werner. *Applied Physics Letters* 84.19 (2004), pp. 3735–3737. DOI: 10.1063/1.1737071.

[23] J. H. Werner, J. Mattheis, and U. Rau. *Thin Solid Films* 480-481 (2005), pp. 399–409. DOI: 10.1016/j.tsf.2004.11.052.

[24] S. Kim et al. *Energy Environ. Sci.* 13.5 (2020), pp. 1481–1491. DOI: 10.1039/D0EE00291G.

[25] K. W. Böer. 2013. DOI: 10.1007/978-3-642-36748-9.

[26] J. V. Li et al. *Applied Physics Letters* 102.16 (2013), p. 163905. DOI: 10.1063/1.4802972.

[27] V. Kheraj et al. *2016 IEEE 43rd Photovoltaic Specialists Conference (PVSC)*. 2016, pp. 2195–2199. ISBN: 978-1-5090-2724-8. DOI: 10.1109/PVSC.2016.7750024.

[28] A. Jimenez-Arguijo et al. *Solar Energy Materials and Solar Cells* 251 (2023), p. 112109. DOI: 10.1016/j.solmat.2022.112109.

[29] B. Das et al. *Phys. Rev. Mater.* 4.2 (2020), p. 024602. DOI: 10.1103/PhysRevMaterials.4.024602.

[30] D. B. Khadka, S. Kim, and J. Kim. *J. Phys. Chem. C* 119.22 (2015), pp. 12226–12235. DOI: 10.1021/acs.jpcc.5b03193.

[31] O. Gunawan et al. *Applied Physics Letters* 100.25 (2012), p. 253905. DOI: 10.1063/1.4729751.

[32] M. J. Koeper et al. *Applied Physics Letters* 111.14 (2017), p. 142105. DOI: 10.1063/1.4996283.

[33] D. W. Miller et al. *Applied Physics Letters* 101.14 (2012), p. 142106. DOI: 10.1063/1.4754834.

[34] W. Chen et al. *Energy Environ. Sci.* 14.6 (2021), pp. 3567–3578. DOI: 10.1039/D1EE00260K.

[35] C. J. Hages et al. *Advanced Energy Materials* 7.18 (2017), p. 1700167. DOI: 10.1002/aenm.201700167.

[36] M. Grossberg et al. *J. Phys. Energy* 1.4 (2019), p. 044002. DOI: 10.1088/2515-7655/ab29a0.

[37] G. Hurkx, D. Klaassen, and M. Knuvers. *IEEE Trans. Electron Devices* 39.2 (1992), pp. 331–338. DOI: 10.1109/16.121690.

[38] S.-H. Wei and S. Zhang. *Journal of Physics and Chemistry of Solids* 66.11 (2005), pp. 1994–1999. DOI: 10.1016/j.jpcs.2005.10.003.

[39] Y. Zhao et al. *Adv Funct Materials* 31.10 (2021), p. 2007928. DOI: 10.1002/adfm.202007928.

[40] O. Gunawan, T. Gokmen, and D. B. Mitzi. *Journal of Applied Physics* 116.8 (2014), p. 084504. DOI: 10.1063/1.4893315.

[41] M. Igalson, M. Bodegård, and L. Stolt. *Solar Energy Materials and Solar Cells* 80.2 (2003), pp. 195–207. DOI: 10.1016/j.solmat.2003.06.006.

[42] F. S.-S. Chien et al. *ACS Appl. Electron. Mater.* 2.3 (2020), pp. 796–801. DOI: 10.1021/acsaelm.9b00852.

[43] A. O. Pudov et al. *Journal of Applied Physics* 97.6 (2005), p. 064901. DOI: 10.1063/1.1850604.

[44] H. Xin et al. *Advanced Energy Materials* 4.11 (2014), p. 1301823. DOI: 10.1002/aenm.201301823.

[45] J. Li et al. *Solar Energy Materials and Solar Cells* 149 (2016), pp. 242–249. DOI: 10.1016/j.solmat.2016.02.002.

[46] D. B. Mitzi et al. *Solar Energy Materials and Solar Cells* 95.6 (2011), pp. 1421–1436. DOI: 10.1016/j.solmat.2010.11.028.

[47] W.-C. Hsu et al. *Solar Energy Materials and Solar Cells* 113 (2013), pp. 160–164. DOI: 10.1016/j.solmat.2013.02.015.

[48] F. Liu et al. *ACS Photonics* 4.7 (2017), pp. 1684–1690. DOI: 10.1021/acsphotonics.7b00151.

[49] J. Moore et al. *2013 IEEE 39th Photovoltaic Specialists Conference (PVSC)*. 2013, pp. 3255–3259. ISBN: 978-1-4799-3299-3. DOI: 10.1109/PVSC.2013.6745146.

[50] J. Keller et al. *Nat Energy* 9.4 (2024), pp. 467–478. DOI: 10.1038/s41560-024-01472-3.

[51] B. L. Williams et al. *Progress in Photovoltaics* 23.11 (2015), pp. 1516–1525. DOI: 10.1002/pip.2582.

[52] S. Banerjee and W. A. Anderson. *Applied Physics Letters* 49.1 (1986), pp. 38–40. DOI: 10.1063/1.97076.

[53] R. K. Ahrenkiel et al. *Solar Energy Materials and Solar Cells* 94.12 (2010), pp. 2197–2204. DOI: 10.1016/j.solmat.2010.07.012.

[54] M. Maiberg et al. *Journal of Applied Physics* 118.10 (2015), p. 105701. DOI: 10.1063/1.4929877.

[55] A. Crovetto et al. *Energy Environ. Sci.* 13.10 (2020), pp. 3489–3503. DOI: 10.1039/D0EE02177F.

CHAPTER 5
Conclusion

5.1 Overview and research answers

This thesis addresses the development, characterization and modeling of kesterite solar cells that constitute an interesting alternative to already existing thin-film technologies due to their abundant constitutive elements and broad range of applications. As detailed in Chapter 1, this is an important pathway towards the diversification of photovoltaics, which shall play an essential role in the future energy sector. The different chapters of this thesis provide building blocks to construct the answer to the research questions raised in Section 1.3, as summarized in the following.

"How mature are the current kesterite solar cell technologies and what are the promising strategies to push them further ?" The performance of kesterite solar cells currently knows a breakthrough due to upgrades in the material quality but there remains 1) an efficiency gap to close with established thin-film technologies and 2) a versatility potential to demonstrate for relevant applications, both of which are likely to be tackled through multinary alloying including Ge.

Chapter 2 comprehensively reviews the great potential of Ge alloying to enhance not only the quality of kesterite materials but also the versatility and performance of the resulting solar cells. Indeed, this strategy enables to mitigate the formation of Sn-related defects while allowing to tune the absorber bandgap, which proves useful to either comply with the requirements of emerging PV sectors or realize band engineering designs to enhance performance. Integrating Ge is possible for most fabrication processes, with important tradeoffs between the physical or chemical deposition routes. Still, literature currently remains limited to a rather narrow composition range of low Ge concentration not yet complying with the specifications of novel applications, which motivates the investigation of new processes for high-Ge kesterites preserving a high-performance potential.

"How can the quality and versatility of kesterite materials be improved ?" The combined alloying of Ag and Ge is herein demonstrated to hold great promises as a key to tune the bandgap of kesterites without compromising their opto-electronic quality, thereby promoting more efficient and versatile solar cells.

Chapter 3 firstly highlights the limited quality of kesterite absorbers with a 50% Ge-alloying ratio sequentially processed by reactive annealing of sputtered metallic stacks, exhibiting high crystalline disorder, improvable morphology and phase mixing. Even though displaying a bandgap gradient towards their back contact, their performance remains poor with a significant V_{oc} deficit. From that starting point, an alternative process relying on the formation of a molecular ink in line with latest record devices and remarkably realized in ambient air is then investigated. This solution allows a much more flexible integration of Ge in the whole composition range while preserving weak band tailing, largely contributing to much lower V_{oc} deficits than in the physical baseline. The device performance and Urbach energy rank among the best within the Ge-alloyed kesterite literature and provide a robust foundation for high-efficiency bandgap-tunable solar cells. This update of the state-of-the-art however only provides the first step, i.e. mitigated radiative V_{oc} losses, towards the next breakthrough in kesterite PV devices efficiency. Indeed, their V_{oc} deficit remains largely higher than commercially established technologies, likely due to a large contribution from non-radiative recombination via defects. This raises the need for an in-depth exploration of the opto-electrical behaviour of these next-generation devices.

"Have there been changes in the behaviour of recently developed kesterite devices and are there still unexplored facets of their opto-electrical response ?" The material quality enhancements in next-generation kesterite solar cells lead to updates in the device behaviour, which facilitates device modeling and understanding, eventually enabling a deeper grasp of the remaining loss mechanisms, some of which still remain overlooked.

Chapter 4 demonstrates through a wholesome analysis of temperature-dependent current-voltage measurements that the reduced band tailing and potential fluctuations of the updated baseline kesterite absorbers in Chapter 3 provide solar cell devices with closer-to-ideal opto-electrical behaviour. A thorough inspection of the values and temperature evolution of diode parameters in the dark enable to hypothesize the nature of the dominant loss mechanism to be a defective kesterite layer close to the buffer interface, by combining theoretical models with SCAPS-1D simulations in semi-quantitative agreement with the critical Sn_{Zn} defect. This hypothesis applies to multiple devices including different absorber com-

positions, hinting towards a general feature of kesterite absorbers processed with this baseline. The reconciliation between dark and light JV responses allow to extend this theory towards real operation conditions and eventually assess different contributions to the V_{oc} deficit. In particular, the saturation current density J_0 appears to be the main culprit for limited performance through non-radiative recombination within the defective kesterite layer. The exploration of reverse bias characteristics also sheds light on the trapping-detrapping phenomenon potentially responsible for shunt leakage through capture of charge carriers by shallow traps, also observed across various samples.

5.2 Kesterite PV outlook

It is essential to integrate the outcomes of this thesis within the broader context of kesterite solar cells so as to emphasize key points of attention for the research field and community. The obtained research answers contribute to addressing two major challenges faced by kesterite PV: enhancing efficiency and demonstrating versatility.

Having brought the kesterite solar cells PCE close to the 16 % milestone is the first step for them to be considered potentially viable for real-life applications and move beyond the lab-scale. Still, there is still a long way ahead for them to compete with other thin-film technologies with efficiencies largely beyond 20 %. This thesis emphasizes the importance to mitigate non-radiative recombination by reducing J_0 so as to counteract this main contributor to the V_{oc} deficit and eventually push performance further. The key to this challenge potentially resides in the formation of a defective layer containing Sn_{Zn} species close to the buffer interface, as hypothesized in Chapter 4. Such conclusions drawn on low-bandgap devices are likely to promote efficiency upgrades for higher-bandgap configurations too.

The latter shall arguably contribute to strengthen the versatility potential of kesterites with regards to emerging sectors such as tandem or indoor PV, which constitute one of the numerous ways to accelerate the deployment of solar cells, urgently needed to defossilize energy production worldwide. In particular, the ability to generate sufficient power in diverse light conditions necessarily requires to preserve material quality when tuning the absorber bandgap, as thoroughly discussed in this thesis. Indeed, Ge alloying enables to maintain weak band tails as the bandgap reaches the 1.5 eV range, coming near the tandem top cells and indoor illumination specifications. Given the expected large-scale deployment of multi-junction solar cells and portable electronics in the future, new applications for which low production cost, material abundance and non-toxicity would be prioritized over highest energy yield are likely to emerge, for which kesterites could become a relevant solution in the future.

Whether it concerns efficiency or versatility, the choice of kesterite absorber processing route is essential with regards to final material quality and device performance. The multiplication of recent PCE record breakthroughs for kesterites was to a large extent enabled by molecular ink recipes, as they allow easier control of the growth mechanism at the lab-scale and permit flexible multinary alloying. However, real applications require devices with much greater area than 0.23 cm^2 as reported for the kesterite 15.8 % PCE record, for which up-scaling attempts reached 14 % PCE for a 1 cm^2 area cell and 12 % PCE for a 10 cm^2 area minimodule[1]. Such solution-based deposition techniques need to demonstrate sufficient up-scaling ability as compared to their physical counterpart, usually preferred in commercially-established thin-film technologies.

5.3 Further investigations

In order to fulfill these ambitions for kesterite PV, various aspects still ought to be tackled in continuation to this thesis, as developed below. These shall in turn enable the development of not only processing routes leading to multinary-alloyed kesterite absorbers of greater quality but also updated characterization procedures and ad hoc models to predict their behaviour, the understanding of which must be further deepened to pinpoint the remaining performance barriers. These follow-up investigations are divided along 3 axes: material development, device characterization and device modeling.

Material development Ge alloying is herein proven to hold great promises for enhancing the quality and versatility of kesterite compounds. This is especially true in the case of the updated molecular ink baseline presented in Chapter 3.

Yet, preserving structural integrity to ensure low shunt leakage and decent device performance for high Ge contents and the corresponding wide absorber bandgaps is not yet resolved, arguably due to the Ge precursor dissolution mechanism. Indeed, while HCl is added to the precursor solution in order to reach complete dissolution of Ge in concentration of 60 % and beyond, the underlying mechanism remains unidentified, whether it concerns the acidic character or the presence of Chlorine ions, among others. To verify this, alternatives to the DMF solvent, the $GeCl_4$ precursor and HCl should be surveyed. Furthermore, the inevitable interaction between $GeCl_4$ and moisture within the updated baseline realized in ambient air may lead to the formation of large organic compounds[2] possibly decomposed during the annealing. The careful inspection of the relationship between absorber morphology and phase purity along its cross-section could be

also investigated more deeply via for instance TEM-EDX or Electron Back Scatter Diffusion (EBSD)-SEM.

Besides the internal chemistry of the solution process in Chapter 3, Chapter 4 also highlighted the important features impacting the behaviour of completed solar cells. In particular, the defective layer hypothesis drawn from the JVTI analysis requires further specific experiments aimed at verifying its existence through profiling techniques (capacitance, photoluminescence, elemental composition, ...) allowing to detect the presence of specific defects such as Sn_{Zn} in a higher concentration in the heterojunction vicinity. To counteract this loss mechanism, one should consider interface passivation schemes using thin oxide layers (HfO_2, SnO_2, $CuAlO_2$[3], ...).

Besides, future investigations ought to verify whether the applicability of the trapping-detrapping mechanism, suggested essential regarding reverse leakage from the dark JVT analysis, can be extended to a larger and more diverse sample set than in Chapter 4. This in turn may contribute to a broader understanding of thin-film solar cells in general. On top of this, the nature of the shallow trap states through which TD takes place in kesterites needs to be further studied, e.g. by comparing the activation energy from dark JVT in reverse bias to low-temperature PL measurements. This may potentially provide a clearer insight into bandgap states that are close to the band edges, and thus possibly related to band tailing or intrinsic doping.

Device characterization The JVTI methodology detailed in Chapter 4 is rich in information about the device response and performance limiting factors, yet its potential can be further exploited.

First, applying this procedure to well-thought sample sets could allow to determine even more precisely the nature of dominant recombination paths and their relationship with material properties. For instance, using alternative materials to CdS might help clarify the role of the buffer doping, already deemed as important with regards to the ideality factor in this thesis. The influence of CdS photodoping would be therewith also studied more in-depth, for which the comparison between dark JVT measurements with and without prior light soaking is highly relevant. Enlarging the database of JVTI response for different kesterite compositions is likely to contribute to a more solid understanding of the link between absorber stoichiometry and heterojunction diode properties. Combinatorial samples with a gradient in the absorber composition, possibly related to the concentration of the Sn_{Zn} defects widely regarded as critical, would be helpful in that regard. Applying this to the case of Ge alloying is also a very relevant study in the continuity to this thesis and could in parallel contribute, under the TD formalism, to a finer grasp of the reason behind

the lowered shunt resistance of high-Ge devices in Chapter 3.

Second, the time physical domain may also be added and/or correlated to the JVTI methodology. Indeed, the transient response of solar cells encompasses useful information about their inner opto-electrical workings, and is already widely used in the literature. An important example is admittance spectroscopy, already investigated in a limited extent in this thesis and essential for experimentally accessing defect properties to be possibly correlated with the defective layer hypothesis in Chapter 4. In that regard, temperature-dependent CVf loss maps appear as a promising tool to resolve the often complex reconciliation with JVTI responses for defective materials such as kesterites.

Third, experimental setups such as the one used in Chapter 4 also allow an in-situ monitoring of solar cells JV response over time at a certain temperature of interest, e.g. the one of the heterojunction annealing used in the updated baseline in Chapter 3. This could enable to assess in what fashion the device behaviour and junction quality evolve when subjected to this important part of the kesterite device processing.

Device modeling Chapter 4 shows that SCAPS-1D allows among others to more accurately define the relationship between device parameters and material properties as compared to semi-analytical models. In particular, this simulation structure provides a clearer picture of the role of deep defects with regards to the ideality factor. However, it does not account for the two other mechanisms, alongside doping, shown herein to be carried out by shallow traps: 1) band tails and potential fluctuations, the mitigation of which in the solution-processed baseline justifies its closer-to-ideal device behaviour, 2) trapping-detrapping, influencing the absorber conductivity and possibly at the origin of reverse leakage. Including both mechanisms in the simulation model would likely contribute to build an even more comprehensive model of current-voltage response. Besides, the convergence issues occurring at low temperatures along with the need for manually adding temperature dependence models for key parameters in SCAPS-1D restrain its potential to facilitate the interpretation of JVTI experiments. Overcoming such limitations could enable to more precisely define the influence of defect properties on the values of J_{00}, herein pinpointed as a main contributor to the V_{oc} deficit of kesterite solar cells. Therefore, future investigations should tackle the development of more elaborate simulation models accounting for the multi-dimensional character of the kesterite absorber on the one hand, i.e. polycrystalline thin-film layer with inhomogeneous composition, defect concentration, crystalline disorder and grain distribution, and the temperature evolution of relevant properties on the other hand. While literature presently remains scarce in that regard, TCAD softwares such as Silvaco Atlas/Victory, Sentaurus Syn-

opsys[4–6] or DEVSIM[7] seems to be promising solutions. This is especially true with regards to the very relevant transition to 2D-3D modeling. Indeed, the current understanding of thin-film solar cells is lacking the proper integration of a realistic polycrystalline absorber morphology to hopefully allow easier comparison between simulations and experiments. In particular, the influence of grain boundaries with regards to carrier transport is a key aspect to investigate in the future. Eventually, the Defect and Dopant ab-initio Simulation Package (DASP)[8] might help attaining a deeper grasp of carrier dynamics in highly defective materials with low lifetime such as kesterites.

Bibliography

[1] M. A. Green et al. *Progress in Photovoltaics: Research and Applications* 33.7 (2025), pp. 795–810. DOI: 10.1002/pip.3919.

[2] R. L. Benoit and P. Clerc. *The Journal of Physical Chemistry* 65.4 (1961), pp. 676–680. DOI: 10.1021/j100822a019.

[3] J. Ma et al. *Solar RRL* 8.2 (2024), p. 2300828. DOI: 10.1002/solr.202300828.

[4] J. Li et al. *Nat Energy* 7.8 (2022), pp. 754–764. DOI: 10.1038/s41560-022-01078-7.

[5] M. Maiberg et al. *Physical Review Applied* 21.3 (2024), p. 034051. DOI: 10.1103/PhysRevApplied.21.034051.

[6] C.-Y. Song et al. *Scientific Reports* 14.1 (2024), p. 2036. DOI: 10.1038/s41598-024-52436-2.

[7] J. E. Sanchez. *Journal of Open Source Software* 7.70 (2022), p. 3898. DOI: 10.21105/joss.03898.

[8] M. Huang et al. *Journal of Semiconductors* 43.4 (2022), p. 042101. DOI: 10.1088/1674-4926/43/4/042101.

List of Disseminations

First author journal articles related to this thesis:

1. R. Scaffidi, A. Jimenez-Arguijo, Y. Gong, G. Brammertz, A. Basak, Z. Jehl Li-Kao, E. Saucedo, D. Flandre, and B. Vermang. "Modelling of current-voltage characteristics of high-efficiency kesterite solar cells". *Newton, accepted* (2025)

2. R. Scaffidi, Y. Gong, A. Jimenez-Arguijo, A. G. Medaille, S. Suresh, G. Brammertz, S. Giraldo, J. Puigdollers, D. Flandre, B. Vermang, and E. Saucedo. "Tuning the bandgap without compromising efficiency: Ambient solution processing of Ge-alloyed (Ag,Cu)2Zn(Sn,Ge)(S,Se)4 kesterite thin-film solar cells". *Materials Today Energy* 46 (2024), p. 101715. DOI: 10.1016/j.mtener.2024.101715

3. R. Scaffidi, G. Brammertz, Y. Wang, A. U. Zaman, K. Sasikumar, J. De Wild, D. Flandre, and B. Vermang. "A study of bandgap-graded CZTGSe kesterite thin films for solar cell applications". *Energy Adv.* 2.10 (2023), pp. 1626–1633. DOI: 10.1039/D3YA00359K

4. R. Scaffidi, G. Birant, G. Brammertz, J. De Wild, D. Flandre, and B. Vermang. "Ge-alloyed kesterite thin-film solar cells: previous investigations and current status – a comprehensive review". *J. Mater. Chem. A* 11.25 (2023), pp. 13174–13194. DOI: 10.1039/D3TA01218B

Other first author journal articles:

1. R. Scaffidi, D. G. Buldu, G. Brammertz, J. de Wild, T. Kohl, G. Birant, M. Meuris, J. Poortmans, D. Flandre, and B. Vermang. "Comparative Study of Al2O3 and HfO2 for Surface Passivation of Cu(In,Ga)Se2 Thin Films: An Innovative Al2O3/HfO2 Multistack Design". *physica status solidi (a)* 218.14 (2021), p. 2100073. DOI: 10.1002/pssa.202100073

Other co-author journal articles and conference proceedings:

1. G. Brammertz, R. Scaffidi, S. Hamtaei, J. Parion, J. de Wild, G. Birant, T. Oris, M. Meuris, M. Van der Vleuten, M. Simor, D. Grynko, A. Nazarov, R. Blomme, N. Poonkottil, J. Dendooven, D. Flandre, T.

Aernouts, J. Poortmans, and B. Vermang. "Investigation of recombination mechanisms in electronic devices using bias-dependent admittance spectroscopy applied to CIGS solar cells". *Under peer review at ACS Applied Materials & Interfaces* (2025)

2. M. Placidi, A. Torrens, Z. Jehl Li-Kao, A. Lopez-Garcia, O. Segura, Y. Gong, A. Jimenez-Arguijo, I. Caño, S. Giraldo, E. Saucedo, G. Alvarez, Y. Sanchez, N. Spalatu, I. Oja, E. Artegiani, A. Romeo, R. Scaffidi, and A. Perez-Rodriguez. "Benchmarking Inorganic Thin-Film Photovoltaics Technologies for Indoor Applications". *Solar RRL* 9.11 (2025), p. 2500030. DOI: 10.1002/solr.202500030

3. O. El Khouja, Y. Gong, A. Jimenez-Arguijo, M. J. Guerra, A. G. Medaille, R. Scaffidi, A. Basak, C. Radu, D. Flandre, B. Vermang, S. Giraldo, M. Placidi, Z. J. Li-Kao, A. C. Galca, and E. Saucedo. "Exploring the Synthesis of Cu2(Zn,Cd)SnS4 at High Temperatures as a Route for High-Efficiency Solar Cells". *Progress in Photovoltaics: Research and Applications* 33.5 (2025), pp. 628–643. DOI: 10.1002/pip.3899

4. Y. Gong, A. Jimenez-Arguijo, I. Caño, R. Scaffidi, C. Malerba, M. Valentini, D. Payno, A. Navarro-Güell, O. Segura-Blanch, D. Flandre, B. Vermang, A. Perez-Rodriguez, S. Giraldo, M. Placidi, Z. Jehl Li-Kao, and E. Saucedo. "Attaining 15.1% Efficiency in Cu2ZnSnS4 Solar Cells Under Indoor Conditions Through Sodium and Lithium Codoping". *Solar RRL* 9.4 (2025), p. 2400756. DOI: 10.1002/solr.202400756

5. S. Hamtaei, A. Debot, R. Scaffidi, G. Brammertz, E. Cariou, S. M. Garner, A. Aguirre, J. Poortmans, P. J. Dale, and B. Vermang. "Fabrication of bendable and narrow bandgap Cu(In,Ga)(S,Se)2 for tandem photovoltaics". *Communications Materials* 6.1 (2025), pp. 1–8. DOI: 10.1038/s43246-024-00706-x

6. Y. Gong, A. Jimenez-Arguijo, A. G. Medaille, S. Moser, A. Basak, R. Scaffidi, R. Carron, D. Flandre, B. Vermang, S. Giraldo, H. Xin, A. Pérez-Rodriguez, and E. Saucedo. "Li-Doping and Ag-Alloying Interplay Shows the Pathway for Kesterite Solar Cells with Efficiency Over 14%". *Adv Funct Materials* (2024), p. 2404669. DOI: 10.1002/adfm.202404669

7. J. Parion, R. Scaffidi, F. Duerinckx, H. Sivaramakrishnan Radhakrishnan, D. Flandre, J. Poortmans, and B. Vermang. "Comparative study of the interface passivation properties of LiF and Al2O3 using silicon MIS capacitor". *Applied Physics Letters* 124.14 (2024), p. 142901. DOI: 10.1063/5.0203484

8. S. Moser, A. Aribia, R. Scaffidi, E. Gilshtein, G. Brammertz, B. Vermang, A. N. Tiwari, and R. Carron. "Controlled Li Alloying by Post-

synthesis Electrochemical Treatment of Cu_2 $ZnSn(S, Se)_4$ Absorbers for Solar Cells". *ACS Appl. Energy Mater.* 6.24 (2023), pp. 12515–12525. DOI: 10.1021/acsaem.3c02483

9. N. Roisin, M.-S. Colla, R. Scaffidi, T. Pardoen, D. Flandre, and J.-P. Raskin. "Band gap reduction in highly-strained silicon beams predicted by first-principles theory and validated using photoluminescence spectroscopy". *Optical Materials* 144 (2023), p. 114347. DOI: 10.1016/j.optmat.2023.114347

10. J. de Wild, R. Scaffidi, G. Brammertz, G. Birant, and B. Vermang. "Dielectric Front Passivation for Cu(In,Ga)Se2 Solar Cells: Status and Prospect". *Advanced Energy and Sustainability Research* 4.2 (2023), p. 2200132. DOI: 10.1002/aesr.202200132

11. J. Parion, R. Scaffidi, D. Flandre, G. Brammertz, and B. Vermang. "Low-temperature admittance spectroscopy for defect characterization in Cu(In,Ga)(S,Se)2 thin-film solar cells". 2023, pp. 99–104. DOI: 10.1109/EUROCON56442.2023.10199008

12. G. Birant, J. Mafalda, R. Scaffidi, J. d. Wild, D. G. Buldu, T. Kohl, G. Brammertz, M. Meuris, J. Poortmans, and B. Vermang. "Rear surface passivation of ultra-thin CIGS solar cells using atomic layer deposited HfOx". *EPJ Photovoltaics* 11 (2020), p. 10. DOI: 10.1051/epjpv/2020007

Conference presentations:

1. R. Scaffidi et al. "Ag and Ge synergy in molecular ink route for bandgap tunable kesterite solar cells with high efficiency", *PVSEC-35*, Numazu, Japan, November 2024.

2. R. Scaffidi et al. "Ge alloying in air-processed kesterites for efficient & versatile tunable bandgap solar cells", *14th European Kesterite Workshop*, Verona, Italy, June 2024.

3. R. Scaffidi et al. "In-depth physical analysis of the current-voltage-temperature (IVT°) behaviour of kesterite thin-film solar cells", *EMRS Spring Meeting 2024*, Strasbourg, France, May 2024.

4. R. Scaffidi et al. "Characterization and modelling of Sn-Ge bandgap-graded kesterite thin-film solar cells", *13th European Kesterite Workshop*, Barcelona, Spain, July 2023.

5. R. Scaffidi et al. "Opto-Electrical Characterization of Back Bandgap-Graded $Cu_2Zn(Sn_x,Ge_{1-x})Se_4$ Kesterite Thin-Film Solar Cells", *MRS Spring Meeting 2023*, San Francisco, USA, April 2023.

6. R. Scaffidi et al. ”Back Bandgap-Graded Kesterite $Cu_2Zn(Sn_x,Ge_{1-x})Se_4$ Thin Films for Solar Cell Applications”, *MATSUS-23*, Valencia, Spain, March 2023.
7. R. Scaffidi et al. ”Front surface passivation of $Cu(In,Ga)Se_2$ Thin Film Solar Cells using ALD Al_2O_3 and HfO_2”, *ICOOPMA 2022*, Ghent, Belgium, July 2022.

Appendix

Experimental details

Characterization technique	Abbreviation	Reference
Scanning Electron Microscopy	SEM	[1]
Elemental Dispersive X-Ray Spectroscopy	EDX	[1]
Raman spectroscopy	Raman	[2]
X-Ray Diffraction	XRD	[3]
Time-of-Flight Secondary Ion Mass Spectrometry	ToF-SIMS	[4]
(Time-Resolved) Photoluminescence	(TR)PL	[5]
X-Ray Fluorescence	XRF	[6]
External Quantum Efficiency	EQE	[7]
Current-voltage	IV/JV	[7]
Capacitance-voltage	CV	[7]

Table A.1: Abbreviation and literature references for the experimental characterization techniques used in this thesis.

Supplementary data - Chapter 2

Ref.	x	y	η(%)	$V_{oc}(mV)$	$J_{sc}(mA/cm^2)$	FF(%)	$E_g(eV)$
[8]	0.002	0	10.5	424 (371)	37.2 (8.5)	66.9 (19.1)	1.05
[9]	0.01	0	8.6	460 (344)	29.3 (15.9)	64.1 (22.1)	1.06
[10]	0.01	0.03	11.5	490 (323)	34.8 (10.0)	67.2 (19.1)	1.07
[11]	0.02	0	10.3	440 (383)	34.7 (9.9)	67.6 (18.8)	1.08
[12]	0.03	0	8.3	442 (353)	31.7 (14.0)	59.0 (27.0)	1.05
[13]	0.04	0	11	463 (332)	36.0 (9.7)	66.3 (19.7)	1.05
[14]	0.06	0.03	13.1	550 (292)	34.3 (9.9)	70.0 (16.6)	1.1
[15]	0.07	0	7.5	445 (340)	31.0 (15.1)	54.7 (31.2)	1.04
[16]	0.08	0.1	9.1	410 (478)	34.3 (8.14)	64.7 (22.5)	1.15
[17]	0.1	0.1	6.1	440 (430)	32.3 (11.1)	43.4 (43.6)	1.13
[18]	0.03	1	7	660 (555)	18.7 (10.3)	57.6 (32.3)	1.5
[19]	0.09	1	3.4	620 (670)	12.4 (13.8)	43.8 (46.6)	1.58
[20]	0.1	1	4.5	590 (541)	15.5 (17.0)	49.0 (40.3)	1.41
[21]	0.11	1	3	600 (690)	11.7 (14.5)	42.4 (48)	1.59
[21]	0.25	1	3	580 (776)	10.1 (14.0)	53.0 (37.7)	1.65
[22]	0.71	1	6	520 (920)	23.3 (-1.9)	49.6 (41.6)	1.74
[23]	0.05	0.38	2	270 (739)	22.4 (13.9)	33.3 (55.1)	1.28
[24]	0.12	0.26	3.3	290 (691)	26.4 (11.2)	42.1 (46.0)	1.25
[25]	0.12	0.46	3.8	430 (495)	18.3 (22.2)	47.0 (40.6)	1.21
[26]	0.13	0.15	12.3	490 (295)	37.1 (9.0)	67.5 (18.4)	1.04
[27]	0.15	0.1	7.9	450 (401)	33.8 (10.3)	52.0 (34.7)	1.11
[28]	0.14	0.02	8.1	400 (479)	32.7 (10.2)	62.5 (24.6)	1.14
[29]	0.22	0	12.3	530 (321)	32.2 (11.9)	72.7 (14.0)	1.11
[30]	0.25	0	11	583 (296)	33.6 (9.3)	55.9 (31.2)	1.14
[31]	0.32	0	10.4	540 (413)	36.0 (3.0)	54.0 (33.8)	1.22
[32]	0.37	0.07	7	450 (420)	29.3 (14.1)	64.0 (23.0)	1.13
[33]	0.39	0	10	540 (385)	29.5 (11.0)	62.7 (24.9)	1.19
[34]	0.4	0	9.1	480 (408)	31.8 (10.6)	60.4 (26.8)	1.15
[35]	0.17	0.5	8.3	470 (362)	29.0 (15.4)	61.8 (24.7)	1.09
[36]	0.2	0.22	5.4	350 (650)	34.6 (2.1)	38.0 (50.3)	1.27
[37]	0.3	0.16	4.8	390 (600)	29.3 (7.8)	42.0 (46.2)	1.26
[38]	0.3	0.5	9.4	460 (465)	31.9 (8.6)	63.8 (23.8)	1.19
[39]	0.46	0.26	7.1	390 (741)	33.0 (-0.5)	55.0 (34.3)	1.41
[40]	0.52	0	6.4	510 (499)	22.4 (13.9)	56.3 (32.1)	1.28
[41]	0.61	0	5.6	500 (509)	21.0 (15.3)	53.2 (35.2)	1.28
[42]	0.7	0.54	6.8	640 (482)	21.5 (11.4)	49.0 (40.3)	1.4
[43]	1	0	8.5	625 (469)	24.4 (9.6)	55.7 (33.4)	1.37
[44]	1	0.27	2.2	670 (723)	9.5 (13.2)	39.0 (51.9)	1.69
[45]	1	0.31	6	620 (567)	15.0 (14.6)	52.0 (37.7)	1.47
[46]	1	0.39	2.8	790 (734)	6.2 (12.6)	56.3 (35.2)	1.83
[47]	1	0.65	2.7	820 (844)	6.4 (8.6)	51.0 (41.1)	1.98
[48]	1	1	1.3	920 (950)	3.2 (7.4)	45.0 (47.8)	2.2

Table A.2: Measured x=Ge/(Ge+Sn) ratio, y=S/(S+Se) ratio, solar cell performance figures-of-merit and bandgap for the reported champion devices per composition point. This table is used to generate the composition maps of efficiency and Shockley-Queisser (SQ) deficits, herein indicated between brackets, in Figure 2.8, using the same colors as the symbols of the 4 different composition groups.

Supplementary data - Chapter 3

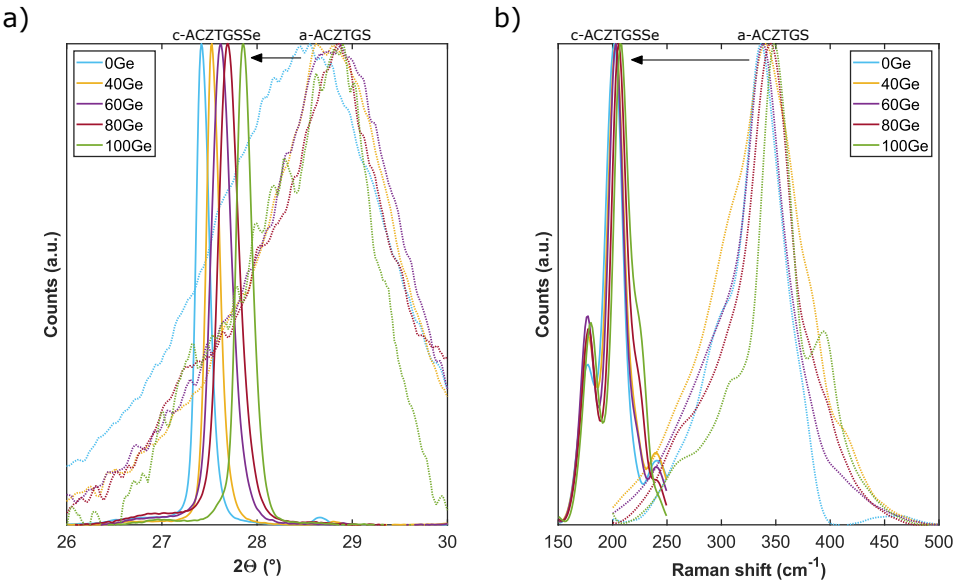

Figure A.1: Evolution of the main kesterite response in the a) XRD diffractogram and b) Raman spectrum from the amorphous kesterite precursor film (a-ACZTGS) to the polycrystalline Se-rich absorbers (c-ACTZGSSe) following the selenization step. The peak narrowing puts in evidence the crystallization process while the shifting position from around 28.5° and 340 cm^{-1} towards 27.5° and 200 cm^{-1} highlights the compositional transition from S-pure precursor to Se-rich absorbers.

Metric	0Ge	40Ge	60Ge	80Ge	100Ge
$J_{sc,SQdef}$ (mA/cm²)	9.55	8.40	10.09	9.93	12.01
$V_{oc,SQdef}$ (mV)	361	343	36	490	559
FF_{SQdef} (%)	21.27	22.81	32.32	44.34	48.59

Table A.3: Shockley-Queisser deficits of the 1 sun IV parameters for the champion device in each Ge concentration batch.

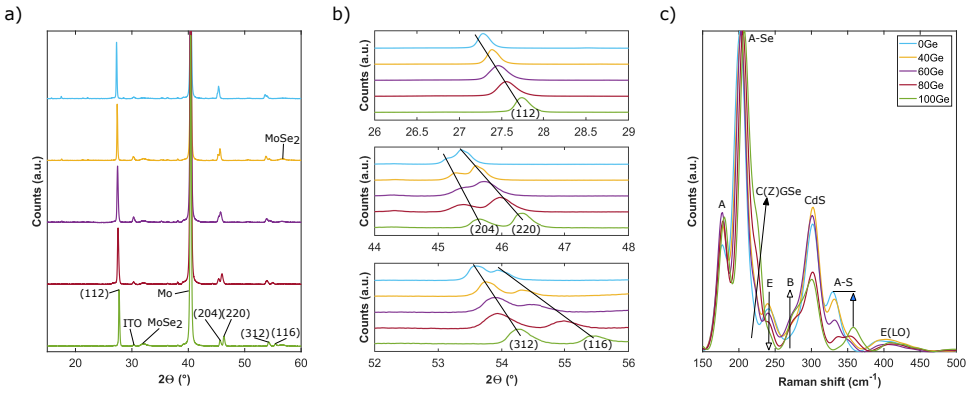

Figure A.2: XRD diffractograms for the different Ge concentrations a) over the full measurement range and b) centered around the main kesterite peaks. The angle range between 30 and 39° shows a series of small peaks, the position of which is not affected by the Ge content, hence likely not related to the kesterite system itself but rather coming from the other layers of the device stack, including ITO and Mo(S_x,Se_{2-x}) also highlighted. The kesterite XRD peaks are all shifted towards higher diffraction angle following the increasing Ge content, which confirms the proper integration of Ge inside the kesterite lattice. The shift of the (112) and (220) peaks are used to obtain the lattice parameters a and c through Bragg's diffraction law $2d\sin(\theta) = n\lambda$ and the tetragonal system formula $d_{hkl} = a/\sqrt{h^2 + k^2 + l^2(\frac{a^2}{c^2})}$. c) Full Raman spectra for the different Ge concentrations. On the Raman spectrum, the blue arrow highlights the relative intensity difference between the A-S mode associated to Sulfur for 0Ge and 100Ge; the two white arrows emphasize the transition from a pronounced E mode at 240 cm^{-1} for 0Ge to a pronounced B mode at 270 cm^{-1} for 100Ge; the black arrow puts in evidence the emergence of another contribution for the high Ge concentration samples, which could be assigned to either one of the main CZGSe modes or a potential Cu_2GeSe_3 secondary phase[49].

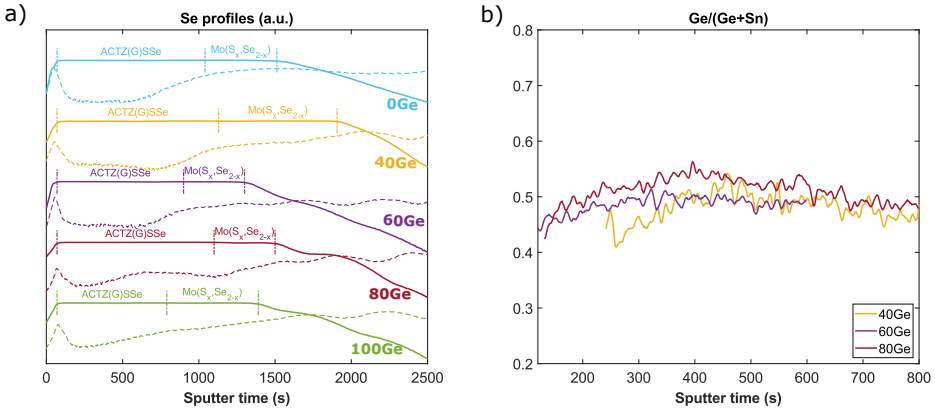

Figure A.3: a) Cs sputtering ToF-SIMS profiles of Se (solid lines) and MoO_2 (dashed lines) for all Ge concentrations, showing the absorber and Mo(S_x,Se_{2-x}) layers relative thicknesses. The Mo(S_x,Se_{2-x}) layer boundaries are determined by the rise of the MoO_2 signal, of higher quality than Mo in negative ion mode, and the downfall of the Se signal. Its thickness is around 1.2 to 2.5 times smaller than the absorber which roughly ranges between 1.5 and 2.5 μm in thickness from SEM images. b) O_2 sputtering ToF-SIMS Ge/(Ge+Sn) ratios for all Ge-Sn mixed samples (40Ge, 60Ge and 80Ge), where only the data corresponding to the absorber region is shown for the sake of clarity. No strong Sn-Ge gradient is observed regardless of the Ge content, which puts in evidence the absence of significant variation of conduction band level and bandgap of the absorber along its thickness, even though the exact value of the Ge/(Ge+Sn) ratio itself is at best semi-quantitative.

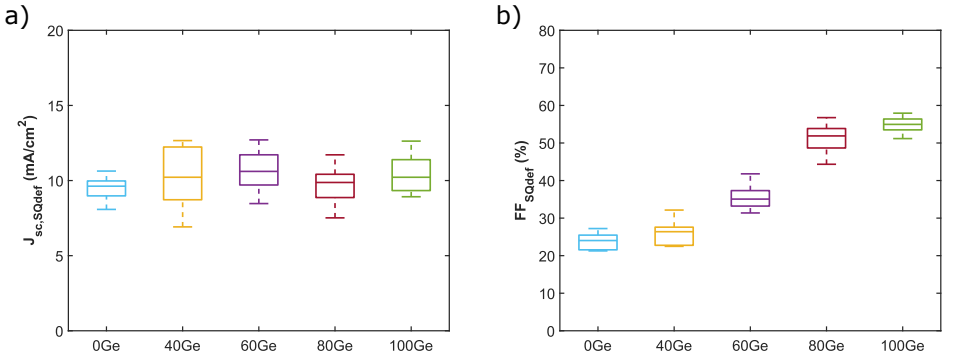

Figure A.4: Statistical dispersion of the a) short-circuit current density (J_{sc}) and b) fill factor (FF) deficit with respect to the Shockley-Queisser limit of representative devices for each Ge content.

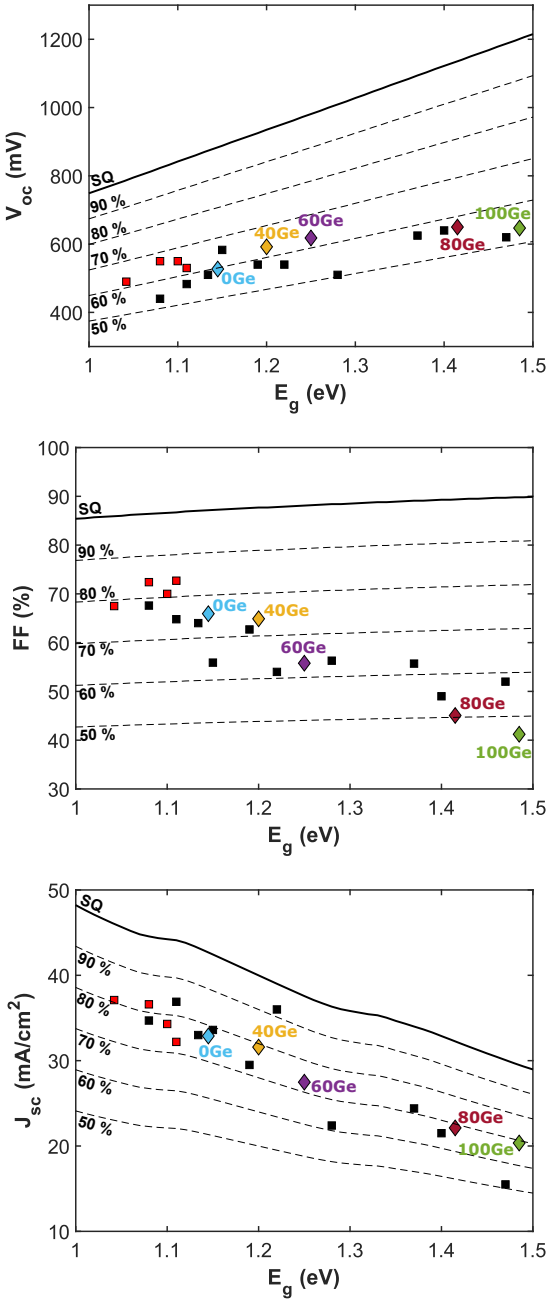

Figure A.5: Representation of the PV figures-of-merit V_{oc}, J_{sc} and FF in function of the absorber bandgap for the champion devices from Table 3.3 (coloured diamonds) in comparison with the same literature reports (black squares for lower PCE than 40Ge, red squares for higher PCE than 40Ge) as in Figure 3.10. The SQ limit is shown as a black solid line, with different completion percentages from 50 to 90 % shown as black dashed lines.

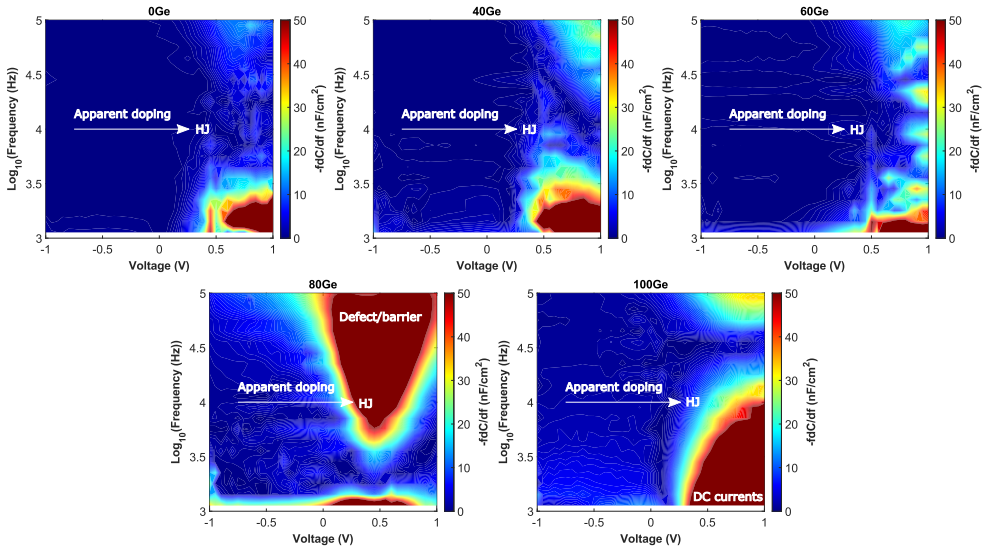

Figure A.6: Admittance spectroscopy data for all the studied samples, represented as loss maps[50,51]. The capacitance derivative with respect to frequency ($-\frac{fdC}{df}$) is plotted against both frequency and voltage at the same time on a contour plot. The white arrow represents the frequency (10 kHz) and voltage (-0.75 V to 0.25 V) used for the apparent doping profiles and is pointed towards voltages corresponding to positions closer to the HJ interface as in the main text. The red areas indicate the activation of charge loss mechanisms, in opposition with blue areas. 80Ge (resp. 100Ge) exhibits a large red response in the top right (resp. bottom right) corner of its loss map, arguably corresponding to a defect/barrier (resp. large DC currents) arising in forward bias. Those red responses likely explain the steep increase towards the HJ (arrow direction) in the apparent doping profiles of 80Ge and 100Ge. For 80Ge, this probably means the existence of a defect-like contribution activated in the device operation range and degrading performance, whereas for 100Ge this could be mostly caused by higher shunt currents.

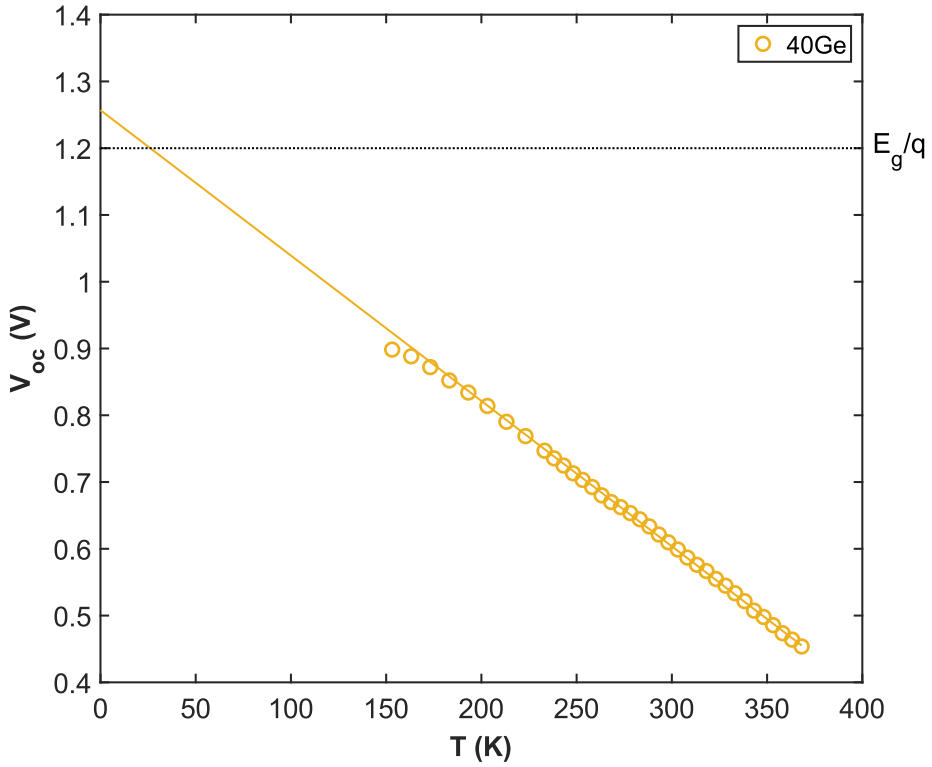

Figure A.7: Evolution of V_{oc} with respect to temperature for the 40Ge champion device with an efficiency of 12.1%, showing the small 50 mV discrepancy between the bandgap E_g/q and extrapolated V_{oc} at 0 K.

Supplementary data - Chapter 4

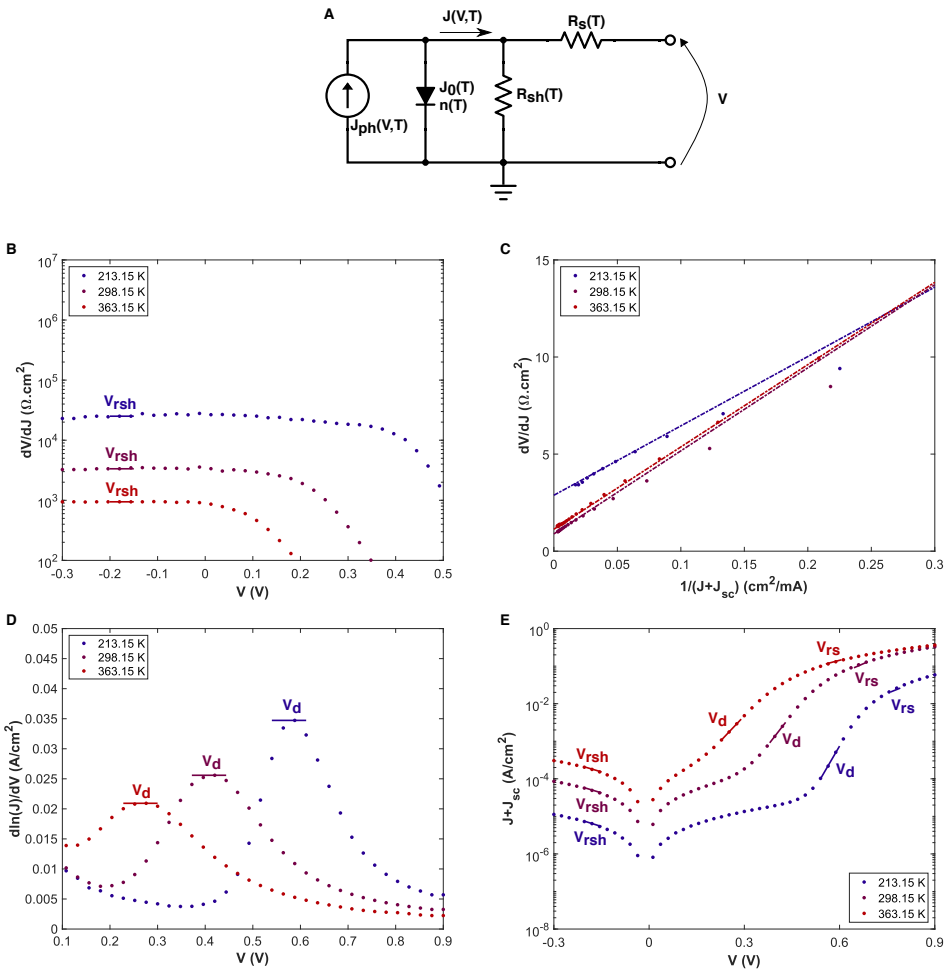

Figure A.8: Detailed extraction of the dark parameters R_s, R_{sh}, J_0 and n at 3 example measurement temperatures of 213.15 K (blue), 298.15 K (purple) and 363.15 K (red) for sample A1. (A) Equivalent circuit of the single diode model with the photo-generated current J_{ph}, pn heterojunction (HJ) diode with saturation current density J_0 and ideality factor n, series resistance R_s and shunt resistance R_{sh} for a total current J at an applied bias V. (B) Derivative of the voltage in function of the current dV/dJ versus voltage V for the extraction of R_{sh} in the voltage range V_{rsh} where the derivative is flat. (c) Derivative of the voltage in function of the current dV/dJ versus inverse current 1/J for the extraction of R_s in the voltage range V_{rs} as the intercept of the linear fit with the vertical axis. (D) Derivative of the current logarithm in function of the voltage dln(J)/dV versus voltage V for the extraction of J_0 and n in the voltage range V_d where the curve has its maximum. The linear fit in V_d provides n as the inverse slope and J_0 as the intercept with the vertical axis. (E) Representation of the three voltage ranges V_{rsh}, V_{rs} and V_d for the 3 example JV curves.

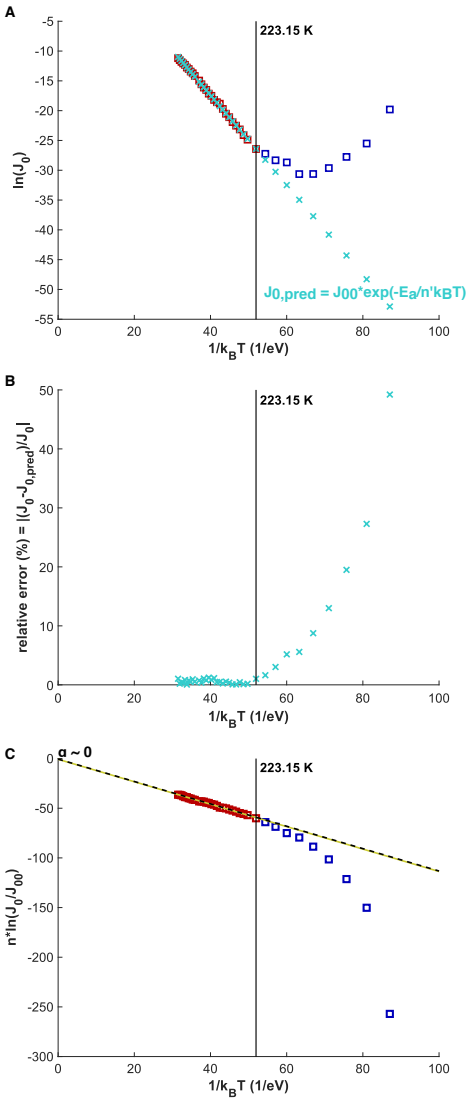

Figure A.9: Temperature dependence of dark diode parameters and the fitting quality of the single diode model for sample A1. In all graphs, the temperature of 223.15 K delimiting the Model Applicability (MA) and Out-of-Model (OoM) range is depicted as a vertical black solid line. (A) Comparison between the experimentally extracted J_0, shown as red and blue squares for the MA and OoM ranges, and the theoretical predictions based on the single diode model using the extracted E_a, J_{00} and n' as described in the main text, shown as cyan crosses, in function of the inverse thermal energy $1/k_BT$. (B) Absolute value of the relative error between the experimental J_0 and the theoretical predictions $J_{0,pred}$, in function of the inverse thermal energy $1/k_BT$. (c) Comparison of the linear slopes of the $n*\ln(J_0/J_{00})$ (solid green line) and $\ln(J_0/J_{00})$ (black dashed line) representations, with the data shown as red and blue squares for the MA and OoM ranges. This demonstrates the benign character of bandgap dependence on temperature and electrostatic potential fluctuations, i.e. $\alpha \sim 0$ as described in the main text.

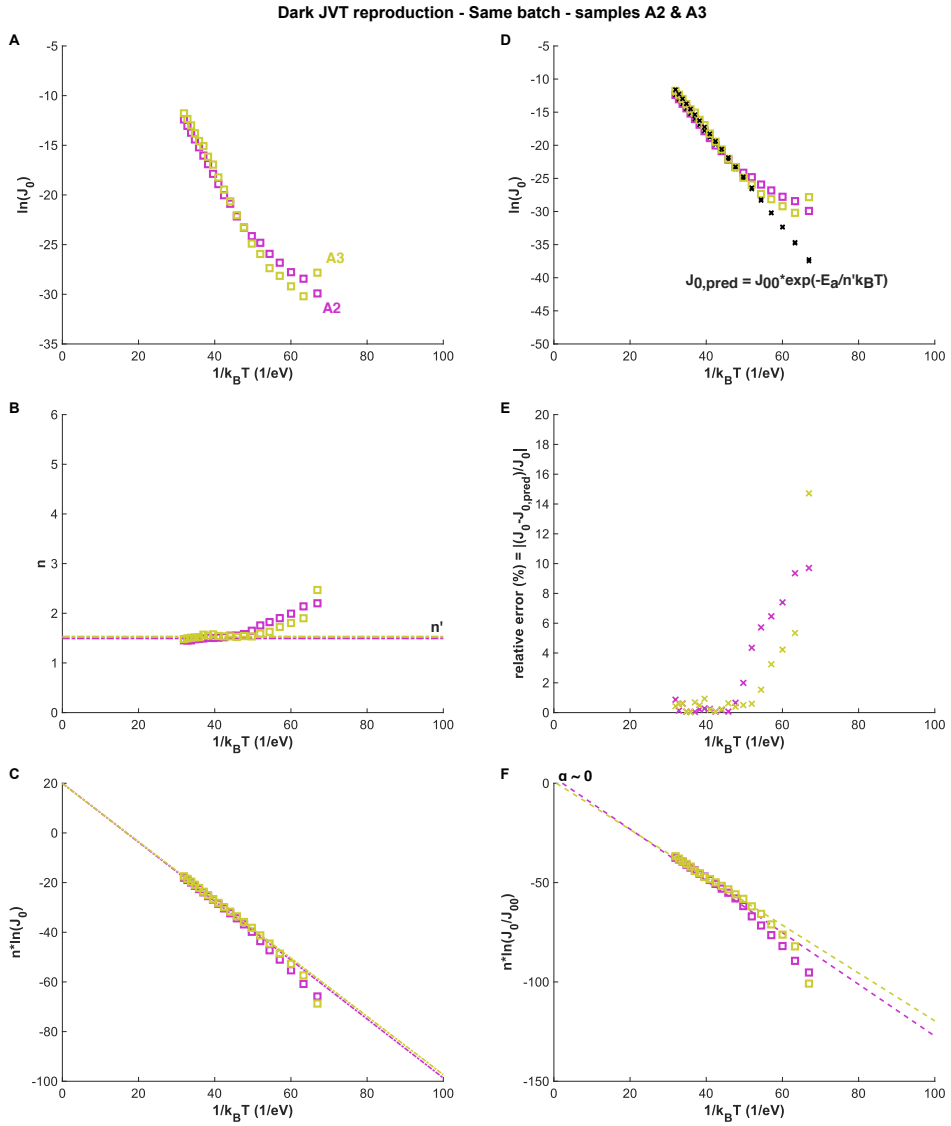

Figure A.10: Reproduction of the dark JVT analysis on samples A2 (pink) and A3 (yellow) having a similar absorber as compared to A1, following the same procedure and notations as in Figure 4.2 and Figure A.9 which can be referred to for complete information. In all graphs, the horizontal axis is the inverse thermal energy $1/k_BT$. (A-C) Evolution of (A) ln(J_0), (B) n, (C) $n * \ln(J_0)$. (D) Comparison between the experimentally extracted J_0 (squares) and the theoretical predictions (crosses) based on the single diode model. (E) Absolute value of the relative error between the experimental J_0 and the theoretical predictions $J_{0,pred}$. (F) Comparison of the linear slopes of the $n*\ln(J_0/J_{00})$ and $\ln(J_0/J_{00})$ representations, demonstrating the benign character of bandgap dependence on temperature and electrostatic potential fluctuations ($\alpha \sim 0$). The parameters extracted from this analysis are provided in Table A.4.

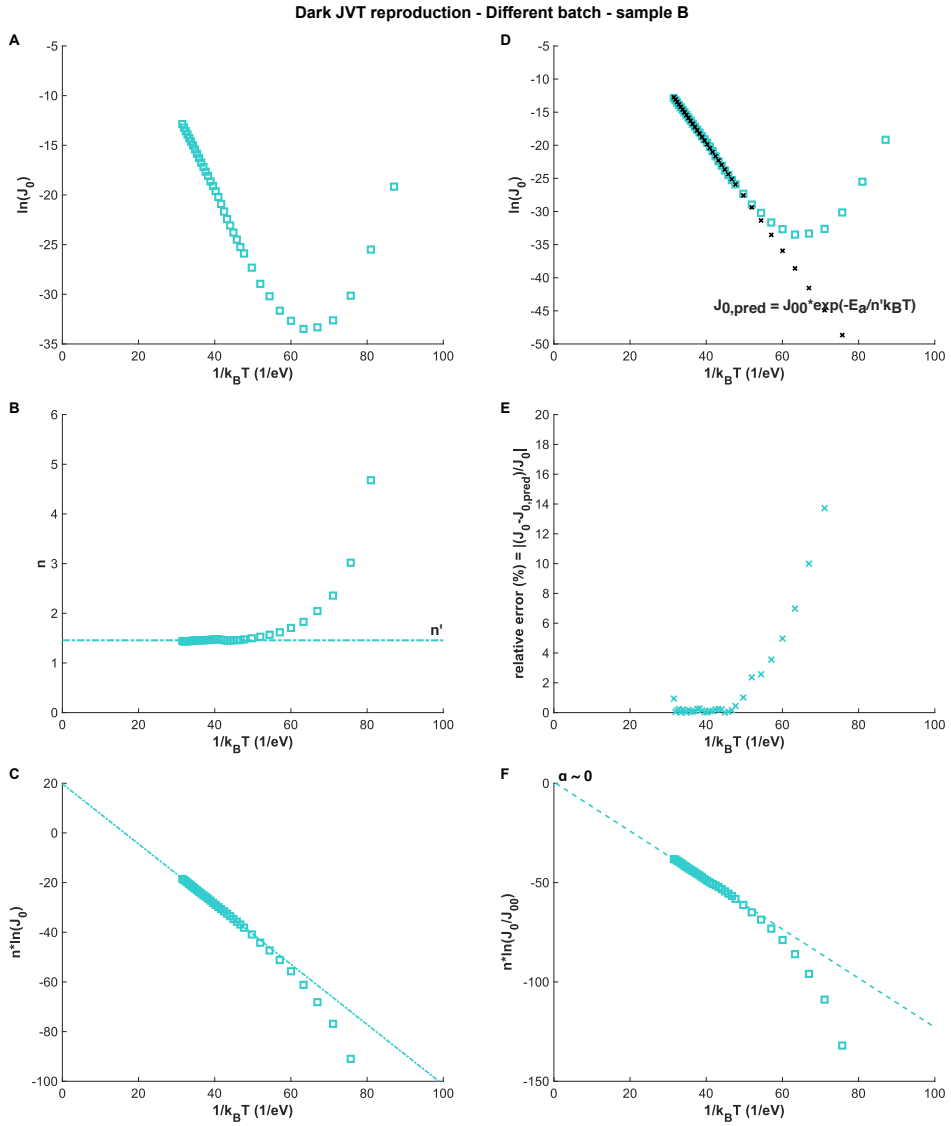

Figure A.11: Reproduction of the dark JVT analysis on sample B having a slightly different absorber as compared to A1, following the same procedure and notations as in Figure 4.2 and Figure A.9 which can be referred to for complete information. In all graphs, the horizontal axis is the inverse thermal energy $1/k_BT$. (A-C) Evolution of (A) $\ln(J_0)$, (B) n, (C) $n * \ln(J_0)$. (D) Comparison between the experimentally extracted J_0 (squares) and the theoretical predictions (crosses) based on the single diode model. (E) Absolute value of the relative error between the experimental J_0 and the theoretical predictions $J_{0,pred}$. (F) Comparison of the linear slopes of the $n * \ln(J_0/J_{00})$ and $\ln(J_0/J_{00})$ representations, demonstrating the benign character of bandgap dependence on temperature and electrostatic potential fluctuations ($\alpha \sim 0$). The parameters extracted from this analysis are provided in Table A.4.

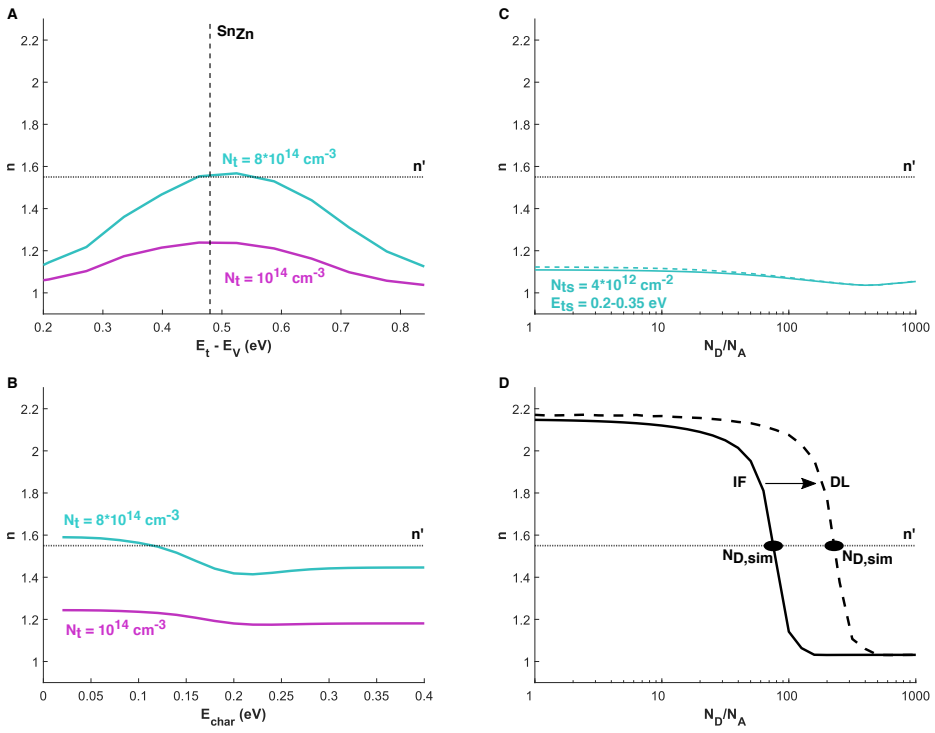

Figure A.12: Results of SCAPS-1D[52] simulations to study the variation of the ideality factor n in function of the buffer doping and different defect properties. Simulations are performed at 300 K with the model described in the main text and using the parameters in Table A.5. In all graphs, the horizontal dotted line represents the true ideality factor n'. (A) Variation of the ideality factor n in function of the bulk defect depth at a low buffer doping ($N_D = 10^{15} cm^{-3}$) and for 2 different defect densities N_t. The vertical dashed line represents the energy depth of the Sn_{Zn} antisite defect identified as detrimental for performance[53]. No significant changes to the ideality factor are observed as compared to the high buffer doping case developed in the main text since purely bulk recombination is not affected by buffer properties. (B) Variation of the ideality factor n in function of the bulk defect gaussian energy distribution width E_{char} for a fixed depth of 480 meV above the absorber valence band at a high buffer doping ($N_D = 10^{17} cm^{-3}$). Energy distributions broader than approximately 125 meV lead to slightly improved ideality factors for $N_t = 8 * 10^{14} cm^{-3}$. (c) Variation of the ideality factor n in function of the HJ doping ratio N_D/N_A for a high-density ($N_{ts} = 4 * 10^{12} cm^{-2}$) acceptor defect at the HJ interface, for 2 different defect depths E_t. (D) Comparison of the ideality factor dependence on the HJ doping ratio N_D/N_A for a medium-density ($N_{ts} = 4 * 10^{11} cm^{-2}$) acceptor defect with an energy level 500 meV above the absorber valence band, either at the interface (IF, black solid line) or within a 10 nm-thick defective layer in the absorber at the HJ interface with equivalent volume density of $N_t = 4 * 10^{17} cm^{-3}$ (DL, dashed solid line).

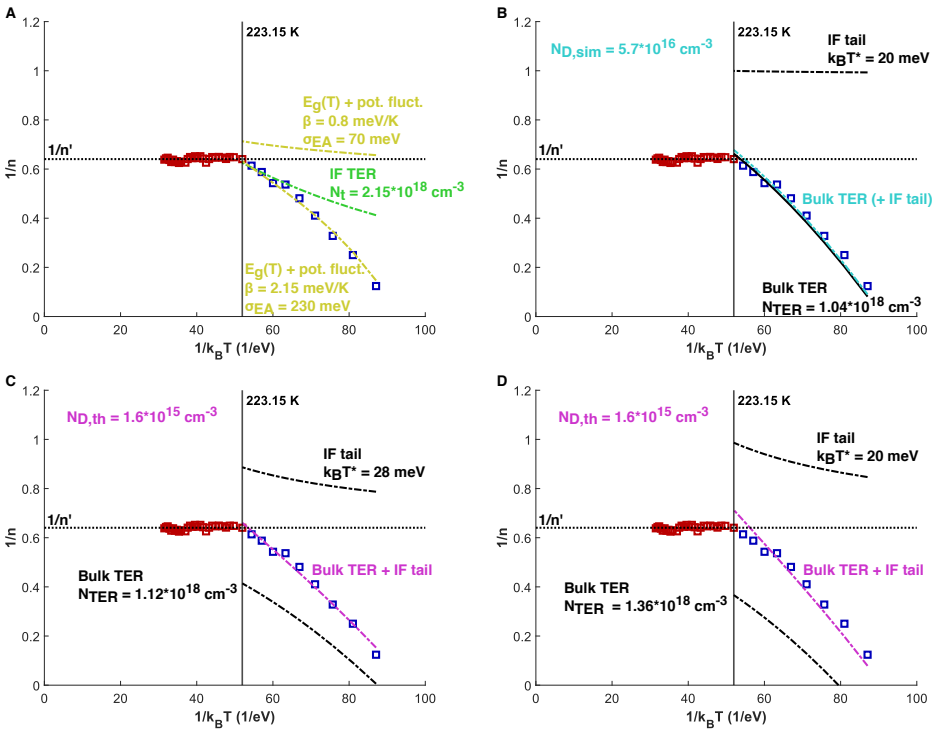

Figure A.13: Fitting of different models to predict the temperature-dependence of the inverse ideality factor $1/n$. In all graphs, the data are shown as red and blue squares for the MA and OoM ranges and in function of the inverse thermal energy $1/k_BT$. The temperature of 223.15 K delimiting the MA and OoM range is depicted as a vertical black solid line. The horizontal dotted line represents the value of the inverse true ideality factor $1/n'$ in MA as described in the main text. (A) Tentative fitting for the tunneling-enhanced recombination at the interface (IF-TER, green dashed line) and the bandgap dependence with temperature and potential fluctuations ($E_g(T)$ + pot. fluct., yellow dashed lines). The IF-TER model is expressed as $1/n(T) = (E_{00}/k_BT) * \coth\ (E_{00}/k_BT)$, the best fitting of which only shows poor agreement with the data, hence ruled out as the origin of $n(T)$ in the OoM range. A previous study[54] provides the bandgap and potential fluctuations model expression $1/n(T) = E_{a0}/(n'E_a(T)) - (\sigma_{EA}^2)/(2n'E_a(T)k_BT)$ with $E_a(T) = E_{a0} - \beta T - (\sigma_{EA}^2)/(2n'k_BT)$. Using the reported values[54] $E_{a0} = 1.2eV$, $\beta = 0.8meV/K$ and $\sigma_{EA} = 70meV$ in the present case does not allow to fit the data as shown by the upper yellow dashed line. Only unrealistic values $E_{a0} = 2.43eV$, $\beta = 2.05meV/K$ and $\sigma_{EA} = 230meV$ not matching with the device behaviour and diode activation energy can lead to close agreement with the experiments (lower yellow dashed line). The associated phenomenon can thus not explain the dependence of n with temperature in the OoM region. (B) In the high CdS doping case $N_D = N_{D,sim} = 5.7 * 10^{16}cm^{-3}$ with k_BT^* fixed at 20 meV, i.e. close to absorber Urbach energy, fitting results are $E_{00} = 19.1meV$ and $N_{TER} = 1.04 * 10^{18}cm^{-3}$. In this case, IF tails have nearly no contributions to $n(T)$ as expected from the corresponding term being inversely proportional to N_D. (c) In the low CdS doping case $N_D = N_{D,th} = 1.6 * 10^{15}cm^{-3}$ with k_BT^* left as parameter, fitting results are $E_{00} = 19.8meV$, $N_{TER} = 1.12 * 10^{18}cm^{-3}$ and $k_BT^* = 28meV$. In this case, IF tails justify $n(T)$ jointly with Bulk-TER. (D) In the low CdS doping case $N_D = N_{D,th} = 1.6 * 10^{15}cm^{-3}$ with k_BT^* fixed at 20 meV, i.e. close to absorber Urbach energy, fitting results are $N_{TER} = 1.36 * 10^{18}cm^{-3}$ and lead to a poorer fit than (C).

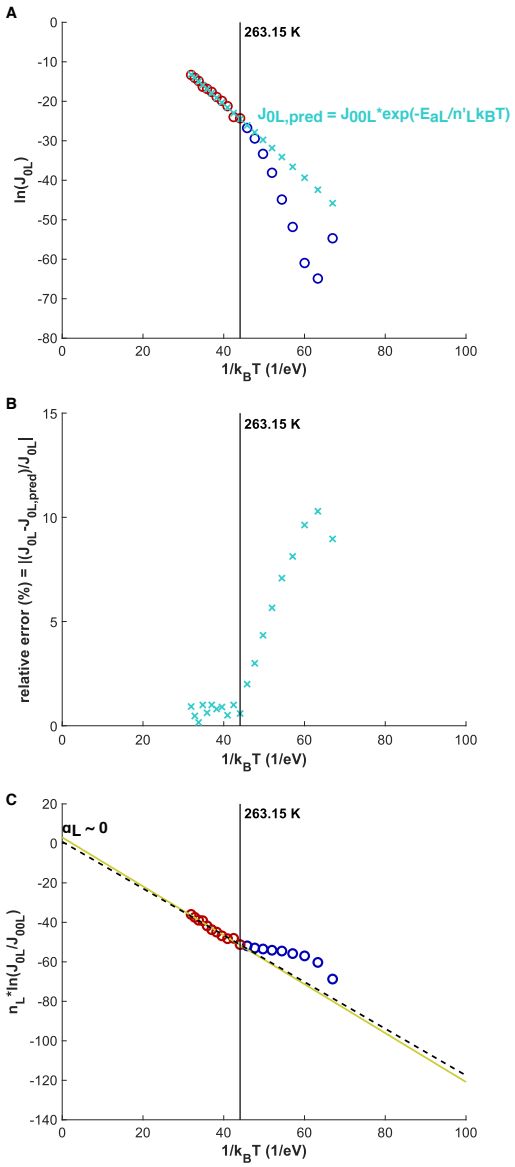

Figure A.14: Temperature dependence of light diode parameters and the fitting quality of the single diode model. In all graphs, the temperature of 263.15 K delimiting the MA and OoM range is depicted as a vertical black solid line. (A) Comparison between the experimentally extracted J_{0L}, shown as red and blue circles for the MA and OoM ranges, and the theoretical predictions based on the single diode model using the extracted E_{aL}, J_{00L} and n'_L as described in the main text, shown as cyan crosses, in function of the inverse thermal energy $1/k_BT$. (B) Absolute value of the relative error between the experimental J_{0L} and the theoretical predictions $J_{0L,pred}$, in function of the inverse thermal energy $1/k_BT$. (c) Comparison of the linear slopes of the $n_L * ln(J_{0L}/J_{00L})$ (solid green line) and $ln(J_{0L}/J_{00L})$ (black dashed line) representations, with the data shown as red and blue circles for the MA and OoM ranges. This demonstrates the benign character of bandgap dependence on temperature and electrostatic potential fluctuations, i.e. $\alpha_L \sim 0$ as described in the main text.

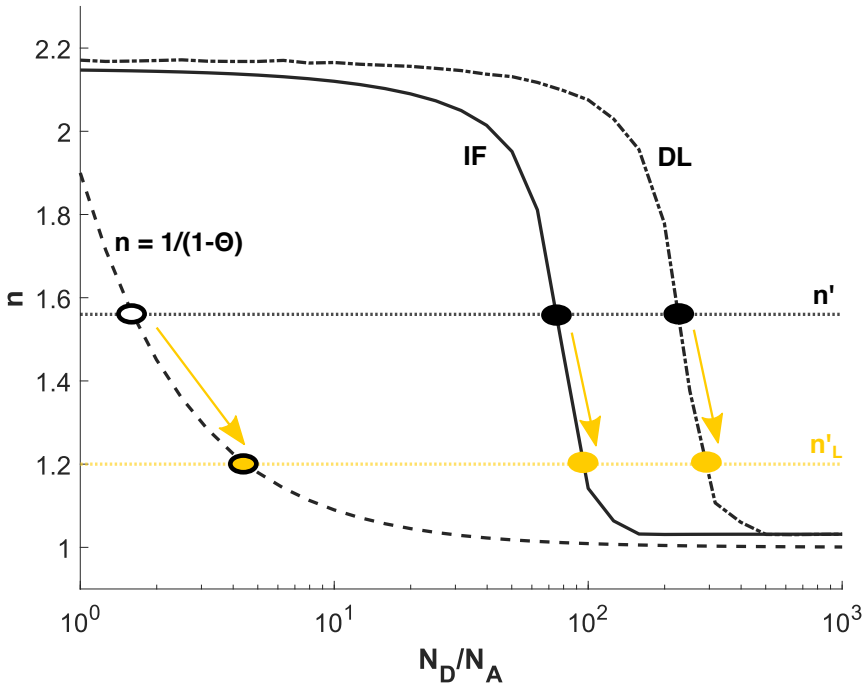

Figure A.15: Results of SCAPS-1D simulations of the ideality factor dependence in function of the buffer doping and its potential change under illumination. Simulations are performed at 300 K using the parameters in Table A.5 and in function of the HJ doping ratio N_D/N_A for a medium-density ($N_{ts} = 4 * 10^{11} cm^{-2}$) acceptor defect with an energy level 500 meV above the absorber valence band, either at the interface (IF, black solid line) or within a 10 nm-thick defective layer in the absorber at the HJ interface with equivalent volume density of $N_t = 4 * 10^{17} cm^{-3}$ (DL, dashdotted black line). The black dashed curve represents the theoretical model $n = 1/(1-\theta)$ related to interface-limited recombination[55]. The black (resp. orange) horizontal dotted lines represent the true ideality factor n' in the dark (resp. under light) while the orange arrows represent the possible effect of CdS photodoping described in the main text.

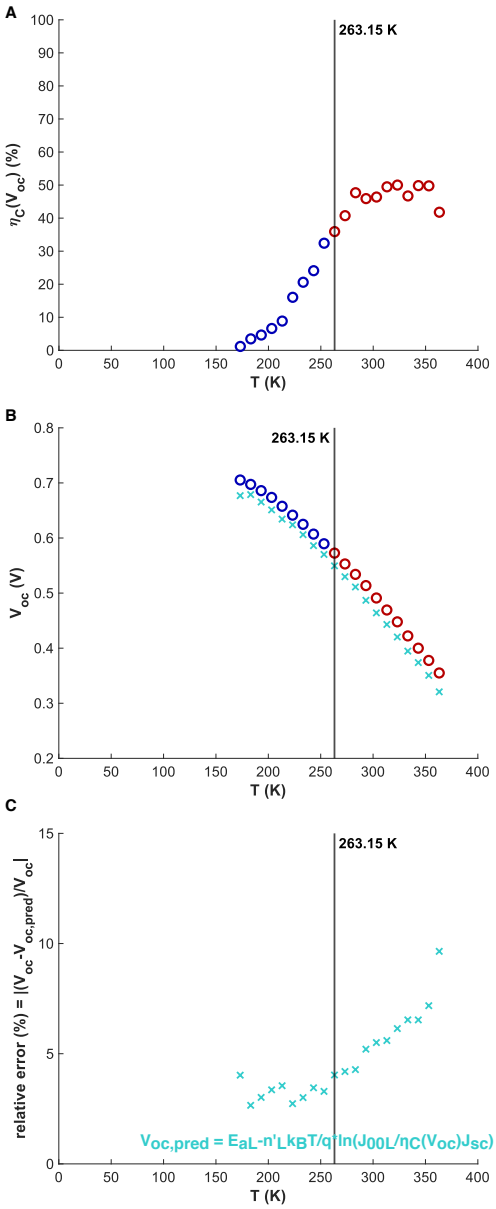

Figure A.16: Estimation of collection efficiency and the theoretical predictions of V_{oc} at 0.95 sun. In all graphs, the temperature of 263.15 K delimiting the MA and OoM range is depicted as a vertical black solid line. (A) Temperature evolution of the collection efficiency evaluated at V_{oc} and 0.95 sun, shown as red and blue circles for the MA and OoM ranges. (B) Comparison between the experimentally extracted V_{oc}, shown as red and blue circles for the MA and OoM ranges and the theoretical predictions $V_{oc,pred}$ based on the single diode model under light using the extracted E_{aL}, J_{00L} and n'_L (cyan crosses) in function of the inverse thermal energy $1/k_BT$. (c) Absolute value of the corresponding relative error.

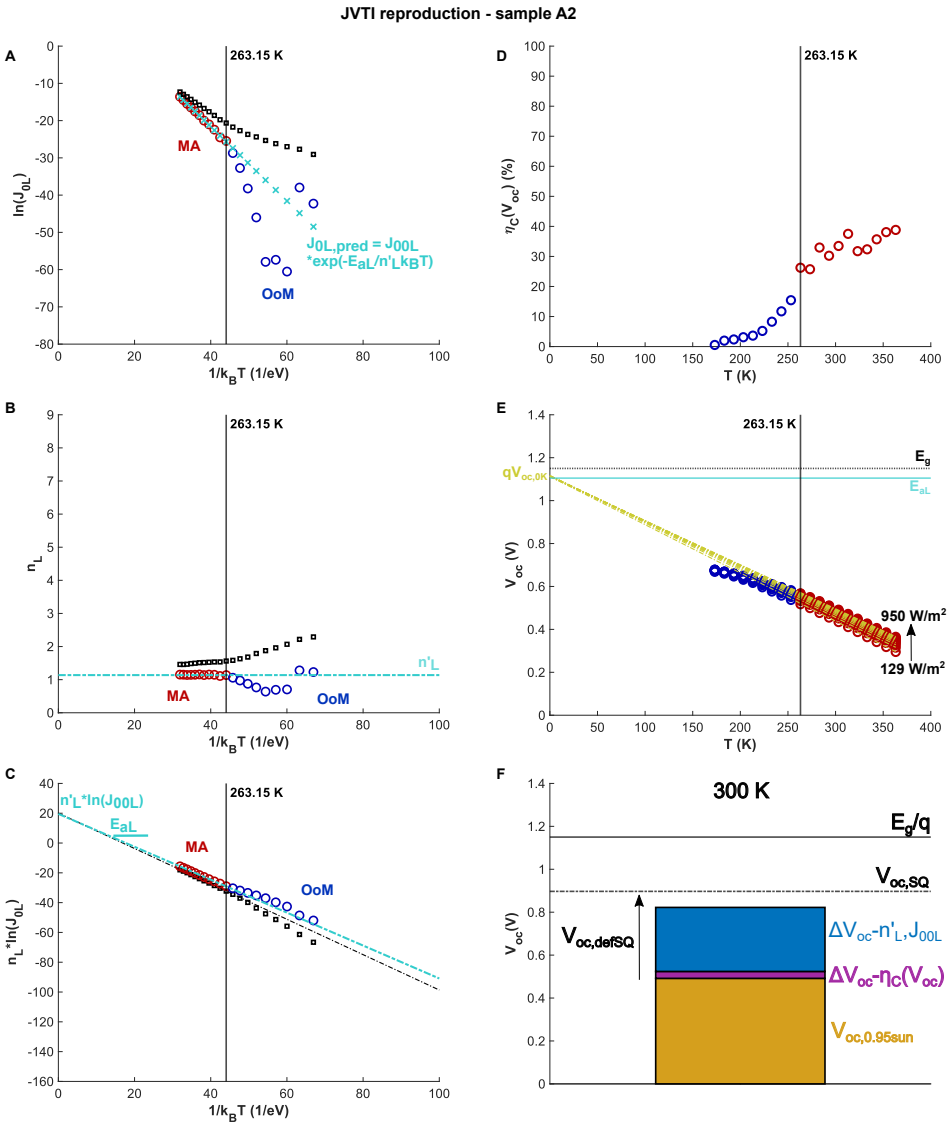

Figure A.17: Reproduction of the JVTI analysis on sample A2. In all graphs except (F), the temperature of 263.15 K delimiting the MA and OoM range is depicted as a vertical black solid line and data points in those ranges are shown as red and blue circles, respectively. The same procedure and notations as in Figure 4.8, Figure 4.9 and Figure A.16 are used. (A-C) Evolution of (A) the saturation current density J_{0L}, (B) the ideality factor n_L and (C) their product $n_L * \ln(J_{0L})$ in function of the inverse thermal energy $1/k_BT$ for the A2 sample, all obtained via the J_{sc}-V_{oc} methodology. The value of the true ideality factor $n'_L = 1.14$ as well as the linear fit to $n_L * \ln(J_{0L})$ leading to $E_{aL} = 1.13eV$ and $J_{00L} = 2.96 * 10^7 A/cm^2$ are shown as cyan dashed lines. The dark results are shown as black squares and black dashed lines for comparison. The parameters extracted from this analysis are provided in Table A.4. (D) Temperature evolution of the collection efficiency $\eta_C(V_{oc}, T)$ evaluated at V_{oc} and 0.95 sun. (E) Temperature evolution of V_{oc} at different light intensities. (F) Graphical representation of the breakdown of potential V_{oc} gains.

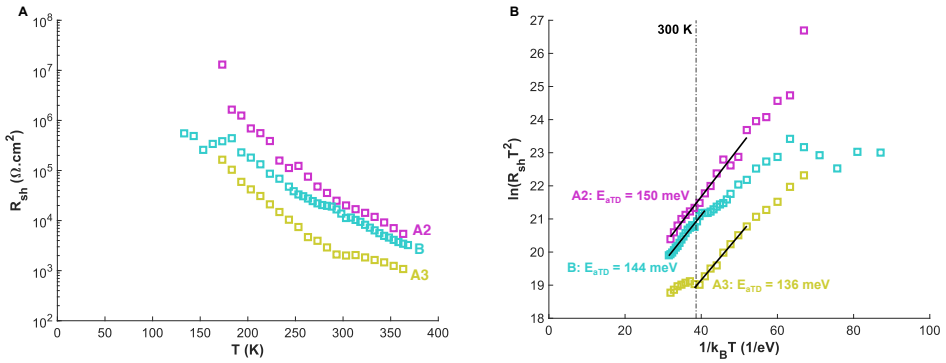

Figure A.18: Reproduction of the reverse bias analysis on samples A2, A3 and B. Evolution of (A) R_{sh} in function of the temperature T and of (B) $\ln(R_{sh}T^2)$ in function of the inverse thermal energy $1/k_BT$ following the dark extraction, with data shown as pink, yellow and cyan squares for respectively the A2, A3 and B samples. The black solid lines represent the linear fitting around room temperature (300 K indicated by the dashed vertical line), providing the activation energies E_{aTD} related to trapping-detrapping (TD).

Sample	n'	J_0 (nA/cm^2) at 300 K	E_a (eV)	J_{00} (A/cm^2)
A1	1.56	66.59	1.15	$1.85 * 10^5$
A1-L	1.20	6.15	1.17	$7.77 * 10^7$
A2	1.50	45.82	1.19	$6.32 * 10^5$
A2-L	1.14	2.06	1.13	$2.96 * 10^7$
A3	1.53	96.72	1.17	$4.49 * 10^5$
B	1.46	8.07	1.21	$8.01 * 10^5$

Table A.4: Dark and light diode parameters for the samples under study. A1, A2, A3 and B correspond to the extraction of n', J_0 at 300 K, E_a and J_{00} in the dark as developed in the dark JVT section, while A1-L and A2-L correspond to the extraction of n'_L, J_{0L} at 300 K, E_{aL} and J_{00L} under light as developed in the JVTI section.

Property	CZTSSe	CdS	i-ZnO	ITO
Thickness (μm)	1.5	0.05	0.05	0.4
E_g (eV)	1.04	2.42	3.3	3.4
χ (eV)	4.3	4.2	4.4	4.4
ϵ	7	10	9	9
N_C (cm^{-3})	$2.2 * 10^{18}$	$1.3 * 10^{18}$	$2.2 * 10^{18}$	$2.2 * 10^{18}$
N_V (cm^{-3})	$1.8 * 10^{19}$	$9.1 * 10^{18}$	$1.8 * 10^{19}$	$1.8 * 10^{19}$
v_{thn} (cm/s)	10^7	$3.1 * 10^7$	10^7	10^7
v_{thp} (cm/s)	10^7	$1.6 * 10^7$	10^7	10^7
μ_n (cm^2/V.s)	40	160	50	100
μ_p (cm^2/V.s)	35	15	5	25
N (cm^{-3})	10^{15} (A)	10^{15} to 10^{18} (D)	$5 * 10^{17}$ (D)	$5 * 10^{20}$ (D)
	Bulk defect (case 1)			
N_t (cm^{-3})	10^{14} to $8 * 10^{14}$			
$E_t - E_V$ (eV)	0.2 to 0.84			
σ_n (cm^2)	10^{-13}			
σ_p (cm^2)	10^{-15}			
E_{char} (eV)	0.02 to 0.4 (G)			
	IF defect (case 2)			
N_{ts} (cm^{-2})	$4 * 10^{10}$ to $4 * 10^{12}$			
$E_t - E_V$ (eV)	0.2 to 0.5			
σ_n (cm^2)	10^{-13}			
σ_p (cm^2)	10^{-15}			
	Defective layer			
N_t (cm^{-3})	$4 * 10^{17}$			
$E_t - E_V$ (eV)	0.5			
σ_n (cm^2)	10^{-13}			
σ_p (cm^2)	10^{-15}			

Table A.5: SCAPS-1D model parameters used for studying the variation of ideality factor in function of defect properties and buffer doping. For the doping densities N, the letter in brackets indicates the type of doping element, A for acceptor and D for donor. In the bulk case, (G) means that the defect energy distribution is Gaussian.

Sample	V_{oc} (V)	J_{sc} (mA/cm^2)	FF (%)	η (%)
A1	0.497	33.47	66.46	11.64
A2	0.492	31.59	65.57	10.72
A3	0.491	34.21	66.37	11.74
B	0.536	29.00	63.26	10.35

Table A.6: PV performance figures-of-merit V_{oc}, J_{sc}, FF and η for the samples under study under AM1.5G $950W/m^2$ (0.95 sun) incident power. Sample A1 is used to develop the methodology presented in the main text, samples A2 and A3 are reproductions of equivalent devices used to strengthen the validity of the model while the absorber of sample B is slightly different to demonstrate the potential applicability to other types of devices. In particular, it has a slightly higher absorber bandgap, explaining its higher V_{oc} and lower J_{sc}.

Bibliography

[1] D. Abou-Ras et al. 2016, pp. 371–420. DOI: 10.1002/9783527699025.ch14.

[2] J. Álvarez-García et al. 2016, pp. 469–499. DOI: 10.1002/9783527699025.ch17.

[3] S. Schorr et al. 2016, pp. 421–440. DOI: 10.1002/9783527699025.ch15.

[4] V. Hoffmann et al. 2016, pp. 523–567. DOI: 10.1002/9783527699025.ch19.

[5] T. Unold and L. Gütay. 2016, pp. 275–297. DOI: 10.1002/9783527699025.ch11.

[6] M. Klenk et al. *Solar Energy Materials and Solar Cells* 58.3 (1999), pp. 299–319. DOI: 10.1016/S0927-0248(99)00014-8.

[7] S. S. Hegedus and W. N. Shafarman. *Progress in Photovoltaics* 12.2-3 (2004), pp. 155–176. DOI: 10.1002/pip.518.

[8] Z. Zhang et al. *Sol. RRL* 4.5 (2020), p. 2000059. DOI: 10.1002/solr.202000059.

[9] M. Neuschitzer et al. *J. Mater. Chem. A* 6.25 (2018), pp. 11759–11772. DOI: 10.1039/C8TA02551G.

[10] Y. Deng et al. *Journal of Energy Chemistry* 61 (2021), pp. 1–7. DOI: 10.1016/j.jechem.2021.02.011.

[11] J. Liu et al. *ACS Appl. Mater. Interfaces* 13.47 (2021), pp. 56302–56308. DOI: 10.1021/acsami.1c16861.

[12] S. Lee et al. *Solar Energy* 194 (2019), pp. 114–120. DOI: 10.1016/j.solener.2019.10.042.

[13] S. Giraldo et al. *Energy Environ. Sci.* 11.3 (2018), pp. 582–593. DOI: 10.1039/C7EE02318A.

[14] J. Wang et al. *Advanced Materials* 34.27 (2022), p. 2202858. DOI: 10.1002/adma.202202858.

[15] C. Andres et al. *Thin Solid Films* 665 (2018), pp. 168–172. DOI: 10.1016/j.tsf.2018.09.022.

[16] Y. Sun et al. *Materials Letters* 195 (2017), pp. 76–78. DOI: 10.1016/j.matlet.2017.02.090.

[17] D. B. Khadka, S. Kim, and J. Kim. *J. Phys. Chem. C* 120.8 (2016), pp. 4251–4258. DOI: 10.1021/acs.jpcc.5b11594.

[18] T. Sanchez et al. *Solar Energy Materials and Solar Cells* 198 (2019), pp. 44–52. DOI: 10.1016/j.solmat.2019.04.011.

[19] S. Sun et al. *International Conference on Optoelectronic and Microelectronic Technology and Application*. 2020, p. 165. DOI: 10.1117/12.2585461.

[20] K.-S. Lim et al. *Materials Science in Semiconductor Processing* 89 (2019), pp. 194–200. DOI: 10.1016/j.mssp.2018.09.020.

[21] N. Saini et al. *Journal of Alloys and Compounds* 880 (2021), p. 160478. DOI: 10.1016/j.jallcom.2021.160478.

[22] I. Kim et al. *Chem. Mater.* 26.13 (2014), pp. 3957–3965. DOI: 10.1021/cm501568d.

[23] J. Li et al. *Materials Letters* 190 (2017), pp. 188–190. DOI: 10.1016/j.matlet.2016.12.106.

[24] L. Sun et al. *Vacuum* 165 (2019), pp. 186–192. DOI: 10.1016/j.vacuum.2019.04.026.

[25] A. Lokhande et al. *Solar Energy Materials and Solar Cells* 161 (2017), pp. 355–367. DOI: 10.1016/j.solmat.2016.12.016.

[26] J. Fu et al. *J. Mater. Chem. A* 8.42 (2020), pp. 22292–22301. DOI: 10.1039/D0TA06318E.

[27] B. H. Lee et al. *Materials Letters* 284 (2021), p. 128981. DOI: 10.1016/j.matlet.2020.128981.

[28] L. Du et al. *Journal of Alloys and Compounds* 737 (2018), pp. 184–188. DOI: 10.1016/j.jallcom.2017.12.040.

[29] S. Kim et al. *Appl. Phys. Express* 9.10 (2016), p. 102301. DOI: 10.7567/APEX.9.102301.

[30] A. D. Collord and H. W. Hillhouse. *Chem. Mater.* 28.7 (2016), pp. 2067–2073. DOI: 10.1021/acs.chemmater.5b04806.

[31] D. Nowak et al. *Applied Sciences* 12.3 (2022), p. 1376. DOI: 10.3390/app12031376.

[32] C. Gao, Y. Sun, and W. Yu. *Coatings* 8.9 (2018), p. 304. DOI: 10.3390/coatings8090304.

[33] S. Kim et al. *Solar Energy Materials and Solar Cells* 144 (2016), pp. 488–492. DOI: 10.1016/j.solmat.2015.09.039.

[34] S. Bag et al. *Chem. Mater.* 24.23 (2012), pp. 4588–4593. DOI: 10.1021/cm302881g.

[35] Q. Guo et al. *Solar Energy Materials and Solar Cells* 105 (2012), pp. 132–136. DOI: 10.1016/j.solmat.2012.05.039.

[36] X. Lv et al. *Ceramics International* 46.16 (2020), pp. 25638–25645. DOI: 10.1016/j.ceramint.2020.07.039.

[37] W. Zhao, D. Pan, and S. Liu. *Nanoscale* 8.19 (2016), pp. 10160–10165. DOI: 10.1039/C6NR00959J.

[38] C. J. Hages et al. *Prog. Photovolt: Res. Appl.* 23.3 (2015), pp. 376–384. DOI: 10.1002/pip.2442.

[39] P. Punathil et al. *Solar Energy* 236 (2022), pp. 599–607. DOI: 10.1016/j.solener.2022.03.027.

[40] A. Ruiz-Perona et al. *Solar Energy* 199 (2020), pp. 864–871. DOI: 10.1016/j.solener.2020.02.082.

[41] A. Ruiz-Perona et al. *Solar Energy* 206 (2020), pp. 555–563. DOI: 10.1016/j.solener.2020.06.044.

[42] G. M. Ford et al. *Chem. Mater.* 23.10 (2011), pp. 2626–2629. DOI: 10.1021/cm2002836.

[43] L. Choubrac et al. *ACS Appl. Energy Mater.* 3.6 (2020), pp. 5830–5839. DOI: 10.1021/acsaem.0c00763.

[44] T. Schnabel, M. Seboui, and E. Ahlswede. *Energies* 10.11 (2017), p. 1813. DOI: 10.3390/en10111813.

[45] T. Schnabel, M. Seboui, and E. Ahlswede. *RSC Adv.* 7.1 (2017), pp. 26–30. DOI: 10.1039/C6RA23068G.

[46] A. Ruiz-Perona et al. *Journal of Alloys and Compounds* 868 (2021), p. 159253. DOI: 10.1016/j.jallcom.2021.159253.

[47] A. Ruiz-Perona et al. *Solar Energy* 226 (2021), pp. 251–259. DOI: 10.1016/j.solener.2021.08.032.

[48] N. Saini et al. *Solar RRL* 6.2 (2022), p. 2100837. DOI: 10.1002/solr.202100837.

[49] D. B. Khadka and J. Kim. *J. Phys. Chem. C* 119.4 (2015), pp. 1706–1713. DOI: 10.1021/jp510877g.

[50] G. Brammertz et al. *IEEE J. Photovoltaics* 10.4 (2020), pp. 1102–1111. DOI: 10.1109/JPHOTOV.2020.2992350.

[51] T. Kohl et al. *Solar Energy Materials and Solar Cells* 231 (2021), p. 111289. DOI: 10.1016/j.solmat.2021.111289.

[52] M. Burgelman, P. Nollet, and S. Degrave. *Thin Solid Films* 361-362 (2000), pp. 527–532. DOI: 10.1016/S0040-6090(99)00825-1.

[53] S. Kim et al. *Energy Environ. Sci.* 13.5 (2020), pp. 1481–1491. DOI: 10.1039/D0EE00291G.

[54] C. J. Hages et al. *Journal of Applied Physics* 115.23 (2014), p. 234504. DOI: 10.1063/1.4882119.

[55] R. Scheer. *Journal of Applied Physics* 105.10 (2009), p. 104505. DOI: 10.1063/1.3126523.